NOVEL CATALYSTS FOR THE ELECTRO- AND PHOTOELECTROCHEMICAL CO2/H2O TRANSFORMATION FOR CHEMICAL PRODUCTION

Roger Miró Serra

UNIVERSITAT ROVIRA i VIRGILI

Novel catalysts for the electro- and photoelectrochemical CO_2/H_2O transformation for chemical production

Roger Miró Serra

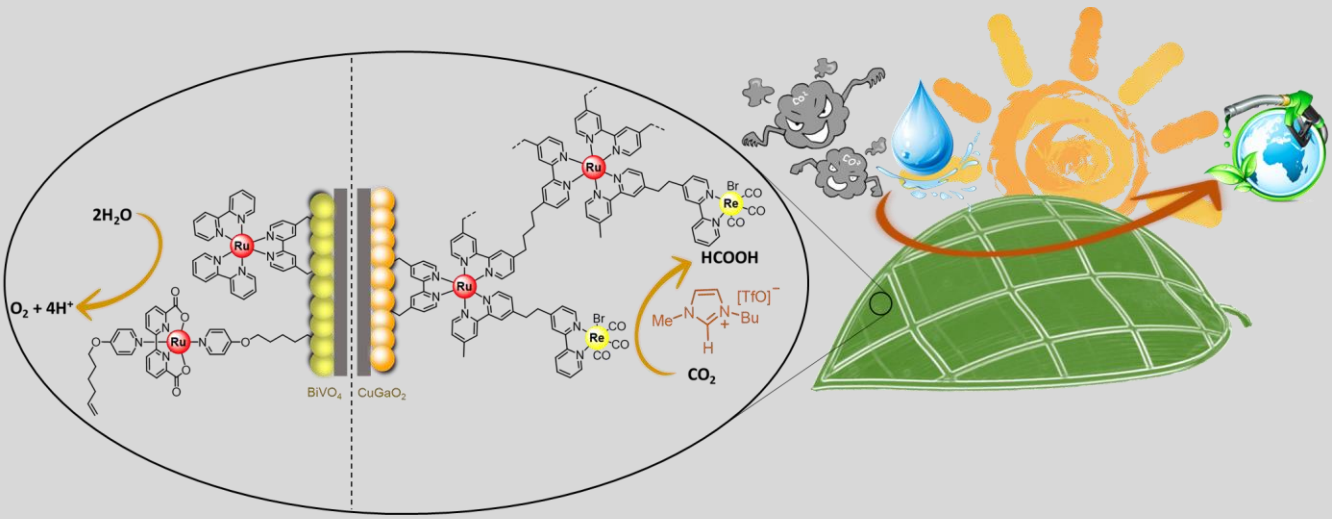

DOCTORAL THESIS
2022

Roger Miró Serra

Novel catalysts for the electro- and photoelectrochemical CO_2/H_2O transformation for chemical production

DOCTORAL THESIS

Supervised by

Dra. Miriam Díaz de los Bernardos, Dr. Aitor Gual and Dr. Cyril Godard

Eurecat, Centre Tecnològic de Catalunya and Universitat Rovira i Virgili

UNIVERSITAT ROVIRA i VIRGILI

Tarragona

2022

Dra. Miriam Díaz de los Bernardos and Dr. Aitor Gual principal investigators at the Unitat de Tecnologia Química of Eurecat and Dr. Cyril Godard professor agregat at the Departament de Química Física i Inorgànica at the Universitat Rovira i Virgili.

We STATE that the present study, entitled "Novel catalysts for the electro- and photoelectrochemical CO_2/H_2O transformation for chemical production", presented by Roger Miró Serra to receive the degree of Doctor, has been carried out under our supervision at the Unitat de Tecnologia Química of Eurecat and fulfills all the requirements to be eligible for the International Doctor Distinction.

Tarragona, June 28th, 2022

Doctoral Thesis Supervisors

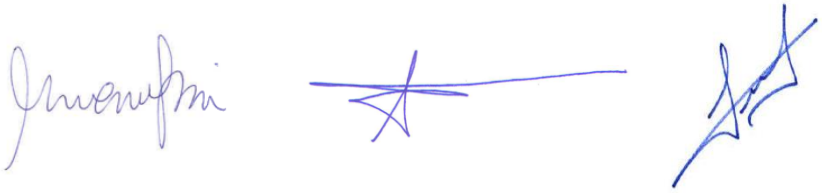

Dra. Miriam Díaz de los Bernardos Dr. Aitor Gual Dr. Cyril Godard

The work performed in the present doctoral thesis has been possible thanks to Eurecat, Centre Tecnològic de la Química de Catalunya for the "Vicente López" PhD Fellowship, to the European Union's Horizon 2020 research and innovation programme under grant agreement No. 862192 (Photoelectrocatalytic device for SUN-driven CO_2 conversion into green CHEMicals**,** SunCOChem), the Ministerio de Economia y Competividad, the Fondo Europeo de Desarrollo Regional FEDER (PID2019-104427RB-I00) and the Generalitat de Catalunya (ILCATSYN project PR19/0015).

Acknowledgments

Primer de tot m'agradaria donar les gràcies als meus directors de tesis, Dra. Miriam Díaz de los Bernardos, Dr. Cyril Godard i Dr. Aitor Gual, per tota l'ajuda i suport que m'heu donat durant tots aquests anys. També m'agradaria donar les gràcies a Eurecat per concedir-me la beca "Vicente López" per la qual he pogut realitzar la tesis durant aquests 3 anys, participar en congressos i haver tingut l'oportunitat de realitzar una estada internacional.

M'agradaria agrair tot el suport i l'ajuda de la meva família, en especial als meus pares i a la meva germana. Sempre m'heu recolzat en tot el que he decidit fer, mai m'ha faltat de res i sé que sempre estareu aquí per el que faci falta. Sense vosaltres no hauria pogut arribar fins aquí. Gràcies per tot!

Després de tants anys al grup han passat moltes persones, m'agradaria donar les gràcies a tots els companys que m'han acompanyat i ajudat durant tots aquests anys, sense vosaltres no hauria sigut el mateix.

Finalment, també voldria donar les gracies a la professora Simelys Hernandez i al seu grup de recerca, on vaig realitzar la meva estada doctoral. Gràcies per l'oportunitat, va ser una experiència molt enriquidora que em va permetre aprendre moltíssim!

Table of contents

Glossary of terms and abbreviations

ACN	Acetonitrile
bda	[2,2'- bipyridine]-6,6'-dicarboxylate
bpy	2,2'-bipyridine
bpyC2bpy	1,2-bis(4'-methyl-[2,2'-bipyridin]-4-yl)ethane
bpym	2,2'-Bipyrimidine
$bpyMe_2$	4,4'-dimethyl-2,2'-bipyridine
bpy-V	4,4'-Divinyl-2,2'-bipyridine
CA	Chronoamperometry
CB	Conduction band
CCU	Carbon capture and utilization
CE	Counter electrode
CO_2RR	Carbon dioxide reduction reaction
CP	Chronopotentiometry
CV	Cyclic voltammetry
DMPA	2,2-Dimethoxy-2-phenylacetophenone
DMF	N,N-Dimethylformamide
DMSO	Dimethyl sulfoxide
DSPEC	Dye sensitized photoelectrochemical cell
DSSC	Dye sensitized solar cell
E	Potential
$E_{1/2}$	Half wave potential
EC	Electrochemical device
EDX	Energy Dispersive X-ray Spectroscopy
$EMI{\cdot}BF_4$	1-ethyl-3-methylimidazolium tetrafluoroborate
EMI·TCB	1-ethyl-3-methylimidazolium tetracyanoborate
E^o	Standard potential
ESEM	Environmental Scanning Electron Microscopy
Et_3N	Triethylamine
EtOH	Ethanol
FE	Faradaic efficiency
$Fe^{III}TPP{\cdot}Cl$	5,10,15,20-Tetraphenyl-21*H*,23*H*-porphine iron(III) chloride
FESEM	Field Emission Scanning Electron Microscopy
FTO glass	Fluorine doped tin oxide coated glass
GC-TCD	Gas chromatography with thermal conductivity detector

Abbreviations

HER	Hydrogen evolution reaction
HRMS	High resolution mass spectroscopy
I2M	Bimolecular interaction mechanism
ICP-MS	Inductively coupled plasma mass spectrometry
IL	Ionic liquid
IPA	Isopropanol
IR	Infrared spectroscopy
J	Current density
KB_i	Potassium borate buffer
LSV	Linear sweep voltammetry
M	Molar
MeOH	Methanol
MPTMS	(3-Mercaptopropyl)trimethoxysilane
MS	Mass spectroscopy
NHE	Normal hydrogen electrode
NMR	Nuclear magnetic resonance
NPs	Nanoparticles
OER	Oxygen evolution reaction
PEC	Photoelectrochemical cell
pic	4-picoline
ppm	Parts per million
PS I	Photosystem I
PS II	Photosystem II
py	pyridine
RE	Reference electrode
Re_{CAT}	Re CO_2 reduction catalyst
rt	Room temperature
RuRe1	Supramolecular Ru-Re complex
RuRe2	Binuclear Ru-Re complex
Ru_{VLA}	Ruthenium visible light absorber
Ru_{WOC}	Ruthenium water oxidation catalyst
SC	Semiconductor
SEM	Scanning electron microscopy
SHE	Standard hydrogen electrode
$TBA{\cdot}BF_4$	Tetrabutylammonium tetrafluoroborate
$TBA{\cdot}PF_6$	Tetrabutylammonium hexafluorophosphate
tda	[2,2':6',2"-terpyridine]-6,6"-dicarboxylate

Abbreviations

TFE	Trifluoroethanol
THF	Tetrahydrofuran
TOF	Turnover frequency
TON	Turnover number
UV-Vis	Ultraviolet–visible spectroscopy
VB	Valence band
VLA	Visible light absorber
vs	versus
VTES	Vinyltriethoxysilane
WE	Working electrode
WNA	Water nucleophilic attack
WOC	Water oxidation catalyst
XPS	X-ray photoelectron spectroscopy
XRD	X-ray diffraction analysis
δ	Chemical shift
λ	Wavelength

Summary

The world energy consumption is increasing every year. A major part of this energy is still depending on fossil fuels production processes. These processes are the main cause of global warming. During the last years, efforts to develop sustainable chemical processes based on the application of renewable energy are increasing.

Among the renewable energy sources, the solar energy is the most relevant as it is inexhaustible, clean, and well dispersed. However, the limitations of the solar energy lie in its intermittent nature, the geographic limitation of application due to zones with lack of irradiation, and the limited application to sectors for which the electrification is very difficult. Therefore, there is a need for the development of processes involving the transformation and storage of the renewable energy in the form of chemical bonds in stable molecules. There are two possible approaches: (i) the direct photochemical or photoelectrochemical transformation of raw materials such as CO_2 and H_2O, the so call artificial photosynthesis, and (ii) the transformation of raw materials such as CO_2 into useful chemicals in electrochemical processes using potentially green-electricity generated from renewable energies.

This thesis has been focused on the development of efficient electro- and photoelectrochemical catalytic systems for water oxidation and CO_2 reduction into value-added chemicals involving the direct use of renewable solar energy by a photoelectrochemical process or the use of renewable electricity by an electrochemical process.

In **Chapter 3**, the influence of ionic liquid (IL) electrolyte structures was applied in the electrochemical CO_2 reduction to CO using a commercial iron (III) porphyrin ($Fe^{III}TPP{\cdot}Cl$). Systematic modifications of the cation and anion structures resulted in a small library of monocationic and dicationic

Summary

imidazolium ILs. These ILs were applied in the CO_2 electroreduction reaction to CO, revealing, for the first time, that the application of dicationic IL electrolytes resulted in higher faradaic efficiencies and lower overpotentials than monocationic ILs. This was attributed to the reduction potential of E Fe^{I}/Fe^{0} caused by the ionic liquid cation-iron complex anion pairing effect and the reduction of the E CO_2/CO overpotential by the push-pull mechanism. In this mechanism, the electrons are pushed into the CO_2 molecule by the electron-rich catalyst and the cleavage of one of the C-O bonds is facilitated by the synergetic contribution of the electron deficient cations of the ionic liquids. The electrochemical CO production was optimized, and the generated CO was directly used in tandem processes for organic synthesis involving different Pd-catalyzed carbonylation reactions and, for the first time, Rh-catalyzed hydroformylation reaction.

In **Chapter 4**, the photoelectrochemical CO_2 reduction using hybrid molecular/semiconductor photocathodes with ILs as electrolytes was evaluated in a H-type reactor at ambient temperature and pressure. The innovation dealt with the preparation of novel complexes and the application of an electropolymerization approach to immobilize Ru and Re molecular complexes onto Cu-based semiconductors (Cu_2O/SnO_2 and $CuGaO_2$). The electropolymerization approach consisted in a two-reaction sequence: first, the silanization of the semiconductor material, and later, the electropolymerization procedure provided a series of molecular and supramolecular hybrid photocathodes for solar driven CO_2 reduction. Focusing on the cathodic half reactions, the most promising conditions for the formation of CO_2 reduction products were determined. The results revealed that the ionic liquid plays a critical role in the conversion of CO_2 to formic acid with the suppression of the hydrogen production. Furthermore, our results revealed, for the first time, that the anchoring of supramolecular complexes

onto this kind of Cu-semiconductor photoelectrocatalyst boosted both the transport of carriers and the catalytic activity to formate as the major product.

Finally, in **Chapter 5,** the photoelectrochemical H_2O oxidation using hybrid molecular/semiconductor photoanodes was evaluated in a one-chamber custom Teflon cell at ambient temperature and pressure. The innovation relied in the preparation of novel complexes and the application of two different strategies to immobilize vinyl-tagged molecular complexes onto $BiVO_4$ and $BiVO_4$@Al_2O_3-layer. The target was to improve the overall performance of the bare $BiVO_4$ photoelectrode in the water oxidation reaction. The strategies were based on: (i) silanization of $BiVO_4$ with vinyltriethoxysilane (VTES) followed by electropolymerization in the presence of vinyl-tagged molecular complexes; and (ii) silanization of $BiVO_4$ with (3-Mercaptopropyl)trimethoxysilane (MPTES) followed by thiol-ene click chemistry reaction with vinyl-tagged molecular complexes. The resulting hybrid materials were tested as photoanodes for solar driven water oxidation reaction, the preliminary results showed in a small improvement of the photocurrent on water oxidation performance.

Chapter 1

General Introduction

Chapter 1

1.1. Fossil fuel dependence

There is an increasing demand of energy for maintaining the current standard of living and extending it around the world. To date, the vast majority of energy is produced by combustion of fossil fuels. These combustion processes resulted in large CO_2 emissions and other greenhouse gases in the atmosphere.

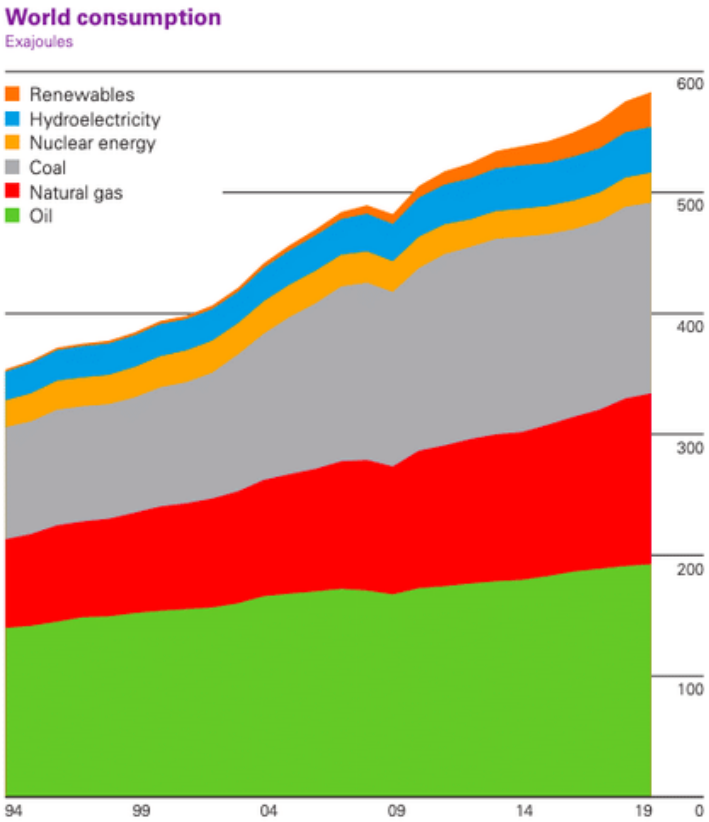

***Figure 1**: World energy consumption (1994-2019). Reprinted from ref [1].*

In particular, the chemical industry dependence on fossil fuels use (both as carbon building blocks for organic synthesis and as fuels for providing energy for driving the chemical transformations) presents an important emissions challenge. In Europe, the chemical industry greenhouse emissions (150 million tons of CO_2) represent 0.6 % of the total world's emissions. The production of

chemical from petroleum sources, such as ethane and naphtha, resulted in large CO_2 emissions. However, the demand of these products is continuously growing due to the need of these feedstocks in the manufacture of consumers goods (personal care items, food preservatives, fertilizers, and furnishings). The problem is that fossil fuels are not a renewable resource, and, eventually, there will be no other choice than to find alternatives. While there are compelling reasons to end fossil fuel dependence, the related cost and the lack of alternatives prevented so far. The cost of renewable energies is decreasing and the fossil fuel concerns are arising, and then, the development of alternatives based in renewable energies is more favorable. However, the complete replacement of fossil fuels is very difficult and probably not possible currently. The largest reservoir of renewable energy comes from wind and solar sources. These sources are enough to produce electrical energy for attaining the world energy demand.[2] Unfortunately, the intermittent nature of these resources limits the electrical energy that they can supply to the grid without causing instability and power fluctuations. Therefore, a more continuous and stable supply of electricity from renewable resources to the grid is necessary. This can be accomplished through an efficient energy storage mechanism that can take energy when an excess is available and release it when needed. Unfortunately, no existing energy storage technology is currently capable of accomplishing this task at the necessary scale and cost.[3]

An alternative carbon source for the production of chemicals and carbon-based products is also necessary to overcome the industrial dependance on fossil fuel derived chemicals. There are a number of alternative electricity sources such as nuclear, geothermal, hydro, wind, solar, and biomass. Biomass is the most accessible alternative source of carbon.[4] However, the use of biomass also has a number of drawbacks. For instance, the production of biomass competes with land currently used for crops for food producing, and only a limited amount of biomass is available before resulting in a negative

environmental and human health-related consequences.[5] These factors restricts the overall use of biomass as a source of carbon-based products.

Conversion of CO_2 to fuels and chemicals through electrochemical, photoelectrochemical or photochemical reduction would avoid the problems associated with biomass. The use of CO_2 as carbon source is one promising solution to energy storage and for the generation of carbon containing compounds.[6]

The next section will discuss the advantages of this approach and the different alternative procedures to accomplish the CO_2 conversion.

1.2. CO_2 conversion

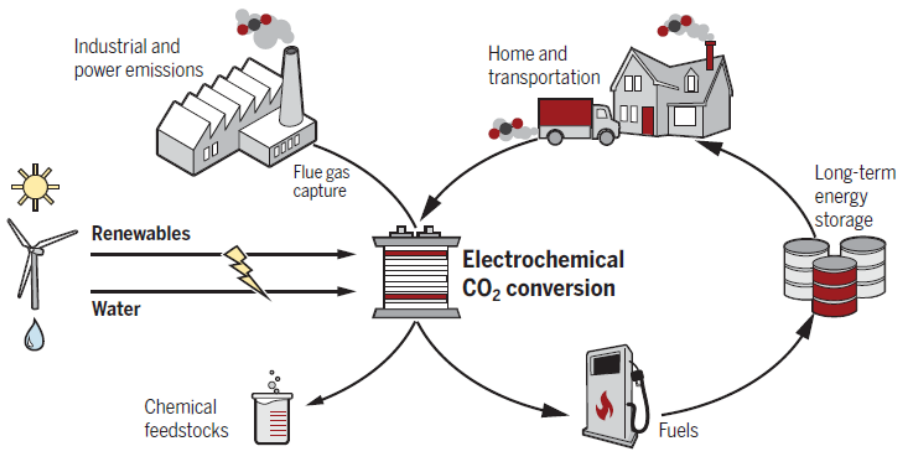

***Figure 2**: Reduction of CO_2 using renewably sourced electricity. Transformation of CO_2 emissions into chemical feedstocks or fuels. Reprinted from ref [3].*

The conversion of CO_2 into fuels and chemicals using energy derived from a renewable source, such as, wind or solar, has the potential to reduce the use of fossil fuels. The conversion of CO_2 would offer a way to indefinitely store energy from intermittent sources as a chemical fuel. Energy could be stored as chemical fuels during the periods of excess electricity generation, and later,

this energy could be extracted via combustion, or electrochemically (i.e., a fuel cell), when the energy output of a wind or solar installation dipped. Carbon-based chemicals could be generated in this way to replace those currently derived from petroleum building blocks. Figure 2 shows the carbon cycle involving the carbon dioxide electrochemical conversion (reduced). This is one focus of this thesis.

The general transformation occurring in the electrochemical device in the Figure 2 is displayed in Eq. 1.1. This general process is divided in two half reactions, namely oxygen evolution reaction (OER) and carbon dioxide reduction reaction (CO_2RR), displayed in Eq. 1.2 and Eq. 1.3, respectively.

$$CO_2 + H_2O \rightarrow C_xH_yO_z + mO_2 \quad \text{(Eq. 1.1)}$$

$$H_2O \rightarrow O_2 + 4H^+ + 4e^- \quad \text{(Eq. 1.2)}$$

$$xCO_2 + yH^+ + ne^- \rightarrow C_xH_yO_z + mH_2O \quad \text{(Eq. 1.3)}$$

For Equation 1.1 to proceed forward, a significant input of energy is needed, in the form of electrical power, which is converted into energy stored in the chemical bonds of the compounds produced. The equilibrium potentials, which are determined solely by thermodynamics, are given for a subset of possible CO_2RR products in Table 1. Both OER and CO_2RR have large kinetic barriers that must be overcome by using catalysts. For both reactions, even with the best available catalysts, an excess of voltage beyond what is thermodynamically required is needed. This excess of voltage is the overpotential. Lowering the overpotential through the discovery of more active catalysts increases the energy efficiency of producing chemicals and fuels electrochemically through carbon dioxide reduction.

***Table 1**: Equilibrium potentials for various CO_2 reduction reactions vs standard hydrogen electrode (SHE). Adapted from ref [7].*

Equation	Reaction	E_{eq} (V vs SHE)
1	$CO_{2(g)} + e^- \leftrightarrow CO_{2(aq)}^{\cdot -}$	-1.99
1'	$CO_{2(aq)} + e^- \leftrightarrow CO_{2(aq)}^{\cdot -}$	-1.90
2	$CO_{2(g)} + 2H_{(aq)}^+ + 2e^- \leftrightarrow HCO_2H_{(aq)}$	-0.61
3	$CO_{2(g)} + 2H_{(aq)}^+ + 2e^- \leftrightarrow CO_{(g)} + H_2O_{(l)}$	-0.52
3'	$3CO_{2(g)} + H_2O_{(l)} + 2e^- \leftrightarrow CO_{(g)} + 2HCO_{3(aq)}^-$	-0.56
4	$CO_{2(g)} + 4H_{(aq)}^+ + 4e^- \leftrightarrow H_2C(OH)_{2(aq)} + H_2O_{(l)}$	-0.49
5	$CO_{2(g)} + 6H_{(aq)}^+ + 6e^- \leftrightarrow CH_3OH_{(aq)} + H_2O_{(l)}$	-0.38
6	$CO_{2(g)} + 8H_{(aq)}^+ + 8e^- \leftrightarrow CH_{4(g)} + 2H_2O_{(l)}$	-0.24
7	$2H^+ + 2e^- \leftrightarrow H_2$	-0.42

Equation 1.3 is written in a general form to demonstrate that many carbon-containing products are possible. The identity of the products formed depends on several factors, and among them, the nature of the catalyst will play one of the most important roles. At the same potential as CO_2RR occurs, it is also possible for water to be reduced to make hydrogen (hydrogen evolution reaction, HER). The ideal catalyst would produce selectively the desired CO_2RR product and reduce the side HER.

Another possibility to achieve carbon dioxide electrolysis is to couple catalysts for the reaction directly to the surface of a semiconductor in a photoelectrochemical device.[8] The difficulty of this approach lies in the discovery of semiconductor(s) with the correct properties to generate the voltage necessary to reduce carbon dioxide. Because catalysts requirements are similar for electrochemical and photoelectrochemical CO_2RR, it is possible to develop the catalysts and semiconductors used in this approach separately. Then, electrocatalysts discovered through purely electrochemical testing could be applied in photoelectrochemical applications by supporting these catalysts onto the appropriate semiconductors. This approach, results in an

economical and sustainable photoconversion of CO_2 with H_2O using solar energy. These systems are known as artificial photosynthesis systems since they used renewable solar energy, mimicking the natural photosynthesis, and achieved the production of solar fuels and high-value chemicals (Figure 3).[9]

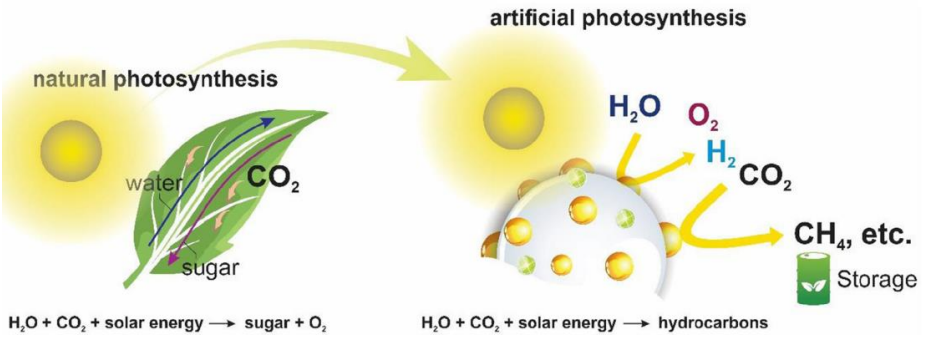

***Figure 3**: Conversion of solar energy by natural photosynthesis and artificial photosynthesis. Reprinted from ref [10].*

The thermochemical conversion of CO_2 is another route to renewable fuels. CO_2 reacts with H_2 at high temperature and under high pressure to produce long chain hydrocarbons (Fischer-Tropsch reaction)[11] or smaller molecules (MeOH synthesis reaction).[12] The main barrier to the formation of renewable fuels and chemicals by these thermochemical routes is the availability of produced hydrogen from renewable sources. Ninety nine percent of hydrogen that is currently on the market comes from fossil fuels. This hydrogen is commonly produced by methane reforming (SMR) or auto thermal reforming (ATR) resulting in grey-hydrogen and large CO_2 emissions to the atmosphere.[13] Recently, blue hydrogen production processes are being developed for the mitigation of the environmental impacts on the planet by approaches that combines steam methane reforming (SMR) or auto thermal reforming (ATR) and the capture and storage of the produced CO_2.[14]

The most promising and environmentally friendly route for the production of hydrogen is the water electrolysis using renewable energy. This process

resulted in the production of green-hydrogen and oxygen with no CO_2 emissions. Similarly, to the case of the CO_2RR, and since these technologies are already under development, new HER catalysts need to be developed for the commercial production of hydrogen by water electrolysis.

Research on both thermochemical and electrochemical CO_2RR routes is needed to improve the performances and optimize these processes. It is generally accepted that the electrochemical route could be more advantageous than the thermochemical route. Since the reaction could be accomplished in a single step and does not require a high temperature or pressure. Then, the implantation of electrochemical routes would result in lower infrastructure costs. Furthermore, the electrochemical route allows the CO_2 reduction in small, portable units, enabling the decentralization of the production of chemicals.

This thesis will focus on the development of electrochemical and photoelectrochemical conversions of raw materials, CO_2 and water, to added-value chemicals.

1.3. Electrochemical Methods

In this thesis, two approaches for the CO_2 electrochemical reduction have been studied:

- Electrocatalysis under dark conditions (e.g., electrolysis cell)
- Photo-assisted electrocatalysis under light illumination (e.g., photoelectrolysis cell)

The next sections will summarize the fundamentals of electrochemical and photoelectrochemical catalytic CO_2 reduction.

1.3.1. Fundamentals of Electrochemical CO_2 Reduction

The development of efficient electrocatalysts is essential for the practical industrial processes application of the CO_2 reduction. The electrocatalyst participates, in both, the electron transfer reaction and the acceleration of the chemical reaction. Thus, for an efficient electrocatalyst, both processes, electron transfer and chemical kinetics, must be fast. Furthermore, an optimal electrocatalyst should show a good thermodynamic match between the standard redox potential (E^0) for the electron transfer reaction and the redox potential of the catalyzed chemical reaction.

An electrocatalyst is an electron transfer agent that ideally operates near the thermodynamic potential of the reaction, E^0 (product/substrate). Some electrochemical reactions require high overpotentials resulting in low conversion efficiencies. The overpotential is the difference between the applied potential and the equilibrium potential, so the kinetic and thermodynamic considerations are both important. To minimize the overpotentials, it is necessary to develop an electrocatalysts with a matching between the formal potential, E^0 ($Cat^{n+/0}$) and the E^0 (product/substrate), as well as, with good rate constants, K_{cat}, for the substrate reduction at this potential. Furthermore, the heterogeneous rate constant, k_h, for the reduction of the electrocatalyst must be high for $V_{applied}$ near E^0 ($Cat^{n+/0}$) (Scheme 1).[15]

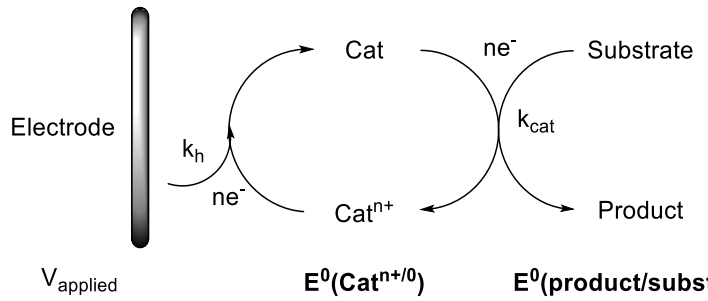

***Scheme 1**: Electrocatalysis with electron source. Adapted from ref* [15].

CO_2 activation and reduction steps constitute a significant challenge due to the high stability of the molecule. Furthermore, CO_2 does not have electrical dipole making the CO_2 activation and reduction very energy demanding and reducing the efficiencies. In Table 1, the equilibrium potentials of the CO_2 reduction reaction and the competitive hydrogen evolution reaction are listed for aqueous media versus standard hydrogen electrode (SHE). These potentials explained the formation of H_2 as the major byproduct in the CO_2 electroreduction in aqueous solution. Another challenge is the reduction of CO_2 with good selectivity due to the small difference in thermodynamic potentials of the different CO_2 reduction products.[16]

The CO_2 reduction is a multi-electron/proton transfer process which can be divided in four steps: i) the first step is the CO_2 dissolution and absorption at the catalyst surface; (ii) in the second step, a high energy impute is required to reorganize the linear CO_2 molecule to a bent radical anion $CO_2^{\cdot-}$, formed by one-electron reduction of the CO_2 (Table 1, Eq. 1'). This is the rate determining step; iii) then, a fast multi electron/proton transfer takes place to generate the target product; (iv) and finally, the desorption of the product into the electrolyte or gaseous fase.[17]

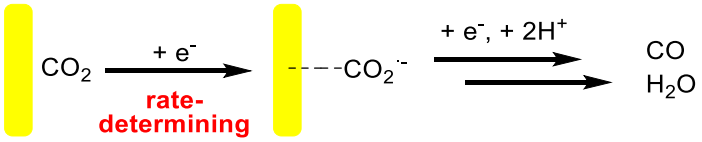

***Figure 4**: Scheme of CO_2 reduction steps. Adapted from ref [17].*

Currently, the main scientific challenges to efficiently perform the CO_2 electroreduction are: (i) the high overpotential required to overcome the energy barrier to form the $CO_2^{\cdot-}$ radical anion, (ii) the hampering of the reaction by the slow kinetics of the CO_2 electroreduction and the limited CO_2 transfer capacity into the reaction system, (iii) the small difference in the

thermodynamic potential between the different CO_2 reduction products difficulted the selective formation of the desired CO_2 reduction product, and (iv) the CO_2 electroreduction reactions are mainly performed in aqueous solution and the competitive hydrogen evolution reaction (HER) take place with a much more positive potential making the CO_2 reduction reaction less effective in terms of faradaic efficiency and selectivity.[16]

1.3.1.1. Electrolytes for CO_2 electroreduction reaction

The electrolyte role is essential since the design of a suitable electrochemical devices requires a good synergy between the electrolyte and the catalyst. The electrolyte provides the medium to perform the reduction reaction which include the interactions with the reactants, electrode surface and intermediates influencing in the reaction pathway.[18]

Various electrolytes such as aqueous electrolytes, organic electrolytes and ionic liquids were used in CO_2 reduction reaction.

Water-based electrolytes

The aqueous electrolytes have limitations, such as: (i) the water limited electrochemical stability by the onset potentials of the proton reduction and water oxidation reactions, (ii) low CO_2 solubility of the reactants, approximately 34 mM at standard conditions, and (iii) the presence of multiple reaction pathways resulting in undesired by-products.

Organic solvents-based electrolytes

In organic electrolytes, such as, acetonitrile, dimethylformamide and methanol, the CO_2 solubility is much higher than in aqueous electrolytes. For instance, the CO_2 solubility in acetonitrile is approximately 270 mM, eight times higher than in aqueous electrolytes. Furthermore, these solvents have lower proton concentration, thus inhibiting the hydrogen evolution reaction.

In organic electrolytes, alternative reaction pathways can take place, favoring the formation of specific products, e.g., in acetonitrile, the main product is CO, whereas in methanol, CO, methane and ethylene are produced.

Ionic liquids-based electrolytes

Finally, during the last decades, the application of ionic liquids (IL) has been extended to many different fields since they displayed much competitive properties respect to aqueous or organic mediums. The general properties and the resulting relevant industrial applications of the ionic liquids are displayed in Figure 5.[19–21]

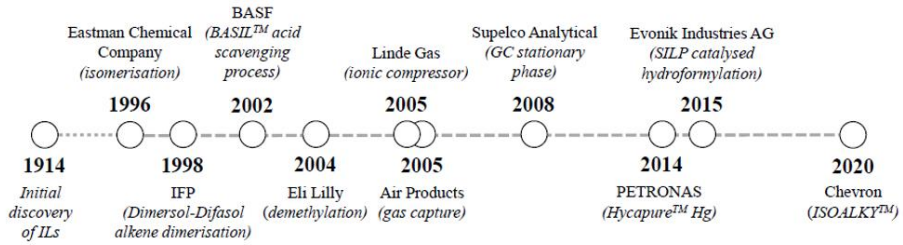

General Properties	Features
Low melting point	• Treated as liquid at ambient temperature • Wide temperature interval for applications
Non volatility	• Thermal stability • Flame retardancy
Composed by ions	• High ion density • High ion conductivity
Organic ions	• Designable/Tuneable • Unlimited combinations possible

***Figure 5**: Ionic liquid properties and industrial applications. Reprinted from* [20,21].

Furthermore, a properties comparison of the organic solvents and ILs is displayed in Figure 6. It is noteworthy, the possibility of fine tuning the properties of the IL makes possible to develop solvents on demand for each particular process by choosing the proper combination of anion and cation structures.[19–21]

Property	Organic Solvents	Ionic Liquids
Number of solvents	>1000	$>10^6$
Applicability in a given process	Single function	Multifunction
Cost	Generally cheap	2 to 100 times more expensive than organic solvents
Recyclability/Toxicity	Green imperative—survey of toxicity of organic solvents is controlled by REACH	Economic imperative—toxicity and biodegradability are often not well known
Vapour pressure	Measurable and generally well-known—several organic solvents have vapour pressure > limit used in the classification of volatile organic compounds (VOCs)	For aprotic ILs: negligible vapour pressure under normal conditions
Flammability	Usually flammable	Usually non-flammable, but some ILs are used as propellants
Tuneability	Limited range of solvents available	Virtually unlimited range means "designer solvents"
Chirality	Rare	Common and tuneable
Catalytic ability	Rare	Common and tuneable
Viscosity/mPa·s	0.2–100	20–97,000
Density/g·cm^{-3}	0.6–1.7	0.8–3.3
Refractive Index	1.3–1.6	1.3–2.2
Electrical conductivity/mS·cm^{-1}	Usually insulator	Up to 120
Thermal conductivity/W·m^{-1}·K^{-1}	0.1–0.6	0.1–0.3

***Figure 6**: Comparison between organic solvents and ionic liquids. Reprinted from ref* [21].

In the specific case of the application of ionic liquid as electrolytes, the combination of the cation and anion is a key parameter that highly affect the process performance as we will demonstrate in this thesis. The following advantages of the IL as electrolytes have been widely recognized in the literature:[18,20,22–24]

- Multifunctional nature of Ionic Liquid electrolytes: Synergy electrolyte-catalyst, stabilization of reaction intermedia, control of the diffusion of the reagents and control on the product selectivity. For instance, ILs electrolytes have different applications in CO_2RR because of high CO_2 adsorption capacity (0.6-0.8 mol CO_2/mol$_{IL}$), high product selectivity, and low energy consumption,[25] as well as their effect on the stabilization of radical and ionic electrochemical active species acting as co-catalyst reducing the overpotential of the CO_2 reduction reaction.[26]
- High electroconductivity and ion conductivity: IL improves efficiency by minimizing ohmic losses.

- High electrochemical stability in appropriate temperature ranges: Water electrochemical stability limited to 1.23 V.
- Non volatility nature: Water application is limited to a wide temperature range (boiling point 100 ºC).
- High safety: IL non-volatile nature minimizes risks of accidental explosion or ignition.
- Non-corrosive materials: IL avoids corrosion observed in highly acidic or basic media in water electrolytes.
- Low environmental impact: The solvent that is substituted for the IL is very harmful (both to the user and to the environment) and by reusing the IL the environmental impact is reduced before disposal.
- IL application: broad range of application in energy devices, i.e., in electrodeposition of metals, electrochemical biosensors, supercapacitors, batteries, and solar cells (See Figure 7).

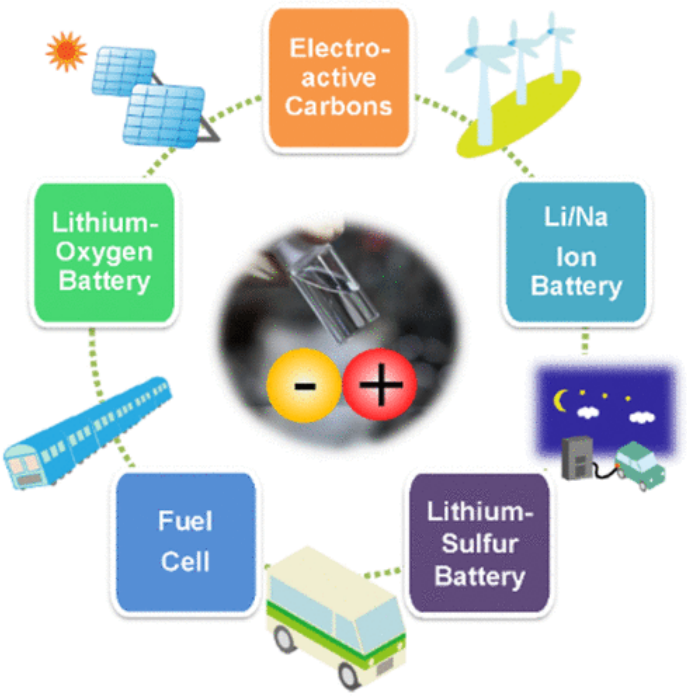

***Figure 7**: Different ionic liquid applications. Reprinted from ref* [23].

The most typical structures of commonly used ILs for the CO_2 electrochemical reduction are summarized in the Figure 8.[18,20] Concerning the cation, imidazolium-based ILs, such as, 1-butyl-3-methyl-imidazolium [BMI] and 1-ethyl-3-methyl-imidazolium [EMI], are among the most studied due to the high stability within oxidative and reductive conditions, low viscosity, and ease of synthesis.[27]

Concerning the anion, different weakly coordinating anions have been studied. Common examples are tetrafluoroborate [BF_4], hexafluorophosphate [PF_6], triflate [TfO], triflimide [NTf_2], and dicyanamide [DCA].[28] Some ILs containing fluorine anions, such as $[PF_6]^-$ or $[BF_4]^-$ are hydrolytically unstable and liberate HF,[29,30] leading to an increase in popularity of water stable anions.

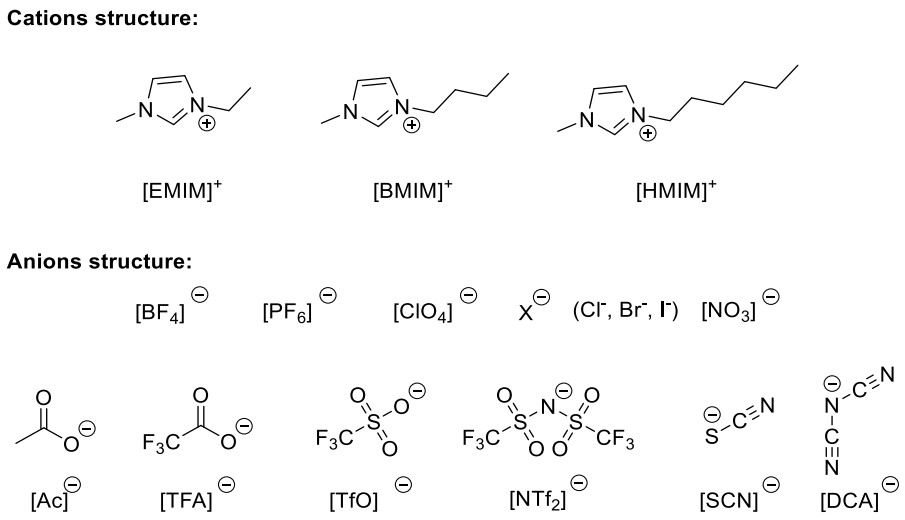

***Figure 8**: Cations and anions structure of the most common ILs used for CO_2 electroreduction.*

In the specific case of the CO_2 electro- and photoelectroreduction, the first use of ionic liquids was reported in 2011 by Masel and co-workers.[31] They observed that the use of ionic liquids shifted the overpotential of the CO_2 reduction to more positive values in a heterogeneous system. This behavior

has been explained by the IL stabilization of the CO_2 reduction reaction intermediates, and thus, facilitating the reduction of these intermediates.

Then, ILs were implemented in both heterogeneous[32–38] and homogeneous[7,39–43] systems. Different imidazolium based ILs, such us [EMIM][BF_4], [BMIM][BF_4] and [BMIM][PF_6] have been widely applied exhibiting excellent performances.[16,44,45] The beneficial effect of the use of IL as electrolyte has been rationalized according to: (i) the strong IL absorption capacity of CO_2, (ii) the tuning of the IL hydrophobicity allows the suppression of the hydrogen evolution reaction (HER) by limiting the diffusion of the water/protons to the surface of the electrodes, and (iii) the reduction of the overpotential and control of the product selectivity by the interaction of the IL with the reaction intermediates.[18]

Most of the studies in the literature have focused on monocationic ILs but less attention has been paid to dicationic ILs respecting electrochemical applications. Dicationic ILs are a new family of ILs. They and consist of a doubly charged cation that are composed of two singly charged cations linked by an alkyl chain spacer and paired with two singly charged anions. There is a large number of possible combinations for cation and anion in dicationic ILs; so dicationic ILs can provide more various properties than monocationic ILs. The density, glass transition temperature (Tg), melting point, surface tension and viscosity of dicationic ILs are higher in comparison with the reference monocationic ILs. The main advantage of dicationic ILs is their higher thermal stability compared to traditional monocationic ILs. In some studies, the ionic conductivity of dicationic ILs, depending on used cations and anions, fall in conductivity range of the monocationic ILs. Studies reported that dicationic ILs, similar to monocationic ILs, can be used equally well as electrolytes in secondary batteries, supercapacitors, solar cells and catalysts especially at high temperatures due to their high stability.[46]

In this thesis, we will study the application of different ionic liquid electrolytes and the selection of the proper combination of anions and cations to boost the catalyst performance in the selected process. For instance, in the **chapter 3**, we will select ionic liquids bearing monocationic and dicationic structures for creating a synergism with the different iron anion intermediates (i.e., $[Fe^{I}]$, $[Fe^{0}]^{2-}$ and $[FeCO_2]^{2-}$). Whereas, in **chapter 4**, the IL structure [BMI][TfO] has been selected for enhancing the CO_2 solubility ([BMI][TfO] displayed one of the greatest CO_2 solubilities among the [BMI] derived ILs) and creating a sufficiently hydrophobic media for reducing the HER.

1.3.1.2. Electrocatalysts for CO_2 reduction reaction

Electrochemical reduction of CO_2 to its reduced oxidation states requires catalysts to accelerate reaction rates and control product selectivities. Indeed, CO_2 can be converted into a variety of products such as formic acid (HCOOH), carbon monoxide (CO), methanol (CH_3OH), methane (CH_4), ethylene (CH_2CH_2), ethanol (C_2H_5OH), and acetate (CH_3COOH). Given the number of possible products, the challenge in this area is the development of catalysts with high reactivity and selectivity toward specific products.

Much research has focused on ways to improve the energy efficiency of CO_2RR. The first real breakthrough occurred in 1985 when Hori *et al.*[47] reported the formation of methane and formate as the major products using copper catalyst in the CO_2RR. Since then, several reports[48–51] have compared the activity of different transition metals and stated that the products of CO_2RR depend on the binding energy of CO to the catalyst.[52] Metals that formed strong bonds with CO produced a few CO_2RR products because they were poisoned by CO or other intermediates formed during CO_2RR. In these cases, hydrogen is the main reaction product. On the other hand, metals that formed weak bonds with CO produced mostly CO as a product. Indeed, with these catalysts, CO is released from the surface and does not undergo further

reduction to products such as alcohols and hydrocarbons. Cu possess an intermediate binding energy for CO, which is believed to be the reason for its unique ability to catalyze the formation of more reduced products. Unfortunately, none of the materials studied to date for CO_2RR catalysis possess the necessary activity to be used commercially. The ideal catalyst should operate at low overpotential with high current densities producing selectively the desired products.

In this context, both homogeneous and heterogeneous metal complex-based catalysts were developed for the electroreduction of CO_2, with a summary of approaches displayed in Figure 9. In homogeneous catalysis, the metal complex acts as a redox shuttle between the electrode and CO_2. In most cases, the catalyst accepts electrons from the electrode, and once reduced, donates electrons to CO_2 in solution, thus regenerating the initial state. The overall reaction is therefore an indirect electrolysis.[53] The organic ligands can be modified to tune the selectivity and efficiency of these catalysts. Catalyst immobilization combines the advantages of homogeneous catalysis (selectivity) with the ability to recycle the catalysts. Moreover, this approach facilitates the electron transfer from the electrode to metal catalysts. Several methods to prepare chemically modified electrodes were developed, among them, the most commonly applied are polymerization, noncovalent surface binding, and surface-chemical binding.[8,54]

The use of high surface area heterogeneous catalysts is an attractive way to carry out electrochemical CO_2 reduction. Compared to conventional electrodes, the use of nanostructured catalysts greatly enhances the reactivity of the surfaces with a sizable fraction of the reactive sites available for catalysis. For CO_2 reduction, nanostructured metal (mono- or bimetallic), and carbon catalysts were investigated as catalysts. The results of a series of studies revealed that control of morphologies and compositions of supported

nanocatalysts leads to high reactivities and selectivities. However, for heterogeneous catalysts, the catalytic reactivity take place at the surface of the electrode, and it is difficult the elucidation of mechanistic details, as well as, the identification of the active sites.[50,53]

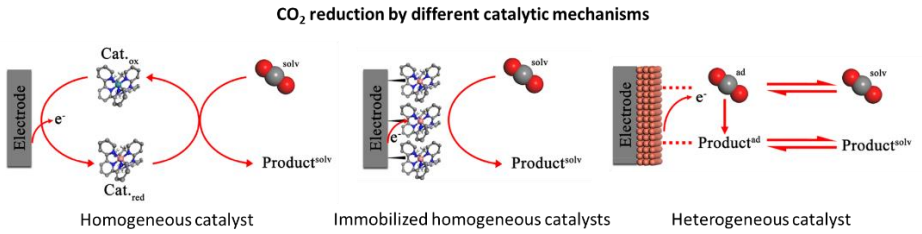

***Figure 9**: CO_2 reduction catalytic mechanisms using different approaches. Adapted from ref [53].*

In this thesis, we will focus on the study of homogeneous catalysts using ionic liquids as electrolytes for the CO_2 electroreduction reaction. The most representative examples are explained in **Chapter 3**.

1.3.2. Fundamentals of photoelectrochemistry

Photoelectrocatalysis is based in the same general principles discussed in the above section of electrocatalysis, but with the difference that the required energy is directly supplied from sunlight. For this physical phenomenon, a semiconductor material that can response to an external excitation e.g., photons from sun irradiation must be used. The electronic structure of a semiconductor consists of an energy void region which is extended from the top of the filled valence band (VB) to the bottom of the vacant conduction band (CB). Under light irradiation, the ground state electron in the VB is promoted to the higher energy CB. This phenoma is known as bandgap photoexcitation, and it can only occur when the photocatalyst is excited with a photon absorption energy equal or higher than the energy difference between the VB and CB. Under the appropriate light irradiation, a photoexcited electron will be accommodated in the higher energy state CB,

thus leaving an empty hole in the lower energy state VB. There is a lifetime in nanoseconds after the photoexcitation process to take place the migration of the photoinduced electrons and holes to the surface of the photocatalysts and participate in the oxidation/reduction reaction with the absorbed reactants.[55] The intrinsic semiconductors are crystalline semiconductors without defects and have the same number of electrons in the VB than holes in the conduction band, but these semiconductors have low conductivity. These materials can be doped introducing atoms which have different valence electrons to increase the conductivity. A p-type (positive charge) semiconductor is obtained by the generation of more holes in the VB than electrons in the CB by doping the semiconductor with atoms with a lower number of valence electrons. In this case, the charge carriers are the holes. Instead, the n-type (negative charge) semiconductors have more electrons in the CB than holes in the VB, and the charge carriers are the electrons (Figure 10).[56]

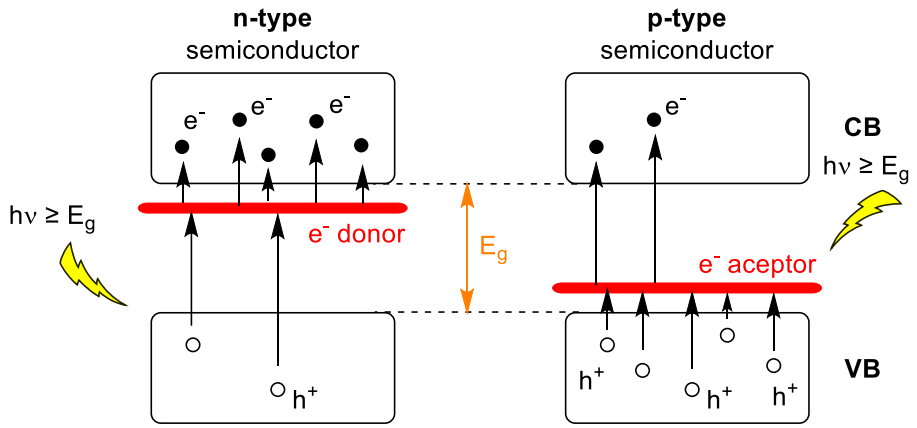

***Figure 10**. Illustration of n-type and p-type semiconductors.*

However, the use of such materials presents two main limitations: (i) the electron-hole pairs recombination is in competition with the charge transfer process. This process takes place in the order of 10^{-9} s whereas the time for the chemical reaction is in the range of 10^{-8} to 10^{-3} s. The deexcitation process

is much lower than the excitation process making the electron-hole pair recombination inevitable,[57] and (ii) to perform the reduction reaction is required a higher potential level of CB than the redox potential of the LUMO of the acceptor molecule, whereas ,for an oxidation reaction, is needed a lower VB potential than the redox potential of the HOMO of the donor molecule.[58]

In this context, the semiconductors have a significant role in the three major steps of the photocatalysis: (i) bandgap photoexcitation to induce the electron-hole pairs formation, (ii) charge migration to the surface of the photocatalyst, and (iii) generation of the active sites to perform the oxidation and reduction reactions. A good photocatalyst should display a narrow bandgap and a strong redox ability. On one hand, a narrow bandgap can extend the photoresponse of the photocatalyst for a higher range of solar light. In the other hand, a higher CB potential and a lower VB potential are more thermodynamically favorable to perform the reduction and oxidation reactions. However, semiconductors with a more negative CB and a more positive VB display wider bandgap with poor results in terms of photoresponse. Both aspects, small bandgap and large overpotential, are significant but at the same time exclusive.[59,60]

Generally, for a single component photocatalyst, it is extremely difficult to fulfill these stringent requirements. Thus, the number of potential candidates as photocatalysts for one-step photoexcitation is limited. In this context, heterostructures constructed by coupling two semiconductors with narrow bandgap and with a suitable band potential constitute a possible alternative. The type-II heterojunction (Figure 11b) is the most typical heterostructure used to improve charge separation efficiency and enhance the photocatalytic performance. An appropriate heterojunction-type photocatalyst induces the spatial separation of charges to suppress the rapid recombination of the

photogenerated electron-hole pairs. Type-II heterojunctions exhibit good charge transfer performance and a limited redox ability of the photocatalyst due to the migration of the electrons and holes to the more electropositive CB and electronegative VB potentials.[61] To overcome these bottlenecks, and inspired by the natural photosynthesis in green plants, the artificial Z-scheme was developed.

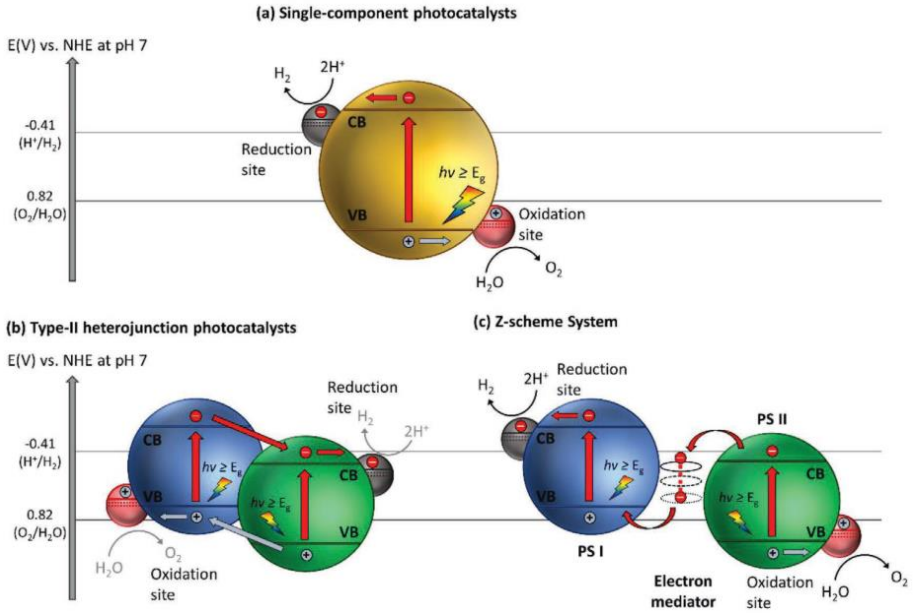

***Figure 11**: Schematic illustration of a) single component photocatalyst, b) type-II heterojunction photocatalyst, c) Z-scheme photocatalytic system. Reprinted from ref [55].*

Z-Scheme:

The Z-scheme consists in two isolated photocatalysts: one of them acts as a reduction site (photosystem I or PS I) while the other acts as oxidation site (photosystem II o PS II). Compared with single component and type II heterojunctions, the artificial Z-scheme exhibits the following three advantages: (i) small bandgap, (ii) good band-edge position with a considerable large overpotential, and (iii) suppression of the recombination of the electron-hole pairs.[62] In the Z-scheme, under light irradiation, the

photoexcitation takes place, and the electrons from the VB of both PS I and II are excited to the CB leaving the photogenerated holes in the VB. Then, the photogenerated electrons in PS II are transported across the system and they are recombined with the holes from VB of PS I. This electron transfer permits the accommodation of the electrons and holes in two separated photocatalysts. The PS II is a hole-rich photocatalysts where the oxidation reaction takes place while the PS I accumulates electrons to perform the reduction reactions.[63,64] The Z-scheme photocatalytic system are classified into three types, depending on the need of an electron mediator or not to perform the electron transfer between both photosystems: (i) traditional Z-scheme, containing a reversible redox ion pair that acts as medium to transfer the charge carriers; (ii) all-solid state Z-scheme, containing an electron conductor to facilitate the charge transfer, and (iii) direct Z-scheme, where no electron mediator is used, with a direct contact between two semiconductors and the formation of an internal electric field drives the charge transfer. These three Z-scheme groups involve distinct synthetic processes, working mechanisms, properties, and applications.[65,66]

1.3.2.1. Molecular photocatalysts for artificial photosynthesis

Photocatalysts based on semiconductors suffers electron-hole recombination when no active sites are available on the surface for the redox reaction. To solve these problems, the loading of a cocatalysts on a light-harvesting semiconductor is one of the most promising approaches. The cocatalyst traps electrons or holes, prevents the unfavorable charge recombination, provides active sites for the surface reactions, improves the selectivity and the catalytic activity, inhibits the side reactions and protects the semiconductors form the photocorrosion.[67]

The advantages of molecular catalysts are: [54]

(1) Clear structure, active site, and catalytic mechanism. Structures and active sites of the molecular catalysts are clearly identifiable and they can be characterized by conventional spectroscopy (UV-Vis, IR, NMR, MS) and X-ray crystallography techniques.
(2) Tunability. The steric configuration and electronic structure can be adjusted through ligand design. This allows the generation of efficient molecular catalysts for various reactions.
(3) Direct improvement of the intrinsic activity. It is possible to enhance the activity of an electrode with two strategies: (i) by the creation of a large number of active sites and (ii) by the improvement of the activity of each active site.
(4) Selectivity. The product selectivity for the CO_2 reduction is one essential factor. The tuneability of molecular catalyst allows a better control of the product selectivity in the CO_2 reduction reaction.
(5) Metal-atom economy. In the homogeneous molecular catalysts, the metal utilization can reach 100%, a value that may be several orders of magnitude higher than with inorganic material-based catalysts.

Several strategies exploiting molecular catalytic systems based on transition metal complexes of Fe (II), Co(II), Cu(I), Ni(II), Mn(I), Re(I), Ru(II) and Ir(III) combined with a redox photosensitizer ($Ru(bpy)_3^{2+}$) have received much attention as potential candidates for photo- and electrocatalytic CO_2 reduction.[8,68] The combination of the photosensitizer and the catalyst complex in supramolecular photocatalysts maximizes the electron transfer between the components to obtain efficient reduction photocatalysts.[69] However, molecular catalysts cannot be directly used in artificial photosynthesis devices due to stability issues.

The heterogenization of the molecular-based catalyst onto a semiconductor constitutes a promising approach for development of efficient photocatalyst for artificial photosynthesis. However, efficient heterogenization strategies are needed to preserve the properties of the original homogenous catalyst. Usually, the main issues are the weak adsorption of metal complexes to the surface of the solid materials (low stability) and the low adsorption amount.[54]

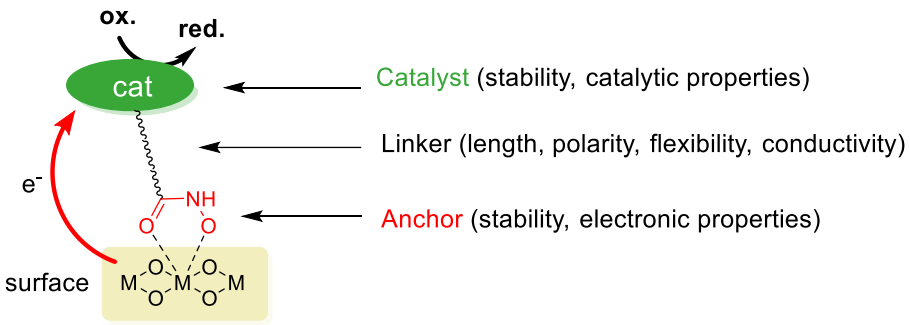

***Figure 12**: Scheme of a heterogenized molecular catalyst on a metal oxide surface, highlighting the main important aspects for the immobilization.*

Immobilized molecular catalysts are constituted by the combination of three moieties (Figure 12): (i) the catalyst, which is the responsible of the reduction reaction, (ii) the anchoring group, which permits the immobilization of the molecular complex to the surface and (iii) the linker, which is responsible of the connection and the electron transfer between the molecular complex and the surface.[8]

For the immobilization of molecular catalysts, there are currently three main strategies (Figure 13): (i) in the electrocatalytic device, the molecular catalyst is immobilized onto a conducting electrode surface from which it directly receives electrons, (ii) in the photocatalytic system, the molecular catalyst is anchored onto a light-harvesting colloidal material which will drive the catalysis upon irradiation, and (iii) in the photoelectrocatalytic system, the molecular catalyst is immobilized onto a light-harvesting semiconductor-

based material affording a photocathode and upon solar irradiation the photoelectrochemical (PEC) production of fuels will take place.

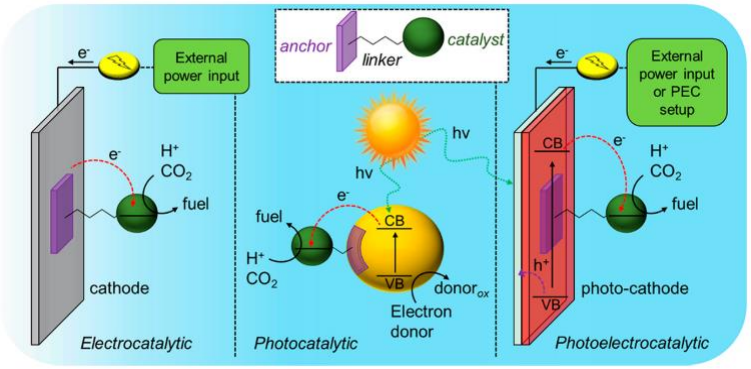

***Figure 13**: Schematic representation of three different configurations to produce solar fuels, electrocatalysis, photocatalysis and photoelectrocatalysis. Reprinted from ref* [8].

In this thesis, we will focus on photoelectrochemical devices using a molecular catalyst and a light-harvesting semiconductor.

1.3.2.2. Strategies for the anchoring of molecular catalysts

The heterogenization of the homogenous catalysts involves the chemical modifications of the ligand structure to introduce an appropriate anchoring unit. The selection of the anchoring group depends on the nature of the material and the type of application, such as, electro-, photo- or photoelectrochemical process.

For photoelectrocatalysis, metal oxides constitute an attractive surface and several efforts to immobilize molecular catalysts onto such materials were reported. Various types of chemical moieties were described for the immobilization of dyes or catalysts with the formation of chemical bonds onto the metal oxide surface. The most used anchoring groups to immobilize the molecular complexes onto the metal oxides are carboxylates, phosphonates, organosilanes/silatranes, hydroxamates and acetylacetonates groups (Figure 14).[70,71]

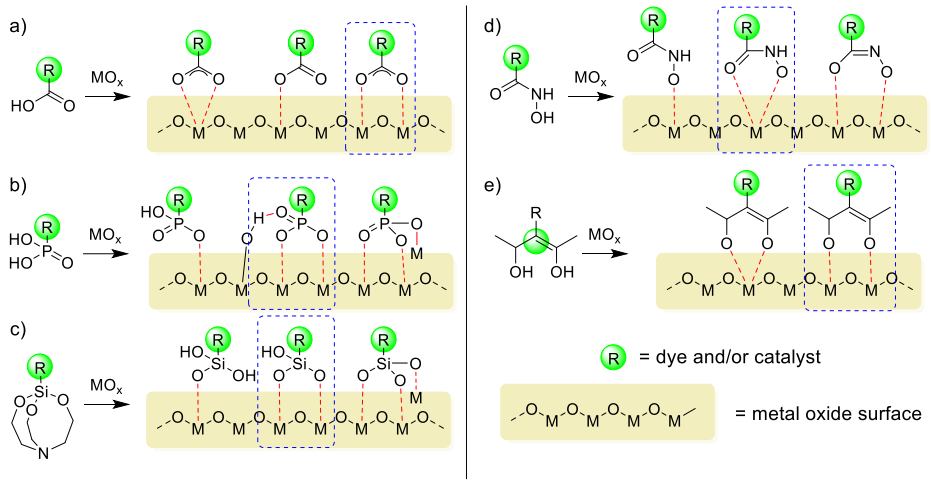

***Figure 14**: Different surface binding modes for each anchor group to immobilize dyes and catalysts onto metal oxides surface: (a) carboxylate group; (b) phosphonate group; (c) silane group; (d) hydroxamates group; and (e) acetylacetonate group. The dominant binding modes are highlighted in blue.*

Carboxylate groups can be easily introduced into the complexes and are widely used as anchors via a condensation reaction with the hydroxy groups at the surface of the metal oxides, resulting in an ester type linkage. A bidentate chelating or bridging binding mode between the carboxylate and the metal oxide are usually preferred. However, the stability of the carboxylate derivatives remains relatively low at neutral and basic pH.[72–74]

Phosphonate groups chelate strongly to metal oxides through a variety of binding modes. A similar condensation than with carboxylic acid takes place with the terminal hydroxyl groups present at the surface of the material. The phosphonates are more strongly immobilized than the carboxylates due to the dianionic nature of the phosphonate ions and the possibility of a tridentate bonding with the surface. The stability of the phosphonate bonds is from neutral to acidic solutions. The stability at basic pH is limited due to the hydrolysis of the P-O bonds.[75,76]

Organosilanes groups are an alternative to the use of carboxylates and phosphonate anchoring groups. The resulting silyl ether-metal bond is very stable over a broad range of pH values. The Si-O bond chemical inertness is usually attributed to a model hyper conjugative interaction. Organosilanes/silatranes have a mono-, bi- or tridentate binding interactions with the metal oxide surfaces. The reaction of the organosilanes with the hydroxyl groups of the metal oxides forms a strong silyl ether-type surface bonding.[77–79]

Hydroxamates groups can form more stable bonds than carboxylates with metal oxide surfaces by unidentate, bidentate and chelating binding modes. Hydroxamates allow a faster electron transfer between the molecular complex and the surface compared with the other anchor groups.[80,81]

Acetylacetonate groups form strong surface adducts by performing stable coordination complexes with the metal cations. Acetylacetonate have bidentate or bridging modes to bind with the metal oxide surfaces.[82,83]

1.3.2.3. Molecular-catalyst-modified dye-sensitized PEC cells (DSPEC cells)

The combination of a photosensitizer and a transition metal complex was reported to successfully catalyze the CO_2 reduction.[84,85] However, to date, the CO_2 reduction coupled with water oxidation has not been achieved using molecular catalysts.[68] On the other hand, semiconductors can catalyze multielectron reactions such as overall water splitting.[86,87] However, to date, the development of an efficient semiconductor photocatalyst for driving the CO_2RR is still challenging since good performances were achieved only using wide band gap semiconductors under UV light irradiation.[88–90] With the combination of different semiconductors, the visible-light driven CO_2 reduction with water oxidation was reported[91] but with low selectivities due

to the competition with the hydrogen evolution reaction.[68] Molecular metal complexes and semiconductors displayed some advantages and disadvantages. However, their weaknesses can be overcome via the construction of a suitable molecule/semiconductor hybrid material that maximizes their advantages.

The dye sensitized photoelectrochemical (DSPEC) cell concept has evolved from the dye sensitized solar cell (DSSC). In the latter, electrical energy is produced from sunlight. Instead, the PEC cell is a device that uses light incident on a photosensitizer/ semiconductor to perform a chemical reaction with the holes and electrons formed instead of producing electrical energy. The DSPEC cell concept was proposed by O'Regan and Grätzel in 1991:[92] They used a new type of solar cell by sensitizing nanocrystalline films of TiO_2 with Ru(II) dyes for molecular light absorption. The characteristics of this device is that the photoexcited electrons of the Ru(II) are injected into the conduction band of the TiO_2 yielding the oxidized Ru(III). Then the Ru(III) is reduced to regenerate the Ru(II) by electron transfer from a redox species in the electrolyte solution which is then reduced at the counter electrode.

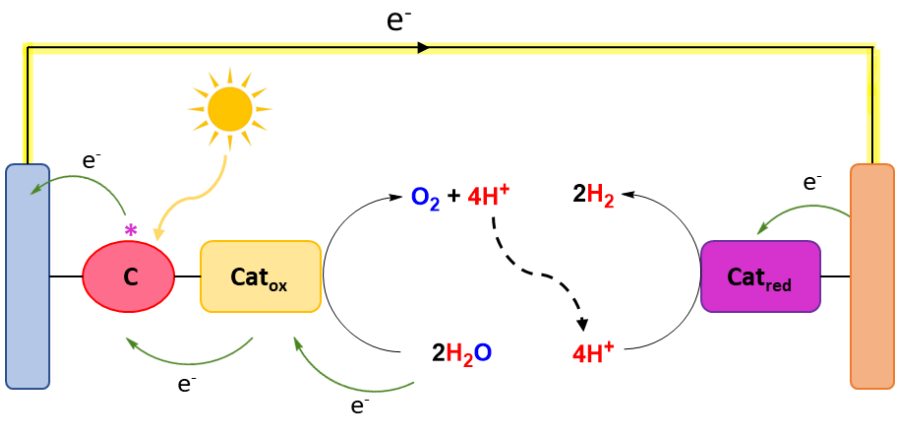

***Figure 15**: DSPEC cell. Adapted from ref [54].*

A DSPEC cell can be modified with a molecular chromophore-catalyst (e.g., WOC, HER or CO_2RR) to drive reactions using the electron flow and to produce chemical fuels instead of generating electricity. As can be observed in Figure 15, the light irradiation excites the chromophore (C) generating the excited state C*. Then, C* which transfers an electron to the conduction band of the semiconductor to form the oxidative state C^+. Later, C^+ is reduced by the electrons that come from the oxidation of H_2O to O_2. The electrons are diffused through the TiO_2 semiconductor film to the conductive contactor and to the cathode. Finally, the cathode uses these electrons to perform the reduction of protons to H_2.[54]

The most important characteristics to build a useful DSPEC cell are: (i) a stable surface binding of the chromophore to the metal oxide, which also provide the correct electron transfer, (ii) a chromophore which can absorb light from the near UV to the Vis, (iii) a bridging ligand to couple the chromophore with the WOC in the photoanode and a catalyst for water reduction or CO_2 reduction in the photocathode, or other strategies to co-immobilize these catalysts with the chromophores, and (iv) a robust and stable WOC or catalyst to perform the water reduction or CO_2 reduction, able to have catalytic rates which significantly exceed the rate of solar radiation, of approximately $2s^{-1}$.[93]

1.3.2.4. DSPEC cells with molecular-catalyst-modified photocathode

A photocathode is a combination of electrochemical and photocatalytic system which can generate fuel during irradiation via the injection of electrons into an immobilized catalyst.[94,95] A molecular catalyst modified photocathode can be achieved by the modification of p-type semiconductor with a light absorbing component, normally a molecular dye, to photoreduce the co-anchored catalyst. The p-type semiconductor acts as a hole-selective layer giving directionality to electron transfer process when the E_{VB} accepts holes from the photoexcited photosensitizer. When the photocathode is coupled

with a photoanode in a PEC tandem cell, the electrons to regenerate the dye can be directly obtained from the half reaction oxidation that takes place in the photoanode. The interest in the DSPEC cells is continuously growing, but there are many more examples for water splitting than for CO_2 transformations. In the recent years, investigations ranging from the search for a suitable immobilization strategy to the development of new novel p-type semiconductors were reported.[8]

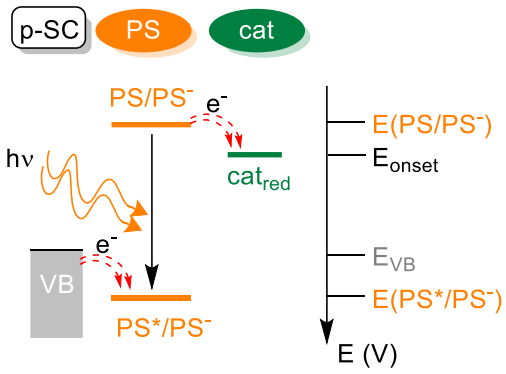

***Figure 16**: Band diagram representing the energy level requirements for a functional DSPEC system.*

In a DSPEC cell, the photosensitizer is responsible for the light absorption, and in most cases, is also the responsible of the charge transfer to a molecular catalyst. To perform all these functions, the photosensitizer need to have various thermodynamic requirements: (i) the excited state reduction potential ($E_{PS^*/PS}$) must be more positive than the flat-band potential of the semiconductor to ensure that the hole quenching by the semiconductor can take place and (ii) the regeneration potential (E^{PS/PS^-}) must be more negative than the E_{onset} of the electrocatalyst (Figure 16). From a kinetic point of view, the photosensitizer must maintain a long-lived charge-separated state for the photoinduced charge injection to compete with the deactivation processes. For the charge separation efficiency, it is also important how fast the catalyst can receive electrons from the reduced dye.[8]

Depending on the semiconductor bandgap, two different strategies were developed.

Wide-bandgap dye-sensitized photoelectrodes

Wide-bandgap semiconductors require an additional co-anchored photosensitizer to achieve an efficient harvesting of the solar light. The requirements for an efficient p-type semiconductor are: (i) a robust grafting of the photosensitizing unit and/or molecular catalyst in the semiconductor surface, (ii) an efficient hole extraction and hole transport kinetics, and (iii) good stability under the operating conditions for the solar fuel generation. With all these requirements, the development of a suitable p-type semiconductor in dye photocathode system is very challenging. Nickel oxide[96] and some ternary oxides (delafossite) with the general formula ABO_2 are suitable wide-bandgap p-type semiconductor materials for proton and CO_2 reduction.[97] The main limitations of these materials are the need of an additional photosensitizer, the low charge mobility within the material, the limited diversity of suitable materials, the rapid charge recombination and surface states (defects). These limitations hinder the performances of this photocathodes.[8]

Narrow-bandgap dye-sensitized photoelectrodes

The narrow-bandgap p-type semiconductors (e.g., Si, GaP, InP or Cu_2O) can directly absorb the visible light without the presence of an additional dye. The narrow-bandgap semiconductors can be directly coupled with a catalyst, the semiconductor needs to have an energy level of the CB more reducing that the E_{onset} of the catalyst (Figure 17). With a suitable VB potential, the electrons are injected into the immobilized catalyst and the holes into the conductive support.[8] These properties can be modified by adjusting the band gap and tuning the physical features, such as, crystal structure, crystallinity and particle size. However, semiconductors with the appropriate bandgap generally show

limited stability and have very low catalytic photocurrent due to the recombination of the majority of the photo-generated electrons and holes on the surface before their use to drive reactions.[98] The modification of the semiconductor surface by the addition of cocatalysts to accelerate the reaction rates are considered to be essential to perform an efficient visible light absorber semiconductor (VLA-SC) based PEC cell.[99,100] Molecular catalysts can efficiently avoid the combination of electrons and holes on the surface facilitating the direct transfer of charge to the catalytic site.

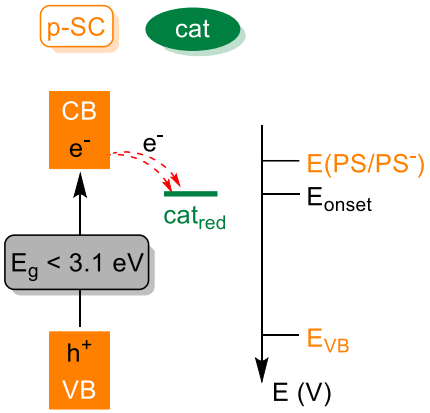

***Figure 17**: Band gap diagram depicting energy level requirements for a successful LAPV system.*

In **Chapter 4,** the most representative examples of hybrid molecular catalysts supported on semiconductors for the photoelectrocatalytic CO_2 reduction are described. **Chapter 4** focuses on the preparation of different hybrid photocathodes using Ru and Re molecular complexes and Cu_2O/SnO_2 or $CuGaO_2$ as semiconductor.

1.3.2.5. Water oxidation reaction

As mentioned above, the photogenerated electrons and holes can be used to perform chemical reactions and transform the solar energy into chemical energy. This process is called artificial photosynthesis and involves the oxidation of a water molecule to form O_2, protons and electrons. These

electrons will be used to reduce other molecules. In this process, one of the key challenges is the oxidation of water to molecular oxygen. The oxidation process of one molecule of water involves the transfer of four electrons, the breakage of four O-H bonds and the formation of the O=O double bound. Nowadays, the water oxidation half reaction constitutes the bottleneck of the development of artificial photosynthesis devices because it requires a high thermodynamic potential, E^0 = 1.23 V *vs* NHE at pH = 0, and a high overpotential is needed to overcome the kinetic barrier. To reduce this kinetic barrier, the development of a robust and efficient water oxidation catalyst (WOC) is necessary. [101]

WOCs are based on redox-active transition metal complexes with unsaturated first coordination spheres. These are the coordination sites for the water molecules. The catalyst must enable the accumulation of multiple charges to generate a high valent metal-oxo (M=O) intermediate. This M=O intermediate is essential for the next step, which is the O-O bond formation. There are two pathways for the O-O bond formation (Figure 18): (i) water nucleophilic attack (WNA) and (ii) interaction of two M=O units (I2M).[102–104] In the WNA pathway, a second molecule of water acts as a nucleophile and attack the electrophilic O of the M=O intermediate. With this nucleophilic attack, the metal center is two-electron reduced and the O-O bond is formed on a metal hydroperoxide intermediate (M-OOH). Then, the oxygen evolution takes place by the oxidation of the M-OOH. Instead, in the I2M pathway, the O-O bond formation takes place through the interaction of two M=O units, leading to an M-O-O-M species from which O_2 is released.[54]

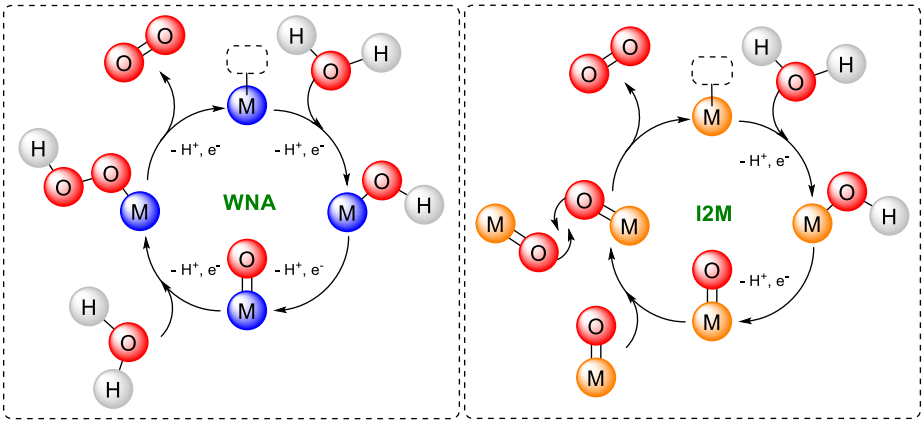

***Figure 18**: Schematic representation of the two different O-O bond formation pathways, water nucleophilic attack (WNA) and interaction between two M=O intermediates (I2M). Adapted from ref [54].*

Several types of water oxidation catalysts were developed but we will focus here on molecular Ru catalysts since they are the most studied WOCs. In 1982, Meyer and co-workers reported the first Ru molecular WOC called "blue dimer" cis,cis-$[Ru^{II}(bp)_2\text{-}(H_2O)]_2(\mu\text{-}O)$ (Figure 19a).[105] They reported a turnover number (TON) of 13 and a turnover frequency (TOF) of 0.0042 s^{-1} using Ce^{4+} as oxidant. Over the last years, important improvements were achieved in this field. In 2009, Sun and co-workers made a breakthrough in the catalytic efficiency of the molecular WOCs by the development of a $[Ru(bda)(pic)_2]$ (where bda is [2,2'- bipyridine]-6,6'-dicarboxylate and pic is 4-picoline) (Figure 19b). They achieved a TON of 2000 and a TOF of 41 s^{-1} using Ce^{4+} as the oxidant.[106] This improvement was attributed to the introduction of carboxylate groups into the ligand, and to the special steric configuration that provided an open site for coordination of the water molecule. In 2015, Llobet and co-workers reported the use of $[Ru(tda)(py)_2]$ (where tda is [2,2':6'2''-terpyridine]-6,6''-dicarboxylato and py is pyridine) (Figure 19c) with a TOF of 8000 s^{-1}. This improvement was attributed to the fact that the Ru center is

seven-coordinated at oxidation state IV, leaving a dangling carboxylate group in the second coordination sphere assisting the WNA step.[107]

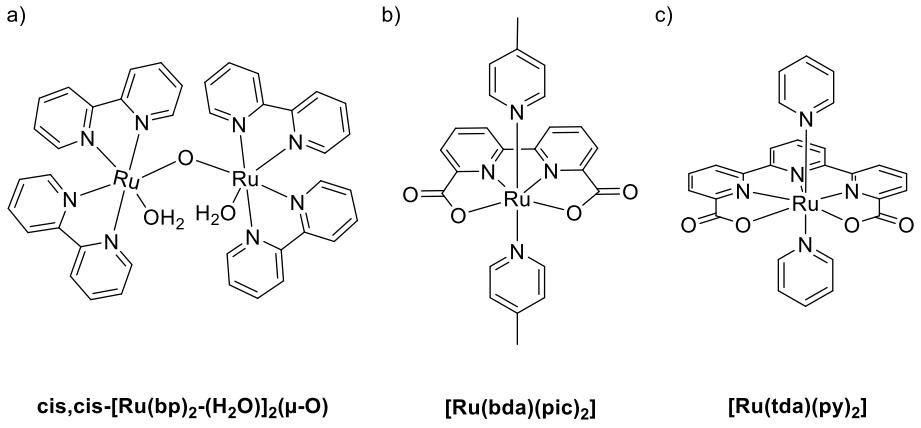

***Figure 19**: Structures of a) cis,cis-[Ru^{II}(bp)$_2$-(H$_2$O)]$_2$(μ-O), b) [Ru(bda)(pic)$_2$] and c) [Ru(tda)(py)$_2$].*

However, molecular catalysts cannot be directly used in a photoelectrochemical cell, and their anchoring on semiconductive surfaces must be performed to achieve an efficient photoanode for useful photoelectrochemical cell devices. The ligands of the complexes must be modified with a functional group without changing their intrinsic activity to immobilize the molecular catalysts onto a photoelectrode surface. Many types of catalysts were developed for water oxidation, but in this section, we will focus on the DSPEC cells with molecular catalyst-semiconductor modified photoanodes. A selection of examples of hybrid molecular-semiconductor photoanodes for water oxidation reaction are described in **Chapter 5**.

Chapter 5 focuses on the preparation of a series of hybrid photoanodes based on the immobilization of Ru-based visible light absorber complexes, and Ru-base water oxidation catalyst onto $BiVO_4$. Different immobilization strategies are presented.

1.4. References

(1) DOĞAN, E.; DOĞAN, B. Ö. Does Wind Energy Affect Economic Growth in Developing Countries? *J. Stat. Appl. Sci.* **2020**, *1*, 99–106.

(2) Cook, T. R.; Dogutan, D. K.; Reece, S. Y.; Surendranath, Y.; Teets, T. S.; Nocera, D. G. Solar Energy Supply and Storage for the Legacy and Nonlegacy Worlds. *Chem. Rev.* **2010**, *110*, 6474–6502.

(3) Luna, P. De; Hahn, C.; Higgins, D.; Jaffer, S. A.; Jaramillo, T. F.; Sargent, E. H. What Would It Take for Renewably Powered Electrosynthesis to Displace Petrochemical Processes? *Science.* **2019**, *364*, 3506.

(4) Dodds, D. R.; Gross, R. A. Chemicals from Biomass. *Science.* **2007**, *318*, 1250–1251.

(5) Field, C. B.; Campbell, J. E.; Lobell, D. B. Biomass Energy: The Scale of the Potential Resource. *Trends Ecol. Evol.* **2008**, *23*, 65–72.

(6) Rafiee, A.; Rajab Khalilpour, K.; Milani, D.; Panahi, M. Trends in CO2 Conversion and Utilization: A Review from Process Systems Perspective. *J. Environ. Chem. Eng.* **2018**, *6*, 5771–5794.

(7) Matsubara, Y.; Grills, D. C.; Kuwahara, Y. Thermodynamic Aspects of Electrocatalytic CO2 Reduction in Acetonitrile and with an Ionic Liquid as Solvent or Electrolyte. *ACS Catal.* **2015**, *5*, 6440–6452.

(8) Dalle, K. E.; Warnan, J.; Leung, J. J.; Reuillard, B.; Karmel, I. S.; Reisner, E. Electro-and Solar-Driven Fuel Synthesis with First Row Transition Metal Complexes. *Chem. Rev.* **2019**, *119*, 2752–2875.

(9) Wang, Y.; He, D.; Chen, H.; Wang, D. Catalysts in Electro-, Photo- and Photoelectrocatalytic CO2 Reduction Reactions. *J. Photochem. Photobiol. C Photochem. Rev.* **2019**, *40*, 117–149.

(10) Nguyen, V. H.; Nguyen, B. S.; Jin, Z.; Shokouhimehr, M.; Jang, H. W.; Hu, C.; Singh, P.; Raizada, P.; Peng, W.; Shiung Lam, S.; Xia, C.; Nguyen, C. C.; Kim, S. Y.; Le, Q. Van. Towards Artificial Photosynthesis: Sustainable Hydrogen Utilization for Photocatalytic Reduction of CO2 to High-Value Renewable Fuels. *Chem. Eng. J.* **2020**, *402*, 126184.

(11) de Klerk, A. *Fischer-Tropsch Refining*; Wiley-VCH Verlag GmbH & Co. KGaA, 2011.

(12) Eley, D.; Pines, H.; Weisz, P. *Advances in Catalysis*; Academic Press, 1982.

(13) Midilli, A.; Dincer, I. Key Strategies of Hydrogen Energy Systems for Sustainability. *Int. J. Hydrogen Energy* **2007**, *32*, 511–524.

(14) Howarth, R. W.; Jacobson, M. Z. How Green Is Blue Hydrogen? *Energy Sci. Eng.* **2021**, *9*, 1676–1687.

(15) Benson, E. E.; Kubiak, C. P.; Sathrum, A. J.; Smieja, J. M. Electrocatalytic and Homogeneous Approaches to Conversion of CO2 to Liquid Fuels. *Chem. Soc. Rev.* **2009**, *38*, 89–99.

(16) Feng, J.; Zeng, S.; Feng, J.; Dong, H.; Zhang, X. CO2 Electroreduction in Ionic Liquids: A Review. *Chinese J. Chem.* **2018**, *36*, 961–970.

(17) Lu, Q.; Jiao, F. Electrochemical CO2 Reduction: Electrocatalyst, Reaction Mechanism, and Process Engineering. *Nano Energy* **2016**, *29*, 439–456.

(18) Yang, D.; Zhu, Q.; Han, B. Electroreduction of CO2 in Ionic Liquid-Based Electrolytes. *Innov.* **2020**, *1*, 100016.

(19) Welton, T. Ionic Liquids: A Brief History. *Biophys. Rev.* **2018**, *10*, 691–706.

(20) Tiago, G. A. O.; Matias, I. A. S.; Ribeiro, A. P. C.; Martins, L. M. D. R. S. Application of Ionic Liquids in Electrochemistry-Recent Advances. *Molecules* **2020**, *25*, 5812.

(21) Greer, A. J.; Jacquemin, J.; Hardacre, C. *Industrial Applications of Ionic Liquids*; 2020; Vol. 25.

(22) Armand, M.; Endres, F.; Macfarlane, D. R.; Ohno, H.; Scrosati, B. Ionic-Liquid Materials for the Electrochemical Challenges of the Future. *Nat. Mater.* **2009**, *38*, 621–629.

(23) Watanabe, M.; Thomas, M. L.; Zhang, S.; Ueno, K.; Yasuda, T.; Dokko, K. Application of Ionic Liquids to Energy Storage and Conversion Materials and Devices. *Chem. Rev.* **2017**, *117*, 7190–7239.

(24) Macfarlane, D. R.; Tachikawa, N.; Forsyth, M.; Pringle, J. M.; Howlett, P. C.; Elliott, G. D.; Davis, J. H.; Watanabe, M.; Simon, P.; Angell, C. A. Energy Applications of Ionic Liquids. *Energy Environ. Sci.* **2014**, *7*, 232–250.

(25) Moura de Salles Pupo, M.; Kortlever, R. Electrolyte Effects on the Electrochemical Reduction of CO2. *ChemPhysChem* **2019**, *20*, 2926–2935.

(26) Dupont, J.; Spencer, J. On the Noninnocent Nature of 1,3-Dialkylimidazolium Ionic Liquids. *Angew. Chem. Int. Ed.* **2004**, *43*, 5296–5297.

(27) Weingarth, D.; Czekaj, I.; Fei, Z.; Foelske-Schmitz, A.; Dyson, P. J.; Wokaun, A.; Kötz, R. Electrochemical Stability of Imidazolium Based Ionic Liquids Containing Cyano Groups in the Anion: A Cyclic Voltammetry, XPS and DFT Study. *J. Electrochem. Soc.* **2012**, *159*, H611–H615.

(28) Rupp, A. B. A.; Krossing, I. Ionic Liquids with Weakly Coordinating [MIII(ORF)4]- Anions. *Acc. Chem. Res.* **2015**, *48*, 2537–2546.

(29) Swatloski, R. P.; Holbrey, J. D.; Rogers, R. D. Ionic Liquids Are Not Always Green: Hydrolysis of 1-Butyl-3- Methylimidazolium Hexafluorophosphate. *Green Chem.* **2003**, *5*, 361–363.

(30) Freire, M. G.; Neves, C. M. S. S.; Marrucho, I. M.; Coutinho, A. P. Hydrolysis of Tetrafluoroborate and Hexafluorophosphate Counter Ions in Imidazolium-Based Ionic Liquids. *J. Phys. Chem. A* **2010**, *114*, 3744–3749.

(31) Rosen, B. A.; Salehi-Khojin, A.; Thorson, M. R.; Zhu, W.; Whipple, D. T.; Kenis, P. J. A.; Masel, R. I. Ionic Liquid-Mediated Selective Conversion of CO2 to CO at Low Overpotentials. *Science.* **2011**, *334*, 643–644.

(32) Medina-Ramos, J.; Dimeglio, J. L.; Rosenthal, J. Efficient Reduction of CO2 to CO with High Current Density Using in Situ or Ex Situ Prepared Bi-Based Materials. *J. Am. Chem. Soc.* **2014**, *136*, 8361–8367.

(33) Iijima, G.; Kitagawa, T.; Katayama, A.; Inomata, T.; Yamaguchi, H.; Suzuki, K.; Hirata, K.; Hijikata, Y.; Ito, M.; Masuda, H. CO2 Reduction Promoted by Imidazole Supported on a Phosphonium-Type Ionic-Liquid-Modified Au Electrode at a Low Overpotential. *ACS Catal.* **2018**, *8*, 1990–2000.

(34) Sun, L.; Ramesha, G. K.; Kamat, P. V.; Brennecke, J. F. Switching the Reaction Course of Electrochemical CO2 Reduction with Ionic Liquids. *Langmuir* **2014**, *30*, 6302–6308.

(35) Oh, Y.; Hu, X. Ionic Liquids Enhance the Electrochemical CO2 Reduction Catalyzed by MoO2. *Chem. Commun.* **2015**, *51*, 13698–13701.

(36) Hollingsworth, N.; Taylor, S. F. R.; Galante, M. T.; Jacquemin, J.; Longo,

C.; Holt, K. B.; de Leeuw, N. H.; Hardacre, C. Reduction of Carbon Dioxide to Formate at Low Overpotential Using a Superbase Ionic Liquid. *Angew. Chem. Int. Ed.* **2015**, *127*, 14370–14374.

(37) Tanner, E. E. L.; Batchelor-Mcauley, C.; Compton, R. G. Carbon Dioxide Reduction in Room-Temperature Ionic Liquids: The Effect of the Choice of Electrode Material, Cation, and Anion. *J. Phys. Chem. C* **2016**, *120*, 26442–26447.

(38) Lau, G. P. S.; Schreier, M.; Vasilyev, D.; Scopelliti, R.; Grätzel, M.; Dyson, P. J. New Insights Into the Role of Imidazolium-Based Promoters for the Electroreduction of CO2 on a Silver Electrode. *J. Am. Chem. Soc.* **2016**, *138*, 7820–7823.

(39) Sung, S.; Kumar, D.; Gil-Sepulcre, M.; Nippe, M. Electrocatalytic CO2 Reduction by Imidazolium-Functionalized Molecular Catalysts. *J. Am. Chem. Soc.* **2017**, *139*, 13993–13996.

(40) Khadhraoui, A.; Gotico, P.; Boitrel, B.; Leibl, W.; Halime, Z.; Aukauloo, A. Local Ionic Liquid Environment at a Modified Iron Porphyrin Catalyst Enhances the Electrocatalytic Performance of CO2 to CO Reduction in Water. *Chem. Commun.* **2018**, *54*, 11630–11633.

(41) Honores, J.; Quezada, D.; García, M.; Calfumán, K.; Muena, J. P.; Aguirre, M. J.; Arévalo, M. C.; Isaacs, M. Carbon Neutral Electrochemical Conversion of Carbon Dioxide Mediated by [Mn+(Cyclam)Cln] (M = Ni2+ and Co3+) on Mercury Free Electrodes and Ionic Liquids as Reaction Media. *Green Chem.* **2017**, *19*, 1155–1162.

(42) Grills, D. C.; Matsubara, Y.; Kuwahara, Y.; Golisz, S. R.; Kurtz, D. A.; Mello, B. A. Electrocatalytic CO2 Reduction with a Homogeneous Catalyst in Ionic Liquid: High Catalytic Activity at Low Overpotential. *J.*

Phys. Chem. Lett. **2014**, *5*, 2033–2038.

(43) Choi, J.; Benedetti, T. M.; Jalili, R.; Walker, A.; Wallace, G. G.; Officer, D. L. High Performance Fe Porphyrin/Ionic Liquid Co-Catalyst for Electrochemical CO2 Reduction. *Chem. Eur. J.* **2016**, *22*, 14158–14161.

(44) Rees, N. V; Compton, R. G. Electrochemical CO2 Sequestration in Ionic Liquids ; a Perspective. *Energy Environ. Sci.* **2011**, *4*, 403–408.

(45) Lim, H.; Kim, H. The Mechanism of Room-Temperature Ionic-Liquid-Based Electrochemical CO2 Reduction: A Review. *Molecules* **2017**, *22*, 536.

(46) Hooshyari, K.; Javanbakht, M.; Adibi, M. Novel Composite Membranes Based on PBI and Dicationic Ionic Liquids for High Temperature Polymer Electrolyte Membrane Fuel Cells. *Electrochim. Acta* **2016**, *205*, 142–152.

(47) Hori, Y.; Kikuchi, K.; Suzuki, S. Production of CO and CH4 in Electrochemical Reduction of CO2 at Metal Electrodes in Aqueous Hydrogencarbonate Solution. *Chem. Lett.* **1985**, *14*, 1695–1698.

(48) Zhao, G.; Huang, X.; Wang, X.; Wang, X. Progress in Catalyst Exploration for Heterogeneous CO2 Reduction and Utilization: A Critical Review. *J. Mater. Chem. A* **2017**, *5*, 21625–21649.

(49) Liu, G.; Tran-Phu, T.; Chen, H.; Tricoli, A. A Review of Metal- and Metal-Oxide-Based Heterogeneous Catalysts for Electroreduction of Carbon Dioxide. *Adv. Sustain. Syst.* **2018**, *2*, 1800028.

(50) Zheng, T.; Jiang, K.; Wang, H. Recent Advances in Electrochemical CO2-to-CO Conversion on Heterogeneous Catalysts. *Adv. Mater.* **2018**, *30*, 1802066.

(51) Long, C.; Li, X.; Guo, J.; Shi, Y.; Liu, S.; Tang, Z. Electrochemical Reduction of CO2 over Heterogeneous Catalysts in Aqueous Solution: Recent Progress and Perspectives. *Small Methods* **2019**, *3*, 1800369.

(52) Gattrell, M.; Gupta, N.; Co, A. A Review of the Aqueous Electrochemical Reduction of CO2 to Hydrocarbons at Copper. *J. Electroanal. Chem.* **2006**, *594*, 1–19.

(53) Zhang, S.; Fan, Q.; Xia, R.; Meyer, T. J. CO2 Reduction: From Homogeneous to Heterogeneous Electrocatalysis. *Acc. Chem. Res.* **2020**, *53*, 255–264.

(54) Zhang, B.; Sun, L. Artificial Photosynthesis: Opportunities and Challenges of Molecular Catalysts. *Chem. Soc. Rev.* **2019**, *48*, 2216–2264.

(55) Ng, B. J.; Putri, L. K.; Kong, X. Y.; Teh, Y. W.; Pasbakhsh, P.; Chai, S. P. Z-Scheme Photocatalytic Systems for Solar Water Splitting. *Adv. Sci.* **2020**, *7*.

(56) Jiang, C.; Moniz, S. J. A.; Wang, A.; Zhang, T.; Tang, J. Photoelectrochemical Devices for Solar Water Splitting – Materials and Challenges. *Chem. Soc. Rev.* **2017**, *46*, 4645–4660.

(57) Tan, L.; Chai, S.; Rahman, A. Synthesis and Applications of Graphene-Based TiO2 Photocatalysts. *ChemSusChem* **2012**, *5*, 1868–1882.

(58) Maeda, K.; Domen, K. Photocatalytic Water Splitting: Recent Progress and Future Challenges. *J. Phys. Chem. Lett.* **2010**, *1*, 2655–2661.

(59) Qu, Y.; Duan, X. Progress, Challenge and Perspective of Heterogeneous Photocatalysts. *Chem. Soc. Rev.* **2013**, *42*, 2568–2580.

(60) Zhong, S.; Xi, Y.; Chen, Q.; Chen, J. Bridge Engineering in Photocatalysis

and Photoelectrocatalysis. *Nanoscale* **2020**, *12*, 5764–5791.

(61) Zhang, W.; Mohamed, A. R.; Ong, W. J. Z-Scheme Photocatalytic Systems for Carbon Dioxide Reduction: Where Are We Now? *Angew. Chem. Int. Ed.* **2020**, *59*, 22894–22915.

(62) Maeda, K. Z-Scheme Water Splitting Using Two Different Semiconductor Photocatalysts. *ACS Catal.* **2013**, *3*, 1486–1503.

(63) Ng, B.; Kurnianditia, L.; Tan, L.; Pasbakhsh, P.; Chai, S. All-Solid-State Z-Scheme Photocatalyst with Carbon Nanotubes as an Electron Mediator for Hydrogen Evolution under Simulated Solar Light. *Chem. Eng. J.* **2017**, *316*, 41–49.

(64) Teh, Y. W.; Goh, W.; Kong, Y.; Ng, B.; Yong, S. Fabrication of Bi2WO6/Cu/WO3 All-Solid-State Z-Scheme Composite Photocatalyst to Improve CO2 Photoreduction under Visible Light Irradiation. *ChemCatChem* **2019**, *11*, 6431–6438.

(65) Xu, Q.; Zhang, L.; Yu, J.; Wageh, S.; Al-Ghamdi, A. A.; Jaroniec, M. Direct Z-Scheme Photocatalysts: Principles, Synthesis, and Applications. *Mater. Today* **2018**, *21*, 1042–1063.

(66) Li, H.; Tu, W.; Zhou, Y.; Zou, Z. Z-Scheme Photocatalytic Systems for Promoting Photocatalytic Performance: Recent Progress and Future Challenges. *Adv. Sci.* **2016**, *3*.

(67) Zhong, S.; Xi, Y.; Wu, S.; Liu, Q.; Zhao, L.; Bai, S. Hybrid Cocatalysts in Semiconductor-Based Photocatalysis and Photoelectrocatalysis. *J. Mater. Chem. A* **2020**, *8*, 14863–14894.

(68) Nakada, A.; Kumagai, H.; Robert, M.; Ishitani, O.; Maeda, K. Molecule / Semiconductor Hybrid Materials for Visible-Light CO2 Reduction: Design Principles and Interfacial Engineering. *Acc. Mater. Res.* **2021**, *2*,

458–470.

(69) Tamaki, Y.; Ishitani, O. Supramolecular Photocatalysts for the Reduction of CO2. *ACS Catal.* **2017**, *7*, 3394–3409.

(70) Vohs, J. M. Site Requirements for the Adsorption and Reaction of Oxygenates on Metal Oxide Surfaces. *Chem. Rev.* **2013**, *113*, 4136–4163.

(71) Pujari, S. P.; Scheres, L.; Marcelis, A. T. M.; Zuilhof, H. Covalent Surface Modification of Oxide Surfaces. *Angew. Chemie Int. Ed.* **2014**, *53*, 6322–6356.

(72) Hagfeldt, A.; Boschloo, G.; Sun, L.; Kloo, L.; Pettersson, H. Dye-Sensitized Solar Cells. *Chem. Rev.* **2010**, *110*, 6595–6663.

(73) Brennan, B. J.; Llansola Portolés, M. J.; Liddell, P. A.; Moore, T. A.; Moore, A. L.; Gust, D. Comparison of Silatrane, Phosphonic Acid, and Carboxylic Acid Functional Groups for Attachment of Porphyrin Sensitizers to TiO2 in Photoelectrochemical Cells. *Phys. Chem. Chem. Phys.* **2013**, *15*, 16605–16614.

(74) Bae, E.; Choi, W.; Park, J.; Shin, H. S.; Kim, S. Bin; Lee, J. S. Effects of Surface Anchoring Groups (Carboxylate vs Phosphonate) in Ruthenium-Complex-Sensitized TiO2 on Visible Light Reactivity in Aqueous Suspensions. *J. Phys. Chem. B* **2004**, *108*, 14093–14101.

(75) Boissezon, R.; Muller, J.; Beaugeard, V.; Monge, S.; Robin, J. J. Organophosphonates as Anchoring Agents onto Metal Oxide-Based Materials: Synthesis and Applications. *RSC Adv.* **2014**, *4*, 35690–35707.

(76) Queffélec, C.; Petit, M.; Janvier, P.; Knight, D. A.; Bujoli, B. Surface Modification Using Phosphonic Acids and Esters. *Chem. Rev.* **2012**, *112*, 3777–3807.

(77) Shambayati, S.; Blake, J.; Wierschke, S.; Jorgensen, W.; Schreiber, S. Structure and Basicity of Silyl Ethers: A Crystallographic and Ab Initio Inquiry into the Nature of Silicon-Oxygen Interactions. *J. Am. Chem. Soc* **1990**, *112*, 697–703.

(78) Herzer, N.; Hoeppener, S.; Schubert, U. S. Fabrication of Patterned Silane Based Self-Assembled Monolayers by Photolithography and Surface Reactions on Silicon-Oxide Substrates. *Chem. Commun.* **2010**, *46*, 5634–5652.

(79) De Angelis, L.; Scafè, E.; Galluzzi, F.; -, al; Bogdanoff, P.; Fiechter, S.; Kölbach, M.; Brennan, B. J.; Keirstead, A. E.; Liddell, P. A.; Vail, S. A.; Moore, T. A.; Moore, A. L.; Gust, D. 1-(3'-Amino)Propylsilatrane Derivatives as Covalent Surface Linkers to Nanoparticulate Metal Films for Use in Photoelectrochemical Cells. *Nanotechnology* **2009**, *20*, 505203.

(80) McNamara, W. R.; Milot, R. L.; Song, H. E.; Snoeberger, R. C.; Batista, V. S.; Schmuttenmaer, C. A.; Brudvig, G. W.; Crabtree, R. H. Water-Stable, Hydroxamate Anchors for Functionalization of TiO2 Surfaces with Ultrafast Interfacial Electron Transfer. *Energy Environ. Sci.* **2010**, *3*, 917–923.

(81) Mcnamara, W. R.; Snoeberger, R. C.; Li, G.; Richter, C.; Allen, L. J.; Milot, R. L.; Schmuttenmaer, C. A.; Crabtree, R. H.; Brudvig, G. W.; Batista, V. S. Hydroxamate Anchors for Water-Stable Attachment to TiO2 Nanoparticles. *Energy Environ. Sci.* **2009**, *2*, 1173–1175.

(82) Warnan, J.; Pellegrin, Y.; Blart, E.; Zhang, L.; Brown, A.; Hammarström, L.; Jacquemin, D.; Odobel, F. Acetylacetone Anchoring Group for NiO-Based Dye-Sensitized Solar Cell. *Dye. Pigment.* **2014**, *105*, 174–179.

(83) Mcnamara, W. R.; Snoeberger, R. C.; Li, G.; Schleicher, J. M.; Cady, C.

W.; Poyatos, M.; Schmuttenmaer, C. A.; Crabtree, R. H.; Brudvig, G. W.; Batista, V. S. Acetylacetonate Anchors for Robust Functionalization of TiO2 Nanoparticles with Mn(II)-Terpyridine Complexes. *J. Am. Chem. Soc* **2008**, *130*, 14329–14338.

(84) Yamazaki, Y.; Takeda, H.; Ishitani, O. Photocatalytic Reduction of CO2 Using Metal Complexes. *J. Photochem. Photobiol. C* **2015**, *25*, 106–137.

(85) Takeda, H.; Cometto, C.; Ishitani, O.; Robert, M. Electrons, Photons, Protons and Earth-Abundant Metal Complexes for Molecular Catalysis of CO2 Reduction. *ACS Catal.* **2017**, *7*, 70–88.

(86) Wang, Q.; Domen, K. Particulate Photocatalysts for Light-Driven Water Splitting: Mechanisms, Challenges, and Design Strategies. *Chem. Rev.* **2020**, *120*, 919–985.

(87) Wang, Q.; Nakabayashi, M.; Hisatomi, T.; Sun, S.; Akiyama, S.; Wang, Z.; Pan, Z.; Xiao, X.; Watanabe, T.; Yamada, T.; Shibata, N.; Takata, T.; Domen, K. Oxysulfide Photocatalyst for Visible-Light-Driven Overall Water Splitting. *Nat. Mater.* **2019**, *18*, 827–832.

(88) Teramura, K.; Wang, Z.; Hosokawa, S.; Sakata, Y.; Tanaka, T. A Doping Technique That Suppresses Undesirable H2 Evolution Derived from Overall Water Splitting in the Highly Selective Photocatalytic Conversion of CO2 in and by Water. *Chem. Eur. J.* **2014**, *20*, 9906–9909.

(89) Anzai, A.; Fukuo, N.; Yamamoto, A.; Yoshida, H. Highly Selective Photocatalytic Reduction of Carbon Dioxide with Water over Silver-Loaded Calcium Titanate. *Catal. Commun.* **2017**, *100*, 134–138.

(90) Iizuka, K.; Wato, T.; Miseki, Y.; Saito, K.; Kudo, A. Photocatalytic Reduction of Carbon Dioxide over Ag Cocatalyst-Loaded ALa4Ti4O15 (A = Ca, Sr, and Ba) Using Water as a Reducing Reagent. *J. Am. Chem. Soc.*

2011, *133*, 20863–20868.

(91) Iwase, A.; Yoshino, S.; Takayama, T.; Ng, Y. H.; Amal, R.; Kudo, A. Water Splitting and CO2 Reduction under Visible Light Irradiation Using Z-Scheme Systems Consisting of Metal Sulfides, CoOx-Loaded BiVO4, and a Reduced Graphene Oxide Electron Mediator. *J. Am. Chem. Soc.* **2016**, *138*, 10260–10264.

(92) O'Regan, B.; Grätzel, M. A Low-Cost, High-Efficiency Solar Cell Based on Dye-Sensitized Colloidal TiO2 Films. *Nature* **1991**, *353*, 737–740.

(93) Ashford, D. L.; Gish, M. K.; Vannucci, A. K.; Brennaman, M. K.; Templeton, J. L.; Papanikolas, J. M.; Meyer, T. J. Molecular Chromophore-Catalyst Assemblies for Solar Fuel Applications. *Chem. Rev.* **2015**, *115*, 13006–13049.

(94) Wang, M.; Yang, Y.; Shen, J.; Jiang, J.; Sun, L. Visible-Light-Absorbing Semiconductor/Molecular Catalyst Hybrid Photoelectrodes for H2 or O2 Evolution: Recent Advances and Challenges. *Sustain. Energy Fuels* **2017**, *1*, 1641–1663.

(95) Tian, H. Molecular Catalyst Immobilized Photocathodes for Water / Proton and Carbon Dioxide Reduction. *ChemSusChem* **2015**, *8*, 3746–3759.

(96) Dini, D.; Halpin, Y.; Vos, J. G.; Gibson, E. A. The Influence of the Preparation Method of NiO x Photocathodes on the Efficiency of P-Type Dye-Sensitized Solar Cells. *Coord. Chem. Rev.* **2015**, *304–305*, 179–201.

(97) Yu, M.; Draskovic, T. I.; Wu, Y. Cu(I)-Based Delafossite Compounds as Photocathodes in p-Type Dye-Sensitized Solar Cells. *Phys. Chem. Chem. Phys.* **2014**, *16*, 5026–5033.

(98) Crespo-quesada, M.; Reisner, E. Emerging Approaches to Stabilise Photocorrodible Electrodes and Catalysts for Solar Fuel Applications. *Energy Environ. Sci.* **2017**, *10*, 1116–1127.

(99) Yang, J.; Wang, D.; Han, H.; Li, C. Roles of Cocatalysts in Photocatalysis and Photoelectrocatalysis. *Acc. Chem. Res.* **2013**, *46*, 1900–1909.

(100) Li, D.; Shi, J.; Li, C. Transition-Metal-Based Electrocatalysts as Cocatalysts for Photoelectrochemical Water Splitting: A Mini Review. *Small* **2018**, *14*, 1–22.

(101) Inoue, H.; Shimada, T.; Kou, Y.; Nabetani, Y.; Masui, D.; Takagi, S.; Tachibana, H. The Water Oxidation Bottleneck in Artificial Photosynthesis: How Can We Get through It? An Alternative Route Involving a Two-Electron Process. *ChemSusChem* **2011**, *4*, 173–179.

(102) Garrido-Barros, P.; Gimbert-Suriñach, C.; Matheu, R.; Sala, X.; Llobet, A. How to Make an Efficient and Robust Molecular Catalyst for Water Oxidation. *Chem. Soc. Rev* **2017**, *46*, 6088–6098.

(103) Meyer, T. J.; Sheridan, M. V; Sherman, B. D.; Meyer, T. J.; Sheridan, M. V; Sheridan, M. Mechanisms of Molecular Water Oxidation in Solution and on Oxide Surfaces. *Chem. Soc. Rev* **2017**, *46*, 6148–6169.

(104) Hessels, J.; Detz, R. J.; Koper, M. T. M.; Reek, J. N. H. Rational Design Rules for Molecular Water Oxidation Catalysts Based on Scaling Relationships. *Chem. Eur. J.* **2017**, *23*, 16413–16418.

(105) Gersten, S. W.; Samuels, G. J.; Meyer, T. J. Catalytic Oxidation of Water by an Oxo-Bridged Ruthenium Dimer. *J. Am. Chem. Soc* **1982**, *104*, 4030–4032.

(106) Duan, L.; Fischer, A.; Xu, Y.; Sun, L. Isolated Seven-Coordinate Ru(IV) Dimer Complex with [HOHOH]- Bridging Ligand as an Intermediate for

Catalytic Water Oxidation. *J. Am. Chem. Soc.* **2009**, *131*, 10397–10399.

(107) Matheu, R.; Ertem, M. Z.; Benet-buchholz, J.; Coronado, E.; Batista, V. S.; Sala, X.; Llobet, A. Intramolecular Proton Transfer Boosts Water Oxidation Catalyzed by a Ru Complex. *J. Am. Chem. Soc* **2015**, *137*, 10786–10795.

Chapter 2

Objectives

Chapter 2

Aiming for a carbon neutral economy and the integration of renewable electricity in the energy system, new technologies that convert electrical renewable energy into chemical energy are currently developed. The electrochemical conversion of CO_2 can generate a variety of valuable carbon-based chemicals with high current efficiency under ambient conditions. These products can be used as feedstocks for chemical synthesis or converted into hydrocarbon fuels. To make this possible, the development of powerful and robust catalysts for water oxidation and CO_2 reduction reactions is of paramount importance. The general objective of the present thesis is the development of efficient electro- and photoelectrochemical catalytic systems for water oxidation and CO_2 reduction towards value-added chemicals.

Inspired by the state-of-the-art described in Chapter 1, the following specific objectives were defined:

- **Objective 1**: To develop the electrochemical CO_2 reduction to CO with the follow-up utilization of CO in tandem carbonylation processes.

Chapter 3 explores the synergistic effect between commercial iron (0) porphyrin catalysts and ionic liquid (ILs) electrolytes in the electrochemical CO_2 reduction reaction to CO using a three-electrode configuration cell. The second part of the chapter focuses on the development of a tandem CO_2 electroreduction reaction to CO with the follow-up utilization of CO for the synthesis of added-value organic compounds via Pd-carbonylation, and Rh-hydroformylation reactions.

IFF and DOW companies expressed interest in the exploitation of these results and will assess the scalability potential to integrate the resulting technology in their unit operations.

- **Objective 2:** To develop an efficient and robust photoelectrocatalyst for the CO_2 reduction to formic acid (HCOOH).

Chapter 4 focuses on the investigation of new hybrid molecular/semiconductor hybrid photocathodes for solar driven CO_2 reduction in the presence of ionic liquids as a CO_2 absorbent /electrolyte. The first part of the chapter deals with the synthesis and characterization of new vinyl-tagged molecular metal complexes and their covalent immobilization onto Cu_2O/SnO_2 and $CuGaO_2$ surface via electropolymerization methodology. In the second part, the activity, stability, and selectivity of the resulting hybrid photocathodes are evaluated in the photoelectrochemical CO_2 reduction reaction with and without ionic liquids.

AVANTIUM company expressed interest in the exploitation of these results and will assess the scalability potential to integrate the resulting technology in their unit operations.

- **Objective 3:** To develop an efficient and robust photoelectrocatalyst for water oxidation.

Chapter 5 focuses on the investigation of new hybrid molecular/semiconductor hybrid photoanodes for solar driven water oxidation reaction. In the first part, different strategies for the immobilization of vinyl-tagged metal complexes onto $BiVO_4$-based photoanode materials was investigated. The strategies evaluated were: (a) electropolymerization of the vinyl derivatized complexes, and (b) thiol-ene click reaction of the vinyl derivatized complexes. Finally, the robustness and the efficiency of the resulting hybrid photoanodes were evaluated in the photoelectrochemical water oxidation reaction using a custom-made one-chamber Teflon cell.

IFF and DOW companies expressed interest on the exploitation of these results and will assess the scalability potential with the aim of integrate the resulting technology in their unit operations.

Chapter 3

Synergism between iron (0) porphyrins and dicationic imidazolium ionic liquids: CO_2 electrochemical reduction to CO and tandem carbonylations

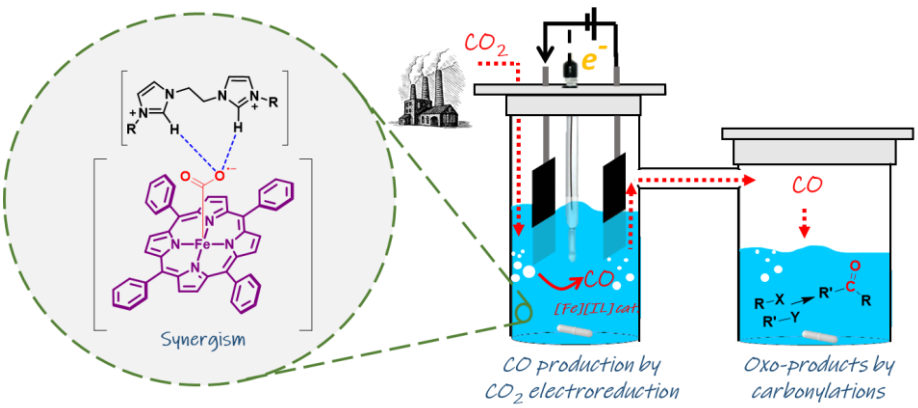

Chapter 3

Abstract

In electrocatalysis, the electrolyte role is of paramount importance in the design of efficient catalytic systems due to the possible synergism between the catalyst and the electrolyte. Ionic liquids (ILs) were established as alternative electrolytes to aqueous media. Herein, a thorough study of the effect of ionic liquid structure in the CO_2 electroreduction was performed using a commercial iron (III) porphyrin ($Fe^{III}TPP{\cdot}Cl$). High faradaic efficiencies and low overpotentials were achieved using dicationic ionic liquids. This behavior can be explained according to the reduction potential of E Fe^{I}/Fe^{0} caused by the ionic liquid cation-iron complex anion pairing effect and the reduction of the E CO_2/CO overpotential via the push-pull mechanism. Indeed, the electrons are pushed into the CO_2 molecule by the electron-rich catalyst and the cleavage of one C-O bond is facilitated by the synergetic contribution of the electron deficient cation of the ionic liquids. The reaction conditions were optimized for the electrochemical CO_2 reduction to CO, which was utilized in tandem reactions to produce organic molecules via Pd-catalyzed carbonylations and Rh-catalyzed hydroformylation.

3.1. Introduction

The worldwide energy consumption is rapidly increasing, due to the exponential growth of world population, the fast development of emerging countries and the change in lifestyle of our society. The fossil fuels like coal, natural gas and oil are currently mainly used as source of energy both in industry an in daily life. The fossil fuels are finite and imply the emission of greenhouse gases and pollutants. Alternatives such as wind, hydro and solar power are sources of sustainable electricity, but their intermittency makes energy storage a challenge.[1] In addition, the renewable electricity does not provide combustible fuels for the transport sector, nor feedstock chemicals, to making plastics, fertilizers and pharmaceuticals. CO_2 is the thermodynamically stable end product of numerous chemical and biological oxidation reactions and the reverse process that can form chemicals from CO_2 require an energy input.[2]

In this context, over the last years, scientists have devoted significant efforts to the conversion of CO_2. Among them, one of the most promising approach is based on the CO_2 electrochemical reduction for the in-situ selective generation of reactive gas intermediates (i.e., carbon monoxide (CO) or syngas mixtures (CO/H_2) and their utilization in organic synthesis. However, this process remains challenging.[3,4]

3.1.1. Transition metal complexes as CO_2 reduction catalysts

Transition metal complexes such as the iron(III) tetraphenylporphyrin chloride ($Fe^{III}TPP{\cdot}Cl$) are particularly suited for the electroreduction of CO_2 at low overpotential because the in-situ formed iron(0) tetraphenylporphyrin ($Fe^{0}TPP$) readily reacts with CO_2. The electron transfer takes place within the metal coordination sphere avoiding the intermediacy of the $CO_2^{\bullet-}$ anion radical along the reaction pathway, which displays a much larger E $CO_2/CO_2^{\bullet-}$

(– 1.97 V vs normal hydrogen electrode (NHE)[5]) compared with the E CO_2/CO (– 0.69 V vs NHE in DMF[6]), and may lead to higher selectivity than the direct electrochemical reduction of CO_2 at inert electrodes which yields mixtures of oxalate, formate, and carbon monoxide (plus carbonate) in aprotic solvents[7] and formic acid[8] in water.[9–18]

The cyclic voltammogram of Fe^{III}TPP·Cl exhibits three chemically reversible waves corresponding to the successive formation of the Fe(II), $Fe(I)^{-}$ and $Fe(0)^{2-}$ complexes. Catalysis takes place at the $Fe(I)^{-}$/$Fe(0)^{2-}$ wave, and it was reported that the tuning of the redox behavior of the iron-catalyst should allow important improvements in CO_2RR performance.

Common strategies for modifying the $Fe(I)^{-}$/$Fe(0)^{2-}$ wave are the modification of the iron-complex structure (Figure 1a) by introduction of functional groups able to contribute to the stabilization of the metallocarboxylate intermediate ($[Fe\text{-}CO_2]^{2-}$ adduct, Scheme 1a) by electronic effects, hydrogen bonding or through-space Coulombic interactions.[19,20] The addition of weak Brönsted acids such as TFE that results in a synergistic effect with the catalysts can also improve the catalysts performance (activity and stability) and the product selectivity (i.e., CO is the main product, while, depending on the acid, formate may also be formed). However, this methodology involves difficult and expensive multistep synthesis. Therefore, this chapter is focused on the development of a simple and effective procedure to improve the efficiency of the iron porphyrin.[14,15]

Previous work using Iron Porphyrin

a) Structure modification

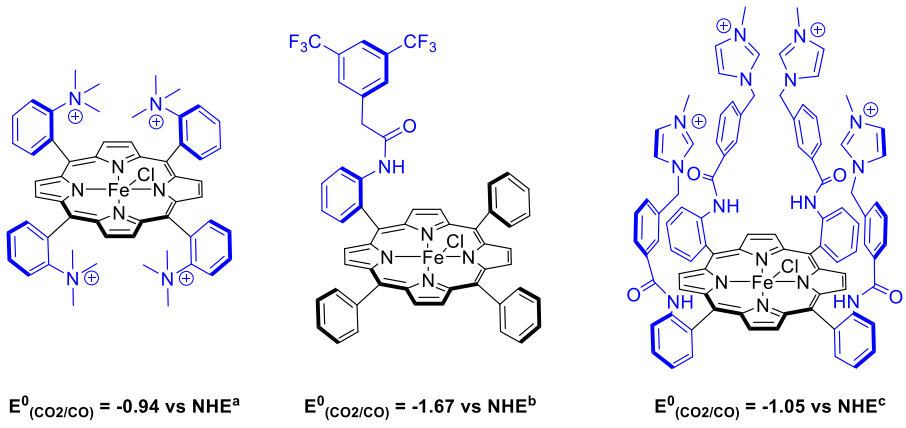

$E^0_{(CO2/CO)}$ = -0.94 vs NHE[a] $E^0_{(CO2/CO)}$ = -1.67 vs NHE[b] $E^0_{(CO2/CO)}$ = -1.05 vs NHE[c]

b) Electrolyte/anion modification

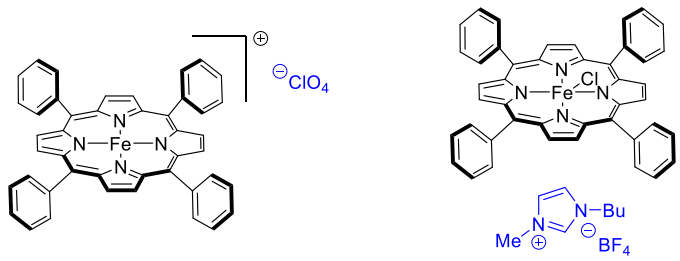

$E^0_{(CO2/CO)}$ = -1.46 vs NHE[d] $E^0_{(CO2/CO)}$ = -1.36 vs NHE[e]

***Figure 1**: Selected examples of Iron Porphyrins CO_2 reduction catalysts. a) Approaches based on iron porphyrin structure modification[a19,b21,c22]; b) recent examples described the improvement of the catalytic activity of $Fe^{III}TPP{\cdot}Cl$ by simple anion exchange process or electrolyte modification.[d23,e6]*

Very recently, some improvement in the performance of this kind of catalyst was achieved by anion exchange of the $Fe^{III}TPP{\cdot}Cl$ to form $Fe^{III}TPP{\cdot}ClO_4$ (Figure 1b), making the iron salt soluble in many different solvents. The authors proposed a distinct mechanism and metallocarboxylate intermediate ($[Fe\text{-}CO_2]^-$ adduct, Scheme 1b) using acetonitrile compared with the mechanism using DMF (Scheme 1a). Furthermore, this complex in acetonitrile provided high TOF ($7.3{\cdot}10^6$ s^{-1}) and high faradaic efficiencies (FE up to 98%).[23]

Chapter 3

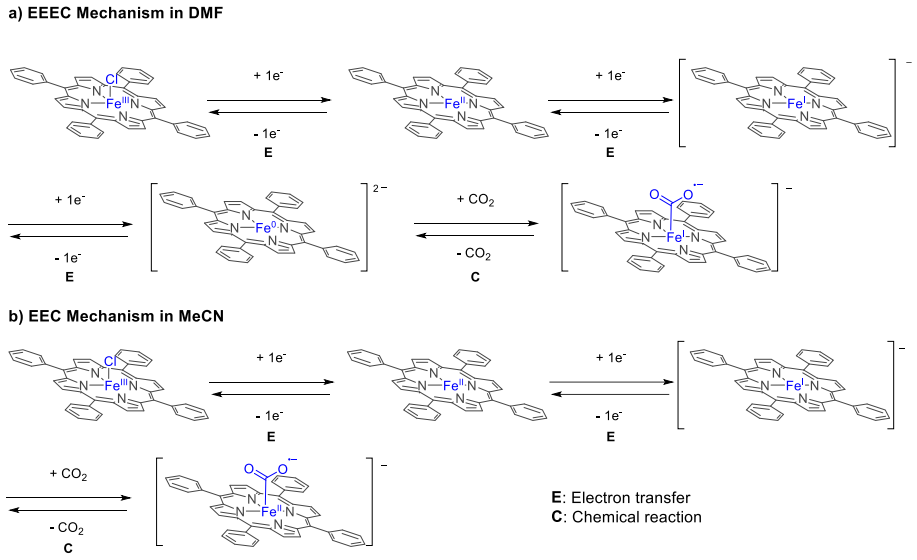

***Scheme 1**: Proposed mechanism for the formation of the metallocarboxylate intermediate of Fe^{III}TPP·Cl a) in DMF via the EEEC mechanism and b) in MeCN via the EEC mechanism. Adapted from ref*[23].

One effect scarcely studied is the that created by the addition of cations with the ability to stabilize anionic species formed under reaction conditions. For instance, the addition of inorganic monocations such as Li^+ and Na^+, and dications such as Mg^{2+}, Ca^{2+} and Ba^{2+} with Lewis acid character also improved the performance of the Fe^{III}TPP·Cl catalyst in the CO_2RR, suggesting that the association of an electron donor catalyst with an electrophilic additive provides more efficient catalysis.[16,17] The observed order of reactivity (Mg^{2+} = Ca^{2+} > Ba^{2+} > Li^+ > Na^+) is in agreement with the enhancements of the $Fe(I)^-/Fe(0)^{2-}$ wave. This behavior was explained by the acceleration of the catalytic process by means of ion-pairing with the negatively charged oxygen atoms of metallocarboxylate intermediate ($[Fe\text{-}CO_2]^{2-}$ adduct, Scheme 1).[16,17] The function of such an electrophilic assistance is to facilitate the breaking of one of the carbon-oxygen bonds of CO_2. In concordance with this mechanism, the analysis of the reaction order showed that only one divalent cation is required in the reaction while two cations are involved in the case of

monovalent cations.[16,17] However, the application of this strategy was hampered by a self-inhibition process resulting from the deposition of insoluble metal carbonates on the electrodes during the reduction process.[16,17]

In this chapter, the effect of ionic liquid organic cations on the iron-catalyst performance was evaluated in the selective CO_2 electroreduction to CO. Moreover, tandem CO_2 electroreduction-carbonylation reactions were also studied.

3.1.2. Ionic Liquids as electrolyte for CO_2 electroreduction catalyzed by metal complexes

As mentioned Chapter 1, the use of ionic liquids (IL) has attracted considerable attention as electrolytes and co-catalysts in the CO_2 reduction.[24–26] After the first report of Masel and co-workers where the decrease in CO_2 reduction overpotential was describe using ionic liquids with a CO faradaic efficiency greater than 96% using a silver foil (Figure 2),[27] various homogeneous catalysts were tested in the presence of ionic liquids in the CO_2 electroreduction.[6,22,28–32]

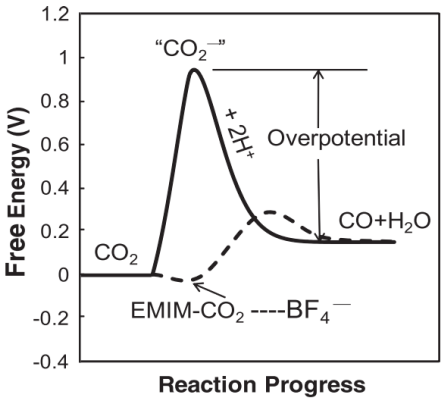

***Figure 2**: Schematic representation of how the free energy of the system changes in the CO_2 reduction by the use of an aqueous electrolyte (solid line) or ionic liquid (dashed line). Reprinted from ref [27].*

Chapter 3

The first homogeneous example of CO_2 electroreduction using ionic liquids was reported by Grills and co-workers.[31] They described the use of the homogeneous catalyst *fac*-ReCl(bpy)$(CO)_3$ using the ionic liquid 1-ethyl-3-methylimidazolium tetracyanoborate ([EMI·TCB]) as both the electrolyte and solvent and observed that the use of IL caused a decrease of the CO_2 reduction overpotential. Later, the same group performed a thorough study on the standard electrode potentials for the CO_2 electroreduction to CO using imidazolium based IL ([EMI·TCB]) and the contribution of imidazolium ionic liquids as co-catalyst.[28] In this report, they showed that the imidazolium cation plays a key role in the catalytic activity by reducing the overpotential and proposed a reaction scheme (Scheme 2).

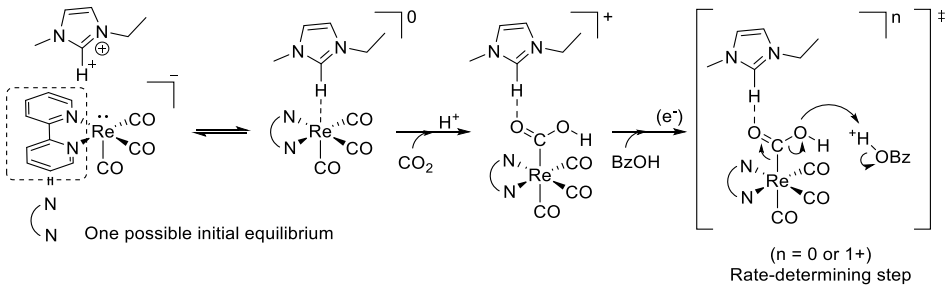

***Scheme 2**. Proposed mechanism for CO_2 electroreduction using imidazolium based ionic liquids. Adapted from ref [28].*

Isaacs and co-workers studied the CO_2 electrochemical reduction using [Ni(cyclam)Cl_2] and [Co(cyclam)Cl_3] as catalysts, 1-butyl-3-methylimidazolium tetrafluoroborate [BMI·BF_4] and 1-butyl-3- methylimidazolium bis(trifluoromethylsulfonyl)imide [BMI·NTf_2] as ionic liquid (Figure 3).[30] The results indicated that [BMI·BF_4] increased the catalytic activity via a faster M(II)/M(I) redox process.

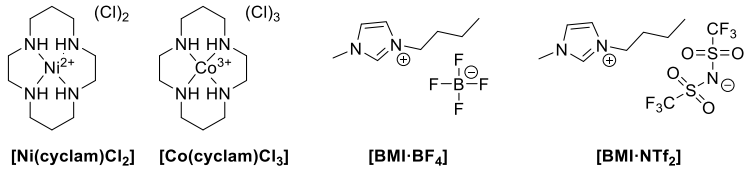

[Ni(cyclam)Cl_2] **[Co(cyclam)Cl_3]** **[BMI·BF_4]** **[BMI·NTf_2]**

***Figure 3**. Structures of [Ni(cyclam)Cl_2], [Co(cyclam)Cl_3], [BMI][BF_4] and [BMI][NTf_2]. Adapted from ref [30].*

Electrolysis experiments performed at −1.4 V vs. Ag/AgCl using BMI·BF_4 revealed a better catalytic performance for [Ni(cyclam)Cl_2] than [Co(cyclam)Cl_3].

The efficiency of the $Fe^{III}TPP{\cdot}Cl$ was also improved by introduction of the IL in the catalyst structure[22] and the use of the monocationic IL ([BMI·BF_4]) as electrolyte [6] (Figure 1). Officer and co-workers developed a CO_2 electroreduction system using $Fe^{III}TPP{\cdot}Cl$, 1-butyl-3-methylimidazolium tetrafluoroborate ([BMI·BF_4]) as ionic liquid and trifluoroethanol (TFE) as proton source in DMF (Figure 1b).[6] In this study, they showed that upon addition of [BMI·BF_4], the catalytic activity was increased. They demonstrated that the IL acts as a co-catalyst and shifts the reduction potential of the $[Fe^0TPP]^{2-}$ to less negative values, obtaining higher current densities and higher CO Faradaic efficiencies (FE_{CO} = 93%).

Aukauloo and co-workers introduced methylimidazolium groups in the iron porphyrin structure with the aim to obtain a pre-organized ionic liquid environment (Figure 1a).[22] They reported a catalytic wave for the CO_2 reduction at E^0_{cat} = -1.05 V vs NHE using the $Fe^{III}TPPIL$, which is 375 mV more positive than that for the unmodified porphyrin. Higher catalytic currents for CO_2 reduction were also obtained using $Fe^{III}TPPIL$ with a FE_{CO} = 91% at -0.948 V vs NHE.

These examples demonstrated a significant role of ionic liquids in the CO_2 reduction process, most likely by complexation. Moreover, the organic cations

of the IL enhance the process via the solubilization of CO_2 and avoid the self-inhibition process since imidazolium carbonates displayed much higher solubility.[33–37]

3.1.3. Tandem CO_2 electroreduction coupled with the production of added-value chemicals

The development of efficient catalytic systems for carbon dioxide (CO_2) reduction to useful C1-building blocks such as carbon monoxide (CO), and the "on-site" utilization of this product in tandem processes is challenging. [2,38–43] In the specific case of CO, transition metal catalyzed carbonylation reactions are one of the most widely applied catalytic process in organic synthesis and industrial production.[44,45] The lack of sustainability of the current process is a consequence of the use of CO from syngas produced by reforming of fossil fuels.[46] Among the current alternative strategies for the CO production,[47,48] one of the most promising is the electrochemical conversion of CO_2 by the use of renewable electrical energy at small decentralized plants to produce CO at the customer's site, thus avoiding expensive cost and safety transportation, storage and manipulation issues.[49,50] As a relevant example, Haldor Topsoe developed the eCOs solid oxide electrolysis cell (SOEC) technology able to deliver large amounts of CO gas per hour.[51] However, the access to this complex and expensive cells and the manipulation of the above-mentioned volumes of CO are hampering the development of sustainable carbonylation protocols by academic and industrial groups. Various methodologies using tandem systems were developed to produce CO in one chamber using surrogates and couple the CO production with a carbonylation reaction.[52] Skrydstrup and co-workers developed a commercial system based on a two-chamber reactor (COware®, Figure 4), in which CO is generated in one reaction chamber in near-stoichiometric amounts with respect to the ensuing carbonylation reaction.[52–54]

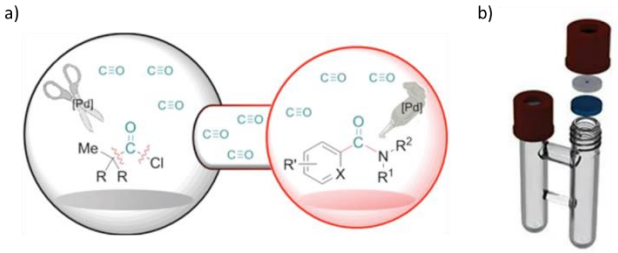

***Figure 4**: a) Scheme of two-chamber reactor using CO surrogates to produce CO coupled with an aminocarbonylation reaction. Reprinted from ref [55]. b) COware® two-chamber reactor.*

However, there are only two reports on CO_2 electrochemical reduction coupled with CO carbonylation.[56,57] The first one, by Skrydstrup and co-workers,[56] adapted the two-chamber reactor concept for the development of a system in which CO_2 is electrochemically reduced to CO in one chamber by an iron(III) tetraphenylporphyrin chloride ($Fe^{III}TPP{\cdot}Cl$) catalyst in the presence of tetrabutylammonium tetrafluoroborate ($TBA{\cdot}BF_4$) as electrolyte, trifluoroethanol (TFE) as proton source and N,N-dimethylformamide (DMF) as solvent under the appropriate cell voltage (-4.3 V) (Scheme 3). In the contiguous chamber, a palladium organometallic complex successfully catalyzed the consumption of the stoichiometrically generated CO via aminocarbonylation, alkoxycarbonylations, carbonylative Sonogashira coupling and carbonylative Suzuki coupling.[56] There is still room for improvement since this protocol displayed some limitations, i.e., kinetics for the electrochemical CO_2 reduction resulted in slow and time dependent CO generation (rate of CO formation around 0.25 $mmol{\cdot}h^{-1}$) and restricted the applicability to a limited number of carbonylation.

Chapter 3

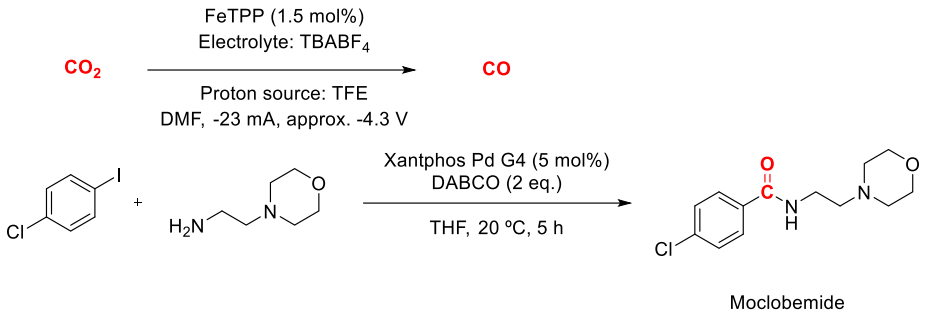

***Scheme 3**: Tandem CO_2 electroreduction coupled with Pd-catalyzed aminocarbonylations. Moclobemide synthesis. Adapted from ref [56].*

The second report was published in 2021 by Fontecave and co-workers.[57] They designed a system to couple a high-pressure CO_2 electroreduction using a ZnAg catalyst for the CO production, purify the gas mixture and use it for the carbonylation of propylene oxide into β-butyrolactone (Scheme 4).

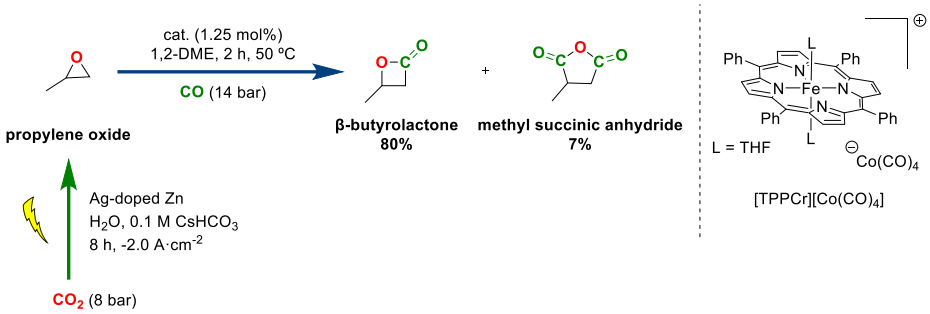

***Scheme 4**: Tandem high pressure CO_2 electrochemical reduction coupled with the thermal propylene oxide carbonylation. Adapted from ref [57].*

With this system, they performed an electrochemical CO_2 reduction using a porous AgZn alloy material as the cathode in a single-compartment high pressure autoclave. They performed an 8 h experiment applying -0.2 $A \cdot cm^{-2}$ with an initial CO_2 pressure of 8 bar obtaining a gas mixture composed of 33% CO, 8% H_2, 59% CO_2 with traces of H_2O and O_2 an 8.5 bar total pressure. Then, purification and repressurization of the gas mixture was performed to obtain a final gas mixture with a partial CO pressure of 14 bar. The carbonylation of

propylene oxide was then performed using [TPPCr][$Co(CO)_4$], 1,2-dimethoxyethane, at 50 °C and under argon atmosphere. After 2 h of reaction they observed full conversion of the propylene oxide with 80% selectivity to the lactone.

In summary, to date, the CO_2 electroreduction to CO coupled with the production of high added-value chemicals was only scarcely studied and the examples described in the literature are limited to Pd-catalyzed carbonylations and Co-catalyzed carbonylations. There is thus room for the exploration of other processes of industrial interest such as hydroformylation reactions.[58,59]

The purpose of the work described in this Chapter was to examine whether organic cations may assist the iron(0) porphyrin catalysis of CO_2 reduction. Bisimidazolium and monoimidazolium cations were selected to elucidate whether the presence of dication is required for observing a synergistic effect. This comparative study was also the occasion of fully determining the product distribution in the presence of ionic liquids bearing organic bisimidazolium cations and to propose a reaction mechanism. The reaction conditions for the CO_2 reduction using IL were optimized to produce CO and use it in tandem reactions.

3.2. Results and discussion

3.2.1. Study of the ionic liquid structure in the CO_2 electroreduction

Although a positive effect was reported for ionic liquids in the CO_2 electroreduction, only imidazolium based ILs containing a proton or a methyl in C2 position were studied with homogeneous catalysts.[6,28,60,61] Here, a systematic study of the ionic liquid structure was performed in the selective CO_2 electroreduction to CO. A series of non-commercial ionic liquids were synthetized following adapted literature procedures.[62,63] The synthesis of non-commercial ionic liquids is described in the supporting information.

3.2.1.1. Study of the anion effect

First, the effect of the IL anion was studied by comparing the performance obtained using electrolytes based on the combination of 1-butyl-3-methyl imidazole ([BMI]) cation with anions exhibiting distinct hydrophobic and hydrophilic properties. In Table 1, the IL tested are listed from the more hydrophilic to the more hydrophobic cation-anion combination. These tests were performed under the same conditions and using an IL concentration of 0.1 M. The experiments were performed in a three electrodes set-up using a single chamber cell containing a glassy carbon, platinum wire and $Ag/AgNO_3$ as working, counter, and reference electrodes, respectively. N,N-dimethylformamide (DMF) was used as a solvent, trifluoroethanol (TFE) as a proton source and meso-tetraphenylporphyrin iron(III) chloride ($Fe^{III}TPP{\cdot}Cl$) as catalyst.

Cyclic voltammetry's (CV) of each sample under N_2 with and without TFE were performed to study the reduction potential ($E_{1/2}$) of the iron porphyrin. The three characteristic peaks of the iron porphyrin reduction were observed (Table 1). As mentioned in the literature,[6] when the TFE is added the first

reduction potential E $Fe(III)^{+}/Fe(II)$ is negatively shifted. In this first reduction potential, the chloride ligand is dissociated.

The reduction potential of the Fe(I)- to $Fe(0)^{2-}$ is the one that directly influences the overpotential of the CO_2 reduction. When different anions were compared, all the reduction potentials E $Fe(I)^{-}/Fe(II)^{2-}$ were between -1.44 V to -1.40 V vs NHE. No relevant shift was observed between these anions.

***Table 1**: Reduction potentials ($E_{1/2}$) of each sample, changing the anion structure, determined by cyclic voltammetry (V vs. NHE, Scan rate: 100 $mV{\cdot}s^{-1}$), from the more hydrophilic to the more hydrophobic IL.*

Entry	IL	Sample	E $Fe^{III/II}$	E $Fe^{II/I}$	E $Fe^{I/0}$	E CO_2/CO	Overpotential
1	**[BMI·CH_3SO_3]**	FeTPP + IL	-0,01	-0,94	-1,43	-1,33	640
		FeTPP + IL + TFE	0,01	-0,94	-1,44		
2	**[BMI·CH_3COO]**	FeTPP + IL	-0,2	-1,07	-1,46	-1,35	660
		FeTPP + IL + TFE	-0,25	-0,98	-1,44		
3	**[BMI·CF_3SO_3]**	FeTPP + IL	-0,02	-0,92	-1,43	-1,33	640
		FeTPP + IL + TFE	-0,33	-0,94	-1,42		
4	**[BMI·CF_3COO]**	FeTPP + IL	0,01	-0,95	-1,39	-1,31	610
		FeTPP + IL + TFE	0	-0,94	-1,43		
5	**[BMI·BF_4]**	FeTPP + IL	-0,1	-0,93	-1,43	-1,34	650
		FeTPP + IL + TFE	-0,17	-0,91	-1,4		
6	**[BMI·PF_6]**	FeTPP + IL	-0,5	-0,92	-1,44	-1,34	650
		FeTPP + IL + TFE	-0,33	-0,94	-1,42		
7	**[BMI·NTf_2]**	FeTPP + IL	-0,05	-0,95	-1,45	-1,35	660
		FeTPP + IL + TFE	-0,33	-0,95	-1,43		

***Reaction conditions**: 0.5 mM $Fe^{III}TPP{\cdot}Cl$, 0.1 M ionic liquid, 1.0 M TFE in DMF under N_2 or CO_2 atmosphere.*

When the CVs were performed under CO_2 atmosphere, for all the ionic liquids, the potential E CO_2/CO is between -1.31 and -1.35 V vs NHE (Figure 5). Therefore, no relevant effect of the anionic moiety of the ILs was detected on the CO_2 reduction.

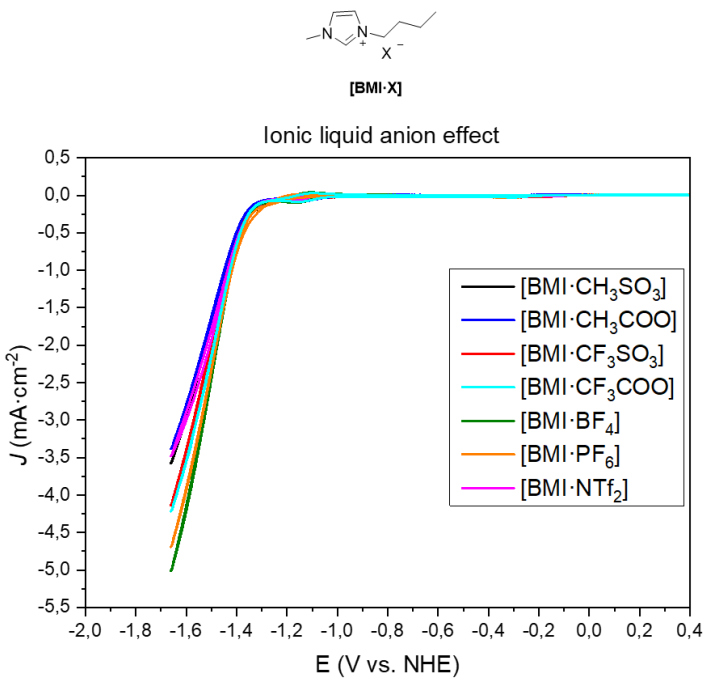

***Figure 5**. Ionic liquid structures and cyclic voltammogram of 0.5 mM $Fe^{III}TPP{\cdot}Cl$, 0.1 M ionic liquid, 1.0 M TFE in DMF under CO_2 atmosphere.*

3.2.1.2. Study of the cation effect

Next, the effect of the cation structure was studied using a series of imidazole structures and BF_4 as the common anion. The results were compared with those obtained using tetrabutylammonium hexafluorophosphate [TBA·PF_6] as benchmark electrolyte.

When electrolytes based on 1-methyl-imidazolium cations [BMI·BF_4] were used, more positive E $Fe(I)^{-}/Fe(0)^{2-}$ and E CO_2/CO (Table 2 and Figure 6) were obtained with respect to those recorded using electrolytes based on 1-methyl-2,3-dimehtyl-imidazolium cations [BMMI·BF_4] and tetrabutylammonium cations [TBA·PF_6]. This observation suggested that the presence of protons in C2-position of the imidazolium ring is important for efficiently reducing the required overpotentials. This behavior was correlated with a possible

hydrogen bonding or Coulombic interactions similar to those observed for chemically modified iron-porphyrin systems.[19,20]

The difference in E $Fe(I)^{-}/Fe(0)^{2-}$ and E CO_2/CO is rationalized also according to the observation of Saveant and co-workers on the beneficial effect of the ion-pairing in the electrochemistry of metal ions (Scheme 5).[12] Besides the classical stepwise pathways (electron-transfer first, followed by ion-pairing or vice versa), ion-pairing may also occur concertedly with electron transfer avoiding high-energy intermediates and reducing the potential.[12]

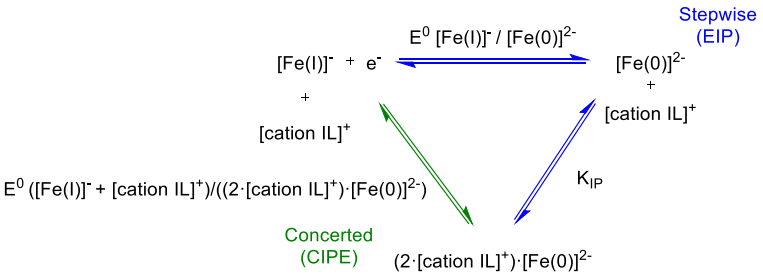

***Scheme 5**: Stepwise and concerted pathways for electron-transfer and ion-pairing.*

When the effect of the aliphatic chain length was evaluated 1-butyl-3-methylimidazolium tetrafluoroborate [BMI·BF_4] and the 1-ethyl-3-methylimidazolium tetrafluoroborate [EMI·BF_4] no differences were observed (Table 2 and Figure 6).

***Table 2**: Reduction potentials ($E_{1/2}$) of each sample, changing the cation structure, determined by cyclic voltammetry (V vs. NHE, Scan rate: 100 mV·s^{-1}).*

Entry	IL	Sample	E $Fe^{III/II}$	E $Fe^{II/I}$	E $Fe^{I/0}$	E CO_2/CO	Overpotential
1	**[TBA·PF_6]**	FeTPP + IL	-0,01	-0,9	-1,54	-1,42	730
		FeTPP + IL + TFE	-0,33	-0,93	-1,53		
2	**[BMI·BF_4]**	FeTPP + IL	-0,1	-0,93	-1,43	-1,34	650
		FeTPP + IL + TFE	-0,17	-0,91	-1,4		
3	**[BMMI·BF_4]**	FeTPP + IL	-0,28	-0,93	-1,5	-1,4	710
		FeTPP + IL + TFE	-0,19	-0,91	-1,49		
4	**[EMI·BF_4]**	FeTPP + IL	-0,02	-0,92	-1,4	-1,34	650
		FeTPP + IL + TFE	-0,3	-0,93	-1,41		
5	**[$C2(MI)_2$·$(BF_4)_3$]**	FeTPP + IL	-0,06	-0,92	-1,33	-1,2	510
		FeTPP + IL + TFE	0	-0,9	-1,31		

***Reaction conditions**: 0.5 mM Fe^{III}TPP·Cl, 0.1 M ionic liquid, 1.0 M TFE in DMF under N_2 or CO_2 atmosphere.*

Finally, the dicationic ionic liquid ([$C2(MI)_2$·$(BF_4)_3$]) was tested. Surprisingly, an important decrease of the overpotential was observed, from 650 mV using the [BMI·BF_4] to 510 mV with the dicationic ionic liquid (the overpotential was calculated using the E^0 CO_2/CO = -0.69 V vs NHE in DMF). This observation suggested, apart from the possible hydrogen bonding or Coulombic interactions through-space similar to those observed for chemically modified iron-porphyrin systems, that there is also an effect similar to those reported for inorganic divalent cations and monovalent cations.[16,17] This behavior could be attributed to a more efficient interaction between the divalent IL cation and the dianionic iron-intermediates, resulting in an stronger synergistic effect than those observed with monovalent IL cations.

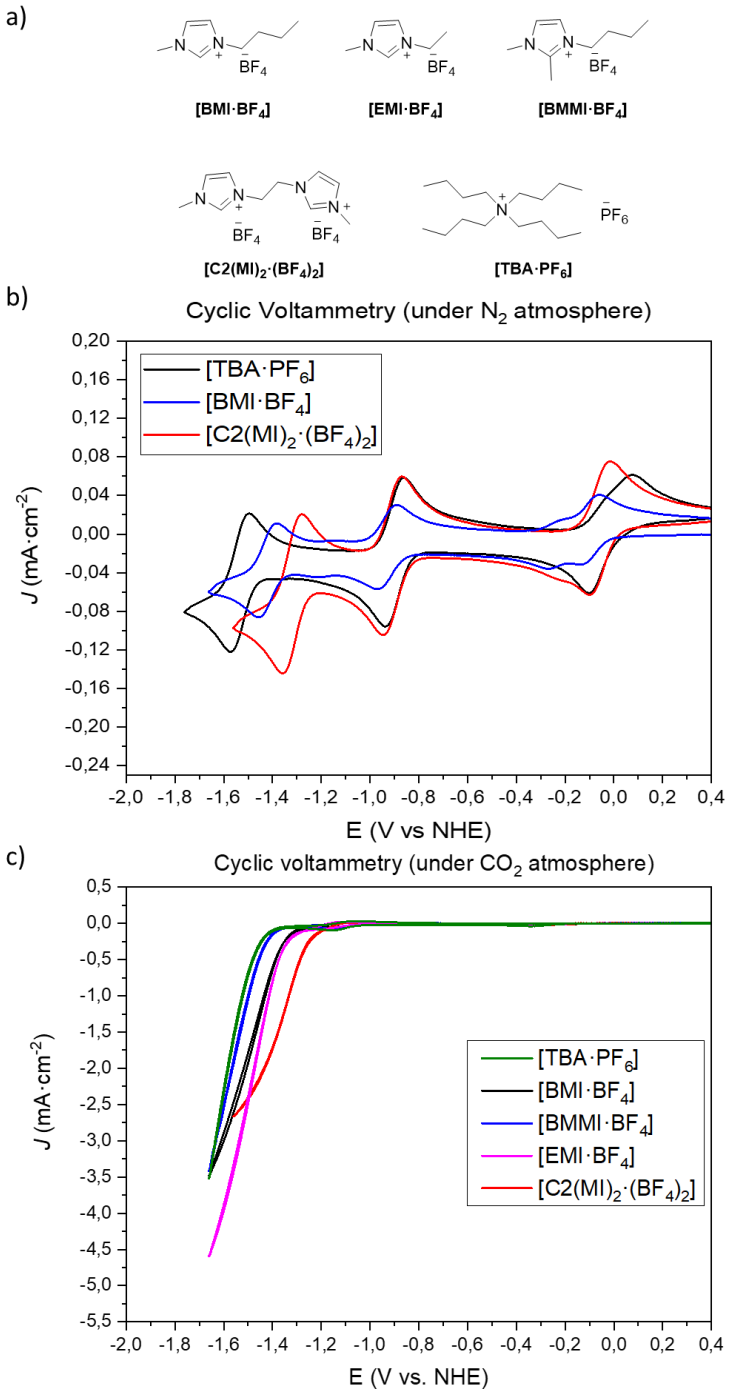

***Figure 6**: a) Ionic liquid structures; b) cyclic voltammogram of 0.5 mM $Fe^{III}TPP{\cdot}Cl$, 0.1 M ionic liquid, in DMF under N_2 atmosphere; c) cyclic voltammogram of 0.5 mM $Fe^{III}TPP{\cdot}Cl$, 0.1 M ionic liquid, 1.0 M TFE in DMF under CO_2 atmosphere.*

3.2.1.3. Study of the dicationic ionic liquid structure

Due to the important decrease of the CO_2 reduction overpotential using the dicationic IL [C2$(MI)_2$·$(BF_4)_2$], two other dicationic ionic liquids were synthetized[64,65] by variation of the chain length between the imidazole moieties, namely [C1$(MI)_2$·$(BF_4)_2$] and [C3$(MI)_2$·$(BF_4)_2$].

***Table 3**: Reduction potentials ($E_{1/2}$) of each sample, changing the bridge length between the imidazole, determined by cyclic voltammetry (V vs. NHE, Scan rate: 100 mV·s^{-1}).*

Entry	IL	Sample	E $Fe^{III/II}$	E $Fe^{II/I}$	E $Fe^{I/0}$	E CO_2/CO	Overpotential
1	**[C1$(MI)_2$·$(BF_4)_2$]**	FeTPP + IL	-0,2	-0,43	-	-	-
		FeTPP + IL + TFE	-0,02	-0,42	-0,89		
2	**[C2$(MI)_2$·$(BF_4)_2$]**	FeTPP + IL	-0,06	-0,92	-1,33	-1,2	510
		FeTPP + IL + TFE	0	-0,9	-1,31		
3	**[C3$(MI)_2$·$(BF_4)_2$]**	FeTPP + IL	0,01	0,98	1,27	-1,2	510
		FeTPP + IL + TFE	0	0,93	1,25		

***Reaction conditions**: 0.5 mM Fe^{III}TPP·Cl, 0.1 M ionic liquid, 1.0 M TFE in DMF under N_2 or CO_2 atmosphere.*

Using the dicationic ionic liquid ([C1$(MI)_2$·$(BF_4)_2$]), a reduction peak at high potentials was observed for the CO_2 reduction. When the experiment was repeated under the same conditions but using N_2 instead of CO_2 the same cyclic voltammetry profile was observed (Figure 7b). This behavior thus indicated that IL decomposition was taking place under the potential applied, preventing CO_2 reduction. Indeed, H_2 was the only product formed in the chronopotentiometry experiment under CO_2 atmosphere. The IL-decomposition products might be responsible for the poisoning of the Fe-catalyst. In Scheme 6 a proposed path of the ionic liquid decomposition is represented. The electrochemical stability window of imidazolium-based ionic liquids as electrolytes is determined by the stability of the anion and cation. The cation is more susceptible to decompose under reductive conditions, and the anion under oxidative conditions.[66]

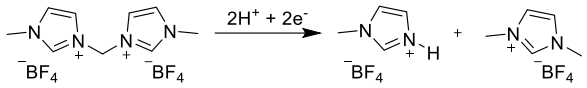

***Scheme 6**: Proposed path for the $[C1(MI)_2{\cdot}(BF_4)_2]$ decomposition.*

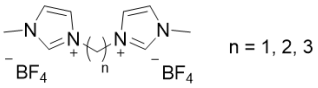

$[C_n(MI)_2{\cdot}(BF_4)_2]$

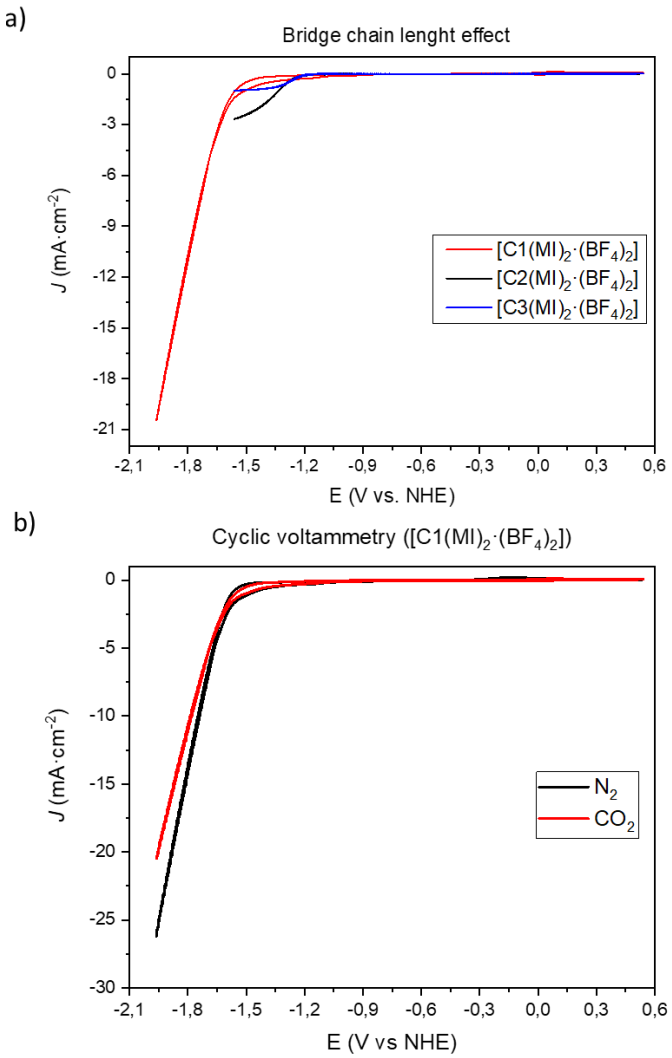

***Figure 7**: Ionic liquid structures and a) cyclic voltammogram of 0.5 mM $Fe^{III}TPP{\cdot}Cl$, 0.1 M ionic liquid, 1.0 M TFE in DMF under CO_2 atmosphere. b) cyclic voltammogram of 0.1 M Dicationic$\cdot BF_4$ n=1, 0.5 mM $Fe^{III}TPP{\cdot}Cl$, 1.0 M TFE in DMF under N_2 and CO_2 atmosphere.*

Comparing the dicationic ionic liquids ($[C2(MI)_2{\cdot}(BF_4)_2]$) and ($[C3(MI)_2{\cdot}(BF_4)_2]$) were used, both CO_2 reduction overpotentials were identical, 510 mV (Table 3, Figure 7a). However, the dicationic IL ($[C2(MI)_2{\cdot}(BF_4)_2]$) showed higher current density than ($[C3(MI)_2{\cdot}(BF_4)_2]$), probably due to more efficient interactions with the iron-porphyrin intermediates (i.e., $[Fe^0]^{2-}$ and $[Fe\text{-}CO_2]^{2-}$) involved in the CO_2 reduction process reaction.

In summary, the results obtained showed an important effect of the cationic moiety of the IL electrolytes on the CO_2 electroreduction. Consequently, the optimization of the reaction conditions for the CO production was performed using the dicationic ionic liquid ($[C2(MI)_2{\cdot}(BF_4)_2]$) as electrolyte.

3.2.2. Reaction conditions optimization

Using ($[C2(MI)_2{\cdot}(BF_4)_2]$) as electrolyte, a study of the reaction conditions was performed. The parameters studied were the IL concentration, TFE concentration, $Fe^{III}TPP{\cdot}Cl$ concentration, and current intensity.

Cyclic voltammetry (CV) experiments were carried out using the above-mentioned set-up. Chronopotentiometry (CP) experiments were also carried out with selected samples using a three electrodes set-up, with two glassy carbon electrodes of 9 cm^2, and $Ag/AgNO_3$ as working, counter, and reference electrode, respectively. Gas samples collected at regular intervals were analyzed by GC-TCD analysis and the CO and H_2 concentration was determined using calibration curves in a broad range of concentrations (from 0.05 to 40.0 % vol/vol). Liquid samples were analyzed by ^1H, ^{13}C and ^{19}F NMR to check the presence of CO_2 reduction byproducts (i.e., formate and carbonates), and also to monitor the stability of the reaction system.

3.2.2.1. Ionic liquid concentration

First, the ionic liquid concentration was optimized using 0.1, 0.3, 0.6 and 1.0 M of $[C2(MI)_2{\cdot}(BF_4)_2]$ in DMF.

***Table 4**: Reduction potentials ($E_{1/2}$) of each sample, changing the concentration of $[C2(MI)_2{\cdot}(BF_4)_2]$ in DMF, determined by cyclic voltammetry (V vs. NHE, Scan rate: 100 $mV{\cdot}s^{-1}$).*

Entry	[IL]	Sample	E $Fe^{III/II}$	E $Fe^{II/I}$	E $Fe^{I/0}$	E CO_2/CO	Overpotential
1	0.1 M	FeTPP + IL	-0,06	-0,92	-1,33	-1,20	510
		FeTPP + IL + TFE	0,0	-0,90	-1,31		
2	0.3 M	FeTPP + IL	-0,02	-0,93	-1,29	-1,12	440
		FeTPP + IL + TFE	-0,03	-0,91	-1,27		
3	0.6 M	FeTPP + IL	0,02	-0,94	-1,26	-1,13	440
		FeTPP + IL + TFE	-0,03	-0,86	-1,27		
4	1.0 M	FeTPP + IL	0,03	-0,94	-1,27	-1,13	440
		FeTPP + IL + TFE	0,0	-0,86	-1,26		

***Reaction conditions**: 0.5 mM $Fe^{III}TPP{\cdot}Cl$, 1.0 M TFE in DMF under N_2 or CO_2 atmosphere, IL concentration [IL] described in each experiment.*

Increasing the ionic liquid concentration resulted in a decrease of the CO_2 reduction overpotential decreases, from 510 mV using 0.1 M to 440 mV using O.3, 0.6 and 1M (Table 4). The overpotential thus remained unaltered at ionic liquid concentration higher than 0.3 M.

In addition, the increase of the ionic liquid concentration resulted in a decrease of the current intensity. The maximum current intensity was achieved using 0.3 M of $[C2(MI)_2{\cdot}(BF_4)_2]$ in DMF. However, at higher IL concentrations, the current intensity decreased (Figure 8a). This decrease could be explained by the higher viscosity of the medium at high IL concentrations, making charge transport more difficult.

Chapter 3

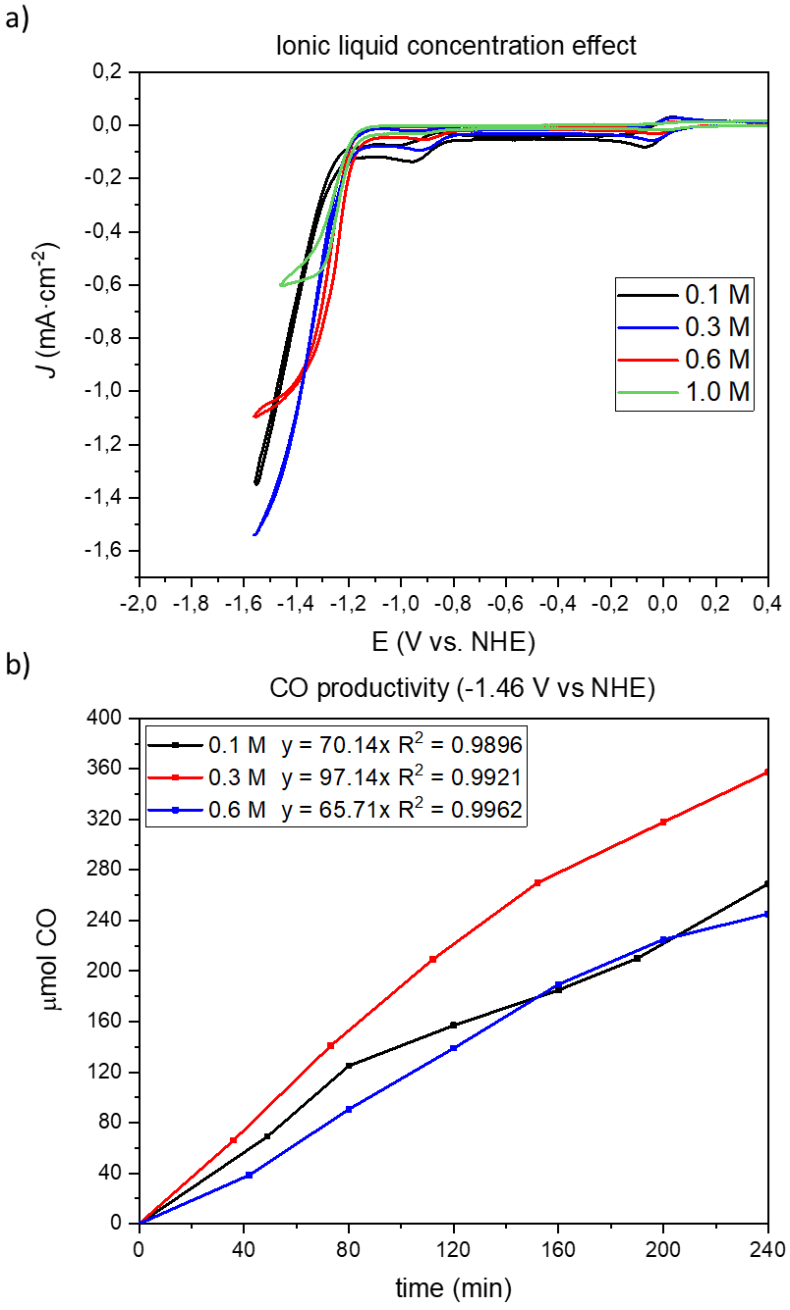

***Figure 8**: a) Cyclic voltammogram of 0.5 mM $Fe^{III}TPP{\cdot}Cl$, 1.0 M TFE varying the dicationic·BF_4 ionic liquid concentration in DMF under saturated CO_2 atmosphere. b) Graphics of CO productivity using different concentration of $[C2(MI)_2{\cdot}(BF_4)_2]$ ionic liquid. Conditions: 0.5 mM $Fe^{III}TPP{\cdot}Cl$, TFE 1.0 M, DMF under saturated CO_2 atmosphere applying -1.46 V vs NHE during 4h.*

A 4-hour test was performed under CO_2 atmosphere using 0.1, 0.3 and 0.6 M of ionic liquid applying -1.46 V vs NHE. The highest CO productivity (0.097 $mmol{\cdot}h^{-1} \approx 0.10\ mmol{\cdot}h^{-1}$) was obtained using 0.3 M of ionic liquid, with a CO Faradaic efficiency of 73%. However, lower, and higher IL concentrations resulted in lower CO productivities, *ca*. 0.06-0.07 $mmol{\cdot}h^{-1}$ (Figure 8b).

3.2.2.2. Current intensity optimization

CO_2 electroreduction experiments were performed applying different current intensities using 0.3 M of $[C2(MI)_2{\cdot}(BF_4)_2]$ in DMF.

At -10 mA, the potential was not constant and varied along the experiment between -2 and -4 V vs NHE. This behavior was explained by the instability of the reaction system (i.e., Fe-catalyst and IL) under these conditions.

At -8 mA, the potential remained stable at -1.37 V vs NHE for 2 hours but gradually became more negative resulting in a stable potential of -3 V at the end of the experiment. This behavior was ascribed to the transformation of the CO_2 dissolved in the solution, and once the CO_2 was totally transformed, the potential became more negative because of the reduction of other species.

The CPs performed at lower potentials (-6 mA, -4 mA and -2 mA) resulted in very stable potentials around 1.27 - 1.40 V vs NHE during at least 4 hours (Figure 9a).

Chapter 3

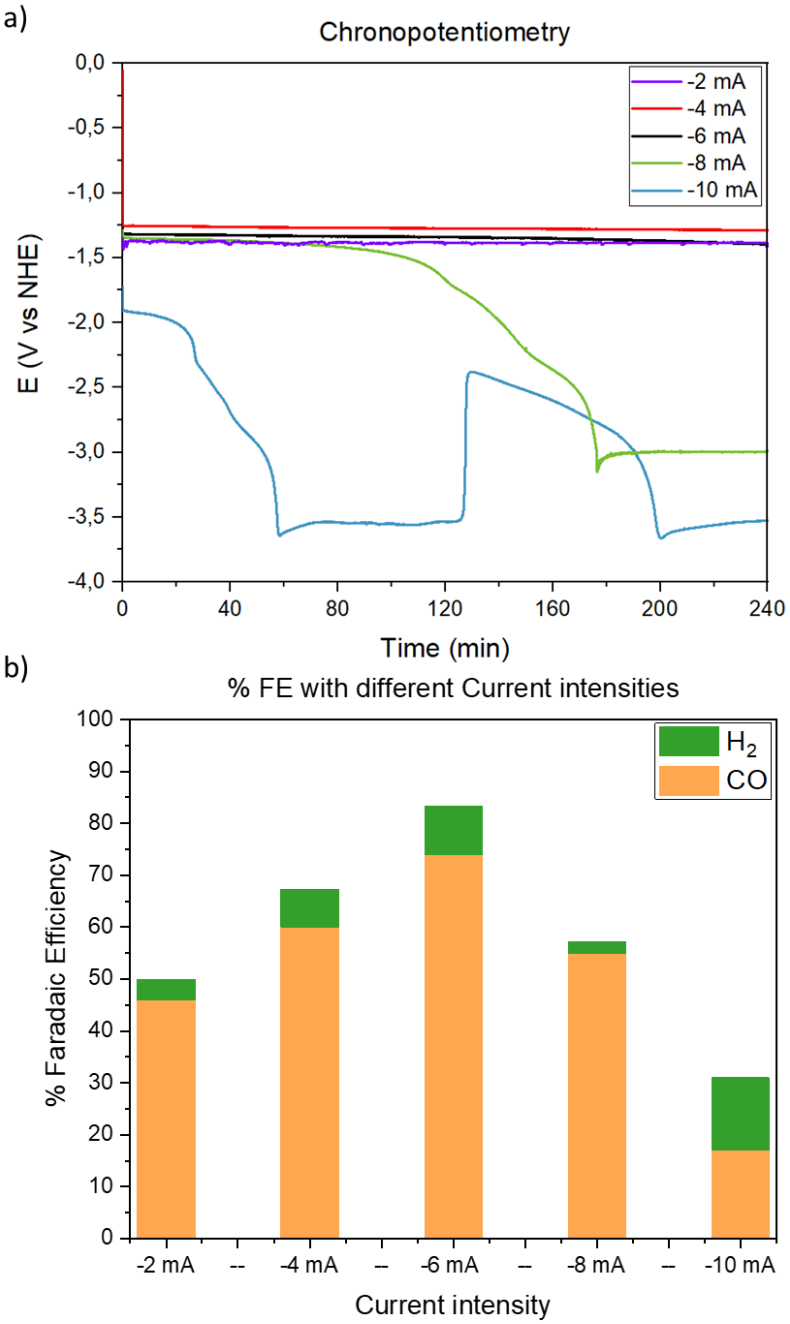

***Figure 9**: a) Chronopotentiometry graphics applying different current intensities b) % CO and H_2 Faradaic Efficiency applying different current intensities. Conditions: 0.5 mM $Fe^{III}TPP{\cdot}Cl$, TFE 1.0 M, 70 mL DMF, 0.3 M $[C2(MI)_2{\cdot}(BF_4)_2]$ ionic liquid under saturated CO_2 atmosphere applying different current intensities for 4h.*

Analyzing the gas phase of the experiments performed at the different current intensities (Figure 9b) it can be observed that applying -2 mA, -4 mA and -6 mA, a constant and selective CO production is formed with an increase of the total faradaic efficiency with the higher current intensities.

The highest CO productivity (0.09 $mmol_{CO}{\cdot}h^{-1}$) together with the highest CO/H_2 Faradaic efficiencies (ratio CO/H_2 Faradaic efficiency 74%/9%) was achieved by applying a current of -6 mA.

As mentioned above, the voltage was not constant when the experiments were carried out using a current of -8 and -10 mA, and also resulted in variations of the CO and H_2 production over the reaction time. Concerning the Faradaic efficiencies, the experiment at -8 mA resulted in lower CO/H_2 Faradaic efficiency (CO/H_2 Faradaic efficiency 55%/2%) whereas the experiment at -10 mA provided much lower CO Faradaic efficiency (CO/H_2 Faradaic efficiency 17%/14%).

In the case of -8 mA, during the first 2 hours the system selectively produced CO with a constant CO faradaic efficiency of 66 %. However, at longer reaction times, the CO production decreased and hydrogen production was initiated. In contrast, at -10 mA, variation in CO and H_2 production was observed from the beginning (Figure 10).

The results obtained at -6 mA improved those previously reported using a similar set-up (Faradaic efficiency up to 60%),[56] although higher Faradaic efficiency was previously reported (>90%) using the $Fe^{III}TPP{\cdot}Cl$ and the $[BMI{\cdot}BF_4]$ in a H-type cell.[6] Since the results described here showed that the use of the dicationic IL $[C2(MI)_2{\cdot}(BF_4)_2]$ improved the catalytic performance compared to those with $[BMI{\cdot}BF_4]$, it can be expected that the catalyst activity and faradaic efficiency could also be improved using a H-type cell.[56] The development of this H-type cell lied out of the scope of this thesis, and will be

the subject of future work in the research group.

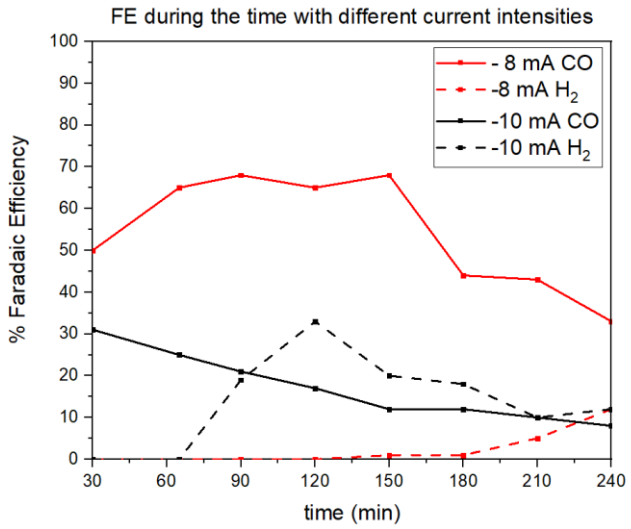

***Figure 10**: CO and H_2 productivity during the time applying current intensities of -8 mA or -10 mA. Conditions: 0.5 mM $Fe^{III}TPP{\cdot}Cl$, TFE 1.0 M, 70 mL DMF, 0.3 M $[C2(MI)_2{\cdot}(BF_4)_2]$ ionic liquid under saturated CO_2 atmosphere applying different current intensities for 4h.*

3.2.2.3. Trifluoroethanol concentration optimization

The CO_2 electroreduction reaction was also optimized through variation of the concentrations of TFE (0.5, 1.0 and 1.5 M in DMF) (Figure 11). These experiments were performed using 0.3 M of the $[C2(MI)_2{\cdot}(BF_4)_2]$ and applying a constant current intensity of -6 mA for 4h.

The results revealed that the increase of the TFE concentration from 0.5 to 1.5 M resulted in an increase of the H_2 production. TFE is a proton source and at higher proton concentrations, the participation of the electrons in the proton reduction to form H_2 was favored, preventing the CO_2 reduction.

Using 0.5 M of TFE in DMF, almost no H_2 was produced at the beginning (FE_{H2} = 2.3 %) with a CO % faradaic efficiency of 78 %. However, after 2 hours of CP, the H_2 production started to increase and the CO production decreased (Figure 11b).

When 1.0 M of TFE was used, a constant CO production was achieved with a CO faradaic efficiency of 74% and a H_2 faradaic efficiency of 9%. When the TFE concentration was further increased up to 1.5 M, the H_2 production increased with constant CO and H_2 faradaic efficiency of 43 and 24 %, respectively.

At TFE concentrations of 1.0 and 1.5 M, a constant and stable voltage (between -1.25 and -1.35 V vs NHE, Figure 11c) was observed during at least 4 hours. This indicated a constant catalytic activity of the system with a constant Faradaic efficiency.

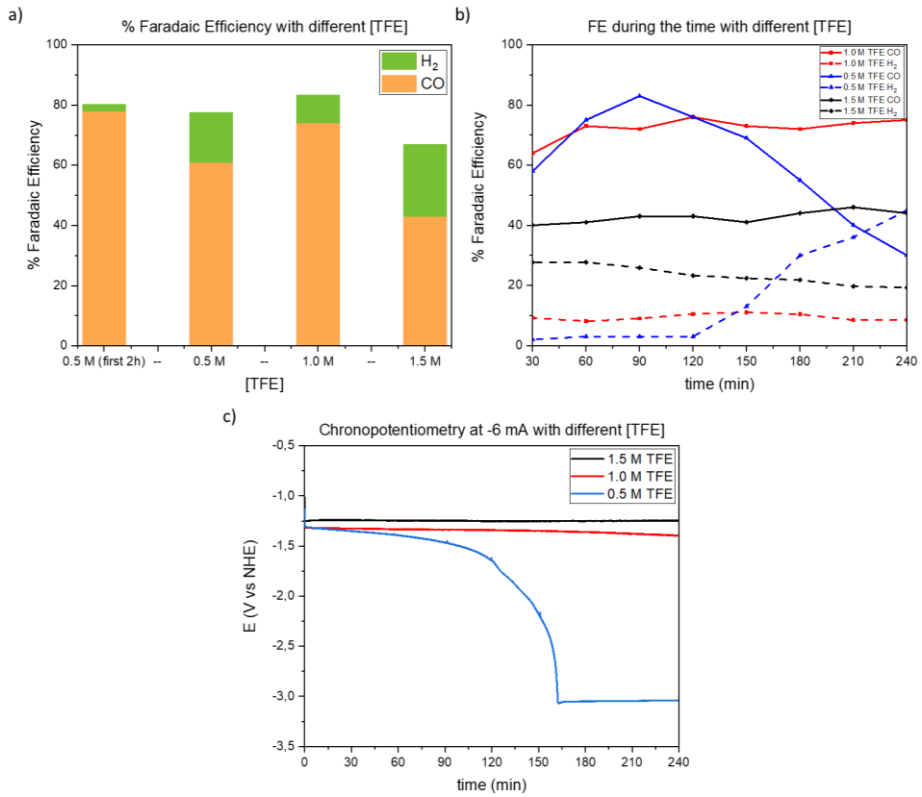

***Figure 11**: a) Total CO and H_2 Faradaic Efficiency with different the TFE concentration. b) CO and H_2 Faradaic efficiency during the time with different TFE concentration. c) Chronopotentiometry graphics at -6 mA performed using different TFE concentrations. Conditions: 0.5 mM $Fe^{III}TPP{\cdot}Cl$, 0.3 M $[C2(MI)_2{\cdot}(BF_4)_2]$ ionic liquid, 70 mL DMF under saturated CO_2 atmosphere applying -6 mA for 4h.*

Moreover, the TFE concentration highly affected the rate of CO formation, after 4 h reaction, the CO formation rate are 0.05, 0.09 and 0.05 $mmol_{CO}·h^{-1}$ using 0.5, 1.0 and 1.5 M, respectively.

3.2.2.4. Fe^{III}TPP·Cl concentration optimization

Finally, the CO_2 electroreduction reaction was optimized by variation of the Fe^{III}TPP·Cl concentration. Three concentrations (0.3, 0.5 and 0.8 mM of Fe^{III}TPP·Cl) were evaluated using a current of -6 mA in a DMF solution containing 1.0 M of TFE and 0.3 M of $[C2(MI)_2·(BF_4)_2]$.

Under these conditions, the selectivity to CO increased at higher Fe^{III}TPP·Cl concentrations (Figure 12a). Using 0.3 mM of Fe^{III}TPP·Cl, H_2 was the main reaction product (CO/H_2 faradaic efficiencies 13%/30%). When 0.5 mM of Fe^{III}TPP·Cl was used, the CO production and selectivity increases with a CO/H_2 faradaic efficiency of 74%/9%. Using 0.8 mM of Fe^{III}TPP·Cl, the CO/H_2 faradaic efficiencies were 81%/0.4%. This behavior was attributed to the higher concentrations of $[Fe^0]^{2-}$ and $[Fe\text{-}CO_2]^{2-}$ intermediates and a kinetically more efficient transport of the electrons.

At Fe^{III}TPP·Cl concentrations of 0.5 and 0.8 mM, the CP experiments had a constant and stable voltage (between -1.30 and -1.35 V vs NHE, Figure 12c) during at least 4 hours. With these systems, a constant catalytic activity and a constant Faradaic efficiency was obtained during the reaction. The Fe^{III}TPP·Cl catalyst concentration highly affected the rate of CO formation: 0.01, 0.09 and 0.10 $mmol_{CO}·h^{-1}$ at Fe^{III}TPP·Cl concentrations of 0.3, 0.5 and 0.8 mM, respectively.

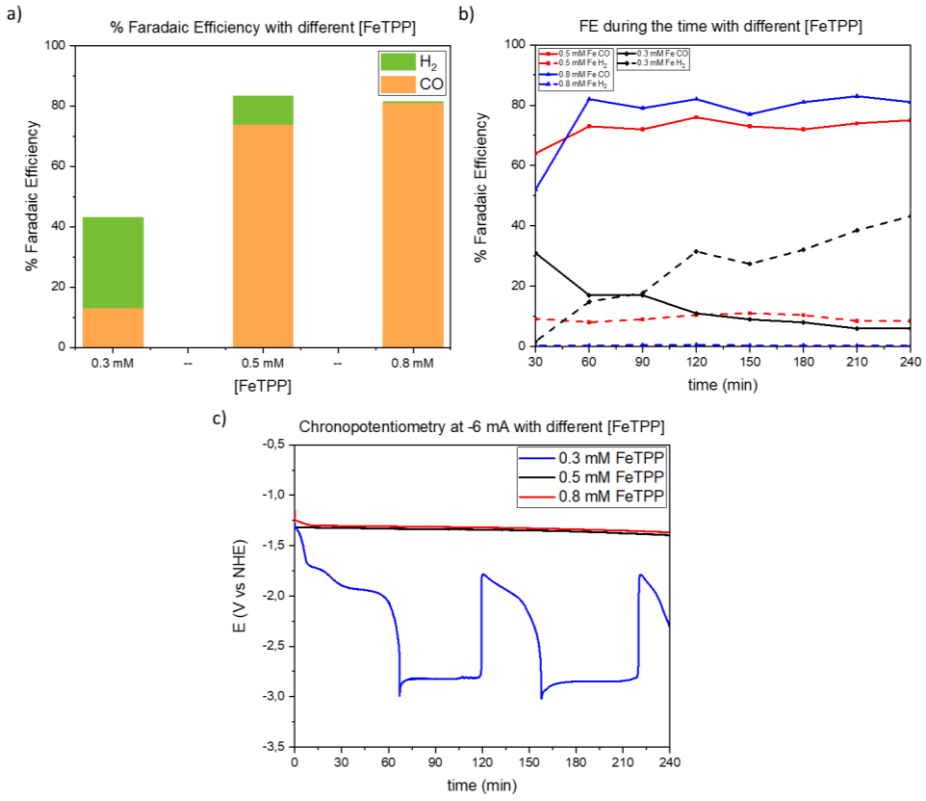

***Figure 12**: a) Total CO and H_2 Faradaic Efficiency with different the $Fe^{III}TPP{\cdot}Cl$ concentration ([FeTPP]). b) CO and H_2 Faradaic efficiency during the time with different $Fe^{III}TPP{\cdot}Cl$ concentration. c) Chronopotentiometry graphics at -6 mA performed using different $Fe^{III}TPP{\cdot}Cl$ concentrations. Conditions: 1.0 M TFE, 0.3 M $[C2(MI)_2{\cdot}(BF_4)_2]$ ionic liquid, 70 mL DMF, under saturated CO_2 atmosphere applying -6 mA for 4h.*

Analysis of the liquid phase by ^{1}H, ^{13}C and ^{19}F NMR after the CP experiments under optimized conditions (0.3 M IL, 1.0 M TFE and 0.8 mM $Fe^{III}TPP{\cdot}Cl$) revealed that no CO_2 reduction byproducts (formate and carbonates) were formed, and that the catalytic system and IL were stable since no decomposition products were observed.

The CP experiments under optimized reaction conditions (0.3 M IL, 1.0 M TFE and 0.8 mM $Fe^{III}TPP{\cdot}Cl$, -6 mA) produce a CO productivity of 0.1 $mmol_{CO}{\cdot}h^{-1}$. The energy used to produce 1 mmol of CO by our system is approximately 0.08

W·h ((0.006 A x 1.36 V x 1 h)/0.1 $mmol_{CO}·h^{-1}$)). This system has a higher energetic efficiency compared with the reported systems.[56]

3.2.3. CO_2 reduction mechanism using dicationic ionic liquids

With these results in hand, a mechanism for the CO_2 electroreduction using the $Fe^{III}TPP·Cl$ and dicationic ionic liquids is proposed. This mechanism is similar to that reported by Saveant[16,17] for inorganic cations and involves a synergism between iron (0) porphyrins and dicationic imidazolium ionic liquids (Scheme 7). The mechanism starts with the reduction of the $Fe(III)^+$ (**1**) to Fe(II) (**2**) followed by the reduction to $Fe(I)^-$ (**3**). At this point, the ionic liquid starts to stabilize the iron complex via iron-pairing. Then, the reduction of the $Fe(I)^-$ (**3**) to $Fe(0)^{2-}$ (**4**) takes place. The dicationic ionic liquid is expected to stabilize more efficiently this species than monocationic ILs. In the next step, the $Fe(0)^{2-}$ (**4**) reacts with the CO_2 forming the metallocarboxylate intermediate (**5**), which is protonated (**6**). The following step includes the intramolecular electron transfer in concert with both the breaking of one C-O bond and the H^+ transfer from TFE and is rate determining. Finally, the loss of H_2O gives the [Fe(II)][CO] (**7**) which undergoes comproportionation with $Fe(0)^{2-}$ (**4**) to liberate CO and regenerate the $Fe(I)^-$ (**3**), thus closing the catalytic cycle.[67] The results described here strongly suggest that the ionic liquid cation-iron complex anion pairing effect resulted in the reduction of the E $Fe(I)^-/Fe(0)^{2-}$ potential and the reduction of the E CO_2/CO overpotential via push-pull mechanism.[16,17] The ion-pairing of the imidazolium salts and iron complexes was previously reported for [BMI][$FeCl_4$] and related complexes, and in particular, in CO_2 reactions, such as, cyclic carbonate synthesis, cooperative effects between the iron metal center and imidazolium cation were also observed.[68]

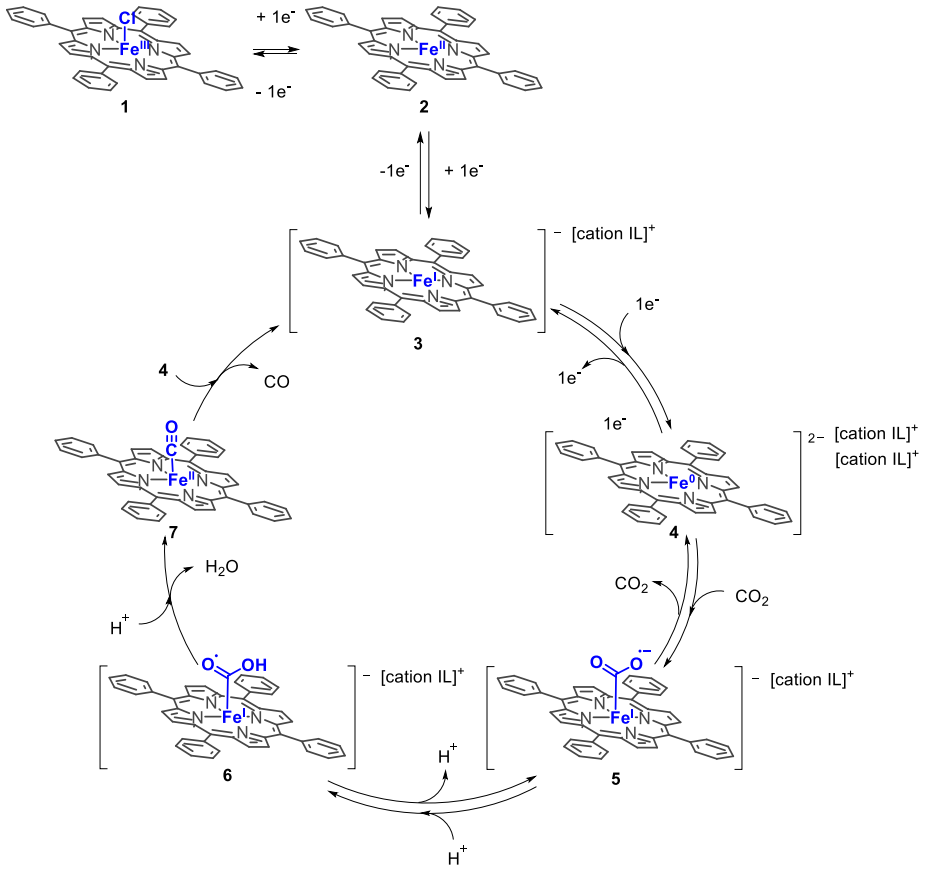

***Scheme 7**: Proposed reaction mechanism involving the synergism of iron (0) porphyrins and dicationic imidazolium ionic liquids.*

3.2.4. Tandem CO_2 reduction - carbonylations

Finally, the coupling of the CO_2 electroreduction with carbonylation reactions to obtain high-added value products was carried out. Similarly to the carbonylation reported by Skrydstrup and co-workers, the CO_2 electrochemical reduction was performed in one chamber while the carbonylation reactions were performed without purification of the gas mixture in another connected chamber.[56]

The reaction set-up was developed based on the concept reported by Skrydstrup and co-workers[56] (See experimental section). However, the

reaction set-up volume was 100 mL and 15 mL, the electrodes were two parallel glassy carbon pieces and a reference electrode was also included for ensuring the correct measurement of the applied potential.

The CO_2 reduction was thus performed in the first chamber using the optimized conditions described in the above sections. In the second chamber, the metal catalyzed carbonylation was carried out using 0.5 mmol of substrate.

The CO was generated at room temperature by CO_2 electroreduction using a potential of -1.36 V vs NHE during 15h. The tested carbonylation reactions catalyzed by palladium were the aminocarbonylation, alkoxycarbonylation, Sonogashira reaction, Suzuki-Miyaura reaction, Heck reaction and finally the double carbonylation of aryl iodide (Scheme 8). After the 15 h of reaction, the crude reaction mixture resulting from the carbonylation reaction was analyzed by ^{1}H NMR using 1,3,5-trimethoxybenzene as internal standard.

The Xanthphos-PdG4-catalyzed aminocarbonylation resulted in 84% yield of the moclobemide product (Scheme 8) using a very low potential (-1.36 V vs NHE) compared to the large potential reported (-4.3 V reported by Skrydstrup and co-workers[56]). Therefore, the application of our reaction system resulted in a more efficient use of the energy for the production of CO (Wh/mol CO) and carbonylation products (Wh/mol carbonylation product).

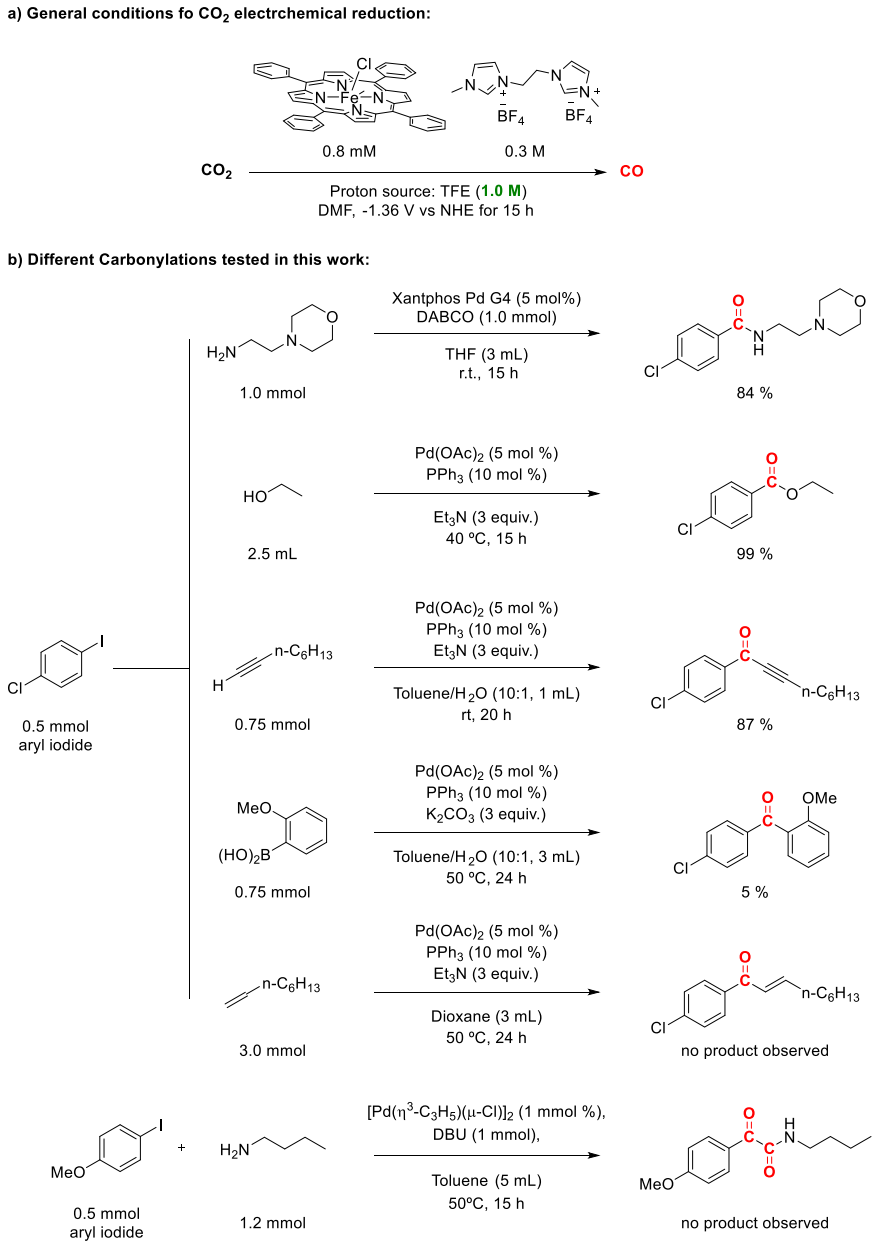

***Scheme 8**: Synthesis of the moclobemide molecule by a tandem CO_2 electroreduction coupled with the Pd-catalyzed aminocarbonylation reaction.*

The Pd/PPh_3-catalyzed ethoxycarbonylation and Sonogashira reaction were successfully performed, obtaining the corresponding products in 99 % and 87 % yields, respectively. Nevertheless, very low yield (5 %) was obtained in the

Suzuki-Miyaura reaction and no conversion was obtained after 24 h in the Heck reaction. This behavior was explained by the much lower reactivity of the alkene and borane compared with the amine, alcohol, and alkyne reagents. Skrydstrup and co-workers observed a similar tendency and suggested that the low CO concentration and mild temperatures used hampered the efficiency of these processes.

The Pd-catalyzed double carbonylation of aryl iodides was also tested under the conditions previously reported by our group.[69] However, the tandem process resulted unsuccessful and no carbonylation product (neither mono or double carbonylation) was observed. Again, this behavior has been attributed to the lower CO concentration generated since the reported experiment used 1 atm of pure CO.

Finally, the CO_2 reduction coupled with a Rh-catalyzed hydroformylation reaction was tested (Scheme 9). In this case, the CO_2 electroreduction was performed using 1.5 M of TFE to increase H_2 production since hydroformylation reactions usually require a ratio CO:H_2 close to 1. The Rh catalyzed hydroformylation of the octene was tested under these mild conditions but only a 2% of aldehyde was observed after 15 h of reaction. This result was again attributed to the low CO and H_2 concentration generated by CO_2 electroreduction.

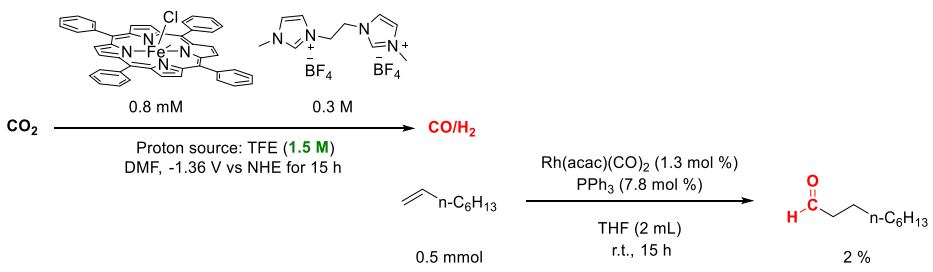

***Scheme 9**: Rh-catalyzed hydroformylation reaction explored using two-chamber cell set-up.*

At this point, a new protocol was tested: it involved the CO generation by CO_2 electroreduction, the transfer of the CO to a reactor using a plastic syringe and the introduction of hydrogen in a reactor for providing the adequate stoichiometry for the hydroformylation reaction. First, the CO_2 reduction reaction was performed in one-chamber cell using the optimized conditions for maximize the CO production. Under this reaction conditions, a potential of -1.36 V vs NHE was applied during 6 h to generate an approximated gas composition of 0.6 mmol of CO and unreacted CO_2 in a 70 mL total death volume. Then, this gas was transferred using a plastic syringe to an auto-clave reactor of 25 mL of volume which was previously charged with the solution of the Rh/PPh_3catalyst and 1-octene (0.5 mmol). Then, the pressure of the reactor was verified (1.2 bar gauge) and hydrogen was added to reach a total pressure of 2.5 bar (gauge) (see detailed conditions in the experimental section). Finally, the reactor was heated at 40 ºC and stirred overnight obtaining a 78 % of aldehyde yield with a selectivity l/b of 3.3 (Scheme 10). To the best of our knowledge, this is the first tandem CO_2 reduction coupled with a Rh-catalyzed hydroformylation reaction.

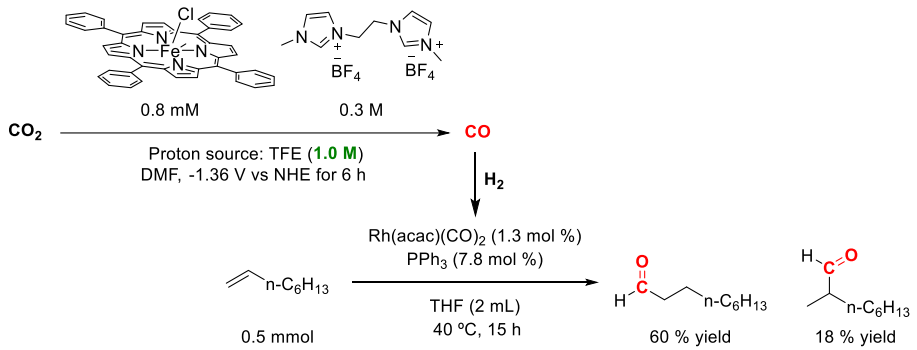

***Scheme 10**: Tandem CO_2 reduction coupled with rhodium-catalyzed hydroformylation of 1-octene*

3.3. Conclusions

To conclude, several ionic liquid structures were tested in the CO_2 electroreduction and the following conclusions can be drawn: (i) the anion structure does not have an important role in the CO_2 electroreduction; (ii) the cation structure is crucial in the CO_2 electroreduction ; with a proton in the C2 of the imidazolium ring, the CO_2 reduction overpotential is decreased, and the dicationic ionic liquid provided the best performance with a smaller CO_2 reduction overpotential compared with the monocationic analogue. To date, this is the first time that a dicationic ionic liquid is used in this process.

An optimization of the reaction parameters was performed showing that by variation of the reaction conditions, it is possible to obtain selectively CO or a syngas mixture (CO/H_2). Tandem CO_2 electroreduction-Pd catalyzed carbonylations were successfully performed, obtaining the corresponding products in high yields. Moreover, a tandem CO_2 electroreduction-Rh catalyzed hydroformylation reaction was successfully performed for the first time, obtaining aldehydes in 78 % yield. This is only the first example, and we are confident that optimization of this protocol will provide an efficient route for the regioselective and enantioselective production of hydroformylation products, which will provide new opportunities for the application of CO_2 as CO-surrogate in carbonylation processes.

Furthermore, in terms of energy, the reaction system reported here yielded efficient carbonylation reactions using much lower overpotentials that those reported, and thus resulted in a higher energetic efficiency (KWh/mol_{CO}).

3.4. Experimental part

3.4.1. General conditions

Reagents: Commercially available reagents and solvents were purchased at the highest commercial quality from Sigma-Aldrich, Fisher scientific, Alfa Aesar and they were used as received, without further purification, unless otherwise stated.

Analytical methods: ^{1}H, and $^{13}C\{^{1}H\}$ NMR spectra were recorded using a Varian Mercury VX 400 (400 and 100.6 MHz respectively). Chemical shift values (δ) are reported in ppm relative to residual solvent peak (^{1}H and $^{13}C\{^{1}H\}$), and coupling constants are reported in Hertz. The following abbreviations are used to indicate the multiplicity: s, singlet; d, doublet; t, triplet; q, quartet; quin, quintuplet; m, multiplet; and bs, broad signal.

3.4.2. Ionic liquid synthesis

The commercial ionic liquids were purchased in Sigma-Aldrich or TCI chemicals and used as received.

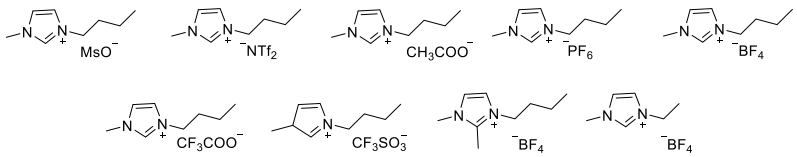

***Figure 13**: Commercial ionic liquids*

The non-commercial ionic liquids were synthetized in two steps: (i) preparation of the IL by refluxing a mixture of the methylimidazole and the corresponding chloride precursor to obtain the ionic liquid with chloride as counter anion, and (ii) in the second step, the anion exchange is performed using the corresponding salt precursor.

Chapter 3

- **General procedure A**:

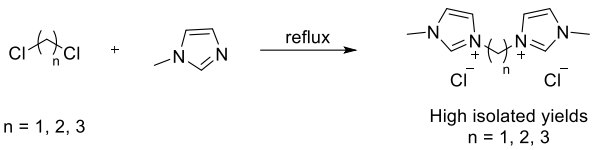

***Scheme 11**: General procedure to synthetize the dicationic ionic liquids with the chloride as counter anion.*

According to a modified literature procedure,[62] a mixture of 2 equivalents of methylimidazole and 1 equivalent of dichloromethane, 1,2-dichloroethane or 1,3-diclhoroporpane was heated at 90 ºC overnight. Then, the reaction was cooled to room temperature and the solid obtained was filtrated and washed with acetonitrile to obtain the corresponding dicationic ionic liquids with chlorine as counter anion in high isolated yields.

Bis(3-methylimidazolium-1-yl)methane dichloride: Synthetized following a modified literature procedure.[64] Synthesis performed using methylimidazole (0.36 mol, 29.6 g) and dichloromethane (0.18 mol, 15.3 g). IL obtained in 46 % yield. **^{1}H NMR** (400 MHz, D_2O) δ (ppm): 3.97 (s, 6H), 6.70 (s, 2H), 7.60 (d, J_{H-H} = 2.0 Hz, 2H), 7.77 (d, J_{H-H} = 2.0 Hz, 2H).

1,2-Bis(3-methylimidazolium-1-yl)ethane dichloride: Synthetized following a modified literature procedure.[70] Synthesis performed using methylimidazole (1.0 mol, 82.1 g) and 1,2-dichloroethane (0.5 mol, 48.5 g). IL obtained in 82 % yield. **^{1}H NMR** (400 MHz, D_2O) δ (ppm): 3.90 (s, 6H), 4.77 (s, 4H), 7.44 (d, J_{H-H} = 2.0 Hz, 2H), 7.52 (d, J_{H-H} = 2.0 Hz, 2H).

1,3-Bis(3-methylimidazolium-1-yl)propane dichloride: Synthetized following a modified literature procedure.[71] Synthesis performed using methylimidazole (0.2 mol, 16.4 g) and 1,3-diclhoroporpane (0.1 mol, 11.3 g), IL obtained in 74 % yield. **^{1}H NMR** (400 MHz, D_2O) δ (ppm): 2.54 (quin, J_{H-H} = 6.9 Hz, 2H), 3.92 (s, 6H), 4.33 (t, J_{H-H} = 7.2 Hz, 4H), 7.49 (s, 2H), 7.53 (s, 2H), 8.80 (s, 2H).

General procedure B:

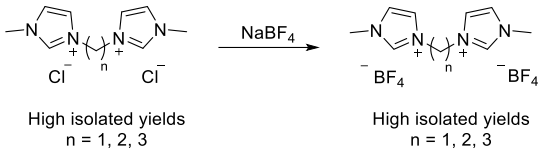

***Scheme 12**: General procedure to perform the anion exchange.*

According to a modified literature procedure,[63] an aqueous solution of the dicationic ionic liquid with the chlorine as counter anion (1 equivalent) and the $NaBF_4$ (2 equivalents) was stirred at room temperature overnight. Then, the water was evaporated using a rotatory evaporator. The resulting solid obtained was dissolved in acetonitrile, filtered to remove the inorganic salts, and evaporated to obtain the pure ionic liquids with the tetrafluoroborate anion ($[BF_4^-]$) as counter anion in high yields.

Bis(3-methylimidazolium-1-yl)methane di(tetrafluoroborate): Synthesis performed using of Bis(3-methylimidazolium-1-yl)methane dichloride (0.04 mol, 10 g) and $NaBF_4$ (0.08 mol, 8.8 g). IL obtained in 93 % yield. **^{1}H NMR** (400 MHz, dmso-d_6) δ (ppm): 3.89 (s, 6H), 6.1 (s, 2H), 7.78 (t, J_{H-H} = 1.3 Hz, 2H), 7.93 (t, J_{H-H} = 1.3 Hz, 2H), 9.32 (s, 2H). **^{13}C{^{1}H} NMR** (100.6 MHz, dmso-d_6) δ: 36.2, 58.2, 121.9, 124.4, 138.0.

1,2-Bis(3-methylimidazolium-1-yl)ethane di(tetrafluoroborate): Synthetized following a modified literature procedure.[65] Synthesis performed using of bis(3-methylimidazolium-1-yl)methane dichloride (0.3 mol, 79 g) and $NaBF_4$ (0.6 mol, 66 g). IL obtained in 96% yield. **^{1}H NMR** (400 MHz, D_2O) δ (ppm): 3.90 (s, 6H), 4.76 (s, 4H), 7.44 (t, J_{H-H} = 1.8 Hz, 2H), 7.52 (t, J_{H-H} = 1.8 Hz, 2H), 8.75 (s, 2H).

1,3-Bis(3-methylimidazolium-1-yl)propane di(tetrafluoroborate): Synthetized following a modified literature procedure.[65] Synthesis performed using 1,3-bis(3-methylimidazolium-1-yl)propane dichloride (0.07 mol, 19.4 g)

and NaBF4 (0.14 mol, 15.4 g). IL obtained in 95% yield.**^{1}H NMR** (400 MHz, D_2O) δ (ppm): 2.52 (quin, J_{H-H} = 7.4 Hz, 2H), 3.91 (s, 6H), 4.32 (t, J_{H-H} = 7.3 Hz, 4H), 7.47 (t, J_{H-H} = 1.8 Hz, 2H), 7.50 (t, J_{H-H} = 1.8 Hz, 2H), 8.75 (s, 2H).

3.4.3. Electrochemical measurements

To perform the electrochemical measurements, two cells were used. A small cell (**Cell 1**) purchased in Bio-logic to perform the study of the ionic liquids and a bigger hand-made cell (**Cell 2**) for the experiments where the gas phase was analyzed. Both cells have a unique chamber. The measurements were performed in a potentiostat form Autolab PGSTAT302N. All potentials in this study were adjusted to NHE reference by adding 0.54 V accordingly to previous measurements with Fc/Fc^+ as the internal reference. The measurements were performed with a scan rate of 0.1 $V{\cdot}s^{-1}$.

Cell 1: three electrodes configuration cell purchased from Bio-logic (Figure 14). In a typical test, the cell was loaded with 0.5 mM of meso-Tetraphenylporphyrin iron(III) chloride ($Fe^{III}TPP{\cdot}Cl$), 0.1 M of the corresponding ionic liquid (IL), 1.0 M of trifluoroethanol (TFE) and N,N-dimethylformamide (DMF) as solvent (35 mL). A polished glassy carbon as the working electrode (surface area: 0,07 cm^2), platinum wire as a counter electrode, and $Ag/AgNO_3$ in acetonitrile as reference electrode were used. Prior to each measurement, the electrolyte solution was purged for 20 mins with N_2 to remove the oxygen present in solution. Afterwards, the solution was saturated for 1 h under a CO_2 flow.

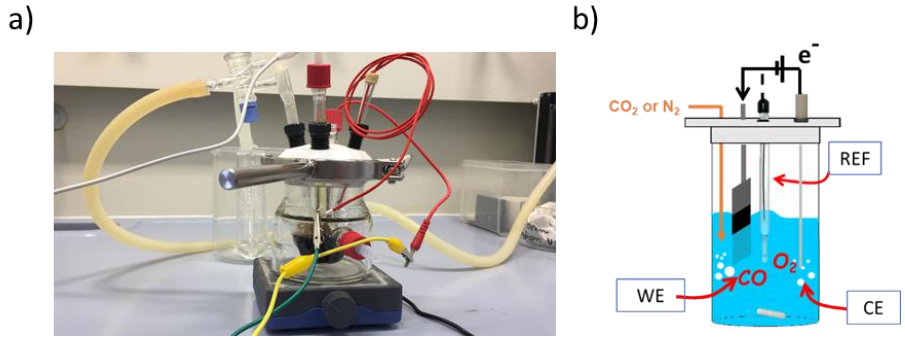

***Figure 14**: a) Image of the cell 1 and b) schematic representation of cell 1.*

Cell 2: Hand-made 3 electrodes configuration cell (Figure 15). In a typical test, the cell was loaded with FeTPP, IL, TFE and 70 mL of DMF, the exact concentrations of FeTPP, IL and TFE are described in each experiment. A polished glassy carbon as the counter and working electrode (surface area: 9 cm^2), and $Ag/AgNO_3$ in acetonitrile as reference electrode were used. Prior to each measurement, the electrolyte solution was purged for 30 mins with N_2 to remove the oxygen present in solution and saturated for 2 h using a CO_2 flow.

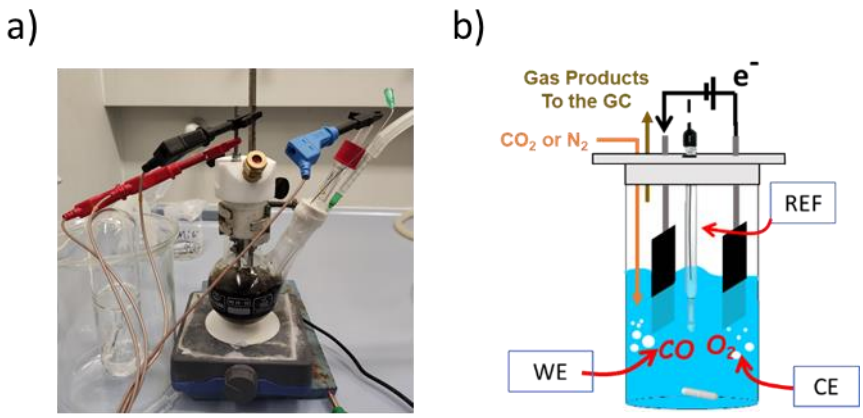

***Figure 15**: a) Image of the cell 2 and b) schematic representation of cell 2.*

3.4.4. Gas product analysis

To analyze the CO and H_2 gas products, a 500 µL HAMILTON syringe was used for gas sampling. During the experiment, samples were directly collected at regular intervals and injected (100 µL) in the gas chromatography system (GC System Agilent 7890A with TCD and Agilent 5975C inert MSD with Triple Axis Detection). Gas products were identified/quantified using calibration curves previously constructed by injecting standard samples of different CO and H_2 concentrations prepared using 3 mass flow controllers (N_2, H_2 and CO) (See Figure S1).

The CO and H_2 productions were determined by areas obtained from GC-TCD analysis and the response factor obtained from the calibration curves (See Figure S2). Faradaic efficiency (%) of each experiment was calculated using the equation below, where F is the Faraday constant (96485 C mol^{-1}), *Q* (C) is the charge passed during the bulk electrolysis, *z* is the number of moles of electrons required to produce one mole of CO or H_2 from CO_2 or H^+ and *n* is the number of moles of product (CO or hydrogen) determined by GC analysis.

$$Faradaic\ Efficiency\ (\%) = \frac{Qexperimental}{Qtheoretic} = \frac{z \cdot n \cdot F}{Q}$$

3.4.5. Liquid product analysis

The liquid phase was analyzed by taking an aliquot of the solution after the experiment. The aliquot (0.2 mL) was diluted with dmso-d_6 to a total volume of 0.6 mL for analysis by ^{1}H, ^{13}C and ^{19}F NMR (See section 3.5.3).

3.4.6. Description of tandem set-up

To perform the tandem CO_2 electrochemical reduction coupled with carbonylation reactions, a hand-made cell with two interconnected chambers

was used (Figure 16). In one chamber, the CO_2 reduction was performed with a 3 electrodes set-up consisting of a polished glassy carbon as the working electrode (surface area: 9 cm^2), a polished glassy carbon as the counter electrode (surface area: 9 cm^2) and a reference electrode of $Ag/AgNO_3$ in acetonitrile. In the first chamber, a solution of the dicationic·BF_4 ionic liquid (0.3 M), FeTPP (0.8 mM), TFE (1.0 M) in DMF (70 mL) was added and the solution purged for 30 mins with N_2 to remove the oxygen present in solution. Afterwards, the solution was saturated for 2 h using a CO_2 flow. Next, a potential of -1.36 V vs NHE was applied during 15h at room temperature and the carbonylation reaction products were analyzed by ^1H NMR using 1,3,5-trimethoxybenzene as internal standard. The Pd-catalyzed carbonylations were performed in the second chamber (Figure 16) using 0.5 mmol of the 1-chloro-4-iodobenzene as substrate in the presence of the Pd-catalyst and the corresponding reagents for aminocarbonylation, alkoxycarbonylations and Sonogashira process. The detailed conditions are described in the Section 3.4.7.

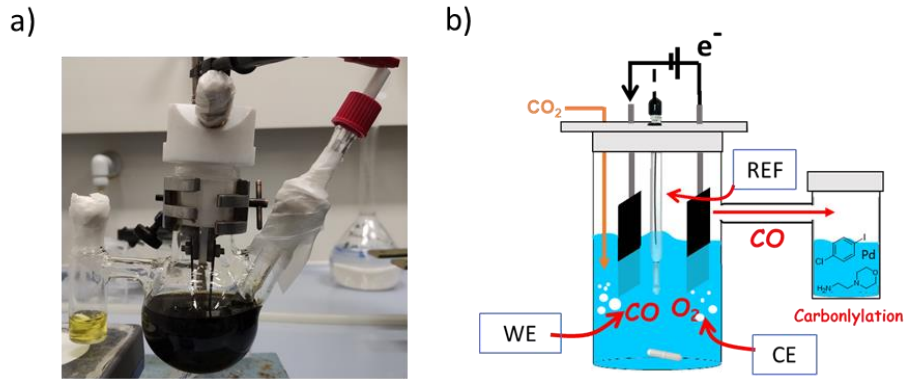

***Figure 16**: a) Image of the cell used for the tandem reaction and b) schematic representation of the cell.*

For the Rh-catalyzed hydroformylation, a plastic syringe (24 mL) was used for transferring the gas generated (70 mL total death volume with and

approximated composition of 0.6 mmol CO and the rest is unreacted CO_2) from the electrochemical cell (Cell 2, Figure 15) to a reactor containing a THF solution of the Rh-catalyst and 1-octene (0.5 mmol) (Figure 17). The reactor (25 mL total volume) was purged with a short vacuum treatment, and later, to fill the reactor 3 times with 24 mL of the gas from the electrochemical cell. Later, the pressure of the reactor system was verified (1.2 bar (gauge)), hydrogen was added to reach a total pressure of 2.5 bar (gauge), and the reactor was heated at the desired temperature for the selected reaction time. The detailed conditions are described in the Section 3.4.8.

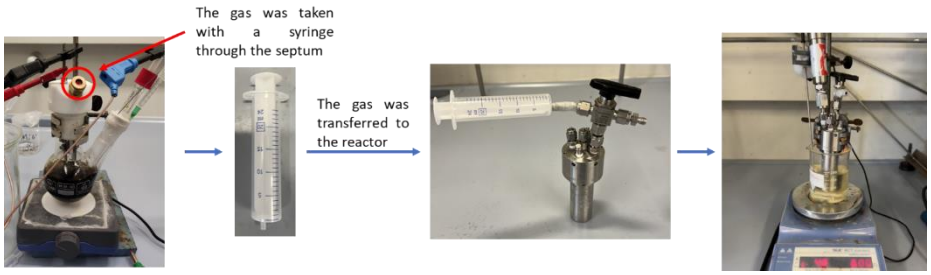

***Figure 17**: Procedure to perform the tandem CO_2 reduction and Rh-catalyzed hydroformylation reaction of the 1-octene using the auto-clave reactor of 25 mL of volume.*

3.4.7. Pd-catalyzed carbonylation reaction conditions

3.4.7.1. Procedure for aminocarbonylation reaction

According to a modified literature procedure,[56] in a two-chamber reactor (Figure 16) charged with stirring bars, 1-chloro-4-iodobenzene (0.5 mmol, 119 mg), 2-morpholinoethylamine (131 µL, 1 mmol), Xantphos Pd G4 (24 mg, 5 mol%), DABCO (113 mg, 1.0 mmol) and THF (3 ml) were added in the carbonylation chamber. The conditions for the CO_2 reduction chamber are described in the Section 3.4.6. The solutions of both chambers were stirred at room temperature. After 15 h applying -1.36 V vs NHE the chemical reaction was analyzed by ^{1}H NMR using naphthalene as internal standard.

3.4.7.2. Procedure for Sonogashira reaction

According to a modified literature procedure,[72] in a two-chamber reactor (Figure 16) charged with stirring bars, 1-chloro-4-iodobenzene (0.5 mmol, 119 mg), 1-octyne (111 µL, 0.75 mmol), $Pd(OAc)_2$ (5.6 mg, 5 mol%), PPh3 (13.1 mg, 10 mol%), Et_3N (209 µL, 1.5 mmol) and toluene/H_2O (10:1, 1ml) were added in the carbonylation chamber. The conditions for the CO_2 reduction chamber are described in the Section 3.4.6. The solutions of both chambers were stirred at room temperature. The potential (-1.36 V vs NHE) was applied during 15 h and the Sonogashira reaction was stirred 5 h more at room temperature. After a total of 20 h the chemical reaction was analyzed by ^1H NMR using 1,3,5-trimethoxybenzene as internal standard.

3.4.7.3. Procedure for ethoxycarbonylation reaction

According to a modified literature procedure,[73] in a two-chamber reactor (Figure 16) charged with stirring bars, 1-chloro-4-iodobenzene (0.5 mmol, 119 mg), ethanol (2.5 mL), $Pd(OAc)_2$ (5.6 mg, 5 mol%), PPh_3 (13.1 mg, 10 mol%) and Et_3N (209 µL, 1.5 mmol) were added in the carbonylation chamber. The conditions for the CO_2 reduction chamber are described in the Section 3.4.6. The carbonylation chamber was stirred at 40 ^oC while the electrochemical CO_2 reduction chamber was stirred at room temperature. After 15 h applying -1.36 V vs NHE, the chemical reaction was analyzed by ^1H NMR using 1,3,5-trimethoxybenzene as internal standard.

3.4.7.4. Procedure for Suzuki-Miyaura reaction

According to a modified literature procedure,[56] in a two-chamber reactor (Figure 16) charged with stirring bars, 1-chloro-4-iodobenzene (0.5 mmol, 119 mg), 2-methoxyphenylboronic acid (0.75 mmol, 114 mg), $Pd(OAc)_2$ (5.6 mg, 5 mol%), PPh_3 (13.1 mg, 10 mol%), K_2CO_3 (1.5 mmol, 207 mg) and toluene/H_2O (10:1, 3ml) were added in the carbonylation chamber. The conditions for the

CO_2 reduction chamber are described in the Section 3.4.6. The carbonylation chamber was stirred at 50 ºC while the electrochemical CO_2 reduction chamber was stirred at room temperature. The potential (-1.36 V vs NHE) was applied during 15 h and the Suzuki-Miyaura reaction was stirred 9 h more at 50 ºC. After a total of 24 h, the chemical reaction was analyzed by ^{1}H NMR using 1,3,5-trimethoxybenzene as internal standard.

3.4.7.5. Procedure for Heck reaction

According to a modified literature procedure,[74] in a two-chamber reactor (Figure 16) charged with stirring bars, 1-chloro-4-iodobenzene (0.5 mmol, 119 mg), 1-octene (3 mmol, 471 µL), $Pd(OAc)_2$ (5.6 mg, 5 mol%), PPh_3 (13.1 mg, 10 mol%), Et_3N (1.5 mmol, 209 µL) and dioxane (3ml) were added in the carbonylation chamber. The conditions for the CO_2 reduction chamber are described in the Section 3.4.6. The carbonylation chamber was stirred at 50 ºC while the electrochemical CO_2 reduction chamber was stirred at room temperature. The potential was applied during 15 h and the Heck reaction was stirred 9 h more at 50 ºC. After a total of 24 h the chemical reaction was analyzed by ^{1}H NMR using 1,3,5-trimethoxybenzene as internal standard.

3.4.7.6. Procedure for double carbonylation reaction

According to a modified literature procedure,[69] in a two-chamber reactor (Figure 16) charged with stirring bars, 4-Iodoanisole (0.5 mmol, 117 mg), butylamine (1.2 mmol, 118 µL), allylpalladium(II) chloride dimer (1.8 mg, 1 mol %), 1,8-diazabicyclo[5.4.0]undec-7-ene (1 mmol, 150 µL), and toluene (5 ml) were added in the carbonylation chamber. The conditions for the CO_2 reduction chamber are described in the Section 3.4.6. The carbonylation chamber was stirred at 50 ºC while the electrochemical CO_2 reduction chamber was stirred at room temperature. The potential was applied during 15 h and the double carbonylation reaction was analyzed by ^{1}H NMR using 1,3,5-trimethoxybenzene as internal standard.

3.4.8. Rh-catalyzed hydroformylation reaction conditions

3.4.8.1. Tandem hydroformylation procedure

In this case, the **Cell 2** was used (Figure 15) to perform the CO_2 electroreduction. The **Cell 2** was equipped with FeTPP (0.8 mM), biscationic·BF_4 IL (0.3 M), TFE (1.0 M) and 70 mL of DMF. A polished glassy carbon as the counter and working electrode (surface area: 9 cm^2), and $Ag/AgNO_3$ in acetonitrile as reference electrode were used. Prior to perform the bulk electrolysis the electrolyte solution was purged for 30 min with N_2 to remove the oxygen present in solution. Afterwards, the solution was saturated for 2 h using a CO_2 flow. Then, a potential of -1.36 V vs NHE was applied for 6h.

After 6 h, the gas produced in **Cell 2** was transferred with a syringe to an auto-clave reactor (Figure 17) previously charged with octene (0.5 mmol, 78.5 µL), $Rh(acac)(CO)_2$ (1.3 mol %, 1.7 mg), PPh_3 (7.8 mol %, 10.2 mg) and THF (2 ml).[75] After adding the gas produced in the **Cell 2** into the auto-clave reactor, the reactor had a pressure of 1.2 bar gauge. The reactor was then charged until 2.5 bar gauge by adding H_2 (1.3 bars of H_2). The hydroformylation reaction was stirred for 15 h at 40 ^oC. Finally, the reaction mixture was analyzed by ^1H NMR using 1,3,5-trimethoxybenzene as internal standard.

3.5. Supporting information

3.5.1. ^{1}H and $^{13}C\{^{1}H\}$ NMR spectra of the synthetized IL

^{1}H NMR (D_2O, 400 MHz)

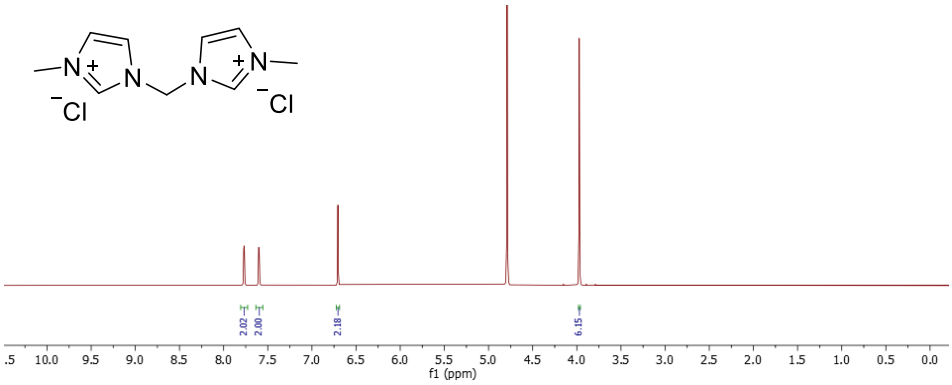

^{1}H NMR (dmso-d_6, 400 MHz)

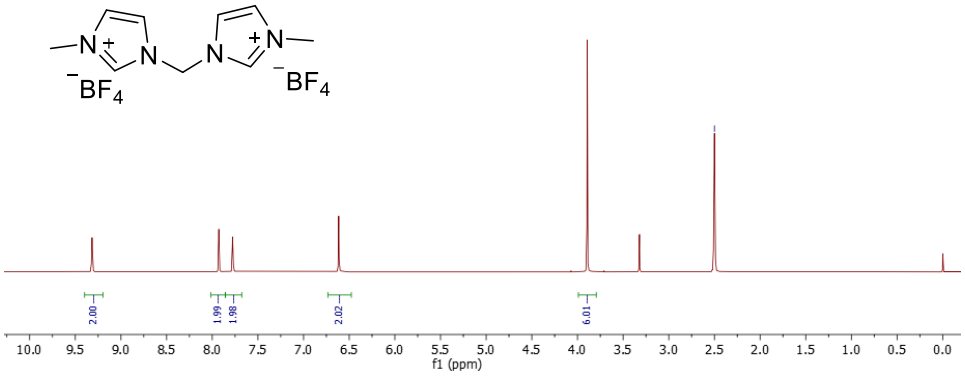

$^{13}C\{^{1}H\}$ NMR (dmso-d_6, 100.6 MHz)

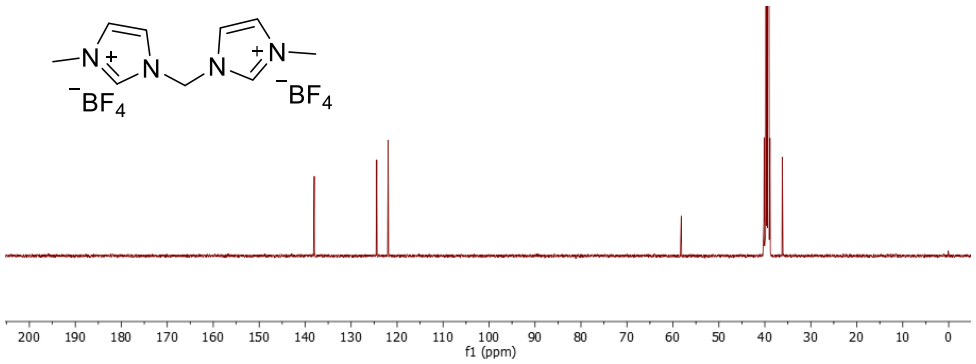

^{1}H NMR (D_2O, 400 MHz)

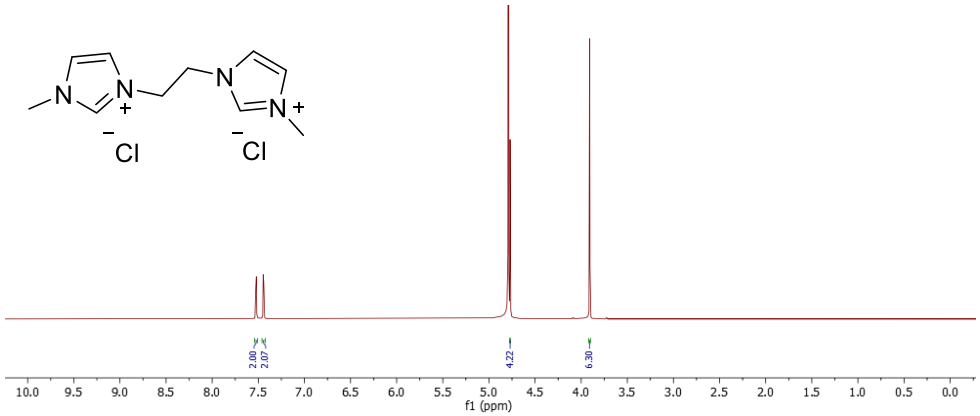

^{1}H NMR (D_2O, 400 MHz)

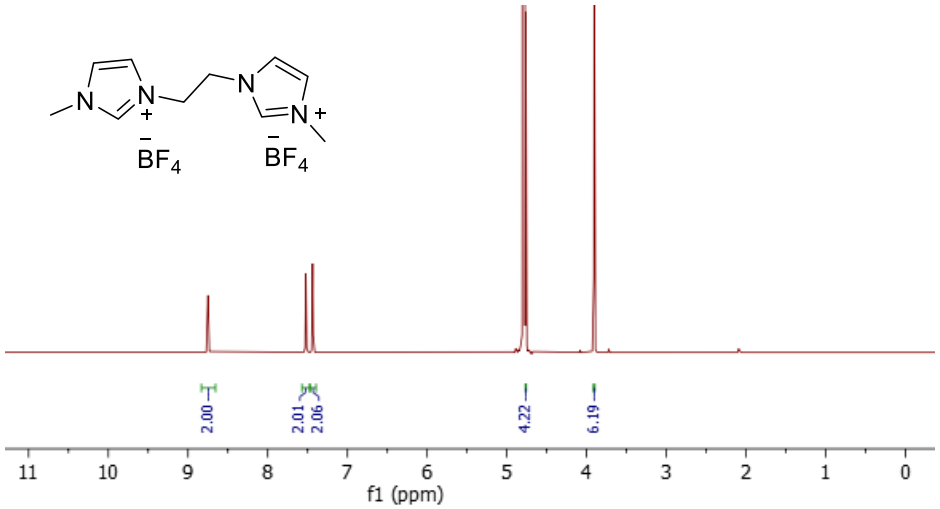

Chapter 3

^{1}H NMR (D_2O, 400 MHz)

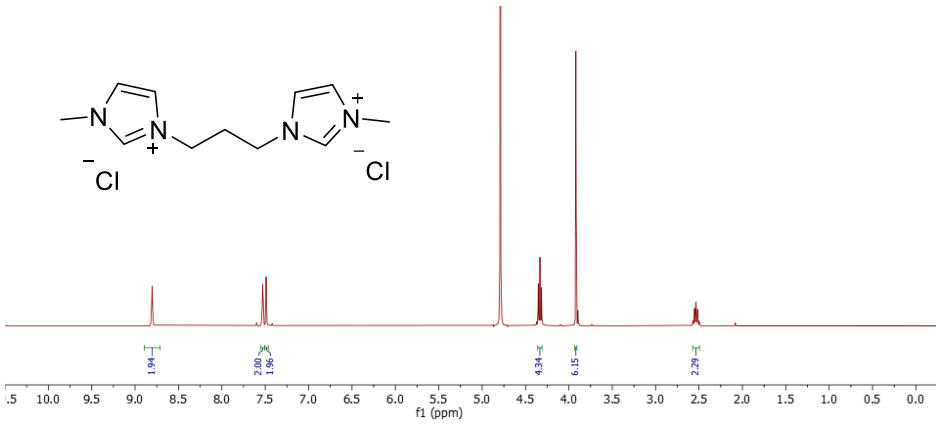

^{1}H NMR (D_2O, 400 MHz)

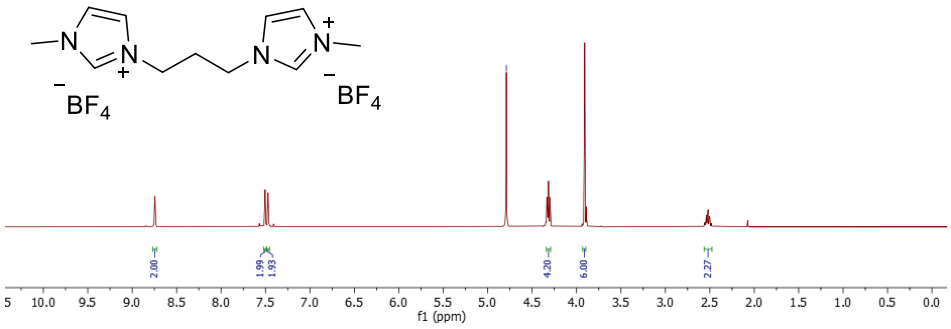

3.5.2. Chromatograms of gas sample analysis

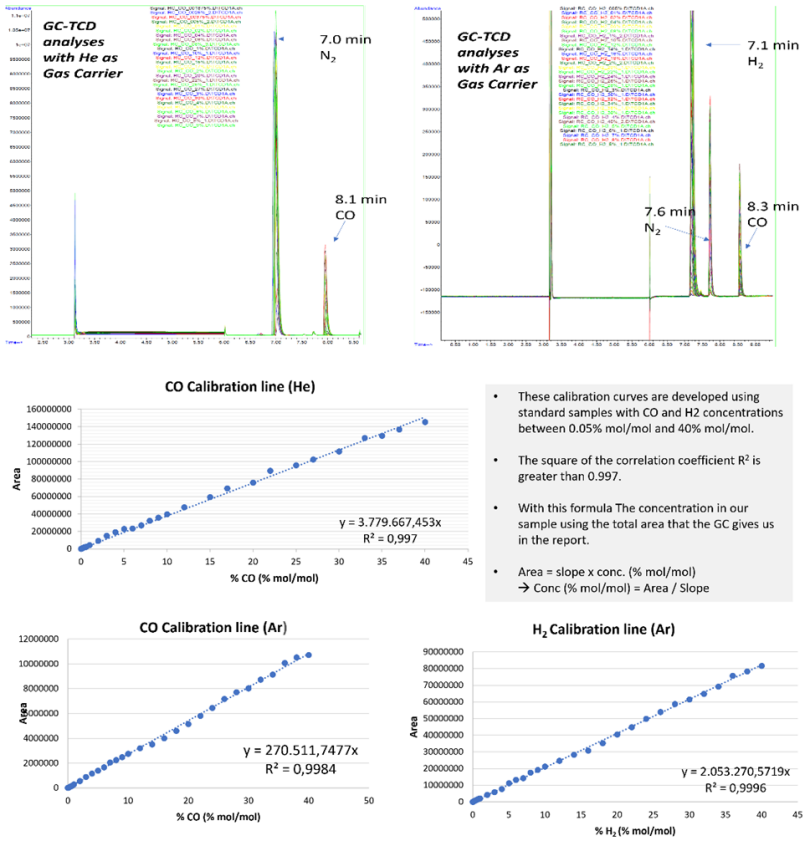

***Figure S1**: GC-TCD analyses of the standard samples and calibration curves*

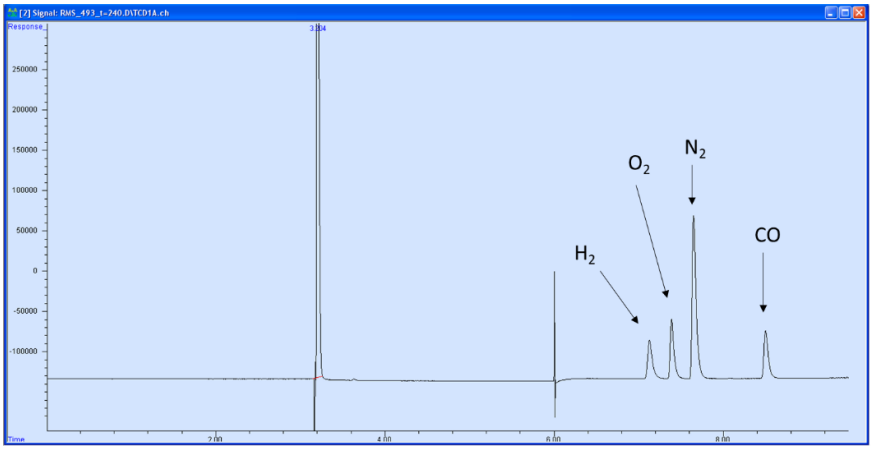

***Figure S2**: Illustrative example of GC-analyses during an experiment.*

3.5.3. NMR of liquids sample analysis

^{1}H NMR (dmso-d_6, 400 MHz):

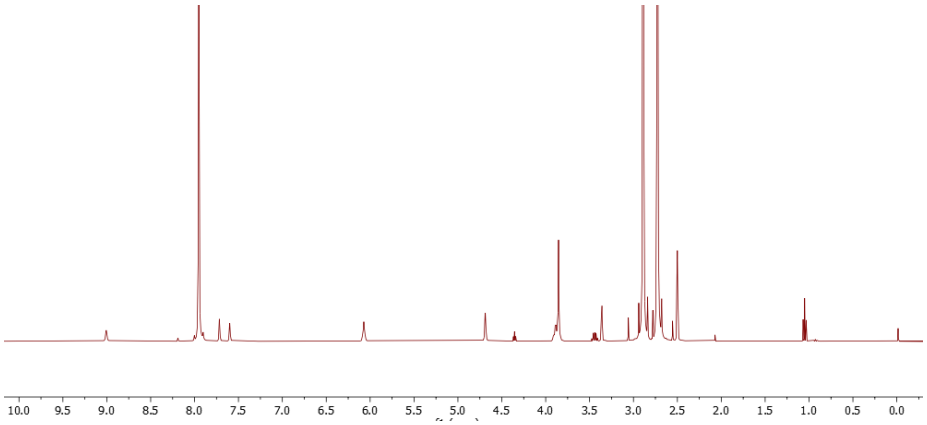

^{19}F NMR (dmso-d_6, 400 MHz):

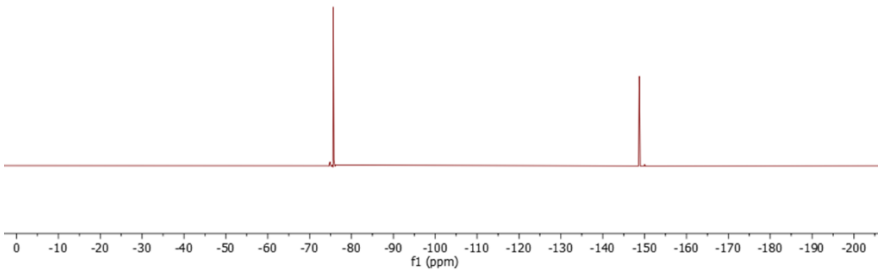

^{13}C NMR (dmso-d_6, 400 MHz):

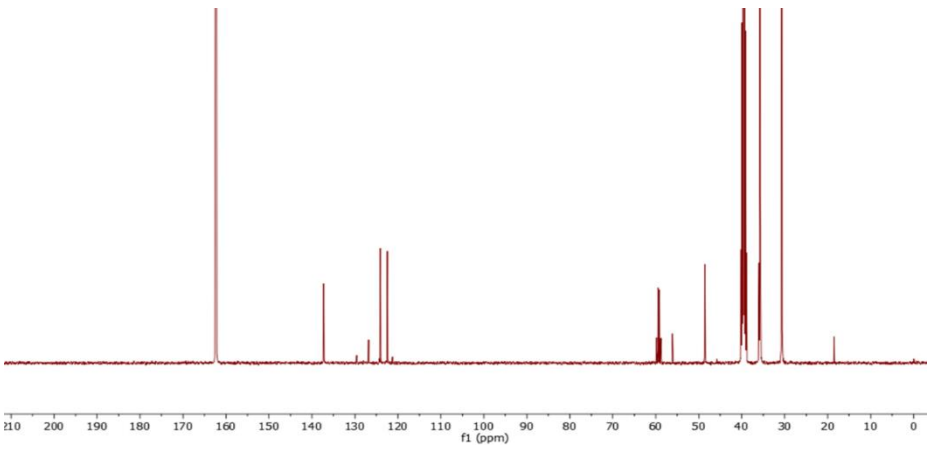

3.5.4. ^{1}H NMR spectra of the Pd-catalyzed carbonylations and Rh-catalyzed hydroformylation

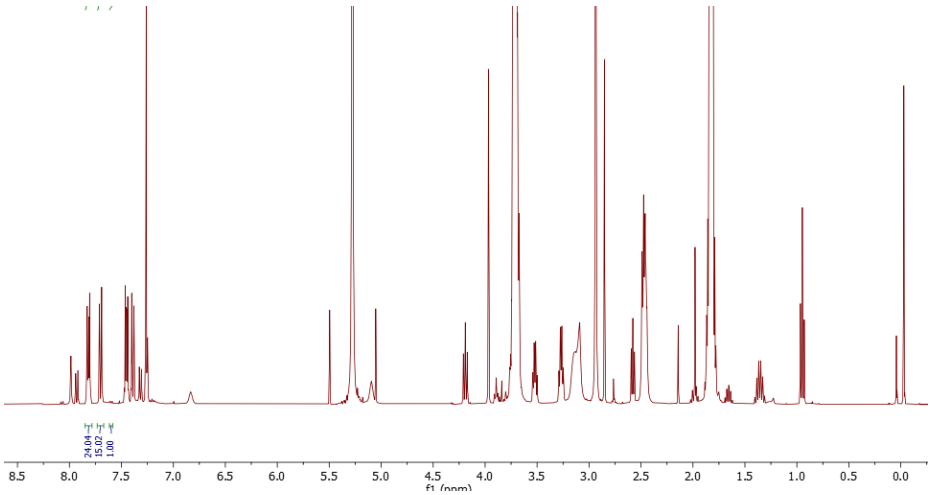

***Figure S3**: ^{1}H NMR of the **aminocarbonylation** reaction mixture after the reaction. Using naphthalene as internal standard to quantify.*

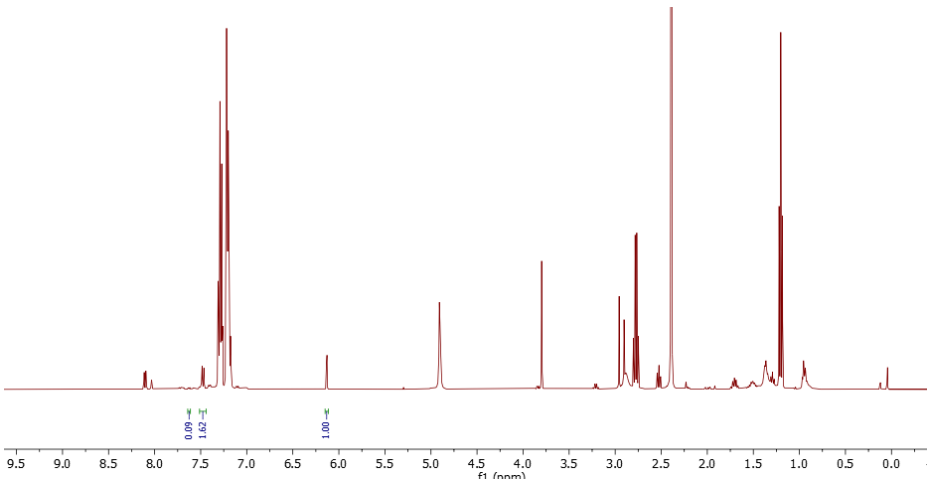

***Figure S4**: ^{1}H NMR of the **Sonogashira** reaction mixture after the reaction. Using 1,3,5-trimethoxybenzene as internal standard to quantify.*

Chapter 3

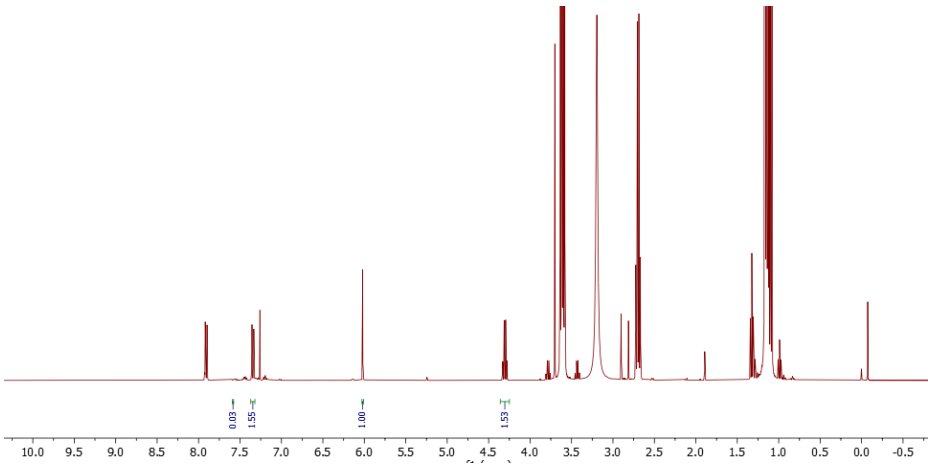

***Figure S5**: [1]H NMR of the **alkoxycarbonylation** reaction mixture after the reaction. Using 1,3,5-trimethoxybenzene as internal standard to quantify.*

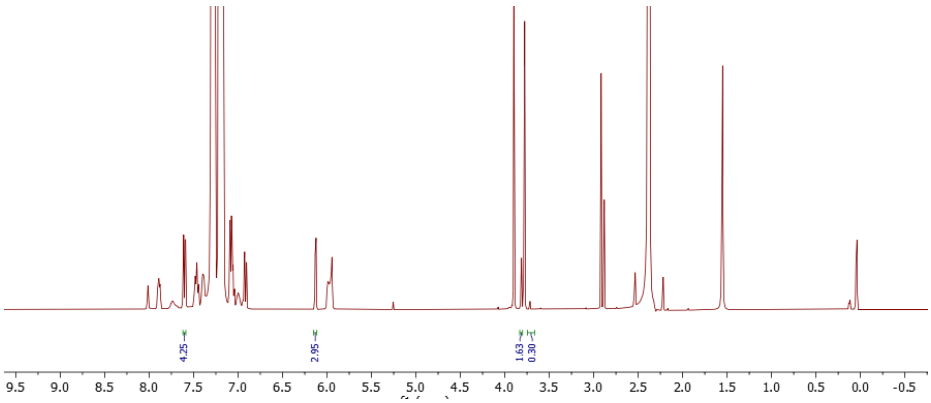

***Figure S6**: [1]H NMR of the **Suzuki-Miyaura** reaction mixture after the reaction. Using 1,3,5-trimethoxybenzene as internal standard to quantify.*

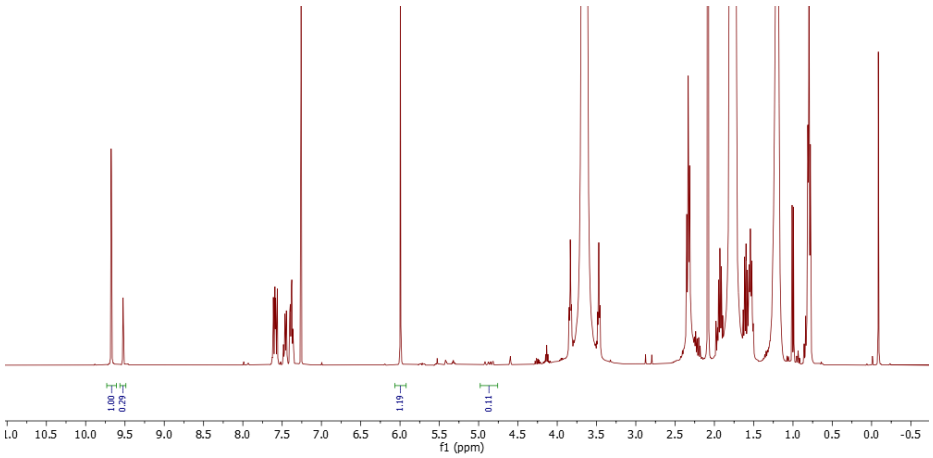

***Figure S7**: ^1H NMR of the **hydroformylation** reaction mixture after the reaction with the tandem procedure. Using 1,3,5-trimethoxybenzene as internal standard to quantify.*

3.5.5. Hydroformylation procedure using syngas

To compare the results obtained with the Rh-hydroformylation of the 1-octene using the tandem procedure a Rh-catalyzed hydroformylation using a syngas mixture (1:1 CO/H_2) was performed. The auto-clave reactor (25 mL of volume) was charged with octene (0.5 mmol, 78.5 µL), $Rh(acac)(CO)_2$ (1.3 mol %, 1.7 mg), PPh_3 (7.8 mol %, 10.2 mg) and THF (2 ml). Then, the reactor was charged until 2.5 bar using a syngas mixture (1:1 CO/H_2). Later, the hydroformylation reaction was stirred for 15 h at 40 ^oC. Finally, the reaction mixture was analyzed by ^1H NMR using 1,3,5-trimethoxybenzene as internal standard obtaining full conversion with an aldehyde yield of 99% with a l/b selectivity of 3.2 (Scheme S1). Therefore, this experiment probed that although the utilization of pure CO for the hydroformylation reaction resulted in slightly higher conversion, both processes resulted in similar selectivities.

Chapter 3

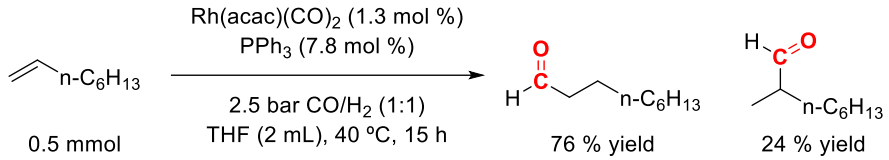

***Scheme S1**: Rh-catalyzed hydroformylation of 1-octene performed using syngas (2.5 bar 1:1 CO/H_2) to compare with the tandem experiment.*

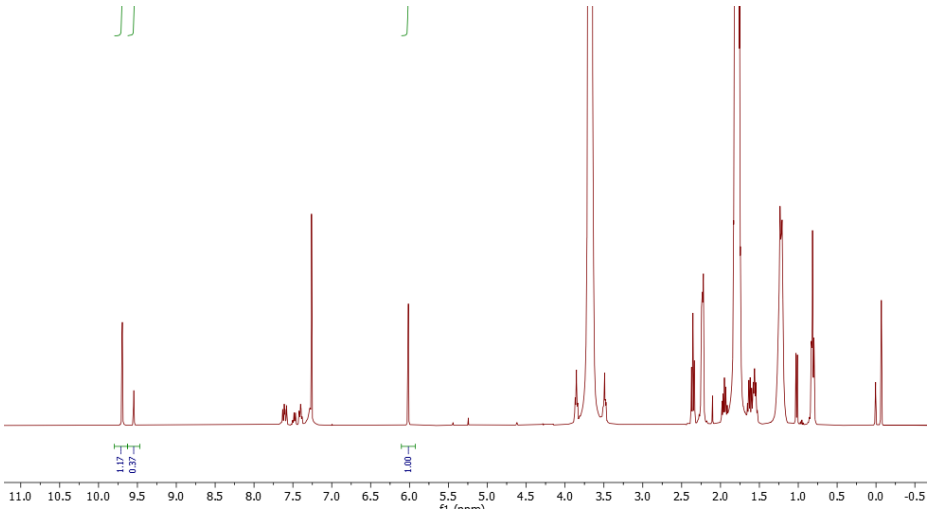

***Figure S8**: ^1H NMR of the hydroformylation reaction mixture after the reaction using a syngas mixture. 1,3,5-trimethoxybenzene was used as internal standard to quantify.*

3.6. References

(1) Gupta, C. L. Role of Renewable Energy Technologies in Generating Sustainable Livelihoods. *Renew. Sustain. Energy Rev.* **2003**, *7*, 155–174.

(2) Dalle, K. E.; Warnan, J.; Leung, J. J.; Reuillard, B.; Karmel, I. S.; Reisner, E. Electro-and Solar-Driven Fuel Synthesis with First Row Transition Metal Complexes. *Chem. Rev.* **2019**, *119*, 2752–2875.

(3) Zhou, J.-H.; Zhang, Y.-W. Metal-Based Heterogeneous Electrocatalysts for Reduction of Carbon Dioxide and Nitrogen: Mechanisms, Recent Advances and Perspective. *React. Chem. Eng.* **2018**, *3*, 591–625.

(4) Francke, R.; Schille, B.; Roemelt, M. Homogeneously Catalyzed Electroreduction of Carbon Dioxide—Methods, Mechanisms, and Catalysts. *Chem. Rev.* **2018**, *118*, 4631–4701.

(5) Lamy, E.; Nadjo, L.; Saveant, J. M. Standard Potential and Kinetic Parameters of the Electrochemical Reduction of Carbon Dioxide in Dimethylformamide. *J. Electroanal. Chem. Interfacial Electrochem.* **1977**, *78*, 403–407.

(6) Choi, J.; Benedetti, T. M.; Jalili, R.; Walker, A.; Wallace, G. G.; Officer, D. L. High Performance Fe Porphyrin/Ionic Liquid Co-Catalyst for Electrochemical CO2 Reduction. *Chem. Eur. J.* **2016**, *22*, 14158–14161.

(7) Amatore, C.; Saveant, J. M. Mechanism and Kinetic Characteristics of the Electrochemical Reduction of Carbon Dioxide in Media of Low Proton Availability. *J. Am. Chem. Soc.* **1981**, *103*, 5021–5023.

(8) Russell, P. G.; Kovac, N.; Srinivasan, S.; Steinberg, M. The Electrochemical Reduction of Carbon Dioxide, Formic Acid, and Formaldehyde. *J. Electrochem. Soc.* **1977**, *124*, 1329–1338.

(9) Costentin, C.; Limoges, B.; Robert, M.; Tard, C. A Pioneering Career in Electrochemistry: Jean-Michel Savéant. *ACS Catal.* **2021**, *11*, 3224–3238.

(10) Costentin, C.; Robert, M.; Savéant, J.-M. Catalysis of the Electrochemical Reduction of Carbon Dioxide. *Chem. Soc. Rev.* **2013**, *42*, 2423–2436.

(11) Savéant, J.-M. Molecular Catalysis of Electrochemical Reactions. Mechanistic Aspects. *Chem. Rev.* **2008**, *108*, 2348–2378.

(12) Savéant, J.-M. Evidence for Concerted Pathways in Ion-Pairing Coupled Electron Transfers. *J. Am. Chem. Soc.* **2008**, *130*, 4732–4741.

(13) Savéant, J.-M. Effect of Ion Pairing on the Mechanism and Rate of Electron Transfer. Electrochemical Aspects. *J. Phys. Chem. B* **2001**, *105*, 8995–9001.

(14) Bhugun, I.; Lexa, D.; Savéant, J.-M. Catalysis of the Electrochemical Reduction of Carbon Dioxide by Iron(0) Porphyrins: Synergystic Effect of Weak Brönsted Acids. *J. Am. Chem. Soc.* **1996**, *118*, 1769–1776.

(15) Bhugun, I.; Lexa, D.; Saveant, J.-M. Ultraefficient Selective Homogeneous Catalysis of the Electrochemical Reduction of Carbon Dioxide by an Iron(0) Porphyrin Associated with a Weak Broensted Acid Cocatalyst. *J. Am. Chem. Soc.* **1994**, *116*, 5015–5016.

(16) Hammouche, M.; Lexa, D.; Momenteau, M.; Saveant, J. M. Chemical Catalysis of Electrochemical Reactions. Homogeneous Catalysis of the Electrochemical Reduction of Carbon Dioxide by Iron("0") Porphyrins. Role of the Addition of Magnesium Cations. *J. Am. Chem. Soc.* **1991**, *113*, 8455–8466.

(17) Bhugun, I.; Lexa, D.; Savéant, J.-M. Catalysis of the Electrochemical

Reduction of Carbon Dioxide by Iron(0) Porphyrins. Synergistic Effect of Lewis Acid Cations. *J. Phys. Chem.* **1996**, *100*, 19981–19985.

(18) Hammouche, M.; Lexa, D.; Savéant, J. M.; Momenteau, M. Catalysis of the Electrochemical Reduction of Carbon Dioxide by Iron("0") Porphyrins. *J. Electroanal. Chem. Interfacial Electrochem.* **1988**, *249*, 347–351.

(19) Azcarate, I.; Costentin, C.; Robert, M.; Savéant, J.-M. Through-Space Charge Interaction Substituent Effects in Molecular Catalysis Leading to the Design of the Most Efficient Catalyst of CO2-to-CO Electrochemical Conversion. *J. Am. Chem. Soc.* **2016**, *138*, 16639–16644.

(20) Bonin, J.; Maurin, A.; Robert, M. Molecular Catalysis of the Electrochemical and Photochemical Reduction of CO2 with Fe and Co Metal Based Complexes. Recent Advances. *Coord. Chem. Rev.* **2017**, *334*, 184–198.

(21) Nichols, E. M.; Derrick, J. S.; Nistanaki, S. K.; Smith, P. T.; Chang, C. J. Positional Effects of Second-Sphere Amide Pendants on Electrochemical CO2 Reduction Catalyzed by Iron Porphyrins. *Chem. Sci.* **2018**, *9*, 2952–2960.

(22) Khadhraoui, A.; Gotico, P.; Boitrel, B.; Leibl, W.; Halime, Z.; Aukauloo, A. Local Ionic Liquid Environment at a Modified Iron Porphyrin Catalyst Enhances the Electrocatalytic Performance of CO2 to CO Reduction in Water. *Chem. Commun.* **2018**, *54*, 11630–11633.

(23) Kosugi, K.; Kondo, M.; Masaoka, S. Quick and Easy Method to Dramatically Improve the Electrochemical CO2 Reduction Activity of an Iron Porphyrin Complex. *Angew. Chem. Int. Ed.* **2021**, *133*, 22241–22245.

(24) Feng, J.; Zeng, S.; Feng, J.; Dong, H.; Zhang, X. CO2 Electroreduction in Ionic Liquids: A Review. *Chinese J. Chem.* **2018**, *36*, 961–970.

(25) Rees, N. V; Compton, R. G. Electrochemical CO2 Sequestration in Ionic Liquids ; a Perspective. *Energy Environ. Sci.* **2011**, *4*, 403–408.

(26) Lim, H.; Kim, H. The Mechanism of Room-Temperature Ionic-Liquid-Based Electrochemical CO2 Reduction: A Review. *Molecules* **2017**, *22*, 536.

(27) Rosen, B. A.; Salehi-Khojin, A.; Thorson, M. R.; Zhu, W.; Whipple, D. T.; Kenis, P. J. A.; Masel, R. I. Ionic Liquid-Mediated Selective Conversion of CO2 to CO at Low Overpotentials. *Science.* **2011**, *334*, 643–644.

(28) Matsubara, Y.; Grills, D. C.; Kuwahara, Y. Thermodynamic Aspects of Electrocatalytic CO 2 Reduction in Acetonitrile and with an Ionic Liquid as Solvent or Electrolyte. *ACS Catal.* **2015**, *5*, 6440–6452.

(29) Khadhraoui, A.; Gotico, P.; Boitrel, B.; Leibl, W.; Halime, Z.; Aukauloo, A. Local Ionic Liquid Environment at a Modified Iron Porphyrin Catalyst Enhances the Electrocatalytic Performance of CO 2 to CO Reduction in Water †. *Chem. Commun.* **2018**, *54*, 11630–11633.

(30) Honores, J.; Quezada, D.; García, M.; Calfumán, K.; Muena, J. P.; Aguirre, M. J.; Arévalo, M. C.; Isaacs, M. Carbon Neutral Electrochemical Conversion of Carbon Dioxide Mediated by [Mn+(Cyclam)Cln] (M = Ni2+ and Co3+) on Mercury Free Electrodes and Ionic Liquids as Reaction Media. *Green Chem.* **2017**, *19*, 1155–1162.

(31) Grills, D. C.; Matsubara, Y.; Kuwahara, Y.; Golisz, S. R.; Kurtz, D. A.; Mello, B. A. Electrocatalytic CO2 Reduction with a Homogeneous Catalyst in Ionic Liquid: High Catalytic Activity at Low Overpotential. *J.*

Phys. Chem. Lett. **2014**, *5*, 2033–2038.

(32) Sung, S.; Kumar, D.; Gil-Sepulcre, M.; Nippe, M. Electrocatalytic CO2 Reduction by Imidazolium-Functionalized Molecular Catalysts. *J. Am. Chem. Soc* **2017**, *139*, 13993–13996.

(33) Zanatta, M.; Simon, N. M.; Dupont, J. The Nature of Carbon Dioxide in Bare Ionic Liquids. *ChemSusChem* **2020**, *13*, 3101–3109.

(34) Simon, N. M.; Zanatta, M.; dos Santos, F. P.; Corvo, M. C.; Cabrita, E. J.; Dupont, J. Carbon Dioxide Capture by Aqueous Ionic Liquid Solutions. *ChemSusChem* **2017**, *10*, 4927–4933.

(35) Klähn, M.; Seduraman, A. What Determines CO2 Solubility in Ionic Liquids? A Molecular Simulation Study. *J. Phys. Chem. B* **2015**, *119*, 10066–10078.

(36) Torralba-Calleja, E.; Skinner, J.; Gutiérrez-Tauste, D. CO_2 Capture in Ionic Liquids: A Review of Solubilities and Experimental Methods. *J. Chem.* **2013**, *2013*, 473584.

(37) Cadena, C.; Anthony, J. L.; Shah, J. K.; Morrow, T. I.; Brennecke, J. F.; Maginn, E. J. Why Is CO2 So Soluble in Imidazolium-Based Ionic Liquids? *J. Am. Chem. Soc.* **2004**, *126*, 5300–5308.

(38) Zhang, B.; Sun, L. Artificial Photosynthesis: Opportunities and Challenges of Molecular Catalysts. *Chem. Soc. Rev.* **2019**, *48*, 2216–2264.

(39) Takeda, H.; Cometto, C.; Ishitani, O.; Robert, M. Electrons, Photons, Protons and Earth-Abundant Metal Complexes for Molecular Catalysis of CO2 Reduction. *ACS Catal.* **2017**, *7*, 70–88.

(40) Nielsen, D. U.; Hu, X.-M.; Daasbjerg, K.; Skrydstrup, T. Chemically and

Electrochemically Catalysed Conversion of CO2 to CO with Follow-up Utilization to Value-Added Chemicals. *Nat. Catal.* **2018**, *1*, 244–254.

(41) Ali, M.; Gual, A.; Ebeling, G.; Dupont, J. Carbon Dioxide Transformation in Imidazolium Salts: Hydroaminomethylation Catalyzed by Ru-Complexes. *ChemSusChem* **2016**, *9*, 1–7.

(42) Ali, M.; Gual, A.; Ebeling, G.; Dupont, J. Ruthenium-Catalyzed Hydroformylation of Alkenes by Using Carbon Dioxide as the Carbon Monoxide Source in the Presence of Ionic Liquids. *ChemCatChem* **2014**, *6*, 2224–2228.

(43) Ponsard, L.; Nicolas, E.; Tran, N. H.; Lamaison, S.; Wakerley, D.; Cantat, T.; Fontecave, M. Coupling Electrocatalytic CO2 Reduction with Thermocatalysis Enables the Formation of a Lactone Monomer. *ChemSusChem* **2021**, *14*, 1–8.

(44) Kollár, L. *Modern Carbonylation Methods*; Wiley-VCH, 2008.

(45) Beller, M.; Wu, X. F. *Transition Metal Catalyzed Carbonylation Reactions: Carbonylative Activation of C-X Bonds*; Springer-Verlag Berlin Heidelberg, 2013.

(46) Rostrup-Nielsen, J.; Christiansen, L. J. *Concepts in Syngas Manufacture*; Imperial College Press, 2011.

(47) Artz, J.; Müller, T. E.; Thenert, K.; Kleinekorte, J.; Meys, R.; Sternberg, A.; Bardow, A.; Leitner, W. Sustainable Conversion of Carbon Dioxide: An Integrated Review of Catalysis and Life Cycle Assessment. *Chem. Rev.* **2018**, *118*, 434–504.

(48) Gabriele, B. *Carbon Monoxide in Organic Synthesis Carbonylation Chemistry.*; John Wiley & Sons, Incorporated, 2021.

(49) Rabiee, H.; Ge, L.; Zhang, X.; Hu, S.; Li, M.; Yuan, Z. Gas Diffusion Electrodes (GDEs) for Electrochemical Reduction of Carbon Dioxide, Carbon Monoxide, and Dinitrogen to Value-Added Products: A Review. *Energy Environ. Sci.* **2021**, *14*, 1959–2008.

(50) Pei, Y.; Zhong, H.; Jin, F. A Brief Review of Electrocatalytic Reduction of CO2—Materials, Reaction Conditions, and Devices. *Energy Sci. Eng.* **2021**, *9*, 1012–1032.

(51) Küngas, R.; Blennow, P.; Heiredal-Clausen, T.; Holt Norby, T.; Rass-Hansen, J.; Primdahl, S.; Hansen, J. B. ECOs – A Commercial CO2 Electrolysis System Developed by Haldor Topsoe. *ECS Transa* **2017**, *78*, 2879–2884.

(52) Gautam, P.; Bhanage, B. M. Recent Advances in the Transition Metal Catalyzed Carbonylation of Alkynes, Arenes and Aryl Halides Using CO Surrogates Prashant. *Catal. Sci. Technol.* **2015**, *5*, 4663–4702.

(53) Wu, L.; Liu, Q.; Jackstell, R.; Beller, M. Carbonylations of Alkenes with CO Surrogates. *Angew. Chemie Int. Ed.* **2014**, *53*, 6310–6320.

(54) Khedkar, V. M.; Khan, R. S.; Lambat, L. T.; Chaudhary, G. R.; Abdala, A. A. CO Surrogates: A Green Alternative in Palladium-Catalyzed CO Gas Free Carbonylation Reactions. *Current Organic Chemistry*. **2020**, pp 2588–2600.

(55) Hermange, P.; Lindhardt, A. T.; Taaning, R. H.; Bjerglund, K.; Lupp, D.; Skrydstrup, T. Ex Situ Generation of Stoichiometric and Substoichiometric 12CO and 13CO and Its Efficient Incorporation in Palladium Catalyzed Aminocarbonylations. *J. Am. Chem. Soc.* **2011**, *133*, 6061–6071.

(56) Jensen, M. T.; Rønne, M. H.; Ravn, A. K.; Juhl, R. W.; Nielsen, D. U.; Hu,

X.-M.; Pedersen, S. U.; Daasbjerg, K.; Skrydstrup, T. Scalable Carbon Dioxide Electroreduction Coupled to Carbonylation Chemistry. *Nat. Commun.* **2017**, *8*.

(57) Ponsard, L.; Nicolas, E.; Tran, N. H.; Lamaison, S.; Wakerley, D.; Cantat, T.; Fontecave, M. Coupling Electrocatalytic CO2 Reduction with Thermocatalysis Enables the Formation of a Lactone Monomer. *ChemSusChem* **2021**, *14*, 2198–2204.

(58) van Leeuwen, P. W. N. M. *Homogeneous Catalysis*; Springer Netherlands, 2004.

(59) Franke, R.; Selent, D.; Börner, A. Applied Hydroformylation. *Chem. Rev.* **2012**, *112*, 5675–5732.

(60) Sung, S.; Kumar, D.; Gil-Sepulcre, M.; Nippe, M. Electrocatalytic CO2 Reduction by Imidazolium-Functionalized Molecular Catalysts. *J. Am. Chem. Soc.* **2017**, *139*, 13993–13996.

(61) Lau, G. P. S.; Schreier, M.; Vasilyev, D.; Scopelliti, R.; Grätzel, M.; Dyson, P. J. New Insights Into the Role of Imidazolium-Based Promoters for the Electroreduction of CO2 on a Silver Electrode. *J. Am. Chem. Soc.* **2016**, *138*, 7820–7823.

(62) Nachtigall, F. M.; Corilo, Y. E.; Cassol, C. C.; Ebeling, G.; Morgon, N. H.; Dupont, J.; Eberlin, M. N. Multiply Charged (Di-)Radicals. *Angew. Chem. Int. Ed.* **2008**, *47*, 151–154.

(63) Cassol, C. C.; Ebeling, G.; Ferrera, B.; Dupont, J. A Simple and Practical Method for the Preparation and Purity Determination of Halide-Free Imidazolium Ionic Liquids. *Adv. Synth. Catal.* **2006**, *348*, 243–248.

(64) Fernández, A.; Vázquez-García, D.; García-Fernández, A.; Marcos-Cives, I.; Platas-Iglesias, C.; Castro-García, S.; Sánchez-Andújar, M.

Diimidazolium Halobismuthates [Dim]2[Bi2X10] (X = Cl-, Br-, or I-): A New Class of Thermochromic and Photoluminescent Materials. *Inorg. Chem.* **2018**, *57*, 7655–7664.

(65) Aher, S. B.; Bhagat, P. R. Convenient Synthesis of Imidazolium Based Dicationic Ionic Liquids. *Res. Chem. Intermed.* **2016**, *42*, 5587–5596.

(66) Kazemiabnavi, S.; Zhang, Z.; Thornton, K.; Banerjee, S. Electrochemical Stability Window of Imidazolium-Based Ionic Liquids as Electrolytes for Lithium Batteries. *J. Phys. Chem. B* **2016**, *120*, 5691–5702.

(67) Costentin, C.; Savéant, J. Towards an Intelligent Design of Molecular Electrocatalysts. *Nat. Rev. Chem.* **2017**, *1*, 0087.

(68) Leu, M. K.; Vicente, I.; Fernandes, J. A.; de Pedro, I.; Dupont, J.; Sans, V.; Licence, P.; Gual, A.; Cano, I. On the Real Catalytically Active Species for CO2 Fixation into Cyclic Carbonates under near Ambient Conditions: Dissociation Equilibrium of [BMIm][Fe(NO)2Cl2] Dependant on Reaction Temperature. *Appl. Catal. B Environ.* **2019**, *245*, 240–250.

(69) Fuente, V. de la; Godard, C.; Zangrando, E.; Claver, C.; Castillón, S. A Phosphine-Free Pd Catalyst for the Selective Double Carbonylation of Aryl Iodides. *Chem. Commun.* **2012**, *48*, 1695–1697.

(70) Diniz, J. R.; De Lima, T. B.; Galaverna, R.; De Oliveira, A. L.; Ferreira, D. A. C.; Gozzo, F. C.; Eberlin, M. N.; Dupont, J.; Neto, B. A. D. Is the Formation of N-Heterocyclic Carbenes (NHCs) a Feasible Mechanism for the Distillation of Imidazolium Ionic Liquids? *Phys. Chem. Chem. Phys.* **2018**, *20*, 24716–24725.

(71) Godajdar, B. M.; Kiasat, A. R.; Hashemi, M. M. Synthesis, Characterization and Application of Magnetic Room Temperature

Dicationic Ionic Liquid as an Efficient Catalyst for the Preparation of 1,2-Azidoalcohols. *J. Mol. Liq.* **2013**, *183*, 14–19.

(72) Fukuyama, T.; Mukai, Y.; Skrydstrup, T.; Ryu, I. Modernized Low Pressure Carbonylation Methods in Batch and Flow Employing Common Acids as a CO Source. *Org. Lett.* **2013**, *15*, 2794–2797.

(73) Khedkar, M. V; Sasaki, T.; Bhanage, B. M. Immobilized Palladium Metal-Containing Ionic Liquid-Catalyzed Alkoxycarbonylation , Phenoxycarbonylation , and Aminocarbonylation Reactions. *ACS Catal.* **2013**, *3*, 287–293.

(74) Hermange, P.; Gøgsig, T. M.; Lindhardt, A. T.; Taaning, R. H.; Skrydstrup, T. Carbonylative Heck Reactions Using CO Generated Ex Situ in a Two-Chamber System. *Org. Lett.* **2011**, *13*, 2444–2447.

(75) Seiche, W.; Schuschkowski, A.; Breit, B. Bidentate Ligands by Self-Assembly through Hydrogen Bonding: A General Room Temperature/Ambient Pressure Regioselective Hydroformylation of Terminal Alkenes. *Adv. Synth. Catal.* **2005**, *347*, 1488–1494.

Chapter 4

Solar-driven CO_2 reduction catalyzed by Hybrid Supramolecular Photocathodes and enhanced by Ionic Liquids

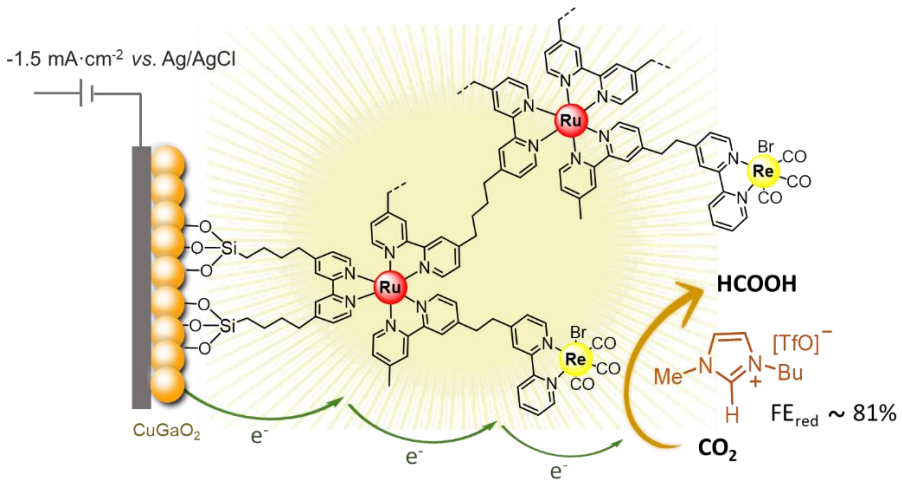

Chapter 4

Abstract

Photoelectrochemical carbon dioxide reduction at ambient temperature and pressure was performed using molecular chromophores and catalyst assemblies onto Cu_2O/SnO_2-based and $CuGaO_2$-based electrodes in an aqueous solution and with an ionic liquid (IL) organic solution acting as CO_2 absorbent and electrolyte. An electropolymerization approach to immobilize molecular catalysts onto the semiconductors based on the silanization of the semiconductor followed by an electropolymerization procedure provided a series of molecular and supramolecular hybrid photocathodes for solar driven CO_2 reduction. Focusing on the cathodic half reactions, the most promising conditions for the formation of CO_2 reduction products were determined. The results revealed that the ionic liquid played a critical role in the conversion of CO_2 to formic acid and suppression of the production of hydrogen, as well as the potentiality of anchoring supramolecular complexes on semiconductor photo-electrocatalysts to boost both carriers transport and catalytic activity.

This work has been done in the framework of the European Union's Horizon 2020 SunCOChem project, Grant Agreement No 862192.[1]

4.1. Introduction

Over the last decade, the increase of the CO_2 concentration in the atmosphere, which could eventually cause irreversible effects on nature, has triggered much attention in chemical research on carbon capture and utilization (CCU) technologies.[2,3] For *CO_2 capture*, the main challenge is to find the ideal absorbent that exhibits high selectivity and high capacity for CO_2. In this context, ionic liquids (ILs) have demonstrated excellent capture capacity for CO_2[4]; in addition, they were also widely adopted as electrolytes in the electrochemical conversion of CO_2 since they exhibit high gas solubility, negligible vapor pressure, high ionic conductivity, and wide electrochemical windows.[5] Furthermore, it was reported that ILs can interact with CO_2 resulting in a decrease of the overpotential and an enhancement of the product selectivity.[6] CO_2 electroreduction studies also demonstrated that the appropriate combinations of IL and catalyst can enhance the generation of CO with faradaic efficiencies up to 96 %.[7–9] Among the ILs, 1-butyl-3-methyl-imidazolium triflate (BMI·TfO) is one of the most promising due to the high CO_2 solubility (0.6-0.8 mol CO_2/mol_{IL}),[10] good electrochemical and thermal stability, and relatively low viscosity. Therefore, although it has not been often used as electrolyte for the CO_2 reduction reaction (CO_2RR), herein it will be exploited instead of the most commonly employed BMI·BF_4 to avoid the issues related to the hydrolysis of the $[BF_4]^-$ and the possible formation of HF under electrochemical CO_2RR conditions.[11]

Regarding *CO_2 conversion*, the main challenge is to efficiently activate and reduce CO_2 to reach the zero-carbon footprint goal. In this respect, visible-light-driven CO_2 reduction in combination with water oxidation is a promising solution as it involves the use of abundant water and inexhaustible solar energy, and constitutes one of the representative models of artificial photosynthesis.[12] Molecular metal complexes and semiconductors are

promising candidates for photocatalysis, that can reduce CO_2 to CO, formic acid, formaldehyde or other hydrocarbons.[13] Although both, molecular metal complexes and semiconductors, have strengths and weaknesses, their main limitations (low oxidation ability and low selectivity for reduction reactions) can be overcome via the construction of suitable molecule/semiconductor hybrid materials. In this approach, the efficiency of electron transfer from a semiconductor to an immobilized molecular catalyst and suppression of back electron transfer are crucial for reducing CO_2 on the molecule/semiconductor hybrid material.[14] To this end, both the conduction band potential of the semiconductor and the reduction potential of the molecular unit should be carefully designed.

Supramolecular hybrid photocatalysts based on ruthenium (Ru(II))-rhenium (Re(I)) complexes were reported to efficiently catalyze CO_2 photoreduction under visible light with faradaic efficiencies up to 85 % with CO and HCOOH as the major products.[13,14] The first molecular hybrid photocathode based on a supramolecular Ru-Re complex (Figure 1a) was designed by Osamu Ishitani and co-workers. They immobilized the RuRe supramolecular complex onto NiO using phosphonic acid as anchoring group.[15] Irradiating ($\lambda > 460$ nm) the NiO-RuRe photocathode at -1.2 V vs $Ag/AgNO_3$ in a DMF-triethanolamine solution containing 0.1 M of tetrabutylammonium tetrafluoroborate ($TBA{\cdot}BF_4$), they obtained a faradaic efficiency of 71 % for 5 h irradiation. Later, they coupled the hybrid NiO-RuRe photocathode with a CoO_x/TaON photoanode separated with a Nafion membrane (Figure 1b).[16] They performed the photoelectrochemical cell with a Z-Scheme configuration for the CO_2 reduction using water as reducing agent. They obtained a O_2 Faradaic efficiency of 68 % and a total cathodic Faradaic efficiency of 37 % by applying visible light irradiation, and electrical bias and chemical bias, -0.3 V and -0.1 V vs cathode, respectively. This difference between the anodic and cathodic part was attributed to the reduction of trivalent nickel ions (Ni^{3+}) that originally

existed in the NiO of the photocathode. The NiO is problematic because of its low conductivity, and the presence of electrochemically inactive surface areas. Despite the use of external electrical and chemical biases, this was the first successful visible-light-driven CO_2 reduction using water.

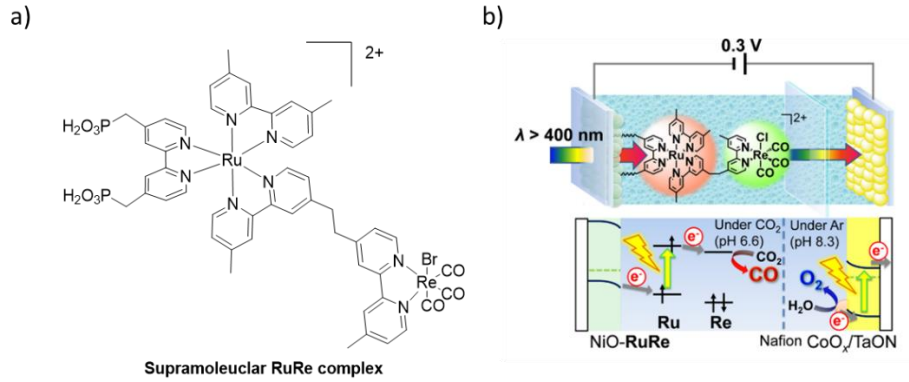

***Figure 1**: a) Supramolecular RuRe complex developed by Osamu Ishitani and co-workers; b) Tandem PEC device for CO_2 reduction with water oxidation composed of a NiO-RuRe hybrid photocathode and CoO_x/TaON photoanode. Reprinted from ref [16].*

Later, to avoid the use of NiO, Osamu Ishitani and co-workers developed an hybrid photocathode based on $CuGaO_2$ and a supramolecular Ru-Re complex (Figure 1a) immobilized with phosphonic acid as anchoring groups.[17] This system allowed them to obtain high faradaic efficiencies (up to 81 %) with a ratio CO:H_2 of 1.5:1 and to exceed the performance observed with the NiO electrode; however, the main drawback was related to the instability of the phosphonic acid.

To improve the stability of the molecular complexes onto the semiconductor different anchor approaches were developed. Meyer and co-workers adopted a new immobilization method based on the silanization of NiO, followed by the two-step electropolymerization of a molecular Ru and a molecular Re complexes (Figure 2).[18] The designed photocathode under solar light irradiation (λ ≥ 400 nm) and with an applied bias of -0.7 V vs. Ag/AgCl provided

a CO Faradaic efficiency of 65 % after 10 h of photoelectrocatalysis maintaining more than 80 % of the initial current density.

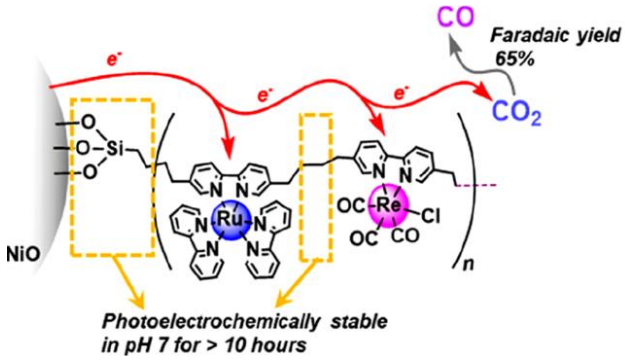

***Figure 2**: Schematic structure of prepared by electropolymerization molecular hybrid photocathode (NiO|Si-poly(Ru^{II})-poly(Re^{I})). Reprinted from ref [18].*

Ishitani and co-workers reported a Ru(II)-Re(I) supramolecular complex and a Ru(II) redox photosensitizer containing phosphonic acid and/or vinyl groups. First, they immobilized the complexes onto a NiO semiconductor by using the phosphonic acid as anchor group followed by the electropolymerization of the other complexes using the vinyl groups presents in the ligands (Figure 3).[19] Using this method, the absorbed amount of metal was increased and the desorption was suppressed. The poly-RuRe/NiO showed a high CO_2 reduction activity, under irradiation (λ > 460nm) and with an applied bias of -0.7 V vs Ag/AgCl, the main product obtained was CO, with H_2 and HCOOH as by-products with a total reduction Faradaic efficiency of 85 %.

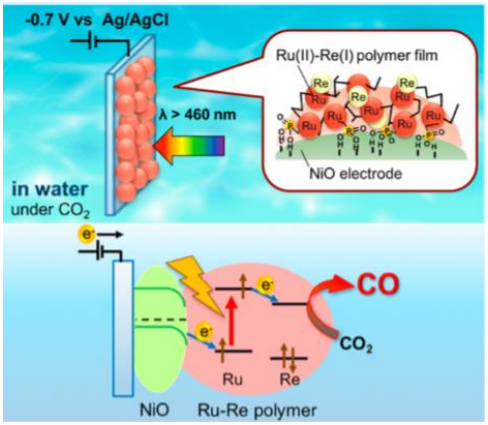

***Figure 3**: Schematic representation of the Ru(II)-Re(I) polymer film after the electropolymerization onto a NiO photocathode. Reprinted from ref [19].*

Recently, Ishitani and co-workers performed a new immobilization process by electropolymerization following a similar approach (Figure 4).[20] In this case, they absorbed the Ru photosensitizer containing both, the phosphonic acid groups, and vinyl groups in the ligand. Then, another different Ru mononuclear complex containing a vinyl group and free diamine ligands were immobilized by electropolymerization followed by the coordination of the Ru catalyst into the non-coordinated diamine unit of the ligand obtaining the final photocathode. After this immobilization procedure, they obtained a high durable and selective system to CO and HCOOH (ratio CO:HCOOH almost 1:1) for CO_2 reduction with a stability for 100 h, and a total faradaic efficiency of 65 % under visible light irradiation at applied potential of -0.7 V vs Ag/AgCl.

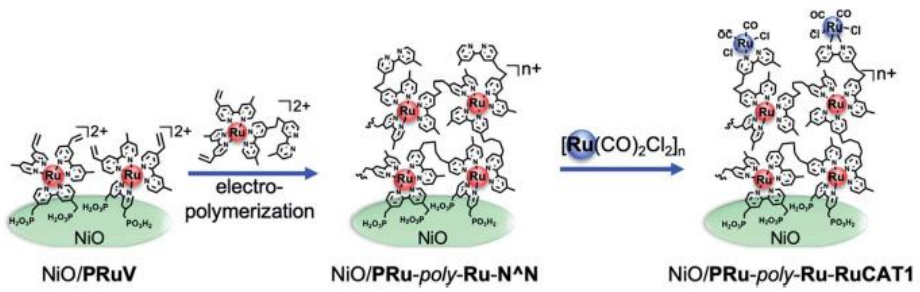

***Figure 4**: Preparation scheme for the photocathode NiO/PRu-poly-Ru-RuCAT by electropolymerization. Reprinted from ref [20].*

In view of the better performance of the $CuGaO_2$ compared with NiO, the use of the copper oxide-based semiconductors, $CuGaO_2$ and Cu_2O/SnO_2, was explored. The $CuGaO_2$ and Cu_2O have p-type semiconducting properties which come from the Cu^+ vacancies.[21] The $CuGaO_2$ has been used as transparent conducting metal oxide material,[22,23] as an alternative to NiO for dye-sensitized photocathodes[24,25] and was also used as electrode for the photocatalytic CO_2 reduction containing immobilized molecular Ru and Re complexes, obtaining high Faradaic efficiencies (FE_{red} = 81 %).[17] The cuprous oxide (Cu_2O) presents a good band gap (2.0-2.3 eV) and high carrier mobility (60-130 $cm^2 \cdot V^{-1} \cdot s^{-1}$) but also photostability issues due to photocorrosion. The Cu_2O can undergo self-oxidation (Cu_2O to CuO) and self-reduction (Cu_2O to Cu) under illumination.[26] Luo and co-workers reported an earth-abundant Cu_2O/SnO_2 catalyst for the CO_2 reduction to CO.[27] They optimized the synthesis of the catalyst achieving up to 90 % of CO faradaic efficiency at low overpotential. The Cu_2O/SnO_2 catalysts exhibited good stability during 18h at -0.5 V vs RHE in an aqueous electrolyte.

Inspired by the progress in capture and conversion of CO_2 using ILs and the results reported with semiconductors and immobilization procedures, we report here the preparation of various hybrid assemblies based on $CuGaO_2$ and Cu_2O/SnO_2 with a series of new molecular and supramolecular Ru and Re complexes and their testing in the photocatalyzed CO_2 reduction using BMI·TfO as catholyte. The results revealed that the photocathodes with supramolecular and binuclear complexes assemblies in the presence of IL promotes the conversion of CO_2, improving the stability of the system, and suppressing the production of H_2 compared to the bare semiconductor as electrode.

4.2. Results and discussions

4.2.1. Synthesis and characterization of Ru and Re molecular complexes

A Ru-based visible-light-absorbing molecular complex (**Ru_{VLA}**), Re-based CO_2 reduction catalysts (**Re_{CAT}**), supramolecular and binuclear Ru-Re complexes (**RuRe1** and **RuRe2**) containing bipyridine-vinyl ligands (**bpy-V**) were successfully synthesized in high yields and characterized by NMR, MS, IR and UV-Vis spectroscopy (Scheme 1).

The synthesis of the **Re_{CAT}** complex was performed using $Re(CO)_5Br$ as precursor. One equivalent of Re precursor and one equivalent of **bpy-V** ligand were dissolved in toluene and heated under reflux overnight. The **Re_{CAT}** complex was formed in high isolated yield (84 %).

Concerning the synthesis of the **Ru_{VLA}**, the $[Ru(COD)Cl_2]$ precursor was first prepared starting from $RuCl_3 \cdot 3H_2O$. Then, the COD ligand was substituted by two 4,4'-dimethyl-2,2'-bipyridine ($bpyMe_2$) ligands in 1,2-dichlorobenzene at 155°C obtaining the $[Ru(bpyMe_2)Cl_2]$ complex. Later, the remaining chloride ligands were substituted by one **bpy-V** ligand in an acetone/water solution obtaining the final desired complex in 74 % isolated yield.

The complexes **RuRe1** and **RuRe2** were synthesized following an adopted synthetic strategy of the previously described **Ru_{VLA}**. First, the $[Ru(COD)Cl_2]$ precursor was prepared, and the $[Ru(bpy\text{-}V)Cl_2]$ complex was obtained by the replacement of the COD ligand with two **bpy-V** ligands. Then, the chloride ligands were replaced by 1,2-bis(4'-methyl-[2,2'-bipyridin]-4-yl)ethane or 2,2'-Bipyrimidine ligand to obtain the corresponding Ru complexes. Finally, the reaction with one equivalent of $Re(CO)_5Br$ complex under reflux yielded the final **RuRe1** and **RuRe2** complexes in good isolated yields (64 % and 67 %, respectively). The coordination of the Re complex was confirmed by IR

spectroscopy via the detection of the characteristic vibration bands of the CO ligands. The ^{1}H and ^{13}C NMR and HRMS analyses confirmed the structure of both complexes (see experimental part for detailed synthetic description and characterization of all the complexes).

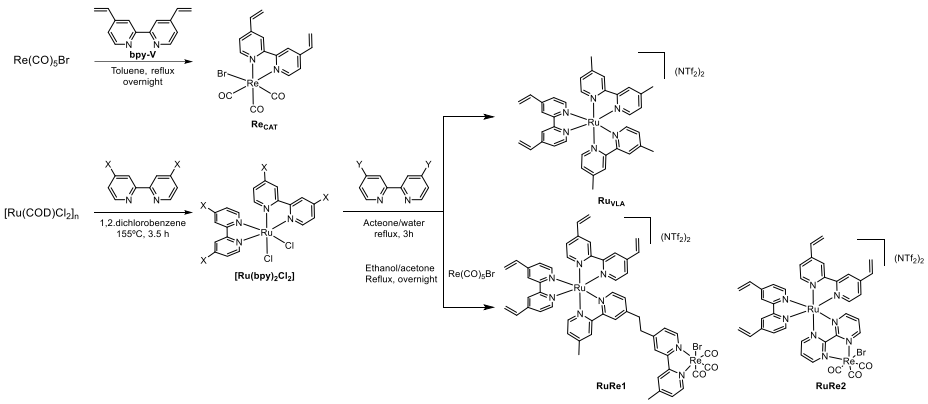

***Scheme 1**: Schematic synthetic route for the preparation of **Ru_{VLA}**, **Re_{CAT}**, **RuRe1** and **RuRe2** complexes.*

4.2.2. Photoelectrochemical reduction of CO_2 using molecular Cu_2O/SnO_2-based photocathodes

In this section, synthesis, characterization, and studies of the photoelectrochemical activity towards CO_2RR of three molecular photocathodes in an aqueous solution and in an IL organic solution were described. The photocathode assemblies included, a silane surface bridge based on vinyltrimethoxysilane (VTES), a i) **Ru_{VLA}**, ii) **Re_{CAT}** and iii) **Ru_{VLA}** + **Re_{CAT}** molecular complex immobilized onto a p-type Cu_2O/SnO_2 semiconductor (Figure 5). As described in the previous section, **Ru_{VLA}** and **Re_{CAT}** molecular complexes were derivatized with vinyl functional groups to assemble surface structures by electropolymerization.[18,19]

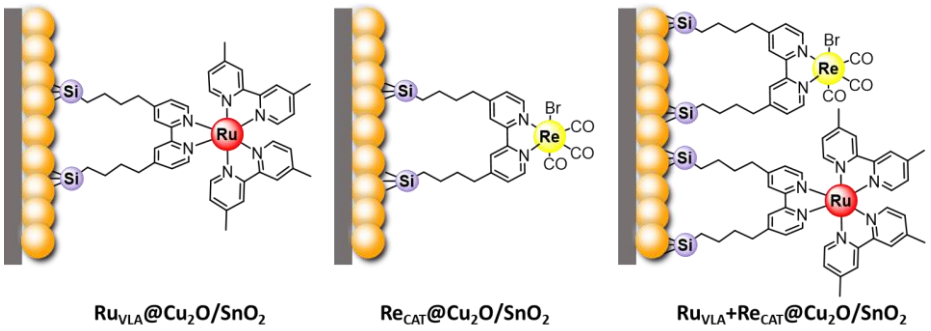

***Figure 5**: Schematic representation of the three different photocathodes assemblies prepared in this part.*

4.2.2.1. Cu_2O/SnO_2 synthesis, functionalization, and characterization

The preparation of the Cu_2O/SnO_2 nanoparticles, functionalization with VTES and characterization was performed in collaboration with Dr. Alberto Lopera and Dra. Maria José López in Laurentia technologies SLL company within the European Union's Horizon 2020 SunCoChem project.[1]

The synthesis of the Cu_2O/SnO_2 was performed according to an adapted reported procedure.[27] The method consists in a two–step process involving (i) wet precipitation, and (ii) coordinating etching. Scanning electron microscope images showed cubic morphologies with sizes ranging from 100–300 nm (Figure 6a). EDX mapping experiments confirmed the presence of copper and tin elements in the Cu_2O/SnO_2 nanoparticles and revealed a molar ratio of 40:1 (Figure 6b).

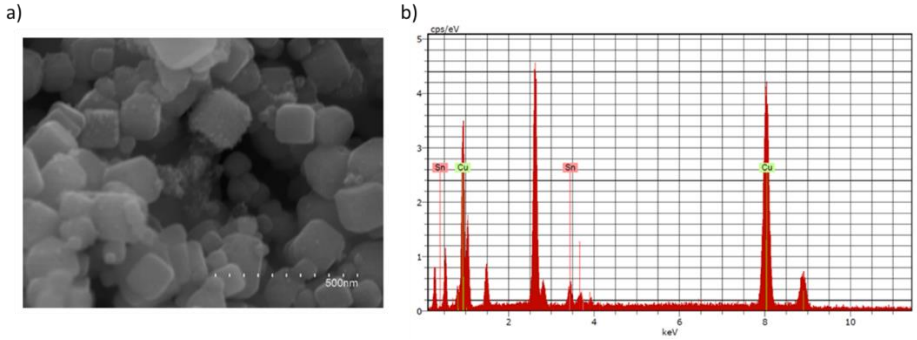

***Figure 6**: a) Scanning electron microscopy images captured and b) Energy Dispersive X–ray (EDX) spectrum for the Cu_2O/SnO_2 nanoparticles.*

Then, the Cu_2O/SnO_2 NPs were functionalized in an isopropanol/water (95/5) solution containing 5 mM of vinyltriethoxysilane (VTES) to form stable surface Si-O bonds. After VTES functionalization, no significant changes in size and shape were observed by SEM analysis in comparison with bare Cu_2O/SnO_2 NPs (Figure 7a). EDX mapping experiments revealed that the elements Sn, Cu and Si are evenly distributing in the whole sample (Figure 7b).

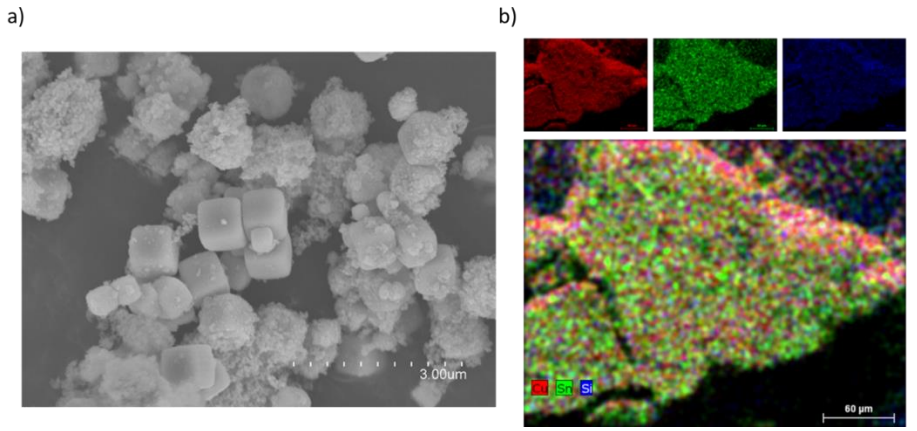

***Figure 7**: a) SEM images captured of the Cu_2O/SnO_2 nanoparticles functionalized VTES. b) EDX mapping experiments of Cu_2O/SnO_2 nanoparticles functionalized with VTES. Red color indicates copper presence. Green color indicates tin presence. Blue color indicates silicon presence.*

4.2.2.2. Preparation of hybrid molecular-based Cu_2O/SnO_2 photocathodes

Electropolymerizations experiments of the silanized Cu_2O/SnO_2-VTES NPs are then performed by performing cyclic voltammetries of a suspension of Cu_2O/SnO_2-VTES NPs onto a 5 mM solution of the corresponding vinyl-tagged metal complex (**Ru_{VLA}** and/or **Re_{CAT}**) through the potential window of 0 to −1.9 V *vs.* $Ag/AgNO_3$ at a scan rate of 100 mV s^{-1} in N_2-degassed acetonitrile solution (Scheme 2).

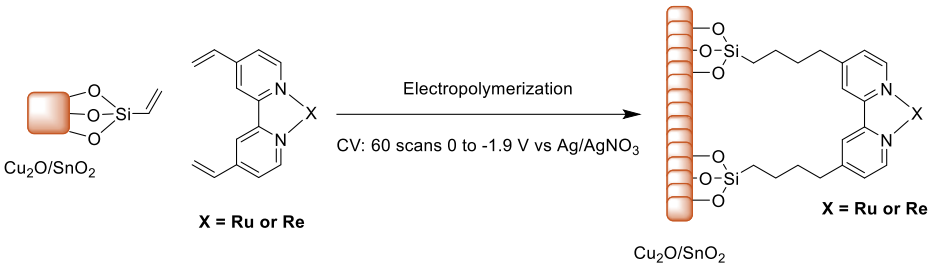

***Scheme 2**: Electropolymerization scheme using Cu_2O/SnO_2-VTES powders.*

The efficiency of the electropolymerization procedure of Cu_2O/SnO_2-VTES with the molecular complexes was corroborated by the continuous enhancement of the current densities after each scan (Figure 8). This behavior confirms the in-situ covalent immobilization of the metal complex onto Cu_2O/SnO_2-VTES. During this electropolymerization process, the reduction of the vinyl groups forms a radical coupling with the subsequent carbon-carbon bond formation.[18,19]

Chapter 4

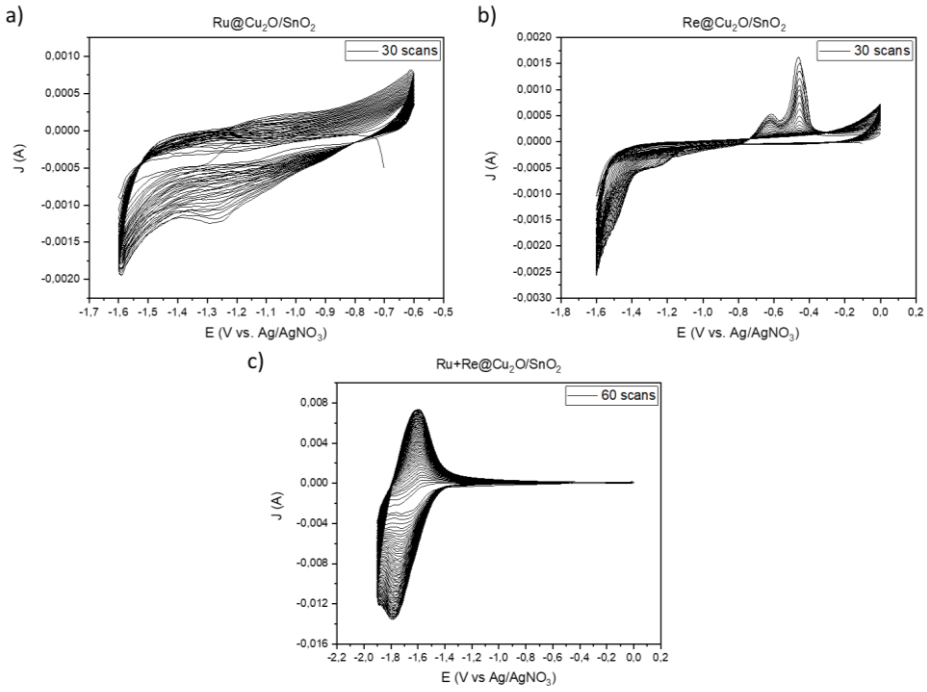

***Figure 8**: Cyclic voltammogram graphics of a) Electropolymerization of **Ru_{VLA}** and Cu_2O/SnO_2-VTES NPs, b) Electropolymerization of **Re_{CAT}** and Cu_2O/SnO_2-VTES and c) Electropolymerization of a mixture of **Ru_{VLA}**, **Re_{CAT}** and Cu_2O/SnO_2-VTES. All the electropolymerizations were performed in a N_2 degassed solution containing 5 mM of each complex and 500 mg of Cu_2O/SnO_2-VTES NPs.*

Three molecular photocathodes assemblies were prepared: (i) **Ru_{VLA}@Cu_2O/SnO_2**, (ii) **Re_{CAT}@Cu_2O/SnO_2**, and (iii) **Ru_{VLA}+Re_{CAT}@Cu_2O/SnO_2**. The surface coverage with the metal complex was quantified by ICP-MS analysis (Table 1).

***Table 1**: ICP-MS quantification analysis.*

Powder	$\mu mol_{Ru}/g_{Cu2O/SnO2}$	$\mu mol_{Re}/g_{Cu2O/SnO2}$
Ru_{VLA}@Cu_2O/SnO_2	2.7	-
Re_{CAT}@Cu_2O/SnO_2	-	3.6
Ru_{VLA}+Re_{CAT}@Cu_2O/SnO_2	2.6	5.3

Finally, the corresponding electrodes were prepared by deposition of a catalytic ink onto a porous carbon support (Toray carbon paper 060, from FuelCellStore) by air-brushing using the corresponding powder.[28] Each electrode was prepared with a geometric area of 1 cm^2 with a catalyst loading of the corresponding powder of 1 $mg \cdot cm^{-2}$.

4.2.2.3. Photoelectrochemical CO_2 reduction performance in $KHCO_3$ aqueous solution

Photoelectrochemical tests of the synthetized molecular photocathodes were performed in collaboration with Maddalena Zoli and Dra. Simelys Hernandez in the Politecnico di Torino (Italy) in the framework of the European project Horizon 2020 SunCOChem.[1]

The photoelectrochemical performance of the photocathodes was first tested in an aqueous solution of 0.1 M $KHCO_3$ as electrolyte, under simulated solar light irradiation in a two-compartment electrochemical cell using a platinum mesh as the counter electrode and with an applied current intensity of -20 $mA \cdot cm^{-2}$. This is the target current potential of the European project Horizon 2020 SunCOChem.

Figure 9 shows a chopped dark/light chronoamperometry (CA) performance of all prepared photocathodes at an applied potential of -250 mV in a 0.1 M $KHCO_3$ aqueous solution. The experiment confirmed the photoactivity of all the catalysts. The bare **Cu_2O/SnO_2** photocathode showed a photocurrent decrease over time, from -0.206 $mA \cdot cm^{-2}$ to 0.105 $mA \cdot cm^{-2}$ (green trace). On the other hand, a constant and similar photocurrent contributions of 0.09 $mA \cdot cm^{-2}$ were obtained during all the experiments with photocathodes modified with **Ru_{VLA}** or **Re_{CAT}** (compare blue and red traces in Figure 9). Interestingly, the co-immobilization of **Ru_{VLA}** and **Re_{CAT}** onto electrode surface outperformed the bare **Cu_2O/SnO_2** photocathode up to 0.130 $mA \cdot cm^{-2}$ (black

trace). We attributed this photocurrent enhancement to the good band alignment and synergistic effects between the two molecular complexes and the semiconductor, leading to higher charge separation efficiencies.

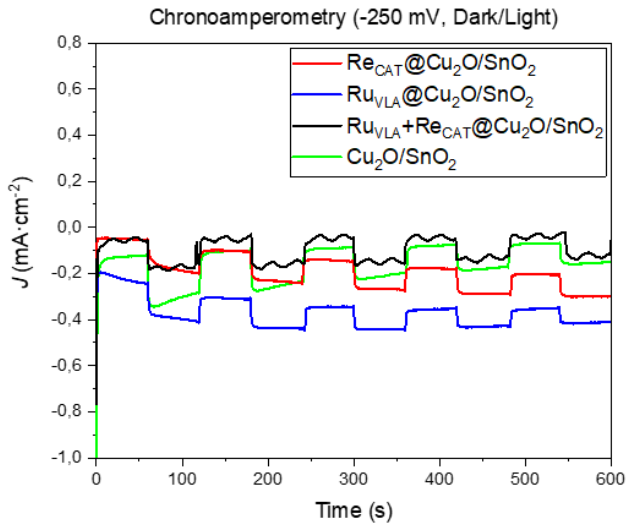

Figure 9**: Chopped Dark/light chronoamperometry of different photocathodes at an applied potential of -250 mV vs Ag/AgCl in an aqueous solution of 0.1 M $KHCO_3$.* ***Cu_2O/SnO_2 *(green),* ***$Ru_{VLA}@Cu_2O/SnO_2$*** *(blue),* ***$Re_{CAT}@Cu_2O/SnO_2$*** *(red),* ***Re_{CAT}+$Ru_{VLA}@Cu_2O/SnO_2$*** *(black).*

Then, the effect of the molecular complexes on the CO_2 photoelectroreduction selectivity is evaluated during a 2 hours chronopotentiometry (CP) by applying a current density of -20 mA·cm^{-2} in an aqueous solution of 0.1 M $KHCO_3$ under simulated sunlight conditions. Figure 10 represents the faradaic efficiencies of the gaseous and liquid products for each photocathode at that current density displayed.

The bare **Cu_2O/SnO_2** electrode, displayed lower total faradaic efficiency (80 %) than those measured with the hybrid materials. The prepared hybrid materials displayed an increase in the faradaic efficiency up to 95 %. This behavior has been attributed to the protective and stabilizing role of the **Ru_{VLA}** and **Re_{CAT}** complexes that hinder the **Cu_2O/SnO_2** modification. Among them, the major product generated with **Ru_{VLA}** or **Re_{CAT}** hybrid photocathodes is H_2 with a FE_{H2}

of 63 and 53 % respectively, followed by formic acid, FE_{HCOOH} of 15 and 24 % using the **Ru_{VLA}** or **Re_{CAT}** hybrid photocathodes, respectively. However, when **Ru_{VLA}** and **Re_{CAT}** are co-immobilized on the surface of the electrode, the hybrid photocathode displayed an enhancement of the formic acid and CO production, and suppression of the H_2 production. As previously mentioned, such results confirmed that the combination of the visible light absorber and the catalyst complex maximized the electron transfer between the components to obtain an efficient reduction photocatalyst and it was also improved the efficiency and selectivity compared to the bare catalyst.

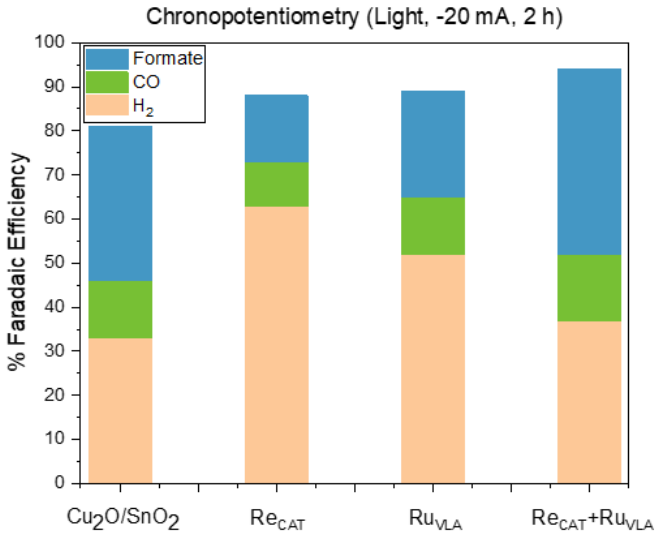

***Figure 10**: Faradaic efficiencies of gas and liquid products produced in a 2 h chronopotentiometry experiment at an applied current density of -20 mA·cm^{-2} in an aqueous 0.1 M $KHCO_3$ solution saturated with CO_2 under simulated sunlight irradiation with the different prepared photocathodes.*

4.2.2.4. Photoelectrochemical CO_2 reduction performance in an IL organic solution

Based in the promising results obtained with the different photocathodes using an aqueous solution of 0.1 M $KHCO_3$ as electrolyte, it was decided to change the electrolyte to an acetonitrile 0.3 M BMI·TfO to enhance the

efficiency and selectivity of the CO_2 reduction. Photoelectrochemical properties of the prepared hybrid molecular photocathodes were studied in the presence of BMI·TfO organic solution and compared with those of using an aqueous electrolyte.

Figure 11a shows a chopped dark/light linear sweep voltammetry (LSV) of all prepared photocathodes. The experiments were performed using simulated sunlight irradiation in an acetonitrile solution containing 0.3 M of BMI·TfO and saturated with CO_2. The current-potential curves showed no significant differences in the current response among all the catalysts. In this case, using the IL as electrolyte, the photoactivity started to be observed between -1.2 and -1.4 V vs Ag/AgCl in comparison with the aqueous media where it was possible to observe the photoactivity at -0.25 V vs Ag/AgCl.

A chopped dark/light chronoamperometry (Figure 11b) performed at an applied potential of -1400 mV confirmed the photoactivity of all the catalysts. At lower applied potential, no photoactivity was observed. The **Ru_{VLA}@Cu_2O/SnO_2** exhibited a photocurrent of 0.202 mA·cm^{-2}, which constituted the highest photo-response among all molecular photocathodes. In the other hand, with the bare **Cu_2O/SnO_2** higher photocurrent contribution than with the **Re_{CAT}@Cu_2O/SnO_2** was obtained, 0.160 and 0.125 mA·cm^{-2}, respectively. With the **Ru_{VLA}+Re_{CAT}@Cu_2O/SnO_2** system a very noisy experiments were obtained and it was not possible to calculate the photocurrent contribution.

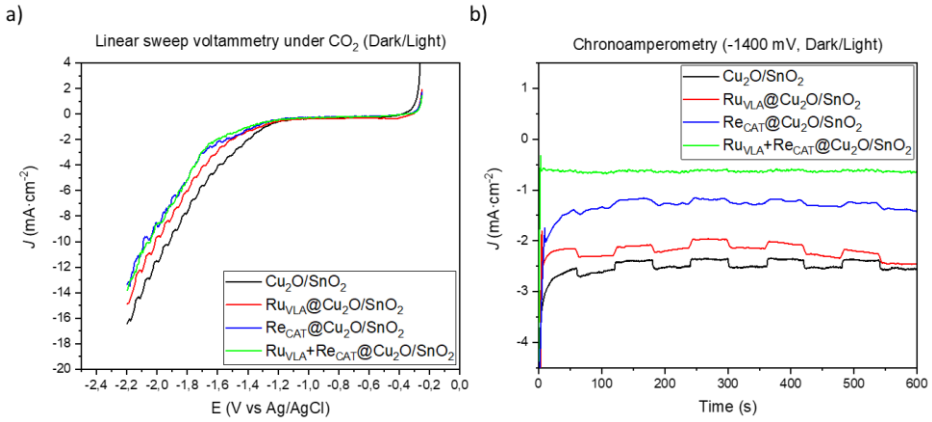

***Figure 11**: a) Chopped dark/light current-potential curves of the different prepared photocathodes under CO_2 saturated 0.3 M BMI·TfO acetonitrile solution. b) Dark/light chronoamperometry of the different prepared photocathodes performed at -1400 mV vs Ag/AgCl under the same conditions of a). **Cu_2O/SnO_2** (black), **$Ru_{VLA}@Cu_2O/SnO_2$** (red), **$Re_{CAT}@Cu_2O/SnO_2$** (blue), **$Re_{CAT}+Ru_{VLA}@Cu_2O/SnO_2$** (green).*

Then, the effect of molecular complexes in the presence of IL as electrolyte on the CO_2 photoelectroreduction selectivity was evaluated during a 2 hours chronoamperometry by applying a current intensity of -20 mA·cm^{-2}. Figure 12 represents the faradaic efficiencies of the gaseous and liquid products measured for each photocathode.

Using an organic BMI·TfO media, lower H_2 production was obtained for all the catalyst than those measured using $KHCO_3$ as electrolyte. The highest FE_{H2} is 23 % with the bare Cu_2O/SnO_2 using the IL. In all the cases, higher selectivity to the CO_2 reduction products (formate and CO) were obtained suppressing the H_2 production than those measured using $KHCO_3$ aqueous solution. A comparison of the bare **Cu_2O/SnO_2** with the **$Re_{CAT}@Cu_2O/SnO_2$** photocathode suggested that the same total FE was obtained but using the **$Re_{CAT}@Cu_2O/SnO_2$** higher selectivity to the formate (FE_{HCOOC} = 33 %) and lower H_2 production (FE_{H2} = 16 %) were achieved confirming the role of a CO_2 reduction catalyst to obtain higher selectivity to the CO_2 reduction products.

Instead, using the **Ru_{VLA}@Cu_2O/SnO_2**, a lower total FE than those measured with the bare **Cu_2O/SnO_2** was obtained. Similar H_2 and formate productions were obtained but with lower CO production. Finally, with the **Ru_{VLA}+Re_{CAT}@Cu_2O/SnO_2**, the total faradaic efficiency was higher (from 60.4 % to 80.5 %) and the H_2 production was much lower. These hybrid photocathodes displayed an increased selectivity to CO (FE_{CO} up to 28 %) and formate (FE_{HCOOH} up to 34 %). These results also demonstrated that with the combination of the visible light absorber and the CO_2 reduction catalyst the electron transfer between the components is maximized. This resulted in an improvement of the reduction photocatalyst, and an improvement of the efficiency and selectivity of the system compared to the bare catalyst.

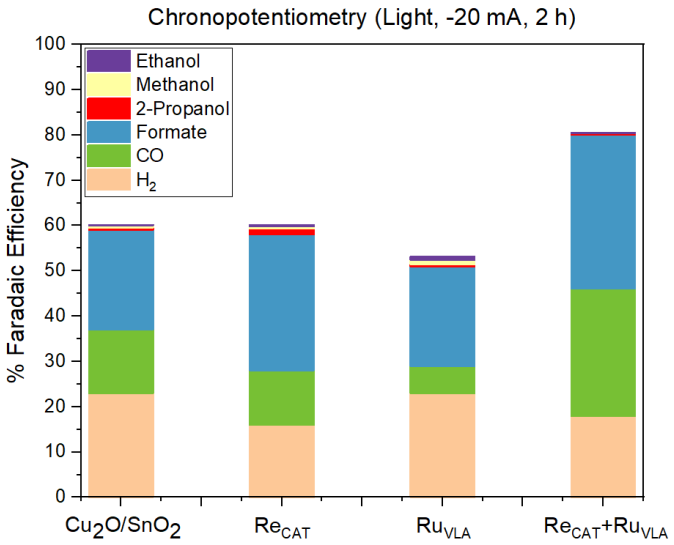

***Figure 12**: Faradaic efficiencies of gas and liquid products produced in a 2 h chronopotentiometry at -20 mA·cm^{-2} in an acetonitrile 0.3 M BMI·TfO solution saturated with CO_2 under simulated sunlight irradiation with the different prepared photocathodes.*

4.2.2.5. Summary and conclusions

Here, the preparation of different hybrid molecular photocathodes based on a p-type silanized Cu_2O/SnO_2 film modified with an electropolymerized

chromophore/catalyst assembly is described. The photocathodes were prepared by electrodeposition of a vinyl-tagged ruthenium-based visible-light-absorber complex and a rhenium-based CO_2 reduction catalyst through electropolymerization on the silanized oxide films. Three different molecular assemblies based on the separate, and the co-immobilization of $\mathbf{Ru_{VLA}}$ and $\mathbf{Re_{CAT}}$ complexes were prepared, and their photoelectrocatalytic CO_2 reduction performances were tested in aqueous $KHCO_3$ and organic/BMI·TfO media. The co-immobilization of $\mathbf{Ru_{VLA}}$ and $\mathbf{Re_{CAT}}$ complexes onto the electrode surface revealed a photoactivity enhancement. The beneficial influence of anchoring molecular complexes onto $\mathbf{Cu_2O/SnO_2}$ photocathodes to boost, both, its carriers transport, and its catalytic activity with respect to the bare semiconductor material was shown.

Two different electrolytes were evaluated showing the highest total faradaic efficiencies with $KHCO_3$ as electrolyte (FE_{TOT} up to 94 %) and with BMI·TfO as IL-electrolyte (FE_{TOT} up to 80.5 %). The highest selectivity towards CO_2 reduction products is obtained using the IL ($FE_{CO+HCOOH}$ up to 62 %) together with the suppression of the H_2 production (from FE_{H2} = 37 % using the $KHCO_3$ to FE_{H2} = 18 % using the IL).

The combination of the BMI·TfO as IL-electrolyte together with the hybrid molecular photocathode was demonstrated to enhance both the CO_2 reduction selectivity (by suppressing the H_2 evolution reaction) and the stability towards its restructuration. This combination resulted in a 20 % increase of the total faradaic efficiency compared to the bare $\mathbf{Cu_2O/SnO_2}$, and in an enhancement of CO_2 reduction products production (CO and HCOOH from 36 % to 62 %).

4.2.3. Photoelectrochemical reduction of CO_2 using hybrid molecular $CuGaO_2$-based photocathodes

In this section the synthesis, characterization, and the study of the photoelectrochemical activity in the CO_2 reduction using molecular hybrid photocathodes was performed. The hybrid photocathodes include the vinyltrimethoxysilane (VTES) as linker, i) **Ru_{VLA}** + **Re_{CAT},** ii) **RuRe1** and iii) **RuRe2** molecular complexes immobilized by electropolymerization onto p-type $CuGaO_2$ semiconductor (Figure 13).

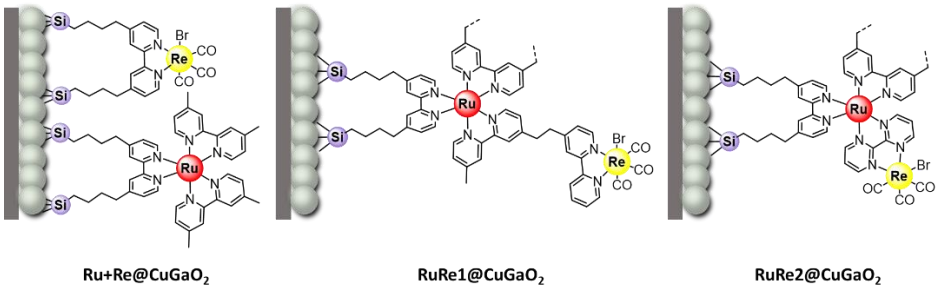

Figure 13: *Schematic representation of the three different photocathodes assemblies prepared in this part.*

4.2.3.1. $CuGaO_2$ synthesis, functionalization, and characterization

The synthesis of the $CuGaO_2$ was carried out using adapted literature procedures using a solid state reaction procedure by mixing an equimolar ratio of Cu_2O and Ga_2O_3.[17] X-ray diffraction analysis confirmed the delafossite structure of the $CuGaO_2$ without any obvious impurity. The diffraction pattern was in agreement with a typical delafossite structure with a hexagonal unit cell (Figure 14b).[29] Calculated unit cell parameters were 2.974 and 17.143 Å for a and c, respectively. The calculated crystallite size is 58.0 ± 1.1 nm. These values were in agreement with the JCPDS data (a = 2.977, c = 17.171 Å, JCPDS data base 77-2495) of $CuGaO_2$.[29] The FESEM image (Figure 14a) of the solid obtained displayed the surface morphology of the $CuGaO_2$ particles exhibiting

a few micrometers size with parallel lines on the surface. These results indicated a laminar structure. EDX analysis of the sample (Figure 14c) confirmed the average Cu:Ga:O molar ratio of 1:1:2.

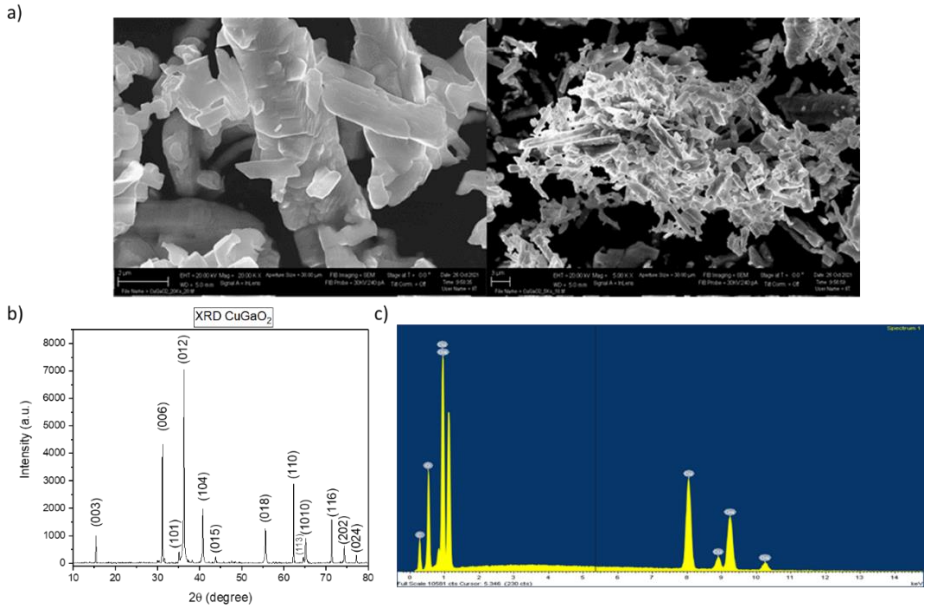

***Figure 14**: a) Scanning electron microscopy images captured for the $CuGaO_2$. b) X-ray diffraction analysis of $CuGaO_2$. c) Energy Dispersive X–ray (EDX) spectrum for the $CuGaO_2$.*

The synthesized $CuGaO_2$ was then functionalized with vinyltriethoxysilane. The synthesis was carried out by the addition of $CuGaO_2$ to a solution of isopropanol and vinyltriethoxysilane. The functionalized $CuGaO_2$ ($CuGaO_2$-VTES) catalyst was analyzed with FESEM-EDX (Figure 15). The results indicated that the morphology remained unchanged after functionalization, while, EDX analysis confirmed the presence of Si with an approximative Cu:Si molar ratio of 16:1.

a)

b)

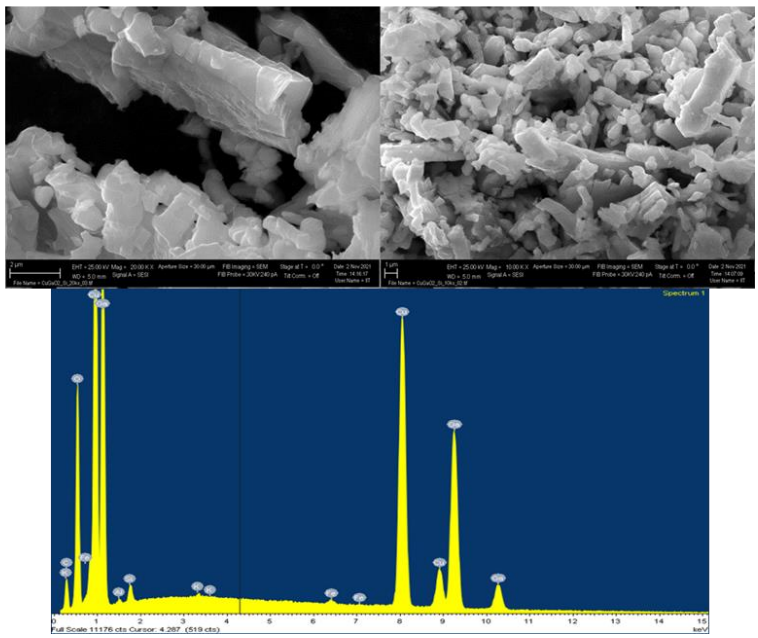

Figure 15: a) FESEM images and b) EDX analysis of $CuGaO_2$-VTES.

4.2.3.2. Preparation of RuRe@$CuGaO_2$ photocathodes

A different electrode preparation was performed for electrodes based on $CuGaO_2$ than those used for Cu_2O/SnO_2. In this case, first, electrodes were prepared by air-brushing of a catalytic ink of $CuGaO_2$-VTES onto a porous carbon support (Toray carbon paper 060, from FuelCellStore). Then, these electrodes were subjected to electropolymerization in presence of the corresponding molecular complex (Scheme 3).[18]

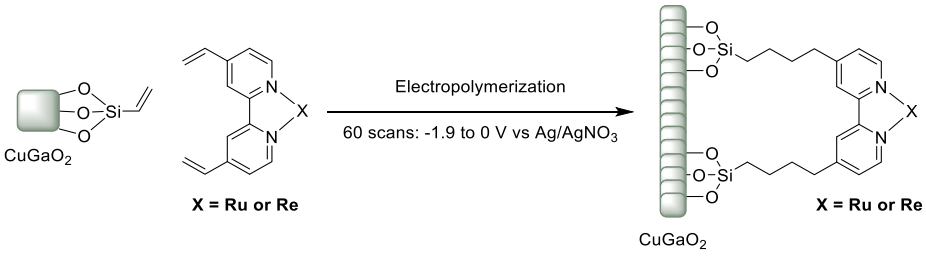

Scheme 3: Electropolymerization scheme using $CuGaO_2$-VTES powders.

The efficiency of the electropolymerization procedure was corroborated by monitoring the continuous enhancement of the current densities after each scan (Figure 16). This observation suggested the in-situ formation of polymeric layers onto the surface of the electrode. Furthermore, the presence of multiple vinyl groups in the diverse Ru and Re complexes probably resulted in a final layer-by-layer assembly of polymer. This protocol generated different combination of interconnected complexes with the obtention of a high molecular loading onto the surface of the electrodes.[18,19] Three different photoelectrodes were prepared by immobilization of three different homogeneous complexes onto the $CuGaO_2$-VTES: (i) Co-immobilization of Ru visible light absorber complex and Re CO_2 reduction catalyst complex (**Ru+Re@CuGaO₂**), (ii) Supramolecular Ru-Re complex (**RuRe1@CuGaO₂**) and (iii) binuclear Ru-Re complex (**RuRe2@CuGaO₂**).

The immobilization of the Ru and Re species onto the $CuGaO_2$-VTES was corroborated by FESEM-EDX analysis. Obtained semi-quantitative results suggested the anchoring of equimolar amounts of Ru and Re species for both supramolecular Ru-Re complexes. Whereas 2 moles of Re per mole of Ru were measured for the mixture of homogenous complexes (Table 2). FESEM-EDX images also displayed random homogeneous dispersions of Ru and Re species on the $CuGaO_2$ support (see SI).

Chapter 4

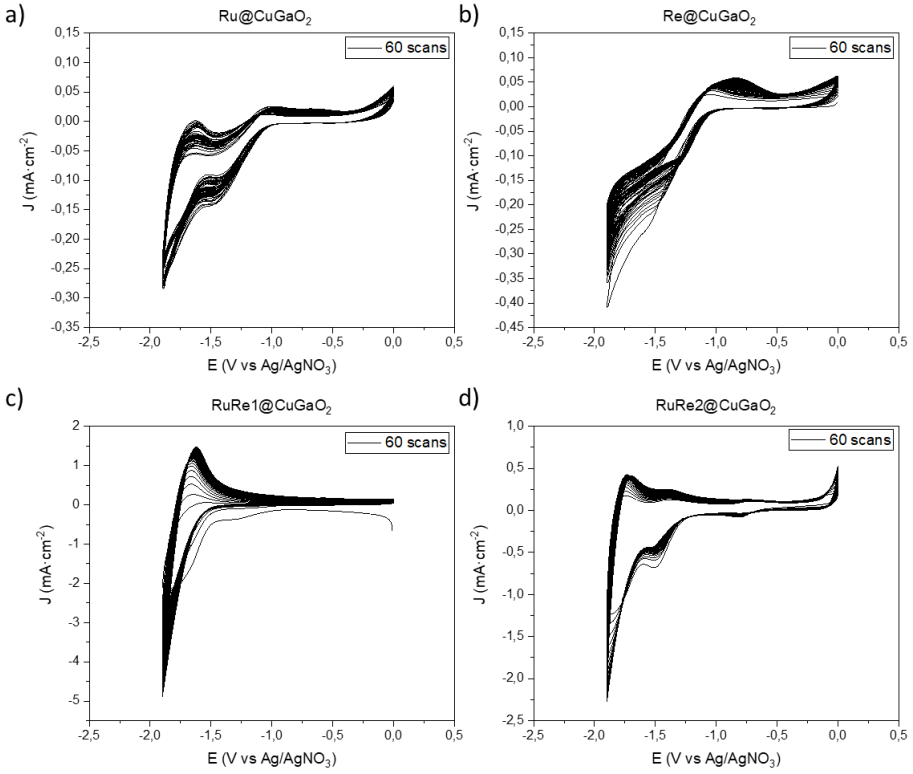

***Figure 16**: Cyclic voltammogram graphics of a) Electropolymerization of the **Ru_{VLA}** complex b) Electropolymerization of the **Re_{CAT}** complex. c) Electropolymerization of the **RuRe1** complex d) Electropolymerization of the **RuRe2** complex. All the CV are performed from 0 to -1.9 V vs $Ag/AgNO_3$ in an acetonitrile solution containing 0.1 M $TBA{\cdot}PF_6$ and 0.5 mM of the corresponding complex.*

***Table 2**: Average of approximated molar ratios and approximated amounts of Ru and Re onto the surface of the electrode analyzed by EDX.*

Electrode	Ratio Cu:Ru ($\mu mol_{Ru}{\cdot}cm^{-2}$)	Ratio Cu:Re ($\mu mol_{Re}{\cdot}cm^{-2}$)	Ratio Ru:Re
Ru+Re@$CuGaO_2$	39:1 (0.155)	19:1 (0.318)	1:2
RuRe1@$CuGaO_2$	1.6:1 (3.78)	1.5:1 (4.03)	1:1.1
RuRe2@$CuGaO_2$	26:1 (0.233)	23:1 (0.263)	1:1.1

Estimations of the relative amount of Ru and Re immobilized respect to the Cu content in the support are calculated to assess the efficiency of the anchoring approach. The approach used in the present work allowed a higher immobilization of the **RuRe1** complex than that of the **RuRe2** complex. Moreover, FESEM images, evidenced the presence of agglomerations in the hybrid electrode containing the **RuRe1** molecular complex. (see FESEM images Figure 17).

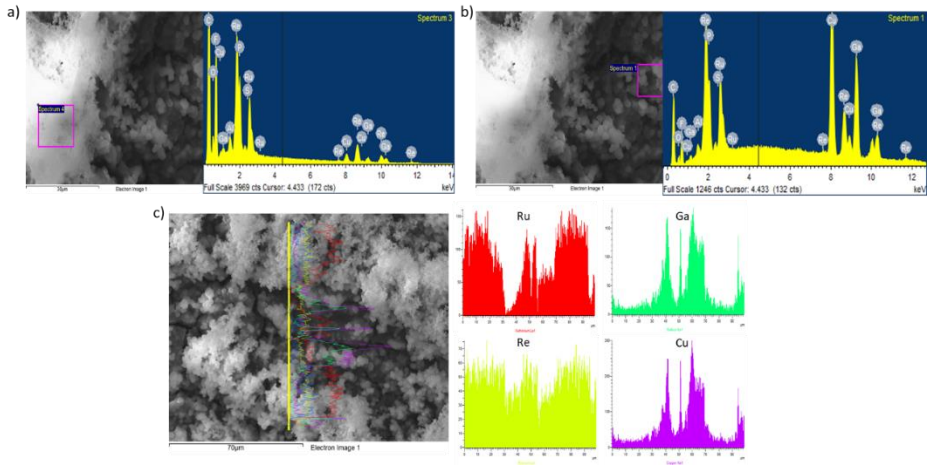

***Figure 17**: FESEM images and EDX analysis of the **RuRe1@CuGaO$_2$** electrode. a) EDX analysis of a region in the agglomeration. b) EDX analysis of a region without agglomeration. c) Line scanning EDX analysis.*

The region containing the agglomeration (Figure 17a) was analyzed by EDX. EDX results revealed a higher content in Ru and Re (Figure 17b) and confirmed that the agglomeration consists in **RuRe1** supramolecular complexes interconnected between them. The line scanning EDX (Figure 17c) performed in both regions, agglomerated and non-agglomerated ones, also confirmed the presence of Ru and Re higher content in the agglomerated regions than in the non-agglomerated ones. Since the **RuRe1** complex contains four anchoring groups, the coupling between molecular complexes could explain the agglomerations formation and the observed high Ru and Re contents.

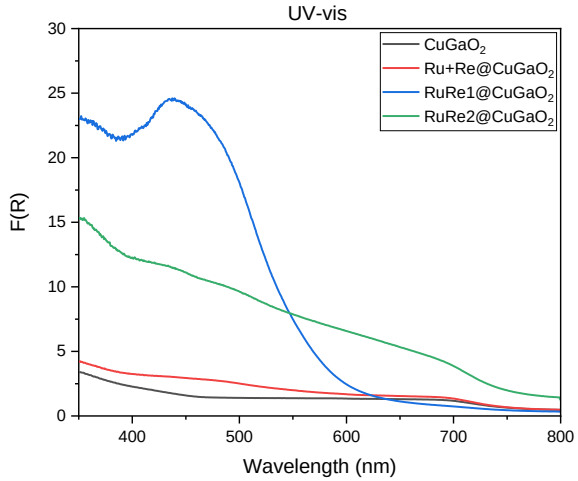

***Figure 18**: Diffuse-Reflectance UV-visible absorption spectrum of the prepared electrodes. (F(R) = (1−R)²/2R: Kubelka-Munk function).*

UV-visible absorption spectra of all the prepared electrodes are measured in the diffuse reflectance mode (Figure 18). The UV-vis spectrum of the bare $CuGaO_2$ indicated no absorption in the visible range.[29,30] However, a different behavior was observed with hybrid photocathodes bearing Ru and Re complexes. Indeed, the electrode containing the molecular $\mathbf{Ru_{VLA}}$ and $\mathbf{Re_{CAT}}$ complexes immobilized separately exhibited a small absorption band which started at λ = 550 nm. Instead, the electrode containing **RuRe1** showed a large absorption band starting at λ = 600 nm, and the **RuRe2** showed an absorption band in all the visible light spectrum. These results were in concordance with previous reports where a characteristic peak appeared in the UV spectrum around 464 nm. This band was attributed to the singlet metal-to-ligand-charge-transfer absorption band of the Ru complex.[19]

4.2.3.3. Photoelectrochemical characterization of $CuGaO_2$

In the literature there is a discussion on the activity of $CuGaO_2$ in the CO_2 reduction reaction.[17,30] Photoelectrochemical and electrochemical properties

of the bare $CuGaO_2$ were studied under dark conditions and under simulated sunlight irradiation. Current-potential curves (Figure 19a) showed a difference in the current between the dark and light conditions. This result indicated that the $CuGaO_2$ was photocatalytically active under sunlight irradiation in an acetonitrile 0.3 M BMI·TfO solution saturated with CO_2. Indeed, from -0.3 to -1.2 V *vs*. Ag/AgCl a difference in the current density value of about 19 $\mu A \cdot cm^{-2}$ between dark and light irradiation was observed.

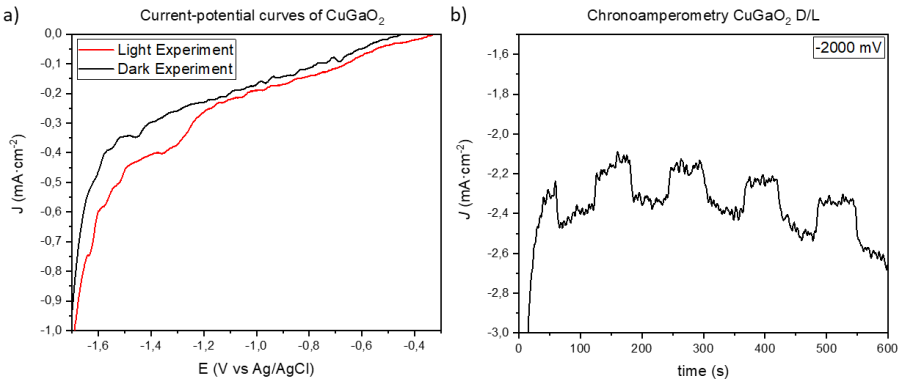

***Figure 19**: a) Current-potential curves of the synthetized $CuGaO_2$ sample with and without simulated sunlight irradiation under CO_2 saturated 0.3 M BMI·TfO acetonitrile solution. b) Dark/light chronoamperometry of $CuGaO_2$ performed at -2.0 V vs Ag/AgCl under the same conditions of a).*

A chopped dark/light chronoamperometry performed at -2.0 V (Figure 19b) confirmed the $CuGaO_2$ photoactivity. This experiment showed an average photocurrent contribution of -0.195 $mA \cdot cm^{-2}$.

4.2.3.4. Photoelectrochemical reduction of CO_2 using the $CuGaO_2$ photocathode

Effects of light and current intensity on the CO_2 reduction performance are investigated on $CuGaO_2$ by performing a current screening under both light and dark conditions and analyzing the gas and liquid products in each experiment. Short chronopotentiometry experiments of 30 min were

performed. Based on the cyclic voltammetry (Figure 20), different current intensities were applied, specifically -0.2, -1.5, -3, -6, -10 and -20 mA·cm^{-2}, in order to monitor the formation of CO_2 reduction products in each experiment.

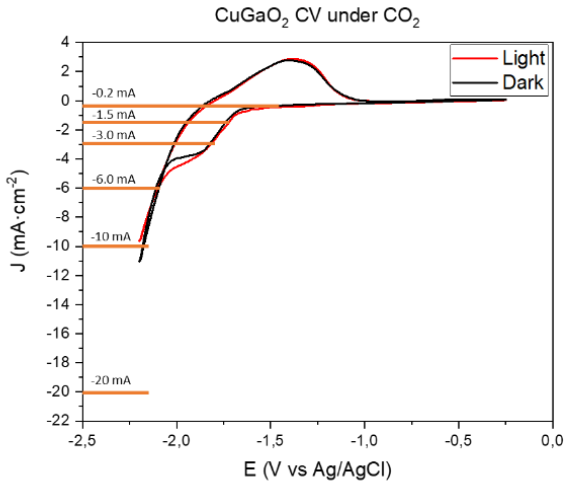

***Figure 20**: Cyclic voltammetry graphic of $CuGaO_2$ in an acetonitrile 0.3M BMI·TfO solution CO_2 saturated with (red) and without (black) simulated sunlight irradiation.*

As can be observed in Figure 21, a significant difference was highlighted between dark and light conditions. Under dark conditions, a major selectivity towards CO_2 reduction products and a Faradaic efficiency to H_2 lower than 10 % were obtained. In contrast, under simulated sunlight irradiation conditions, a substantial increase in hydrogen production was observed. In both cases, the total Faradaic efficiency decreased when higher current densities were applied. This behavior was attributed to the instability of the catalyst, i.e., self-reduction of the $CuGaO_2$.[26]

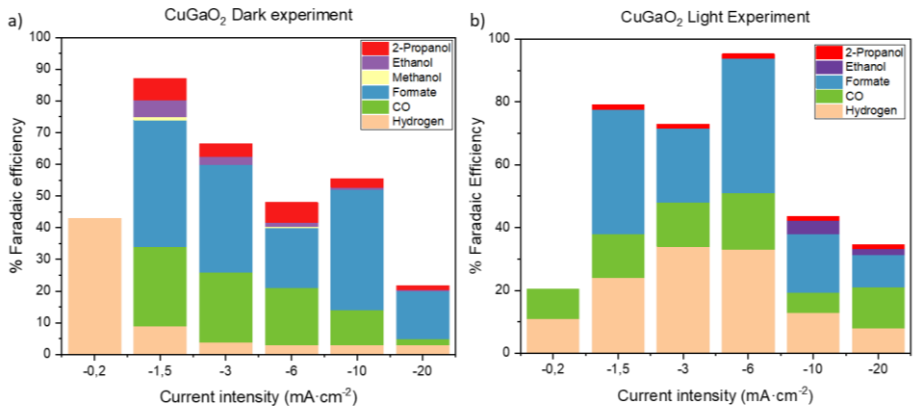

***Figure 21**: Faradaic efficiencies of gas and liquid products produced in 30 min chronopotentiometry measurements at different current intensities on $CuGaO_2$ electrodes in a CO_2 saturated 0.3 M BMI·TfO acetonitrile solution. a) Experiment without simulated sunlight irradiation. b) Experiment under simulated sunlight irradiation.*

Under both dark and light conditions, formate was the major CO_2 reduction product, followed by CO. Small quantities of propanol, ethanol, and methanol were also detected. The production of CO and H_2 was monitored during the experiment and was stable during the time of chronopotentiometry.

Figure 22 shows the comparison of chronopotentiometry measurements between dark and light conditions. These chronopotentiometries performed at the same current intensity under visible light irradiation (dashed line) and in dark (solid line) revealed a difference in the corresponding potential values. In general, lower potential values (in absolute values) were measured under light conditions than in dark conditions. However, the opposite behavior was observed when the chronopotentiometry was performed at -10 and -20 $mA \cdot cm^{-2}$.

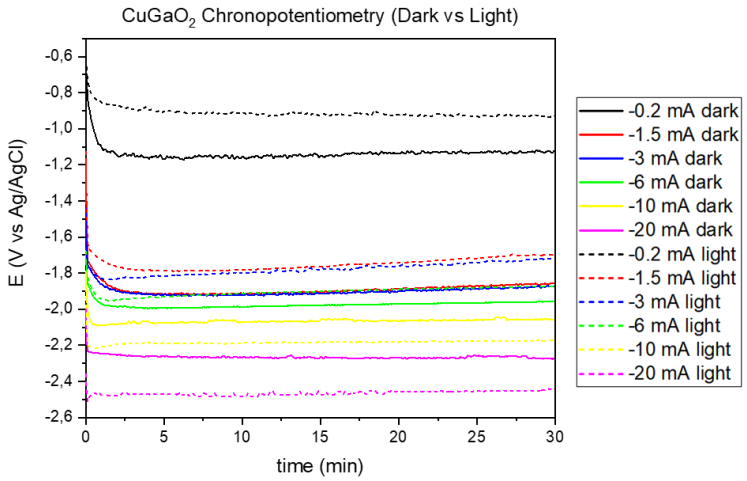

***Figure 22**: Chronopotentiometry curves applying different current intensities under light irradiation (dashed line) and in dark (solid line) on $CuGaO_2$ electrodes in a CO_2 saturated 0.3 M BMI·TfO acetonitrile solution. Colors are the same for the chronopotentiometries performed at the same current intensity.*

Chronopotentiometry (CP) experiments for 120 minutes were performed in the dark and under visible light irradiation by applying -1.5 $mA \cdot cm^{-2}$ to evaluate the stability of CO_2RR over time with the $CuGaO_2$ bare material. During the initial stages of the reaction, CO was the main product. Later, the CO production decreased under both dark and light conditions (Figure 23). When the experiment was performed in the dark, a constant decrease of CO selectivity was observed along with a constant H_2 production. Under light irradiation, the CO production decreased more rapidly with a constant increase of H_2 production, after 40 min the H_2 became the main product. The results obtained showed that the total Faradaic efficiencies were higher in the dark (FE_{total} = 70.7 % in the dark vs 52.4 % under light), and confirmed the quick deactivation of the bare $CuGaO_2$ under light irradiation. These results were in agreement with previously reported data.[30]

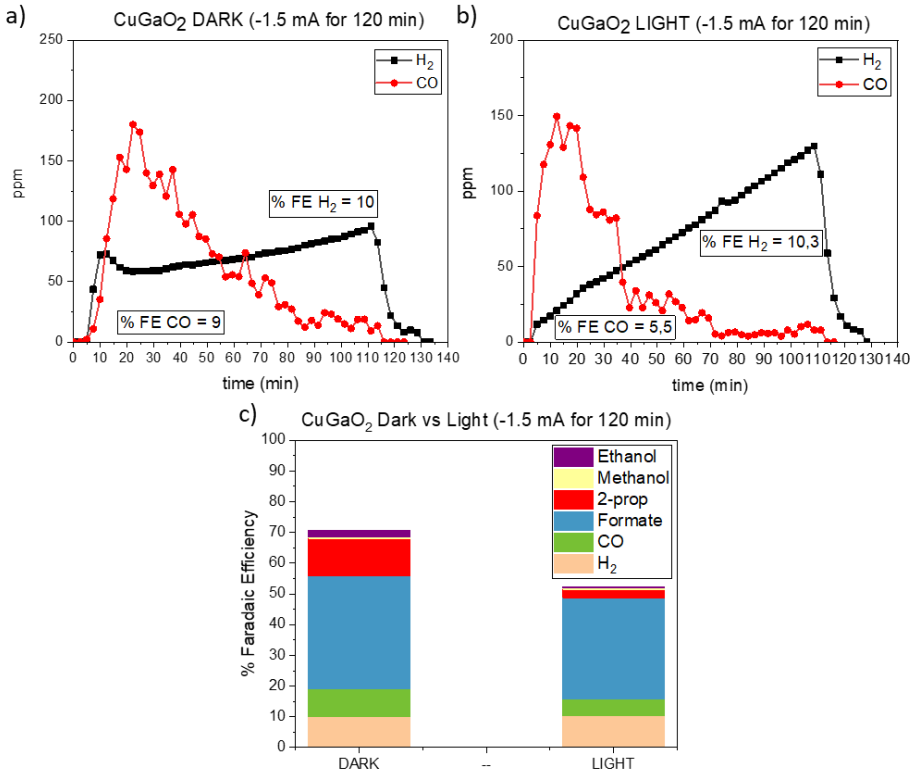

***Figure 23**: Chronopotentiometry performed at -1.5 mA·cm^{-2} for 120 min in acetonitrile 0.3 M BMI·TfO solution saturated with CO_2. a) CO and H_2 production under dark conditions. b) CO and H_2 production under light conditions. c) Faradaic efficiencies under dark and light conditions.*

4.2.3.5. Photoelectrochemical properties of Ru+Re@$CuGaO_2$

Photoelectrochemical properties of the prepared $CuGaO_2$ electrode bearing the mixture of the **Ru_{VLA}** and **Re_{CAT}** (**Ru+Re@$CuGaO_2$**) were studied and compared with those of the bare $CuGaO_2$ electrode. These experiments were performed using simulated sunlight irradiation in an acetonitrile solution containing 0.3 M of BMI·TfO and saturated with CO_2. Current-potential curves (Figure 24a) showed a difference in the current response between dark and light conditions. Interestingly, **Ru+Re@$CuGaO_2$** exhibited an approximate current difference of 32 µA·cm^{-2}. This value constituted a higher photo-response than that measured with the bare $CuGaO_2$ (19 µA·cm^{-2}). This result

suggested that this higher photocurrent was induced by the injection of electrons from the $CuGaO_2$ to the Ru photosensitizer.

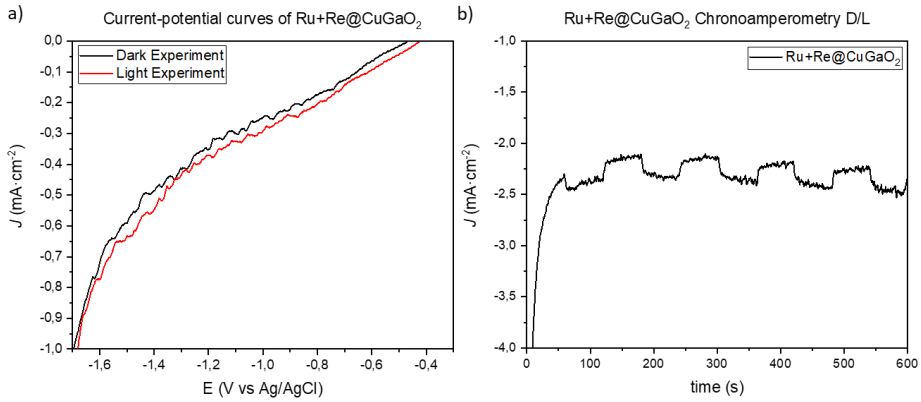

***Figure 24**: a) Current-potential curves of the synthesized **Ru+Re@CuGaO₂** with and without light irradiation. b) Dark/light chronoamperometry of **Ru+Re@CuGaO₂** electrode performed at -2.0 V vs Ag/AgCl in a CO_2 saturated 0.3 M BMI·TfO in acetonitrile solution.*

A dark/light chronoamperometry performed at -2.0 V (Figure 24b) confirmed the activity under light irradiation of the **Ru+Re@CuGaO₂** photocathode. This experiment showed an average photocurrent contribution of -0.204 $mA \cdot cm^{-2}$ in a CO_2 saturated 0.3 M BMI·TfO acetonitrile solution. A comparison between Figure 19b and Figure 24b evidenced that the two photoelectrodes provided similar average photocurrent contributions at this fixed potential value. Nonetheless, the **Ru+Re@CuGaO₂** displayed a more stable behavior over time.

4.2.3.6. Photoelectrochemical reduction of CO_2 using the Ru+Re@CuGaO₂ photocathode

The selectivity of the **Ru+Re@CuGaO₂** electrode for the CO_2RR was evaluated under simulated sunlight irradiation. As for the bare $CuGaO_2$, short chronopotentiometries experiments of 30 min were performed at different constant current densities: -0.2, -1.5, -3, -6, -10 and -20 $mA \cdot cm^{-2}$, respectively. These results are displayed in Figure 25.

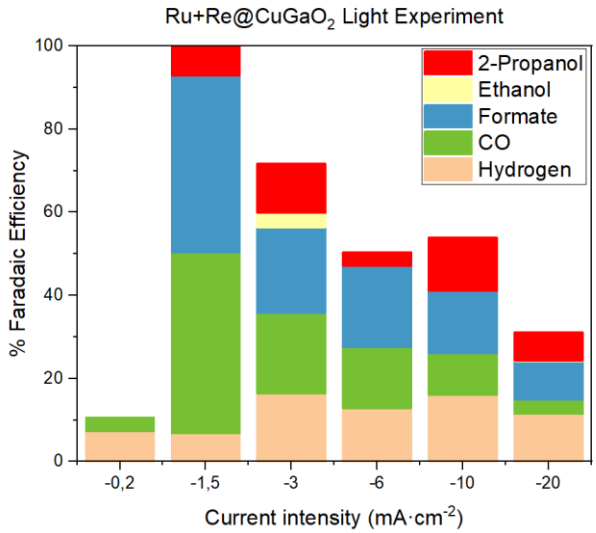

***Figure 25**: Faradaic efficiencies of gas and liquid products produced in a 30 min chronopotentiometry at different current intensities in an acetonitrile 0.3 M BMI·TfO solution saturated with CO_2 under simulated sunlight irradiation with the **Ru+Re@CuGaO₂** electrode.*

In general, the formation of CO_2 reduction products was enhanced by the immobilization of Ru and Re molecular complexes onto the $CuGaO_2$ semiconductor. More specifically, at current density values lower than -10 $mA{\cdot}cm^{-2}$, the H_2 production was reduced and the formation of CO_2 reduction products was increased. It should be noted that the **Ru+Re@CuGaO₂** electrode displayed a total faradaic efficiency of 99.8 % at -1.5 $mA{\cdot}cm^{-2}$, and a FE_{H2} of only 6.8 %. A detrimental effect was evidenced at more negative currents with a clear decrease in the total FE. This observation could be due to the catalyst modification under those conditions. In view of these results, the current value of -1.5 $mA{\cdot}cm^{-2}$ was selected for conducting subsequent analyses.

Next, the effect of the reaction medium was evaluated. Reactions were carried in three different CO_2 saturated solutions: (i) 0.3 M BMI·TfO in acetonitrile. This solution was selected in view of the good results obtained using this IL in some recent studies,[7–9] (ii) 0.3 M TBA·PF_6 in acetonitrile. This solution was

selected to compare the use of an IL to that of a simple quaternary ammonium salt[31,32] and (iii) aqueous solution of 0.1 M $KHCO_3$. This solution was selected to compare the organic *vs.* aqueous electrolyte; specifically, the $KHCO_3$ based electrolyte was selected as a typical aqueous electrolyte.[33]

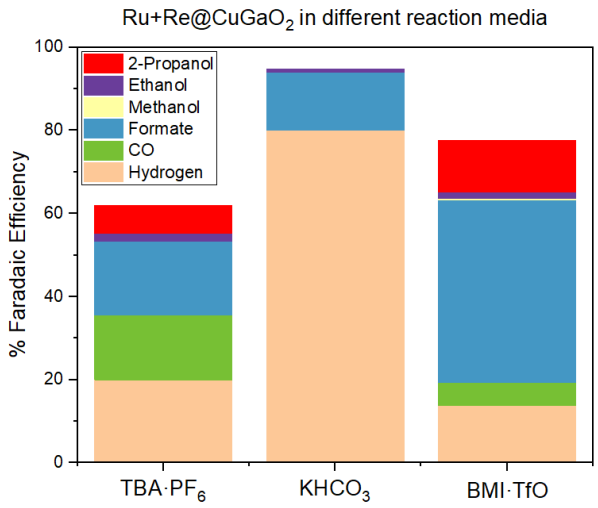

***Figure 26**: Faradaic efficiencies of gas and liquid products produced in a 120 min chronopotentiometry at -1.5 mA·cm^{-2}, under continuous simulated sunlight irradiation, using different electrolytes, 0.3 M TBA·PF_6 in acetonitrile, 0.1 M $KHCO_3$ in H_2O and 0.3 M BMI·TfO in acetonitrile, all saturated with CO_2.*

In aqueous media, a constant H_2 production was obtained with a total FE of 80 % and a FE to formate (the main CO_2RR product) of 14 % (Figure 26). In contrast, in organic media (acetonitrile solution of BMI·TfO or TBA·PF_6), higher selectivities to CO_2 reduction products are obtained, and formate was the major product. This selectivity shift may be explained by the low solubility of CO_2 in aqueous solution, whereas ILs acted as a strong CO_2 absorption medium, and enhanced the selectivity to the CO_2 reduction products by decreasing mass transfers limitations.[6] Interestingly, other than the commonly produced C_1 reduction products, C_{2+} products like ethanol and propanol were also promoted in the organic solvents, and in particular with the IL electrolyte. This suggested a role of the imidazolium and ammonium-based electrolytes as

co-catalysts that may also influenced the CO_2RR reaction mechanism. Indeed, C_{2+} products formation required the presence of adsorbed CO (CO*) and CHx (CHx*) intermediates, which reacted by CO*-CO*dimerization or CO*-CHx* coupling at the catalyst surface.[34]

Comparing the chronoamperometry curves, the experiments with aqueous solution of 0.1 M $KHCO_3$ and acetonitrile 0.3 M BMI·TfO as electrolytes revealed stable voltages of -1.6 V and -1.9 V vs Ag/AgCl, respectively (Figure 27a). Whereas the use of acetonitrile 0.3 M TBA·PF_6 as electrolyte resulted in a variation of the voltage along the potential window from -1.8 V to -1.6 V. It should be highlighted that the potential associated to the experiments seemed to correlate with the product selectivity, since high hydrogen faradaic efficiencies and low formate faradaic efficiencies were achieved in aqueous solution of 0.1 M $KHCO_3$ at -1.6 V, whereas the opposite trend was observed using acetonitrile 0.3 M BMI·TfO as electrolyte at -1.9 V. In the case of acetonitrile 0.3 M TBA·PF_6 as electrolyte, the selectivity varied with the potential along the experiment. In fact, considering the H_2 and CO production during the test, in presence of TBA·PF_6 (Figure 27b), the CO production decreased severely after 40 min with a concomitant increase of the hydrogen production.

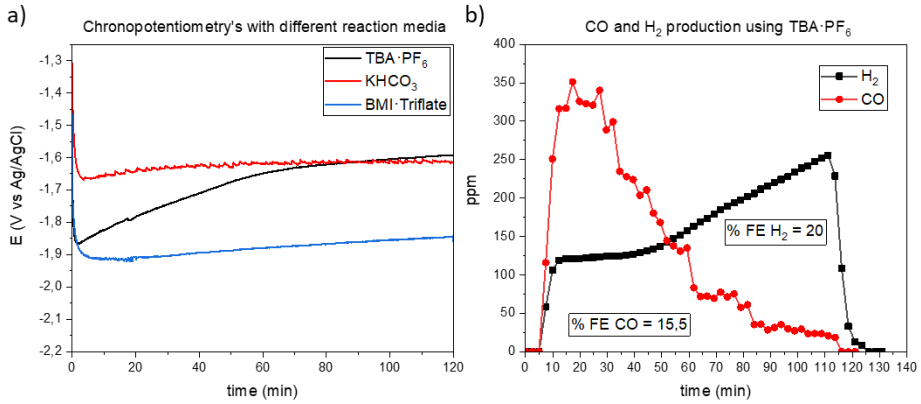

***Figure 27**: a) 120 min chronopotentiometry using the **Ru+Re@CuGaO$_2$** catalyst applying -1.5 mA·cm^{-2} under simulated sunlight irradiation in a CO_2 saturated solution using different reaction media. b) CO and H_2 production during the 120 min chronopotentiometry using the **Ru+Re@CuGaO$_2$** catalyst at -1.5 mA·cm^{-2} under the same conditions of a).*

Based on these results, the 0.3 M BMI·TfO in acetonitrile was selected as electrolyte to study the immobilization of the different molecular complexes synthesized onto the $CuGaO_2$ semiconductor.

4.2.3.7. Ru and Re complex effect on the photoelectrochemical reduction of CO_2 in ionic liquid

The current-potential curves under dark and light irradiation for the **RuRe1@CuGaO$_2$** and **RuRe2@CuGaO$_2$** materials are displayed in Figure 28.

In both cases, differences in the current response between dark and light conditions are observed (Figure 28). Slight differences on the measured photocurrent were observed for the electrodes containing the supramolecular complexes. The **RuRe1@CuGaO$_2$** provided an average photocurrent of 36 µA·cm^{-2}, and the **RuRe2@CuGaO$_2$** shown a value of 37 µA·cm^{-2}, from -0.4 to -1.2 V vs Ag/AgCl. However, both electrodes exhibited a higher photoactivity than the **Ru+Re@CuGaO$_2$** (with an average photocurrent of 32 µA·cm^{-2} from -0.4 to -1.2 V vs Ag/AgCl).

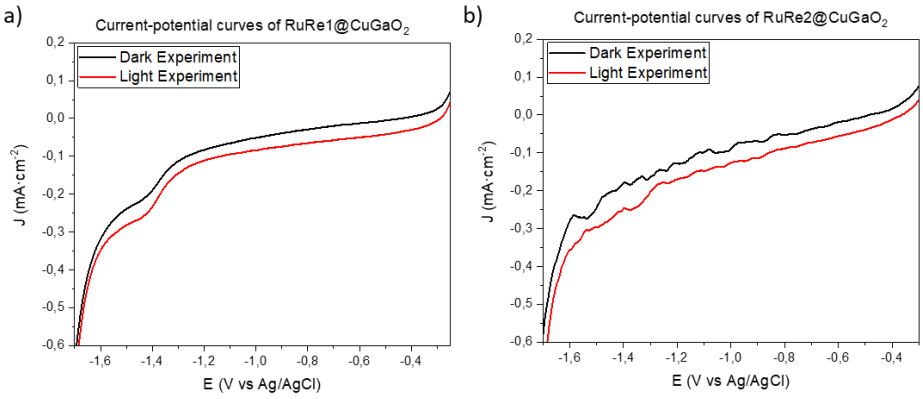

***Figure 28**: Current-potential curves with and without light irradiation under CO_2 saturated 0.3 M BMI·TfO acetonitrile solution of the a) **RuRe1@CuGaO₂** electrode and b) **RuRe2@CuGaO₂** electrode.*

Nevertheless, when a dark/light chronoamperometry at -2.0 V was performed (Figure 29), the electrodes containing the supramolecular complexes showed a lower average photocurrent contribution, -0.156 (**RuRe1@CuGaO₂**) and -0.150 mA·cm^{-2} (**RuRe2@CuGaO₂**) than the **Ru+Re@CuGaO₂** electrode, -0.204 mA·cm^{-2}.

Chapter 4

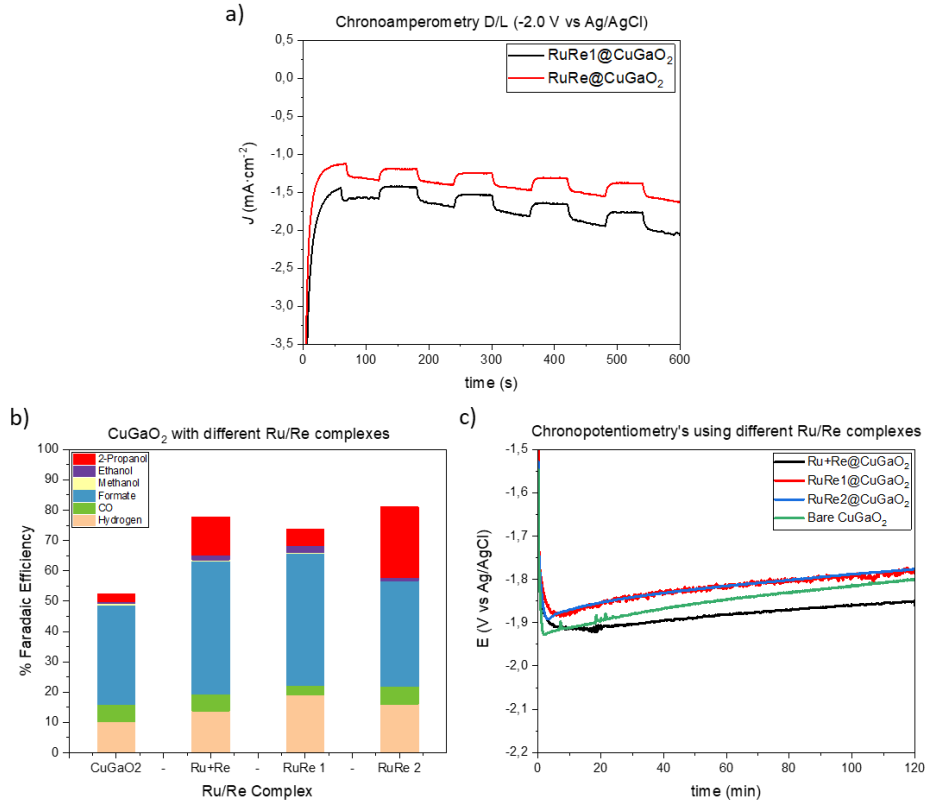

***Figure 29**: a) Dark/light chronoamperometry of **RuRe1@CuGaO₂** (red line) and **RuRe2@CuGaO₂** (blue line) performed at -2.0 V vs Ag/AgCl in an acetonitrile 0.3 M BMI·TfO saturated with CO_2. b) Faradaic efficiencies of gas and liquid products produced in 120 min chronopotentiometry tests at -1.5 mA·cm^{-2}, under continuous simulated sunlight irradiation in an acetonitrile 0.3 M BMI·TfO CO_2 saturated solution using different Ru and Re complexes. c) 120 min chronopotentiometry recorded curves applying -1.5 mA·cm^{-2} under the same conditions of b) using different Ru and Re complexes*

Subsequently, the effect of the different Ru/Re complexes on the CO_2 photoelectroreduction selectivity was evaluated during a 120 min chronopotentiometry by applying -1.5 mA·cm^{-2} under simulated sunlight conditions. In Figure 29b, the Faradaic efficiencies of the gaseous and liquid products for each catalyst at that current density value are displayed. Using the bare $CuGaO_2$ electrode, a low total Faradaic efficiency was obtained (52 %). Hybrid photocathodes displayed an increase in the faradaic efficiency up

to 81 %. These results evidenced the protective and stabilizing role of the Ru and Re complexes that hinder the $CuGaO_2$ modification. Among them, similar faradaic efficiencies for H_2 and CO_2RR products were obtained. However, with the **RuRe1** and **RuRe2** complexes, lower external potentials were necessary at the same current intensity. This observation evidenced a higher generated photovoltage and a more efficient electron transfer provided by photocathode bearing the supramolecular system rather than immobilizing separately $\mathbf{Ru_{VLA}}$ and $\mathbf{Re_{CAT}}$ complexes (Figure 29c). This behavior was in agreement with their superior UV-vis light absorption. Using these hybrid materials, higher faradaic efficiencies to formic acid are obtained compared with that of the bare $CuGaO_2$, ca. 45 % vs. 30 %, respectively. Interestingly, ethanol and propanol production were enhanced by the hybrid materials, and in particular, by the binuclear **RuRe2** complex. As previously mentioned, such results highlighted the role of the Ru and Re complexes in co-catalyzing the multi-electron processes. These processes are subsequent to the formate and CO formation at the catalyst surface.

Moreover, the hybrid materials synthesized in this work not only enhanced the faradaic efficiency of the process but also showed higher stability than the bare $CuGaO_2$. Finally, the stability of the hybrid materials was corroborated by analyzing the electrodes after the CP experiments by FESEM-EDX. A similar morphology of the hybrid materials was observed after the CPs. This result indicated a positive effect of the immobilization of the molecular complexes (see SI). Additionally, semi-quantitative EDX results suggested similar loading of the Ru and Re species before and after the CP experiments, thus confirming the stability of these systems under the reported reaction conditions (Table 3).

***Table 3**: Average of approximated molar ratio and approximated Ru and Re amounts onto the surface of the electrode analyzed by EDX before and after the CP experiments.*

Electrode	Ratio Cu:Ru (Before/After)	Ratio Cu:Re (Before/After)	Ratio Ru:Re (Before/After)
Ru+Re@CuGaO$_2$	39:1 / 40:1	19:1 / 22:1	1:2 / 1:1.8
RuRe1@CuGaO$_2$	1.6:1 / 2.3:1	1.5:1 / 2.5:1	1:1.1 / 1:1.1
RuRe2@CuGaO$_2$	26:1 / 33:1	23:1 / 43:1	1:1.1 / 1:1.3

4.2.3.8. Conclusions

Three different hybrid materials were prepared with the synthesized molecular complexes, and their photoelectrocatalytic CO_2 reduction performances were tested in different electrolytes.

The electropolymerization process was used, for the first time, for the immobilization of supramolecular Ru-Re complexes on VTES-modified $CuGaO_2$. A comparison of the co-immobilization procedure of the separate **Ru$_{VLA}$** and **Re$_{CAT}$** complexes with the supramolecular **RuRe1** and the binuclear **RuRe2** complexes demonstrated an enhanced photovoltage generation and electron transfer for the photocathodes containing these supramolecular and binuclear complexes.

The potential of this approach for anchoring molecular complexes onto $CuGaO_2$ photo-electrocatalyst to boost, both, its carriers transport and catalytic activity, with respect to the bare semiconductor material was shown.

Furthermore, various electrolytes were evaluated, and the use of ionic liquids was demonstrated to enhance both, the CO_2 reduction selectivity (by suppressing the H_2 evolution reaction) and the stability of the photo-electrocatalytic performance. The combination of the use of IL and the hybrid materials at the photocatalyst surface increased the semiconductor stability towards its restructuration, which resulted in a 30 % increase of the total

faradaic efficiency *vs.* the bare $CuGaO_2$, and in an enhancement of the formic acid production (from 30 % to 45 %) as well as C_{2+} alcohols formation, suppressing the H_2 production.

Further investigations will be devoted for the elucidation of the role of these supramolecular and binuclear complexes, and of the IL, in co-catalyzing multi-electron CO_2 reduction reaction pathways under photo-electrochemical conditions.

4.3. Conclusions

As general conclusions, a series of four new molecular complexes containing a vinyl group as coupling agent was successfully synthesized and characterized.

The different molecular complexes were immobilized onto a VTES modified Cu_2O/SnO_2 or $CuGaO_2$ semiconductor showing higher molecular loadings using the $CuGaO_2$-VTES pathway which consisted in two steps: first, preparation of the electrodes with the $CuGaO_2$ powder, and second step, electropolymerization.

In general, the hybrid photocathodes displayed an enhancement of carriers transport and catalytic activity respect to the bare semiconductor. The co-immobilized complexes resulted in better performances compared to the immobilization of only the $\mathbf{Re_{CAT}}$ or $\mathbf{Ru_{VLA}}$. Higher photovoltage generation and electron transfer was obtained with photocathodes bearing supramolecular **RuRe1** and the binuclear **RuRe2** complexes compared with the photocathodes obtained by co-immobilization procedure of the separate $\mathbf{Ru_{VLA}}$ and $\mathbf{Re_{CAT}}$ complexes.

Finally, various electrolytes were evaluated observing that the ionic liquids-based electrolytes displayed an enhancement of both the CO_2 reduction selectivity (by suppressing the H_2 evolution reaction) and the stability of the system. Reaction performed using this electrolyte resulted in a up to 30 % increase of the total faradaic efficiency *vs*. the bare semiconductor and an enhancement of the CO_2 reduction products production (CO, HCOOH and C_{2+} alcohols).

4.4. Experimental part

4.4.1. General considerations

Reagents: Commercially available reagents and solvents were purchased at the highest commercial quality from Sigma-Aldrich, Fisher scientific, Alfa Aesar and were used as received, without further purification, unless otherwise stated.

Analytical methods: ^{1}H, and $^{13}C\{^{1}H\}$ NMR spectra were recorded using a Varian Mercury VX 400 (400 and 100.6 MHz respectively). Chemical shift values (δ) are reported in ppm relative to residual solvent peak (^{1}H and $^{13}C\{^{1}H\}$), and coupling constants are reported in Hertz. The following abbreviations are used to indicate the multiplicity: s, singlet; d, doublet; t, triplet; q, quartet; m, multiplet; bs, broad signal.

High-resolution mass spectra (HRMS) of the synthetized molecular complexes were recorded on an Agilent Time-of-Flight 6210 using ESI-TOF (electrospray ionization-time of flight). Samples were introduced to the mass spectrometer ion source by direct injection using a syringe pump and were externally calibrated using sodium formate. The instrument was operating in the positive ion mode.

Fourier transform infrared spectroscopy (FT-IR) spectra of the synthetized molecular complexes were obtained by using a Bruker Vertex-70 instrument with Attenuated Total Reflectance (ATR) sample holder by acquiring 16 cumulative scans with resolution of 4 cm^{-1} from 4000 to 400 cm^{-1}.

Ultraviolet-visible (UV-Vis) absorption spectra (350 nm to 800 nm) of the synthetized molecular complexes were recorded of the synthetized molecules in standard solutions 30 mg/L in dichloromethane. Analyses were carried out

using quartz cuvette with 1 cm of optical path using a UV-1800 Shimadzu apparatus.

Reactions were monitored by TLC carried out on 0.25 mm E. Merck silica gel 60 F254 glass or aluminum plates. Developed TLC plates were visualized under a short-wave UV lamp (254 nm) and by heating plates that were dipped in potassium permanganate. Flash column chromatography was carried out using forced flow of the indicated solvent on Merck silica gel 60 (230-400 mesh).

Physicochemical properties of $CuGaO_2$ catalysts and prepared electrodes were analyzed by X-Ray Diffraction (XRD, Panalytical X'Pert PRO diffractometer) and Field Emission Scanning Electron Microscopy (FESEM) with Energy Dispersive X-ray Spectroscopy (ZEISS Auriga, equipped with an OXFORD X-MAX EDS detector). Electrodes were analyzed before and after the CO_2RR tests to confirm the presence of Ru and Re and to determine the morphology and approximated composition. UV-Vis reflectance spectra ($F(R) = (1-R)^2/2R$: Kubelka-Munk function) of prepared electrodes were collected with a spectrophotometer (Varian Cary 5000 spectrophotometer).

4.4.2. Photoelectrochemical measurements

Photoelectrochemical (PEC) measurements were performed in an H-type cell (made in quartz) with a three-electrodes configuration. In a typical test, the anodic chamber was equipped with 28 mL of a 0.1 M KOH aqueous solution and a Pt mesh as counter electrode. The cathodic chamber was instead equipped with 50 mL of 0.3M BMI·TfO acetonitrile solution, 0.1M $KHCO_3$ aqueous solution or 0.3M TBA·PF_6 acetonitrile solution (electrolyte specified in each experiment), an Ag/AgCl (KCl sat.) as reference electrode and a $CuGaO_2$-based electrode as working electrode. The cathodic and anodic chambers were separated by a Fumasep® FBM bipolar exchange membrane

(from FUMATECH BWT GmbH). Prior to each measurement, the electrolyte solution was purged for 20 mins with a nitrogen (N_2) flow rate of 20 mL/min to remove the oxygen present in the solution. Afterwards, the solution was saturated for 20 min under a CO_2 flow rate of 20 mL/min. During the experiments, a constant CO_2 flow rate of 20 mL/min was maintained.

PEC measurements were carried out with a Voltalab potentiostat (from Radiometer Analytical SAS). Linear sweep voltammetry (LSV) and cyclic voltammetry curves were recorded in dark and under continuous or chopped simulated solar light illumination conditions, in the range between -0.20 and -2.2 V vs Ag/AgCl (KCl sat.) (with a sweep rate of 20 $mV \cdot s^{-1}$). Chronoamperometry (CA) measurements were performed at -2.0 V vs Ag/AgCl (KCl sat.) over 1 min dark and 1 min simulated irradiation intervals. Chronopotentiometry (CP) measurements were performed both in dark and under continuous simulated solar light irradiation conditions by using a Newport 450 W Xe lamp equipped with an AM 1.5G filter. The H-type cell was illuminated from the cathodic side maintaining the intensity of the light at 1000 $W \cdot m^{-2}$ by adjusting the distance between the light source and the PEC cell.

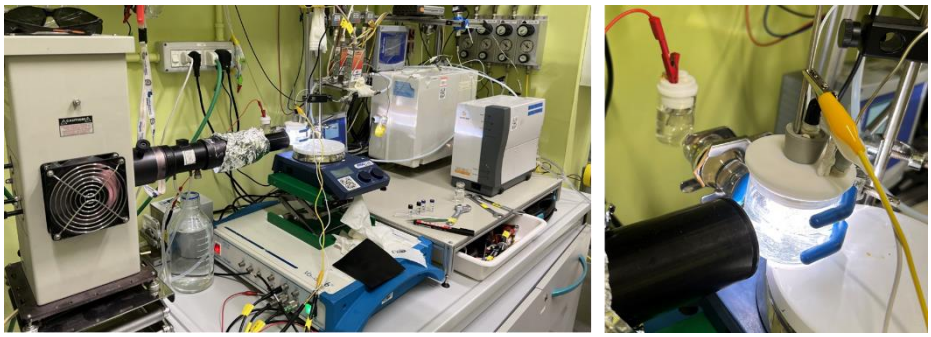

***Figure 30**: Image of the set-up used to perform the CO_2 reduction tests*

Gas products (H_2 and CO) were determined continuously during all the experiments using a micro gas-chromatograph (Varian 490-GC from Agilent)

directly connected to the cell. Samples of the liquid products were analyzed at the beginning and at the end of each experiment, by means of high-performance liquid chromatography (Shimadzu HPLC) and gas chromatograph (Perkin Elmer GC with a Mass Spectrometer) with a head space for the quantification of formate and alcohols, respectively.

4.4.3. Ru and Re molecular complexes synthesis

Ru visible light absorbers (**Ru_{VLA}**) and Re CO_2 reduction co-catalysts (**Re_{CAT}**) were synthetized based on the state-of-the-art. The supramolecular catalyst contained the Ru and Re molecular complexes linked by a ligand. The molecular catalysts are properly functionalized with the double bound functional group required for the covalent immobilization onto the different semiconductors.

4.4.3.1. Non-commercial organic ligands synthesis

First, the non-commercial organic ligands were synthetized following adapted reported procedures.

4,4'-Divinyl-2,2'-bipyridine (bpy_V)

The first ligand synthetized was a bipyridine modified with vinyl groups in the para position (**bpy_V**). The scheme of the synthetic route for the **bpy_V** ligand is described in the Scheme 4.

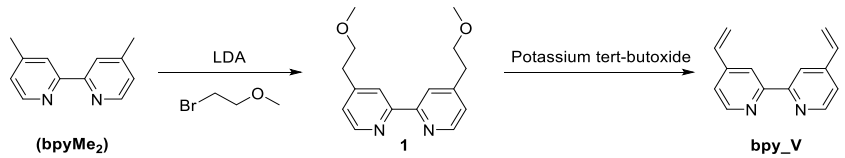

***Scheme 4**: Ligand **bpy_V** synthetic route.*

The **bpy_V** synthesis started with the commercial 4,4'-Dimethyl-2,2'-bipyridine (**$bpyMe_2$**). The synthesis of the **bpy_V** was a 2-step synthetic route,

where the first step was the deprotonation of the methyl's of the bipyridine using LDA followed by the nucleophilic attack to the bromomethyl methyl ether to give the ether **1**. In the second step, take place an elimination reaction using potassium tert-butoxide obtaining the final **bpy_V** ligand.

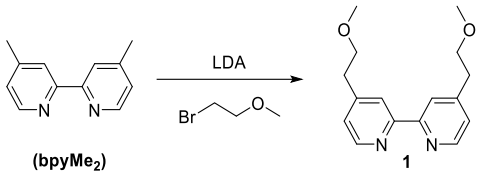

***Scheme 5**: First synthesis step of **bpy_V**.*

4,4'-Bis(2-methoxyethyl)-2,2'-bipyridine (1): The synthesis was performed according to an adapted reported procedure.[35] To a solution of diisopropylamine (1.68 mL, 11.94 mmol) in dry THF (15 mL) was added nBuLi in hexane (1.6 M, 7.5 mL, 11.94 mmol) at 0 °C under a nitrogen atmosphere. Then, to the mixture a solution of 4,4'-dimethyl-2,2'-bipyridine (**$bpyMe_2$**) (1.0 g, 5.43 mmol) in THF (20 mL) was added dropwise. The resulting solution was stirred at 0 °C for 30 min. Then, this solution was warmed to room temperature for a further 30 min and cooled down to -78 °C. Then, a solution of bromomethyl methyl ether (1.06 mL, 13.03 mmol) in dry THF (5 mL) was added dropwise. The reaction mixture was warm up to room temperature, quenched with saturated $NaHCO_3$ solution (5 mL) and diluted with ethyl acetate (20 mL). The aqueous phase was extracted with CH_2Cl_2 (3 x 20 mL). The combined organic layers were dried over magnesium sulphate, filtered and concentrated under reduced pressure. The oil obtained was purified by flash chromatography (96:4 dichloromethane/methanol) to give 4,4'-bis(2-methoxyethyl)-2,2'-bipyridine **1** as a yellow oil obtained in 82 % yield (1.21 g). **^{1}H NMR** (400 MHz, $CDCl_3$) δ (ppm): 2.97 (t, J_{H-H} = 6.8 Hz, 4 H), 3.36 (s, 6 H), 3.69 (t, J_{H-H} = 6.8 Hz, 4 H), 7.20 (dd, J_{H-H} = 1.7, 5.0 Hz, 2H), 8.26 (s, 2H), 8.58 (d, J_{H-H} =

5.0 Hz, 2H). These signals are in agreement with those reported in the literature.

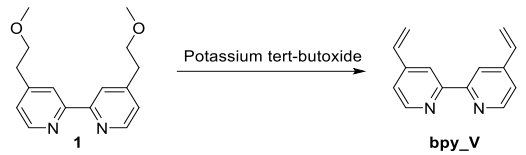

***Scheme 6**: Second step of synthesis of **bpy_V**.*

4,4'-Divinyl-2,2'-bipyridine (bpy_V): The synthesis was performed according to an adapted reported procedure.[35] To a solution of 4,4'-bis(2-methoxyethyl)-2,2'-bipyridine **1** (1.0 g, 3.67 mmol) in dry THF (10 mL) was added portion-wise t-BuOK (906.7 mg, 8.1 mmol) under nitrogen atmosphere at -78 °C. After the addition, the mixture was allowed to warm up to room temperature over 1 h. Then, the reaction mixture was quenched with water (0.3 mL), diluted with AcOEt (30 mL), dried over magnesium sulphate, filtrated and concentrated under reduced pressure to afford 4,4'-divinyl-2,2'-bipyridine as a yellow solid obtained in 92 % yield (705 mg). **^{1}H NMR** (400 MHz, $CDCl_3$) δ (ppm): 5.53 (d, J_{H-H} = 11.2 Hz, 2 H), 6.10 (d, J_{H-H} = 17.6 Hz, 2 H), 6.78 (dd, J_{H-H} = 10.8, 17.6 Hz, 2 H), 7.32 (dd, J_{H-H} = 1.6, 5.1 Hz, 2 H), 8.41 (s, 2 H), 8.64 (d, J_{H-H} = 5.3 Hz, 2 H). These signals are in agreement with those reported in the literature.

<u>1,2-bis(4'-methyl-[2,2'-bipyridin]-4-yl)ethane (bpyC2bpy)</u>

The second ligand synthetized is the 1,2-bis(4'-methyl-[2,2'-bipyridin]-4-yl)ethane (**bpyC2bpy**) ligand which was synthetized in only one step synthesis. This reaction is described in the Scheme 7.

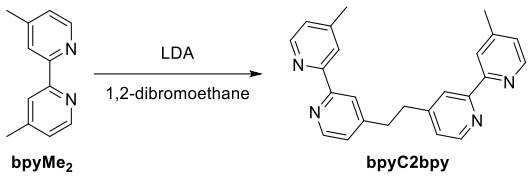

***Scheme 7**: Synthesis scheme of **bpyC2bpy** ligand.*

1,2-bis(4'-methyl-[2,2'-bipyridin]-4-yl)ethane (bpyC2bpy): The synthesis was performed according to an adapted reported procedure.[36] A solution of **bpyMe$_2$** (2 g, 10.97 mmol) in THF (40 mL) was cooled at -78 ºC. After cooling the solution LDA (2 M, 5.5 mL, 10.97 mmol) was added dropwise and the reaction mixture was stirred for 2 h at -78 ºC. Then, 1,2-dibromoethane (1.9 mL, 21.95 mmol) was added quickly and the reaction mixture was warmed to room temperature. Water (50 mL) was added, and the product was extracted with diethyl ether (3 x 100 mL). The organic phases were combined, dried over $MgSO_4$ and the solvent evaporated under vacuum. The crude product was purified by flash column chromatography (96:4 dichloromethane/methanol) yielding the pure **bpyC2bpy** ligand as a white solid obtained in 62 % yield (1.24 g). **^{1}H NMR** (400 MHz, $CDCl_3$) δ (ppm): 2.44 (s, 6 H), 3.10 (s, 4 H), 7.12 (dd, J_{H-H} = 1.7, 5.0 Hz, 2 H), 7.15 (dq, J_{H-H} = 1.0, 5.0 Hz, 2 H), 8.24 (t, J_{H-H} = 0.8 Hz, 2 H), 8.32 (d, J_{H-H} = 1.0 Hz, 2 H), 8.55 (d, J_{H-H} = 5.0 Hz, 2 H), 8.57 (dd, J_{H-H} = 0.7, 5.0 Hz, 2 H). These signals are in agreement with those reported in the literature.

4.4.3.2. Ru visible light absorber synthesis (Ru_{VLA})

The synthesis of the Ru visible light absorber (**Ru_{VLA}**) was performed with a bipyridine containing a vinyl group as a coupling agent (**bpy_V**). In the Scheme 8, there is the schematic synthetic route for **Ru_{VLA}**.

Chapter 4

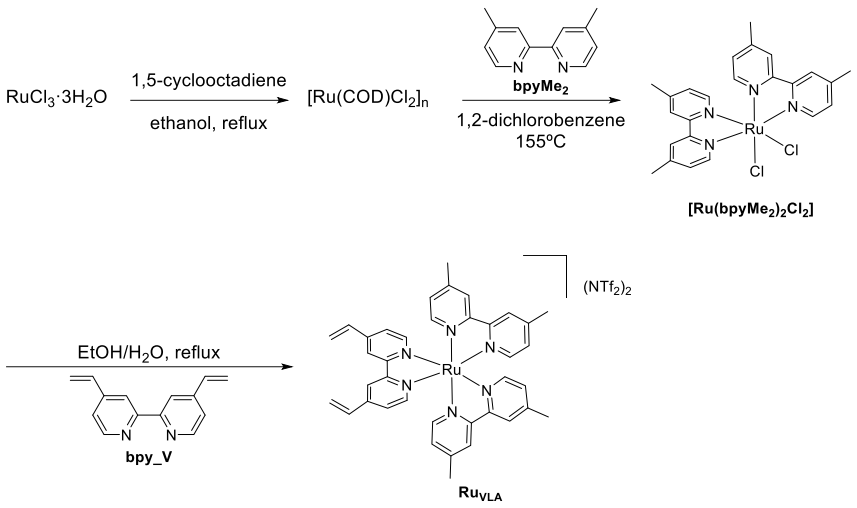

***Scheme 8**: Ruthenium visible light absorber synthetic route.*

The synthesis for both **Ru_{VLA}** started with the commercial $RuCl_3 \cdot 3H_2O$ precursor. The first step was the preparation of the polymeric $[Ru(COD)Cl_2]_n$ where the $RuCl_3$ was reduced to Ru(II). The next step was the substitution of the COD ligand by two **bpyMe₂** and the formation of the corresponding $[Ru(bpyMe_2)_2Cl_2]$. Then, it was performed the substitution of the two chloride ligands by the modified bipyridine **bpy_V**. The final **Ru_{VLA}** is obtained in 74 % isolated yield after the substitution of the two chlorides for the **bpy_V**.

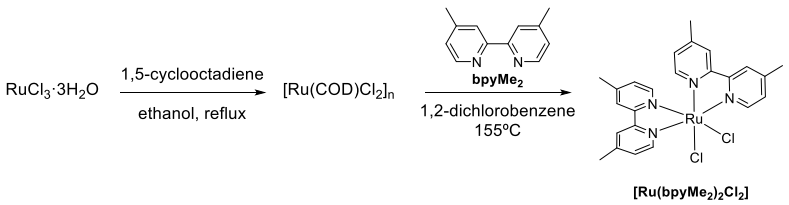

***Scheme 9**: Synthesis of $[Ru(bpyMe_2)_2Cl_2]$, two-step procedure.*

$[Ru(Me_2bpy)_2Cl_2]$: The synthesis was performed according to an adapted reported procedure.[37] $RuCl_3 \cdot 3H_2O$ (0.55 g, 2.7 mmol) was added to a mixture of 1,5-cyclooctadiene (3.25 mL, 27 mmol) and ethanol (12 mL), and refluxed under argon atmosphere for 64 h. After cooling to room temperature, a

precipitate was formed and it was collected by filtration affording dichlorido(1,5-cyclooctadiene)ruthenium(II) polymer ($[Ru(COD)Cl_2]_n$) as brown solid (0.52 g, 88 %). A suspension of $[Ru(COD)Cl_2]_n$ (0.251 g, 0.89 mmol) and $bpyMe_2$ (0.332 g, 1.8 mmol) in o-dichlorobenzene (3.8 mL) was stirred at 155 ^oC under argon-gas atmosphere for 3.5 h. After cooling to room temperature, resulting precipitates were collected by filtration and dried in vacuo, afforded $[Ru(Me_2bpy)_2Cl_2]$ as black powders obtained in 84 % yield (0.43 g). This compound was used in the following step without any purification and characterization.

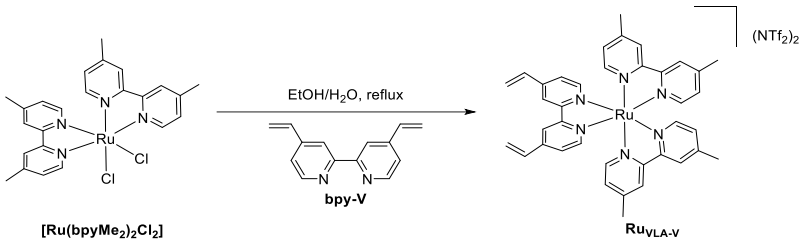

***Scheme 10**: Synthesis of **Ru_{VLA-V}**, third step.*

Ru_{VLA} complex: The synthesis was performed according to an adapted reported procedure.[38] A solution of the **bpy_V** ligand (104.13 mg, 0.5 mmol) and (324.3 mg, 0.6 mmol) of **$[Ru(Me_2bpy)_2Cl_2]$** in a 50 mL mixture of EtOH/H_2O (9:1 v:v) was heated at reflux in the dark under an argon atmosphere for 3 h. The solvents were removed, and the product was purified on silica gel column. Elution with an acetone/water mixture (8:2 v:v) removed the unreacted $Ru(Me_2bpy)_2Cl_2$. More rinsing with an acetone/water/KNO_3 saturated aqueous solution (10 drops of KNO_3 added to a mixture of 80 mL of acetone and 20 mL of water) afforded the desired ester complex with NO_3^- as counteranion. Pure fractions of this product were collected and evaporated under reduced pressure. The product was redissolved with dichloromethane and 0.2 g of $AgNTf_2$ was added and stirred during 10 min. $MgSO_4$ was added and the organic phase was filtered and dried to give the product **Ru_{VLA}** as a red powder

obtained in 49 % yield (0.36 g). **^{1}H NMR** (400 MHz, CD_2Cl_2) δ (ppm): 2.57 (d, J_{H-H} = 2.5 Hz, 12 H), 5.72 (d, J_{H-H} = 10.8 Hz, 2 H), 6.22 (d, J_{H-H} = 17.5 Hz, 2 H), 6.85 (dd, J_{H-H} = 10.9, 17.5 Hz, 2 H), 7.22 (t, J_{H-H} = 7.8, 4 H), 7.42 (dd, J_{H-H} = 1.7, 6.0 Hz, 2 H), 7.51 (t, J_{H-H} = 5.5 Hz, 4 H), 7.62 (d, J_{H-H} = 6.0 Hz, 2 H), 8.22 (s, 4 H), 8.34 (s, 2 H). **^{13}C{^{1}H} NMR** (100.6 MHz, CD_2Cl_2) δ (ppm): 21.5, 115.5, 118.6, 121.4, 121.8, 122.9, 124.6, 125.0, 125.3, 128.8, 129.1, 129.2, 133.1, 146.9, 150.6, 150.7, 150.8, 150.9, 151.4, 156.6, 156.7, 156.8, 157.5. **ESI-HRMS:** Calculated for $C_{38}H_{36}N_6Ru^{2+}$. Exact: M^{2+}: 339.1017; Experimental: M^{2+}: 339.1026.

4.4.3.3. Re CO_2 reduction co-catalyst synthesis (Re_{CAT})

The synthesis of the Re CO_2 reduction co-catalyst is also performed using the **bpy_V** ligand. The synthesis is performed in one only step where take place the substitution of two CO ligands of the $Re(CO)_5Br$ precursor for one **bpy_V** obtaining the final Re complex (**Re_{CAT}**) in 84 % yield (Scheme 11).

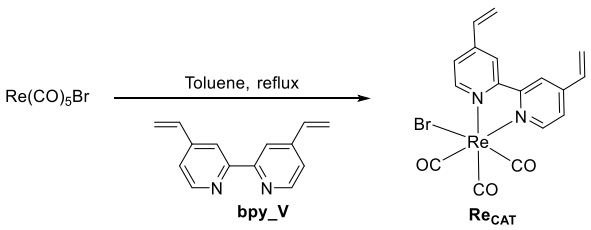

*Scheme 11: Synthesis scheme of complex **Re_{CAT}**.*

Re_{CAT} complex: The synthesis was performed according to an adapted reported procedure.[39] The $Re(CO)_5Br$ (0.1 g, 0.246 mmol) and the **bpy_V** ligand (51.21 mg, 0.246 mmol) were dissolved in toluene (60 mL) and stirred at reflux for 3 h. Then, the solvent was evaporated under vacuum and the product precipitated upon the addition of Et_2O. The precipitated was filtered and washed with Et_2O giving the **Re_{CAT}** complex as an orange solid obtained in 84 % yield (114.7 mg). **^{1}H NMR** (400 MHz, dmso-d_6) δ (ppm): 5.86 (d, J_{H-H} = 11.0 Hz, 2 H), 6.55 (d, J_{H-H} = 17.6 Hz, 2 H), 6.95 (dd, J_{H-H} = 10.9, 17.6 Hz, 2 H), 7.79 (dd, J_{H-H} = 1.6, 5.8 Hz, 2 H), 8.90 (s, 2 H), 8.94 (d, J_{H-H} = 5.8, 2 H). **^{13}C{^{1}H} NMR**

(100.6 MHz, dmso-d_6) δ (ppm): 121.0, 124.0, 124.5, 133.2, 148.1, 153.2, 155.7, 189.6, 197.4. **ESI-HRMS:** Calculated for $C_{17}H_{16}BrN_3O_3Re^+$. Exact: $(M+NH_4)^+$: 575.9927; Experimental: $(M+NH_4)^+$: 575.9901.

4.4.3.4. Synthesis of the Supramolecular RuRe1 complex

The first supramolecular **RuRe1** complex was synthetized with the **bpyC2bpy** ligand as a linker between the Ru and the Re complex. In this case there is a bridge of two carbons between the Ru and Re. This complex was synthetized with four steps synthesis procedure (Scheme 12).

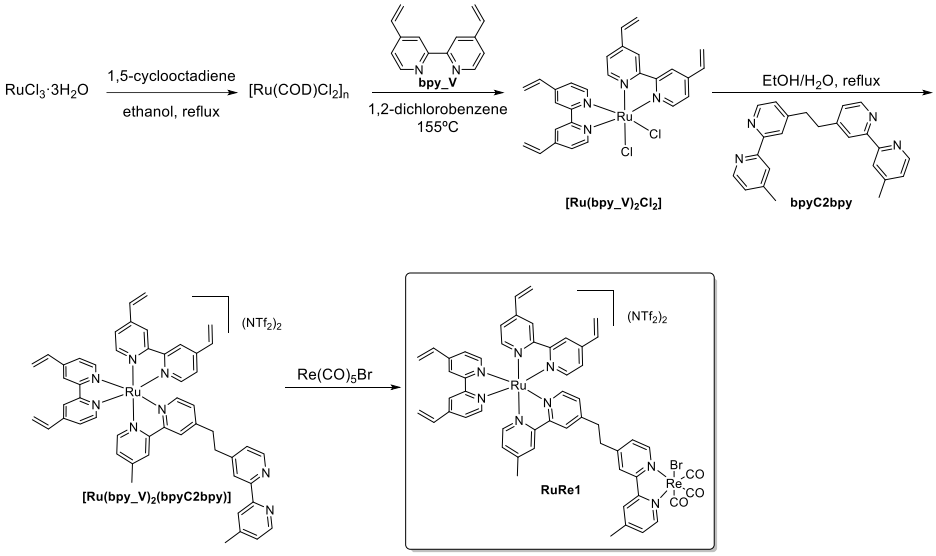

***Scheme 12**: Synthetic strategy to synthetize the **RuRe1** complex.*

The complex **RuRe1** was synthetized following the same synthetic strategy than for the $\mathbf{Ru_{VLA}}$. First, the $[Ru(COD)Cl_2]$ precursor is prepared, followed by the substitution of the COD ligand for two **bpy-V** ligand obtaining the **$[Ru(bpy\text{-}V)_2Cl_2]$** complex. Then, the chloride ligands were substituted for the 1,2-bis(4'-methyl-[2,2'-bipyridin]-4-yl)ethane (**bpyC2bpy**) ligand to obtain the corresponding Ru complex **$[Ru(bpy\_V)_2(bpyC2bpy)]$**. Finally, reaction with 1

equivalent of the $Re(CO)_5Br$ complex at reflux obtaining the final **RuRe1** in 64 % yield.

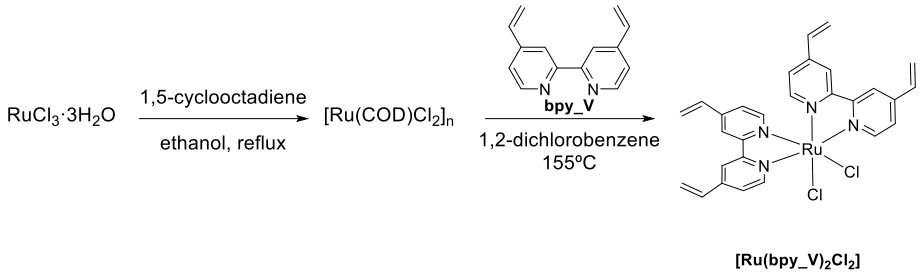

***Scheme 13**. Ru complex **[Ru(bpy-V)$_2$Cl$_2$]** synthetic route.*

Ru complex [Ru(bpy-V)$_2$Cl$_2$]: The synthesis of the Ru complex **[Ru(bpy-V)$_2$Cl$_2$]** is described in the section 4.4.3.2 in the Scheme 9 but using the **bpy_V** ligand (374.9 mg, 1.8 mmol) instead of the **bpyMe$_2$** ligand. The complex **[bpyC2bpy]** was obtained in 87 % yield.

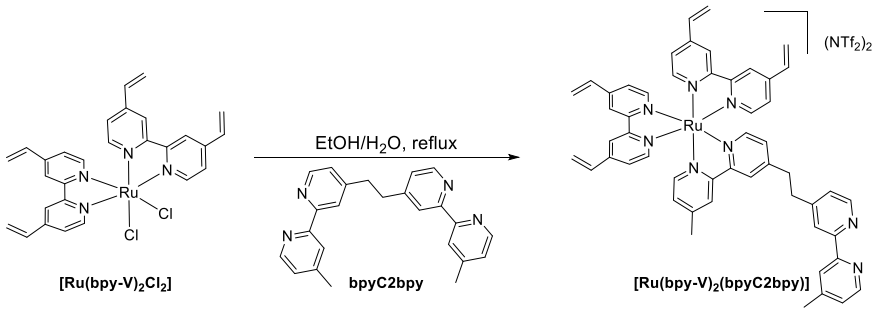

***Scheme 14**: Synthesis of Ru complex **12**.*

Ru complex [Ru(bpy-V)$_2$(bpyC2bpy)]: The synthesis was performed according to an adapted reported procedure.[38] A solution of the ligand **bpyC2bpy** (259 mg, 0.71 mmol) and (530 mg, 0.85 mmol) of Ru complex **[bpyC2bpy]** in a 71 mL mixture of EtOH/H_2O (9:1 v:v) was heated at 95 ºC in the dark under an argon atmosphere for 3 h. The solvents were removed, and the product was purified on silica gel column by using a mixture of acetone/water (8:2 v:v) containing KNO_3 saturated aqueous solution (10 drops of KNO_3 added to a

mixture of 80 mL of acetone and 20 mL of water). Pure fractions of the products were collected and evaporated under reduced pressure. The product was redissolved with dichloromethane, 0.27 g of $AgNTf_2$ are added and the mixture was stirred during 10 min. $MgSO_4$ was added and the organic phase was filtered and dried. The solid was redissolved with acetone and precipitated with diethyl ether to give the pure product **[Ru(bpy-V)$_2$(bpyC2bpy)]** as a red powder obtained in 58 % yield (0.592 g). **^{1}H NMR** (400 MHz, CD_2Cl_2) δ (ppm): 2.54 (s, 3H), 2.59 (s, 3H), 3.24 (m, 4H), 5.73 (m, 4H), 6.23 (m, 4H), 6.85 (m, 4H), 7.21 (d, J_{H-H} = 5.4 Hz, 1H), 7.33-7.50 (m, 8H), 7.63 (m, 5H), 8.19-8.52 (m, 10H). **^{13}C{^{1}H} NMR** (100.6 MHz, CD_2Cl_2) δ (ppm): 21.3, 21.4, 35.6, 36.0, 115.4, 118.6, 121.5, 121.6, 121.8, 122.8, 122.9, 123.4, 124.3, 124.7, 124.8, 125.0, 126.0, 126.9, 128.4. 129.1, 133.0, 133.1, 147.0, 147.1, 150.3, 150.7, 150.9, 151.1, 151.4, 151.5, 151.6, 151.9, 152.2, 152.8, 153.2, 153.6, 156.7, 157.1, 157.2, 157.3, 157.4, 157.5. **ESI-HRMS:** Calculated for $C_{52}H_{46}N_8Ru^{2+}$. Exact: M^{2+}: 442.1439; Experimental: M^{2+}: 442.1437.

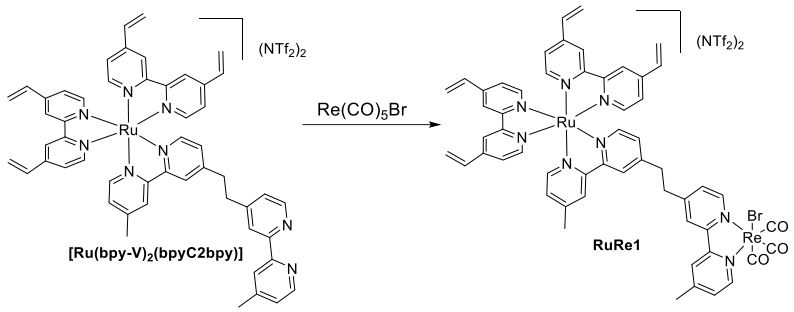

***Scheme 15**. Synthesis of the supramolecular **RuRe1** complex.*

RuRe1: The synthesis was performed according to an adapted reported procedure.[40] 60.7 mg (0.042 mmol) of the Ru complex **[Ru(bpy-V)$_2$(bpyC2bpy)]** and 34.12 mg (0.084 mmol) of $Re(CO)_5Br$ were refluxed in a 30 mL mixture acetone/ethanol (1:1) overnight. The solvent was evaporated and the solid was redissolved in the minimum amount of acetone. Then, a precipitate was formed by the addition of diethyl ether. This precipitate was

the pure **RuRe1** obtained in 48 % yield (35.9 mg). **^{1}H NMR** (400 MHz, CD_2Cl_2) δ (ppm): 2.54 (m, 6H), 3.21 (m, 4H), 5.73 (dd, J_{H-H} = 1.9, 10.9 Hz, 4H), 6.22 (m, 4H), 6.84 (m, 4H), 7.17-7.48 (m, 9H), 7.59 (m, 5H), 8.23-8.50 (m, 8H), 8.76 (m, 2H). **^{13}C{^{1}H} NMR** (100.6 MHz, CD_2Cl_2) δ (ppm): 21.3, 21.5, 35.6, 35.7, 115.4, 118.6, 121.4, 121.6, 121.8, 123.1, 124.4, 124.5, 124.6, 124.7, 124.9, 125.0, 125.2, 126.2, 127.4, 128.3, 128.5, 129.1, 130.0, 133.0, 133.1, 147.0, 147.1, 147.1, 150.2, 151.1, 151.3, 151.4, 151.5, 151.6, 152.4, 152.5, 152.8, 152.9, 154.1. 154.2, 155.6, 155.7, 156.4, 156.4, 156.6, 157.1, 157.3, 157.4, 157.5, 189.6, 197.9, 198.1. **ESI-HRMS:** Calculated for $C_{55}H_{46}BrN_8O_3ReRu^{2+}$. Exact: M^{2+}: 617.0733; Experimental: M^{2+}: 617.0722.

The coordination of the Re complex in the Ru complex **[Ru(bpy-V)$_2$(bpyC2bpy)]** was confirmed by performing an IR analyses of the complex before and after the coordination of the Re complex.

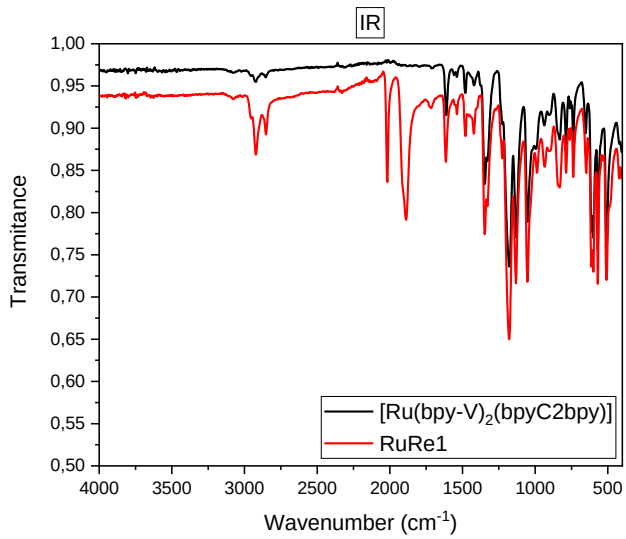

***Figure 31**. IR Spectrums: **RuRe1** (red) Ru complex **[Ru(bpy-V)$_2$(bpyC2bpy)]** (black).*

As it can be observed in the Figure 31, the IR spectrum of the Ru complex did not display any characteristic peak of the CO bond. Instead, when the Re

complex is coordinated, it is possible to observe two peaks corresponding to the CO bond in 2016 and 1889 cm^{-1}. These peaks confirmed that the Re complex was coordinated to the Ru complex **[Ru(bpy-V)$_2$(bpyC2bpy)]**.

4.4.3.5. Synthesis of the Supramolecular RuRe2 complex

To compare the effect of the ligand between the Ru and Re, a new supramolecular RuRe complex was synthetized with the 2,2'-Bipyrimidine **(bpym)** as ligand (**RuRe2**). The **RuRe2** complex was synthetized with four steps synthetic procedure (Scheme 16).

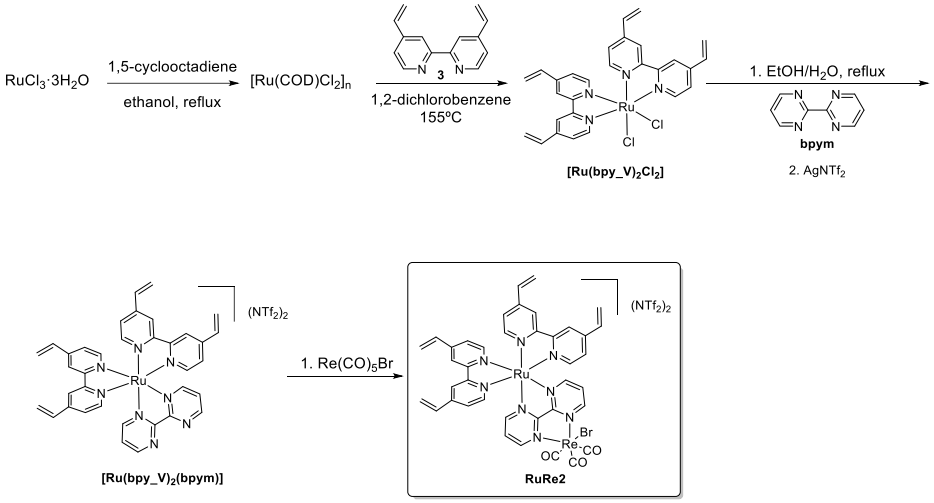

***Scheme 16**. Synthesis of the **RuRe2** complex.*

The synthesis of the **RuRe2** complex is the same than for the **RuRe1** complex but using the 2,2'-Bipyrimidine **(bpym)** ligand instead of the ligand **bpyC2bpy** ligand.

Chapter 4

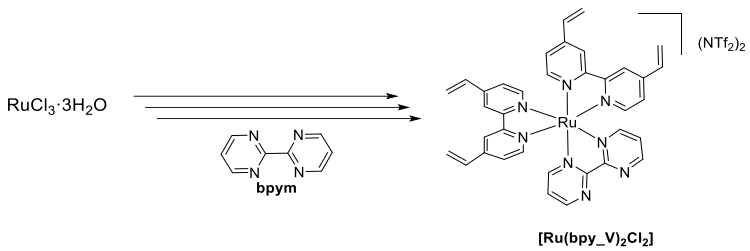

***Scheme 17**: Synthesis of Ru complex **[Ru(bpy_V)$_2$Cl$_2$]**.*

Ru complex [Ru(bpy_V)$_2$(bpym)]: The synthesis procedure of the Ru complex **[Ru(bpy_V)$_2$(bpym)]** is described in the section 4.4.3.4 in the Scheme 14. To synthetize the complex **[Ru(bpy_V)$_2$(bpym)]**, the synthesis was performed with the ligand **bpym** instead of the **bpyC2bpy** ligand. The pure Ru complex **[Ru(bpy_V)$_2$(bpym)]** was obtained in 57 % yield (404.5 mg). **^{1}H NMR** (400 MHz, CD_3OD) δ (ppm): 5.75 (dd, J_{H-H} = 5.0, 10.9 Hz, 4H), 6.39 (dd, J_{H-H} = 4.0, 17.6 Hz, 4H), 6.93 (m, 4H), 7.56 (m, 4H), 7.71 (d, J_{H-H} = 5.9 Hz, 2H), 7.41 (m, 2H), 7.80 (dd, J_{H-H} = 5.0, 5.8 Hz, 2H), 7.93 (d, J_{H-H} = 5.9 Hz, 2H), 8.41 (dd, J_{H-H} = 1.9, 5.8 Hz, 2H), 8.83 (s, 4H), 9.18 (dd, J_{H-H} = 1.9, 4.9 Hz, 2H). **^{13}C{^{1}H} NMR** (100.6 MHz, CD_3OD) δ (ppm): 119.6, 122.7, 122.8, 122.9, 123.3, 125.6, 125.8, 126.8, 134.3, 134.3, 149.0, 152.5, 153.4, 158.5, 158.7, 159.2, 162.0, 162.7. **ESI-HRMS:** Calculated for $C_{36}H_{30}N_8Ru^{2+}$. Exact: M^{2+}: 338.0813; Experimental: M^{2+}: 338.0816.

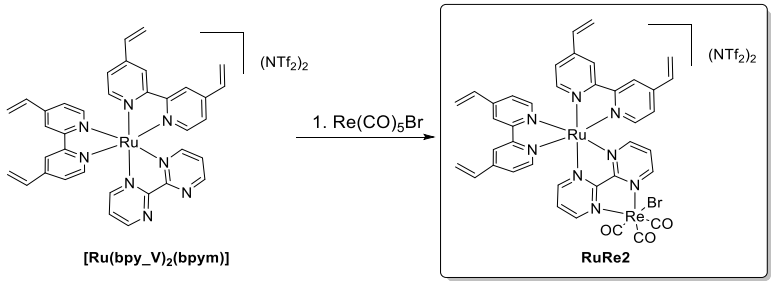

***Scheme 18**. Synthesis of **RuRe2** complex.*

RuRe2 complex: The synthesis was performed according to an adapted reported procedure.[40] 100 mg (0.08 mmol) of the Ru complex

[Ru(bpy_V)$_2$(bpym)] and 65 mg (0.16 mmol) of $Re(CO)_5Br$ were refluxed overnight in a 60 mL mixture acetone/ethanol (1:1). The solvent was evaporated and the solid was redissolved in the minimum amount of acetone. Then, the product was precipitated with diethyl ether and the pure **RuRe2** complex was obtained in 59 % yield (74.2 mg). **^{1}H NMR** (400 MHz, Acetone-d_6) δ (ppm): 5.76 (dt, J_{H-H} = 2.0, 10.8 Hz, 4H), 6.41 (m, 4H), 6.95 (m, 4H), 7.65 (m, 4H), 8.00 (m, 5H), 8.58 (d, J_{H-H} = 5.9 Hz, 1H), 8.79 (dd, J_{H-H} = 1.4, 5.6 Hz, 1H), 8.98 (m, 5H), 9.54 (dt, J_{H-H} = 1.5, 5.5 Hz, 2H). **^{13}C{^{1}H} NMR** (100.6 MHz, Acetone-d_6) δ (ppm): 116.2, 119.4, 122.1, 122.3, 122.4, 122.6, 123.5, 123.6, 123.7, 125.1, 125.4, 125.6, 125.8, 127.1, 127.5, 134.0, 134.1, 134.2, 148.4, 148.5, 148.6, 152.9, 153.4, 154.2, 155.6, 158.0, 158.1, 158.4, 158.5, 160.0, 160.5, 162.4, 162.6, 162.7, 167.4, 167.8, 196.5. **ESI-HRMS:** Calculated for $C_{39}H_{30}BrN_8O_3ReRu^{2+}$. Exact: M^{2+}: 513.0107; Experimental: M^{2+}: 513.0099.

The coordination of the Re complex in the Ru complex **[Ru(bpy_V)$_2$(bpym)]** was confirmed by IR analysis. IR analyses of **RuRe 2** complex was carried out before and after the coordination of the Re complex.

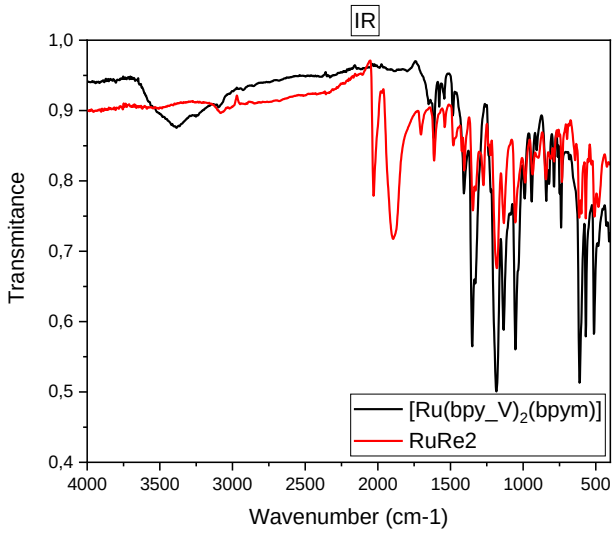

***Figure 32**. IR Spectrums: **RuRe2** (red) Ru complex **[Ru(bpy_V)$_2$(bpym)]** (black).*

A similar trend was observed for the **RuRe2** to that previously observed for **RuRe1**. In the IR spectrum of the Ru complex **[Ru(bpy_V)$_2$(bpym)]** (Figure 32,) there was not any characteristic peak of the CO bond. Instead, when the Re complex was coordinated, it was possible to observe two peaks corresponding to the CO bond in 2030 and 1895 cm^{-1}. These peaks confirmed that the Re complex was coordinated to the Ru complex **[Ru(bpy_V)$_2$(bpym)]**.

4.4.4. Cu_2O/SnO_2 synthesis and functionalization

The synthesis of the Cu_2O/SnO_2 was performed according to an adapted reported procedure.[27] The Cu_2O nanoparticles were obtained during wet precipitation process by adding dropwise a 2 M NaOH aqueous solution (50 mL) into a 0.01 M $CuCl_2{\cdot}2H_2O$ aqueous solution (500 mL). The mixture was stirred for 30 min, and then, 0.6 M aqueous solution of L–ascorbic acid (50 mL) was dropwise added. The precipitate was collected and washed. Then, it was dried giving the product as an orange powder. The Cu_2O/SnO_2 nanoparticles were obtained during coordination etching process dispersing the Cu_2O

nanoparticles in a mixture of isopropanol (300 mL) and a 0.2 M NaCl aqueous solution (10 mL). Then, a $SnCl_4 \cdot 5H_2O$ solution (with 40:1 Cu_2O:SnO_2 molar ratio) in isopropanol (300 mL) was dropwise added. The precipitate was collected and dried giving the Cu_2O/SnO_2 nanoparticles as an orange powder.

The Cu_2O/SnO_2 nanoparticles (1.00 g) were dispersed in a 5 mM VTES solution (250 mL) in a mixture isopropanol/H_2O 95/5. The precipitate was collected and washed. Then, it was dried giving the product as an orange powder.

4.4.5. RuRe@Cu_2O/SnO_2 photocathode preparation

A general procedure to immobilize the complexes containing the vinyl groups with the functionalized Cu_2O/SnO_2-VTES has been used.[18] The electropolymerization was carried out using a dispersion prepared by mixing a nitrogen degassed acetonitrile solution (50 mL) containing 0.6 mM of the corresponding complex, 0.1 M of tetraethylammonium hexafluorophosphate ($TBA \cdot PF_6$) and the Cu_2O/SnO_2-VTES powder (0.5 g). The electropolymerization of the complexes was performed using a three electrodes set-up with a glassy carbon electrode for both, working and counter electrode, and $Ag/AgNO_3$ as reference electrode. Then, CV was performed through the potential window of -0.6 to -1.6 V vs $Ag/AgNO_3$ for the Ru complex; 0.0 to -1.6 V vs $Ag/AgNO_3$ for the Re complex; and 0.0 to -1.9 V vs $Ag/AgNO_3$ for the mixture of Ru and Re complex. The applied voltage was scanned multiple times with a scan rate of 100 $mV \cdot s^{-1}$. After 30 scans for the Ru and Re complex for separated and 60 scans for the mixture of Ru and Re, the powders were filtrated, washed with acetonitrile, and dried under vacuum.

The electrodes were prepared by air-brushing of a catalytic ink onto a porous carbon support (Toray carbon paper 060, from FuelCellStore) using an adapted literature process.[28] The catalytic ink was constituted by various components: (i) the corresponding **Ru/Re@Cu_2O/SnO_2** catalyst in the powder

form, (ii) NAFION® (dispersion, 5 % wt in water and 1-propanol, from Sigma Aldrich) as a binder for the particles, and (iii) ethanol (from Sigma Aldrich), as a carrier for the ink deposition considering that the ink must be fluid to be uniformly spread on the area of interest. Each electrode was prepared with a geometric area of 1 cm^2 with a catalyst loading of 1 $mg \cdot cm^{-2}$. The deposition process was performed by placing the carbon paper on a heating plate at 50 ^oC to ensure complete solvent evaporation. A pressure of 1.5 bar for the carrier gas (nitrogen) in the airbrush inlet was selected to have a continuous ink flow, and in order to avoid undesired liquid drops. Then, all the electrodes were kept on the heating plate at 50 ^oC for 15 min before their use.

4.4.6. $CuGaO_2$ synthesis and functionalization

The synthesis of the $CuGaO_2$ was carried out using a solid state reaction procedure adapted from literature.[17] A mixed powder of starting materials, Cu_2O (1.76 mmol, 251.9 mg, Sigma-Aldrich, 99.99 % purity) and Ga_2O_3 (1.76 mmol, 330.0 mg, Sigma-Aldrich, 99.99 % purity), was heated up from room temperature to 1100 ^oC at 5 ^oC/min under N_2 flow. Then, the mixture was maintained for 15 h at 1100 ^oC, and finally, cooled down to room temperature under N_2 flow. After calcination, 333.8 mg of a white-green powder was obtained.

Then, the synthesized $CuGaO_2$ was functionalized with vinyltriethoxysilane (VTES) by adding 0.1 g of $CuGaO_2$ to a 20 mL solution of isopropanol containing 10 mM of vinyltriethoxysilane. The dispersion was stirred overnight at room temperature. Then, it was filtrated, and washed with isopropanol.

4.4.7. RuRe@$CuGaO_2$ photocathode preparation

The electrodes were manufactured by airbrushing a catalytic ink onto a porous carbon support (Toray carbon paper 060, from FuelCellStore).[28] The catalytic ink was constituted by various components: (i) $CuGaO_2$-VTES catalyst in the

powder form; (ii) NAFION® (dispersion, 5 %wt in water and 1-propanol, from Sigma Aldrich) as a binder for the particles and ionomer, and (iii) ethanol (from Sigma Aldrich), as a carrier for the ink deposition, since the ink must be fluid to be uniformly spread on the area of interest. Each $CuGaO_2$-VTES electrode was prepared with a geometric area of 1 cm^2 and a catalyst loading of 1 $mg \cdot cm^{-2}$. The deposition process was performed by placing the carbon paper on a heating plate at 50°C to ensure the complete solvent evaporation. A pressure of 1.5 bar for the carrier gas (nitrogen) in the airbrush inlet was selected to have a continuous ink flow, in order to avoid undesired liquid drops. Then, all the electrodes were kept on the heating plate for 15 min before their use.

Next, the prepared electrodes containing the $CuGaO_2$-VTES were subjected to electropolymerization of the corresponding molecular complexes.[18] The electropolymerization of the complexes was performed employing a three electrodes set-up with the $CuGaO_2$-VTES, platinum wire and $Ag/AgNO_3$ as working, counter, and reference electrodes, respectively. Electrodes were submerged in an argon degassed acetonitrile solution containing the corresponding complex in a 0.5 mM concentration and tetraethylammonium hexafluorophosphate ($TBA \cdot PF_6$, 0.1 M) as electrolyte. Cyclic voltammetries were performed from 0 to -1.9 V vs $Ag/AgNO_3$, and the applied voltage was scanned multiple times with a scan rate of 100 $mV \cdot s^{-1}$. After 60 scans, the electrode was removed and washed with acetonitrile.

Chapter 4

***Figure 33**: Image of the set-up used to perform the molecular complexes electropolymerization onto the semiconductor*

4.5. Supporting information

4.5.1. UV-Vis spectra of the molecular complexes

The UV-Vis of the different molecular complexes were performed to check the absorbance wavelength of each complex.

4.5.1.1. Ru visible light absorber

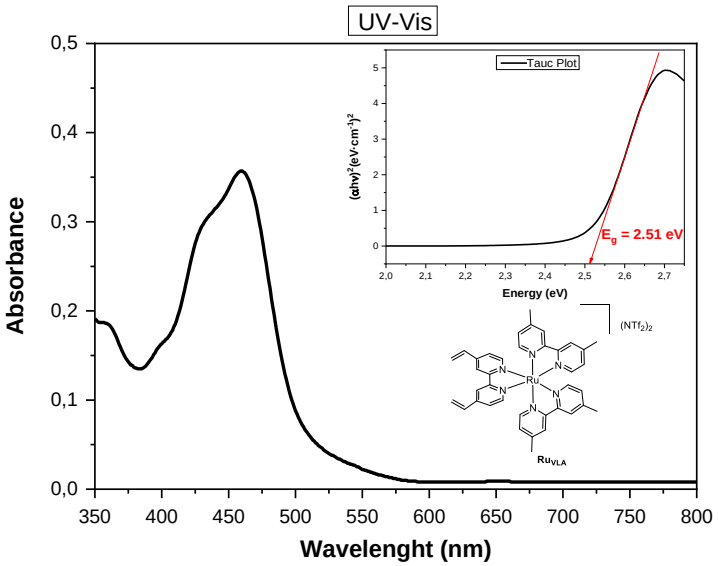

***Figure S1**: UV-Vis spectra and Tauc plot of the **Ru_{VLA}** complex.*

4.5.1.2. Re CO_2 reduction co-catalyst

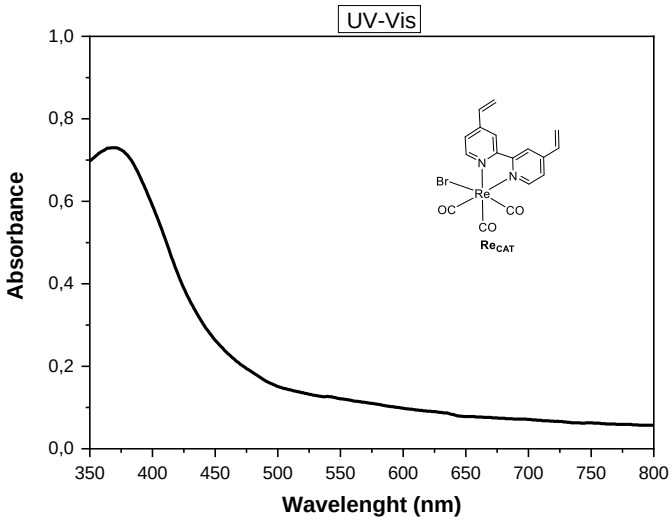

***Figure S2**: UV-Vis spectra and Tauc plot of the **Re_{CAT}** complex.*

4.5.1.3. Supramolecular RuRe1

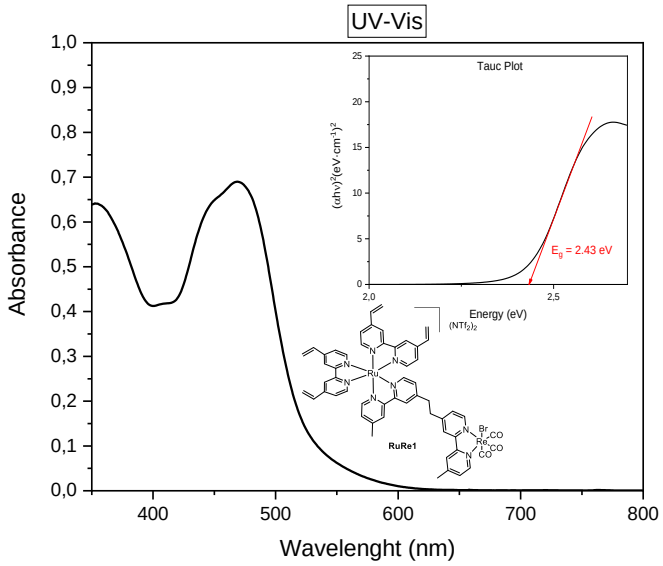

***Figure S3**: UV-Vis spectra and Tauc plot of the **RuRe1**.*

4.5.1.4. Supramolecular RuRe2

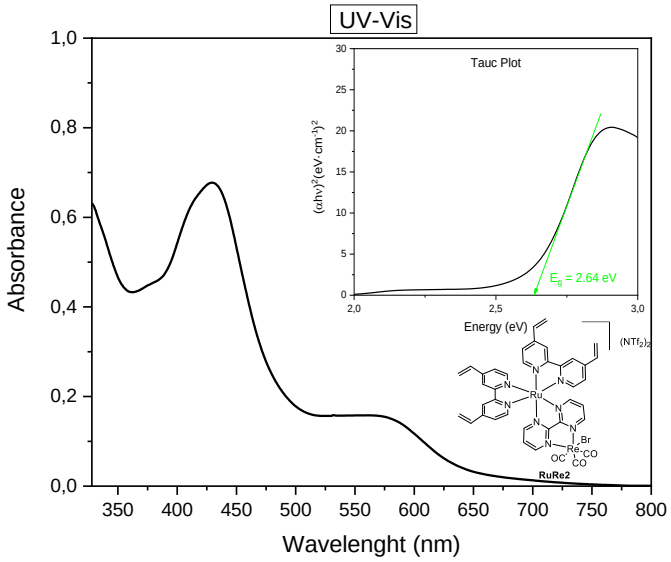

***Figure S4**: UV-Vis spectra and Tauc plot of the **RuRe2**.*

4.5.2. ^1H and $^{13}C\{^1H\}$ NMR spectra

^1H NMR ($CDCl_3$, 400 MHz)

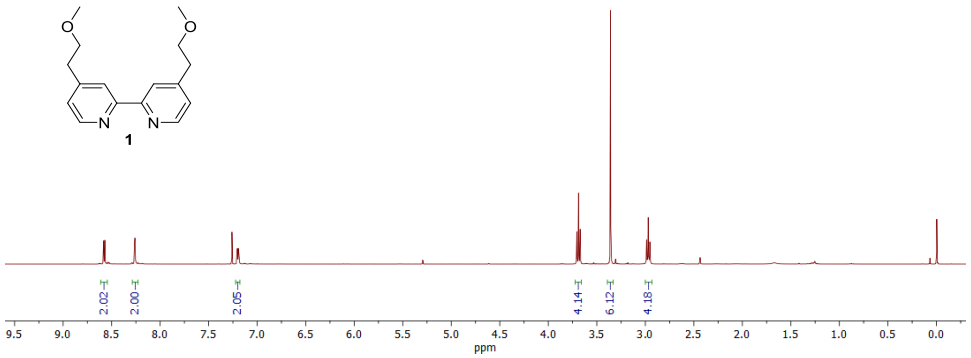

Chapter 4

^{1}H NMR ($CDCl_3$, 400 MHz)

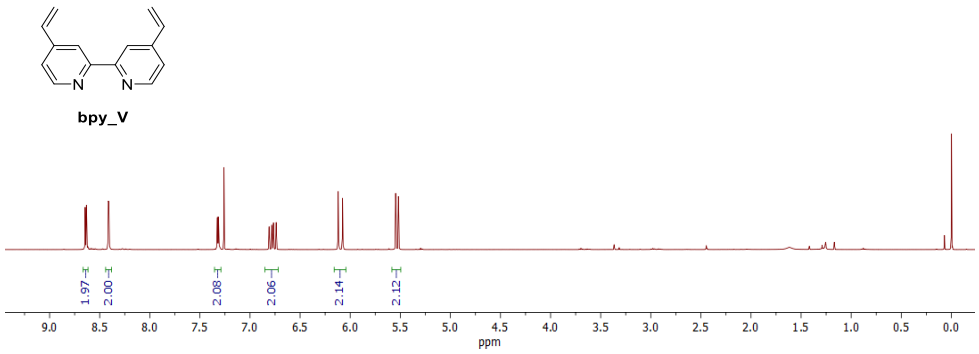

^{1}H NMR ($CDCl_3$, 400 MHz)

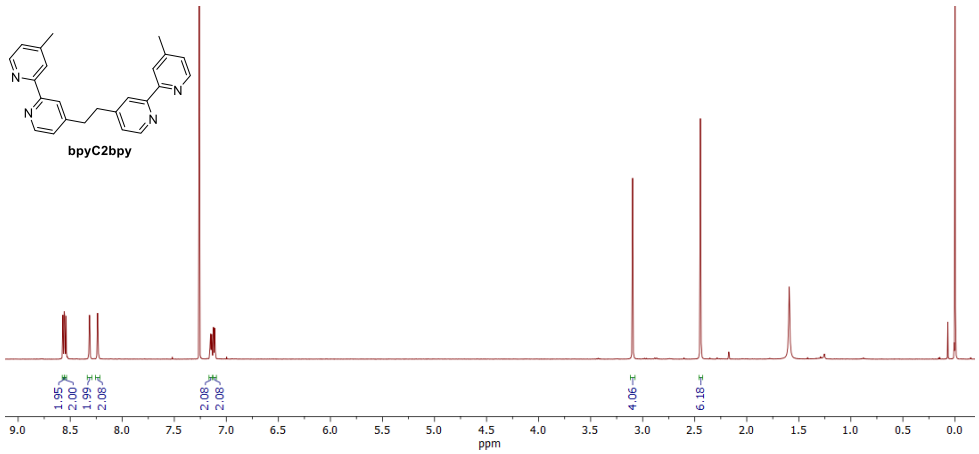

^1H NMR (CD_2Cl_2, 400 MHz)

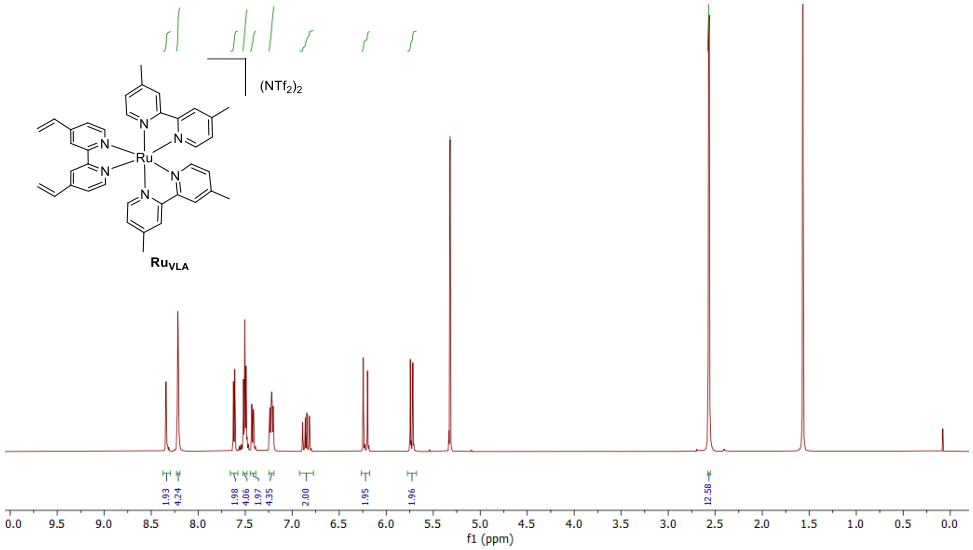

$^{13}C\{^1H\}$ NMR (CD_2Cl_2, 100.6 MHz)

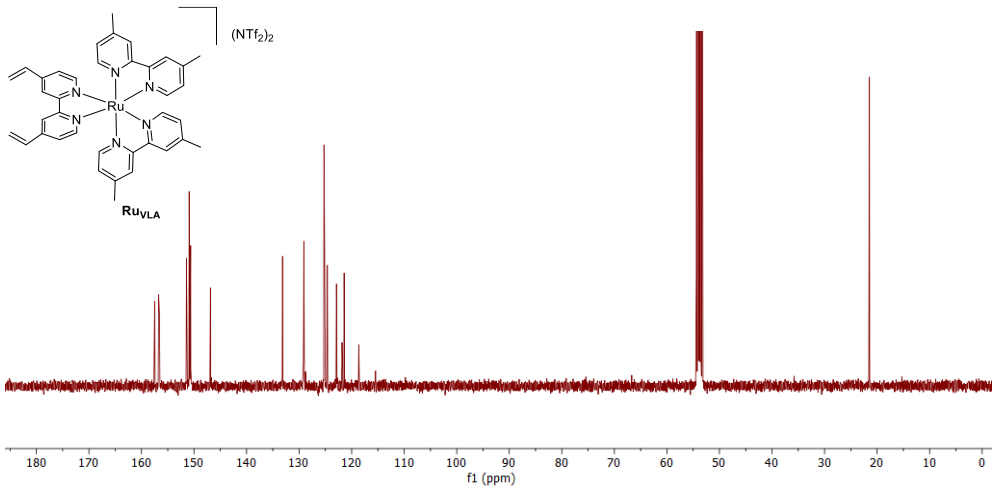

Chapter 4

^{1}H NMR (dmso-d_6, 400 MHz)

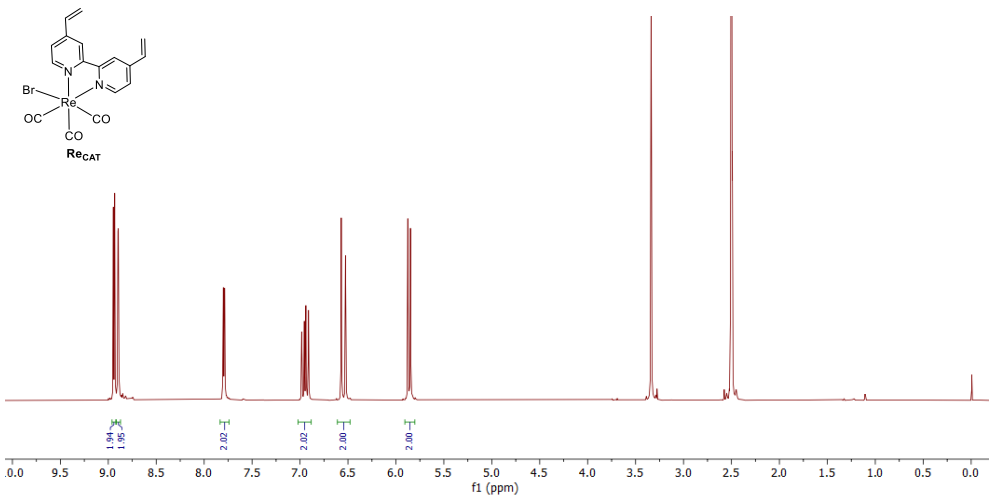

^{13}C{^{1}H} NMR (dmso-d_6, 100.6 MHz)

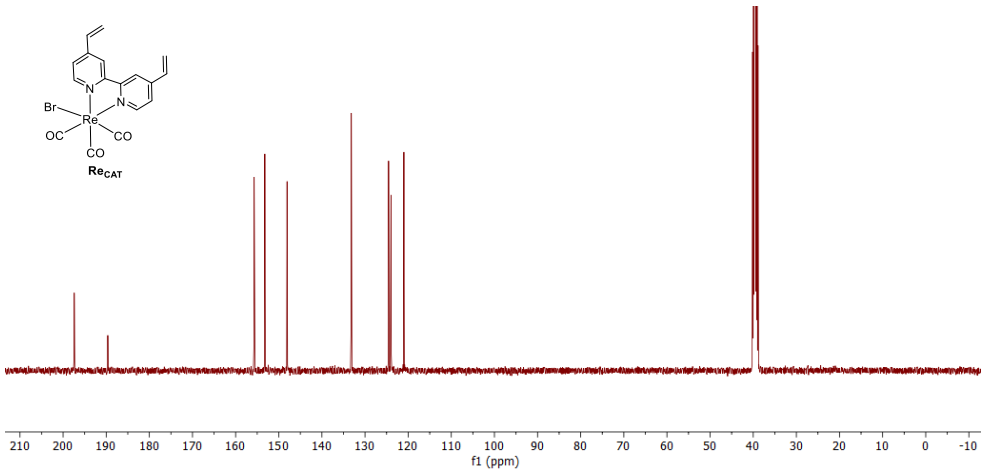

^{1}H NMR (CD_2Cl_2, 400 MHz)

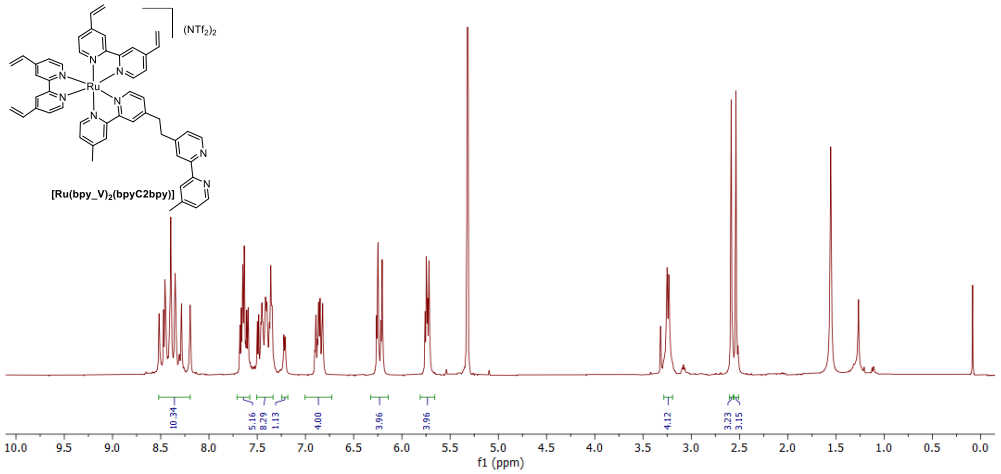

^{13}C{^{1}H} NMR (CD_2Cl_2, 100.6 MHz)

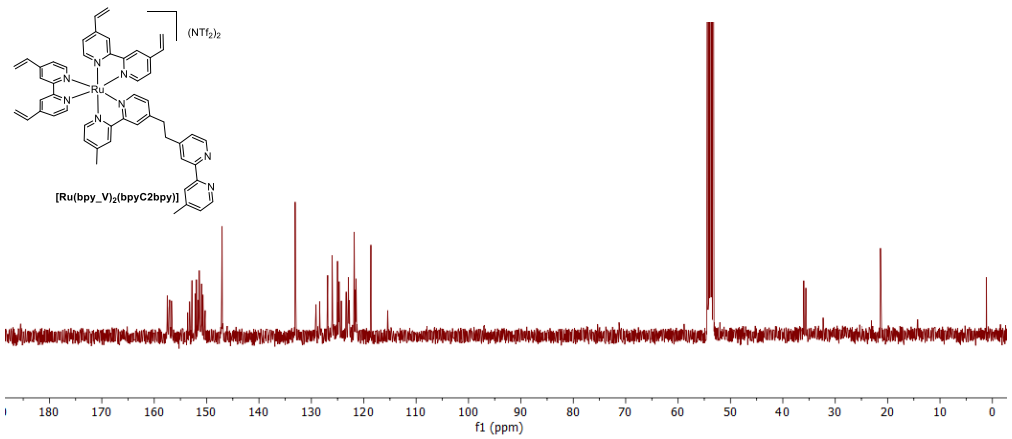

^{1}H NMR (CD_2Cl_2, 400 MHz)

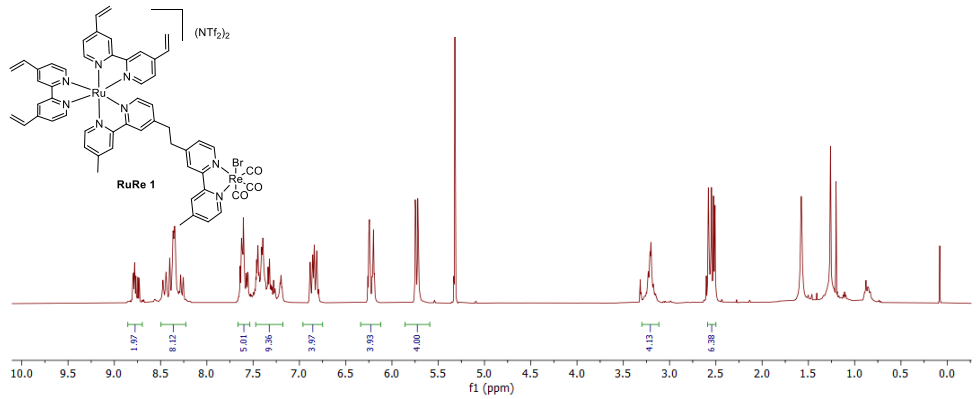

Chapter 4

$^{13}C\{^{1}H\}$ NMR (CD_2Cl_2, 100.6 MHz)

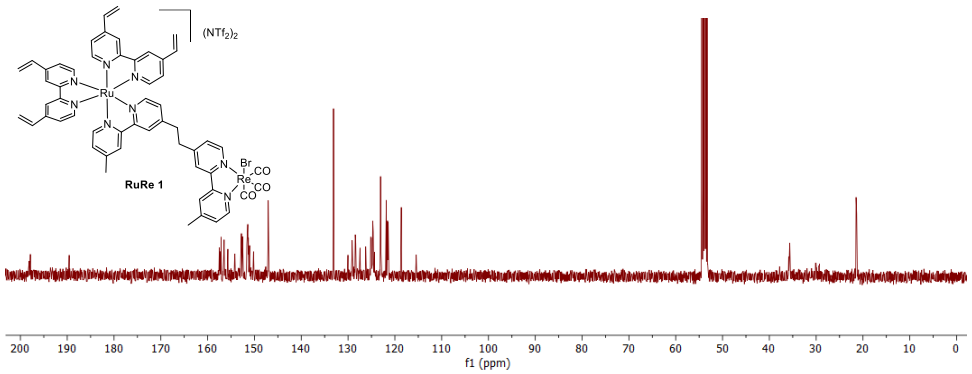

^{1}H NMR (CD_3OD, 400 MHz)

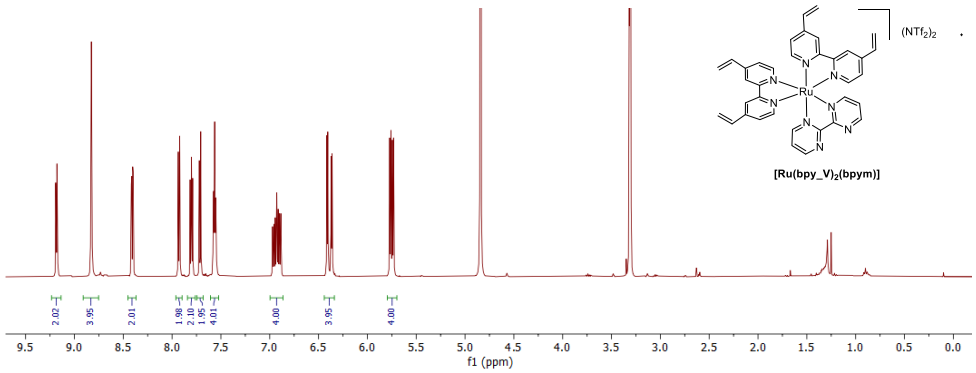

$^{13}C\{^{1}H\}$ NMR (CD_3OD, 100.6 MHz)

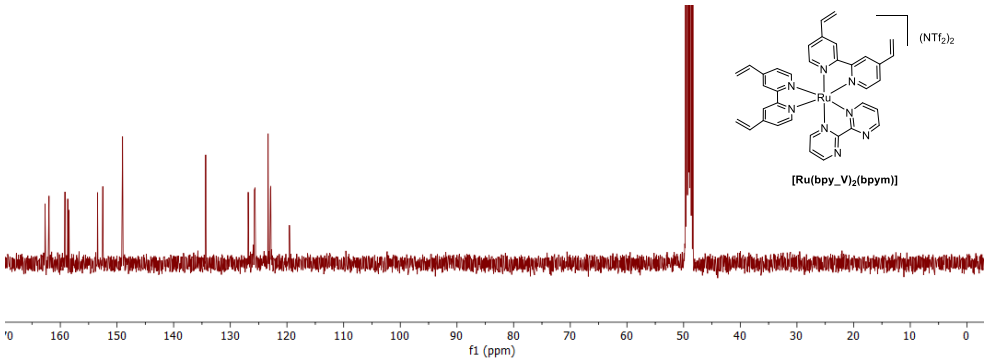

^{1}H NMR (acetone-d_6, 400 MHz)

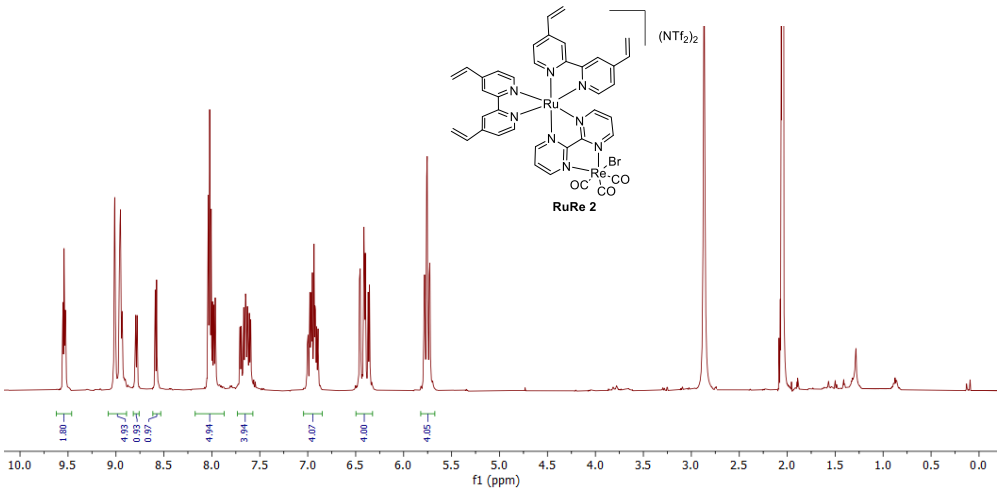

$^{13}C\{^{1}H\}$ NMR (acetone-d_6, 100.6 MHz)

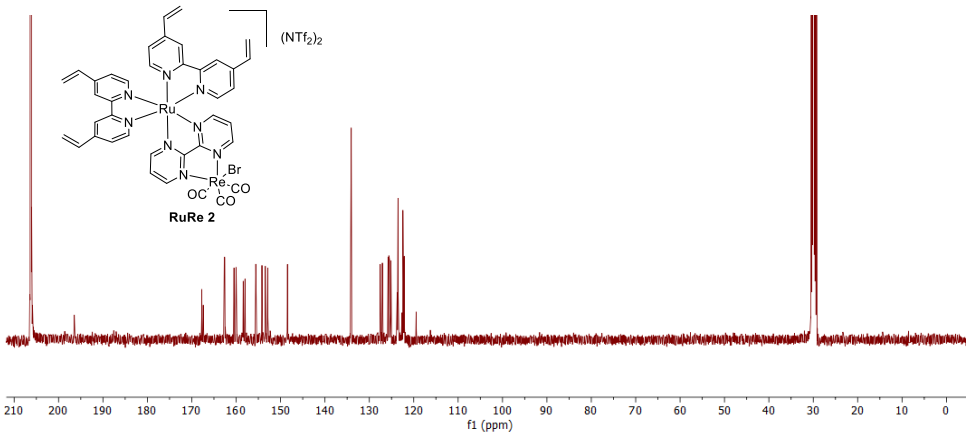

4.5.3. FESEM images and EDX analysis of the electrodes after electropolymerization

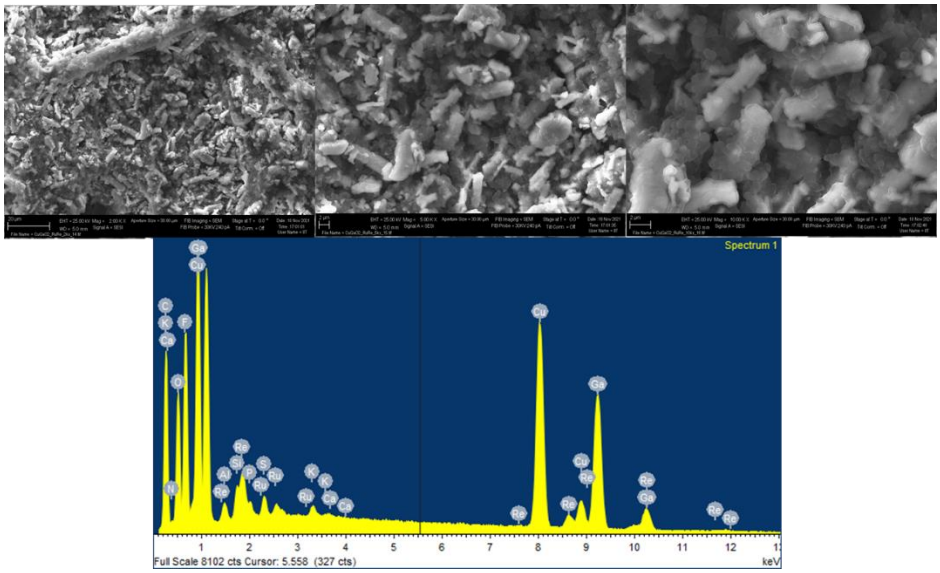

***Figure S5**: FESEM images and EDX analysis of the **Ru+Re@CuGaO$_2$** electrode after the electropolymerization.*

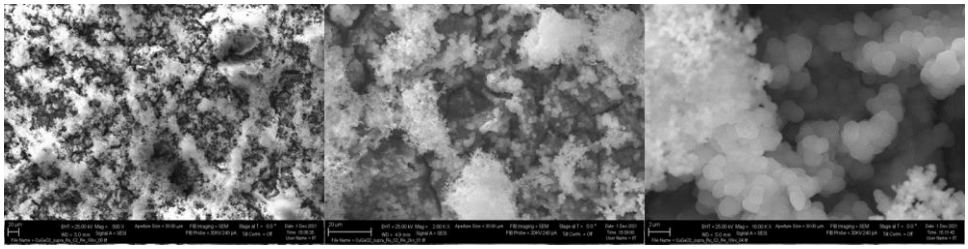

***Figure S6**: FESEM images of the **RuRe1@CuGaO$_2$** electrode after the electropolymerization.*

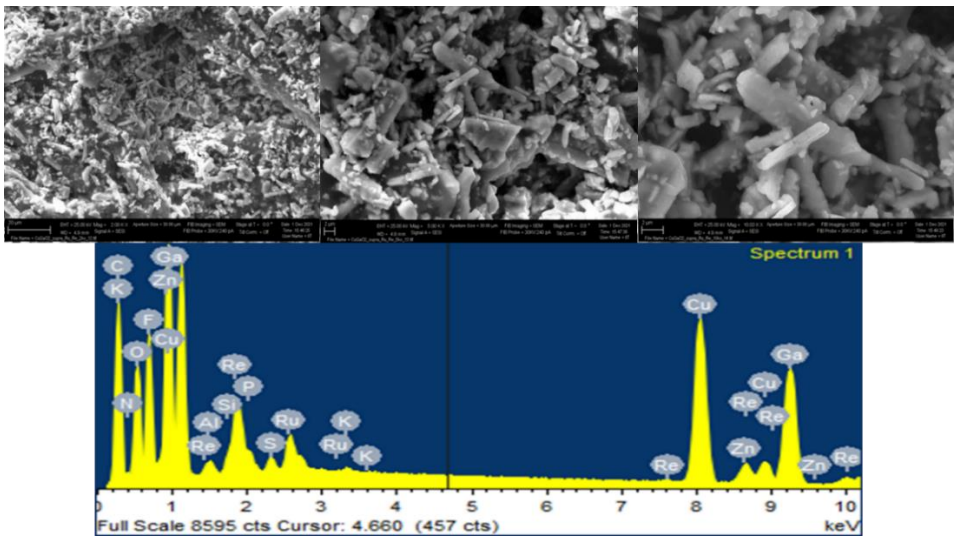

***Figure S7**: FESEM images and EDX analysis of the **RuRe2@CuGaO₂** electrode after the electropolymerization.*

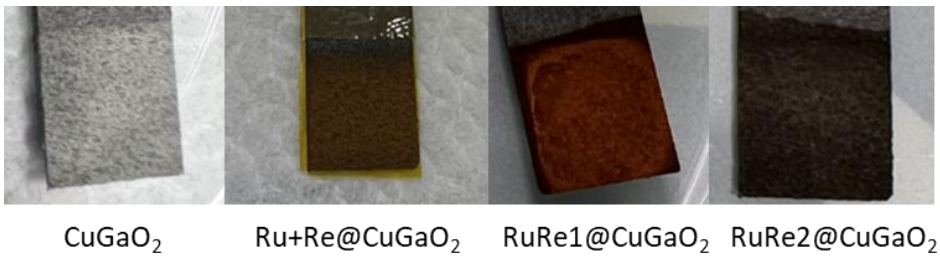

***Figure S8**: Images of the electrodes before and after the electropolymerization procedure.*

4.5.4. FESEM images and EDX analysis of the tested electrodes

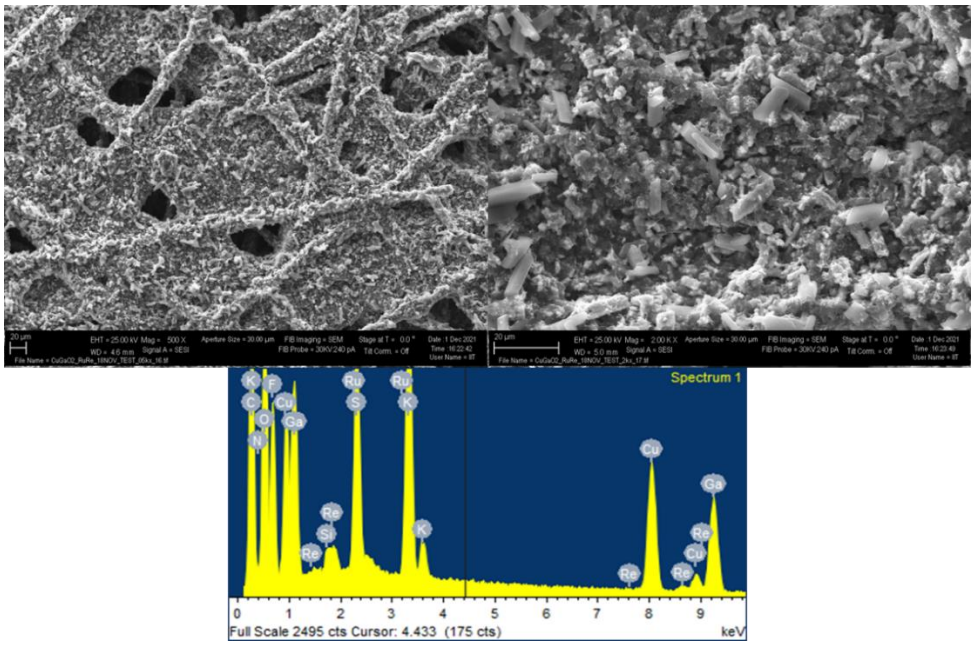

***Figure S9**: FESEM images and EDX analysis of the tested **Ru+Re@CuGaO$_2$** electrode.*

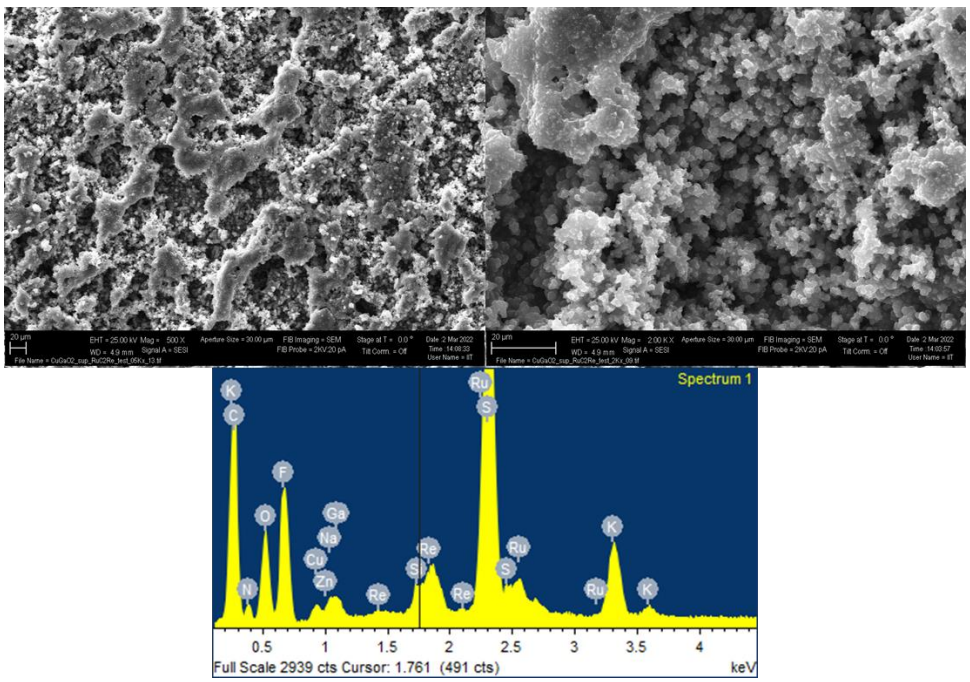

***Figure S10**: FESEM images and EDX analysis of the tested **RuRe1@CuGaO$_2$** electrode.*

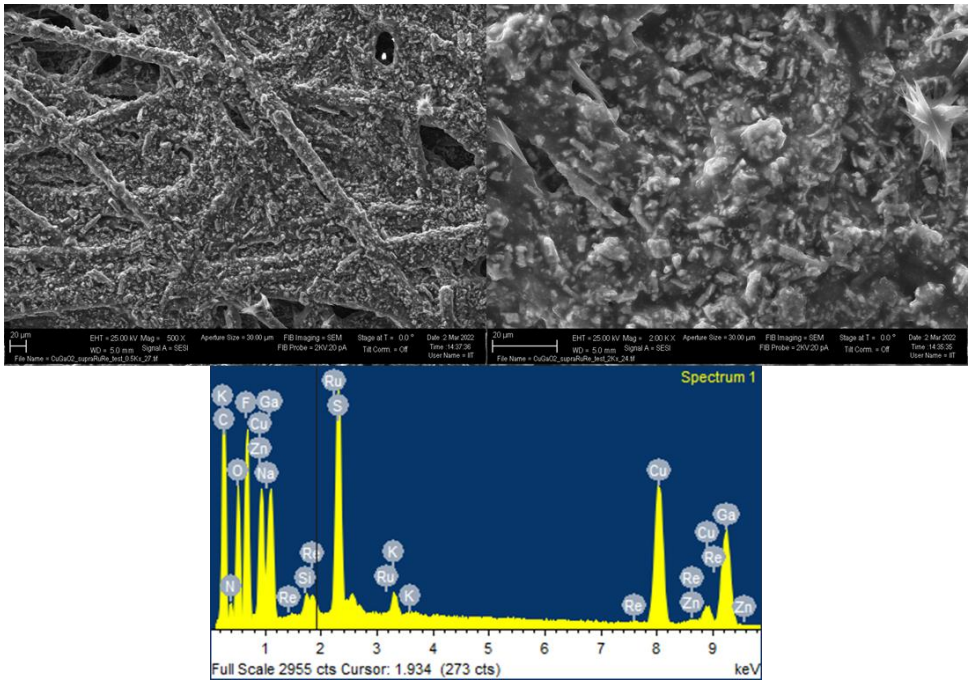

***Figure S11**: FESEM images and EDX analysis of the tested **RuRe2@CuGaO$_2$** electrode.*

4.6. References

(1) Photoelectrocatalytic device for SUN-driven CO2 conversion into green CHEMicals https://cordis.europa.eu/project/id/862192/es (accessed 2022 -06 -12).

(2) Rafiee, A.; Rajab Khalilpour, K.; Milani, D.; Panahi, M. Trends in CO2 Conversion and Utilization: A Review from Process Systems Perspective. *J. Environ. Chem. Eng.* **2018**, *6*, 5771–5794.

(3) Alper, E.; Yuksel Orhan, O. CO2 Utilization: Developments in Conversion Processes. *Petroleum* **2017**, *3*, 109–126.

(4) Lian, S.; Song, C.; Liu, Q.; Duan, E.; Ren, H.; Kitamura, Y. Recent Advances in Ionic Liquids-Based Hybrid Processes for CO2 Capture and Utilization. *J. Environ. Sci.* **2021**, *99*, 281–295.

(5) Macfarlane, D. R.; Forsyth, M.; Howlett, P. C.; Pringle, J. M.; Sun, J.; Annat, G.; Neil, W.; Izgorodina, E. I. Ionic Liquids in Electrochemical Devices and Processes: Managing Interfacial Electrochemistry. *Acc. Chem. Res.* **2007**, *40*, 1165–1173.

(6) Feng, J.; Zeng, S.; Feng, J.; Dong, H.; Zhang, X. CO2 Electroreduction in Ionic Liquids: A Review. *Chinese J. Chem.* **2018**, *36*, 961–970.

(7) Medina-Ramos, J.; Dimeglio, J. L.; Rosenthal, J. Efficient Reduction of CO2 to CO with High Current Density Using in Situ or Ex Situ Prepared Bi-Based Materials. *J. Am. Chem. Soc.* **2014**, *136*, 8361–8367.

(8) Medina-Ramos, J.; Pupillo, R. C.; Keane, T. P.; Dimeglio, J. L.; Rosenthal, J. Efficient Conversion of CO2 to CO Using Tin and Other Inexpensive and Easily Prepared Post-Transition Metal Catalysts. *J. Am. Chem. Soc.* **2015**, *137*, 5021–5027.

(9) Zhang, Z.; Chi, M.; Veith, G. M.; Zhang, P.; Lutterman, D. A.; Rosenthal, J.; Overbury, S. H.; Dai, S.; Zhu, H. Rational Design of Bi Nanoparticles for Efficient Electrochemical CO2 Reduction: The Elucidation of Size and Surface Condition Effects. *ACS Catal.* **2016**, *6*, 6255–6264.

(10) Aki, S. N. V. K.; Mellein, B. R.; Saurer, E. M.; Brennecke, J. F. High-Pressure Phase Behavior of Carbon Dioxide with Imidazolium-Based Ionic Liquids. *J. Phys. Chem. B* **2004**, *108*, 20355–20365.

(11) Freire, M. G.; Neves, C. M. S. S.; Marrucho, I. M.; Coutinho, A. P. Hydrolysis of Tetrafluoroborate and Hexafluorophosphate Counter Ions in Imidazolium-Based Ionic Liquids. *J. Phys. Chem. A* **2010**, *114*, 3744–3749.

(12) Dalle, K. E.; Warnan, J.; Leung, J. J.; Reuillard, B.; Karmel, I. S.; Reisner, E. Electro-and Solar-Driven Fuel Synthesis with First Row Transition Metal Complexes. *Chem. Rev.* **2019**, *119*, 2752–2875.

(13) Zhang, B.; Sun, L. Artificial Photosynthesis: Opportunities and Challenges of Molecular Catalysts. *Chem. Soc. Rev.* **2019**, *48*, 2216–2264.

(14) Nakada, A.; Kumagai, H.; Robert, M.; Ishitani, O.; Maeda, K. Molecule/Semiconductor Hybrid Materials for Visible-Light CO2 Reduction: Design Principles and Interfacial Engineering. *Acc. Mater. Res* **2021**, *2*, 458–470.

(15) Sahara, G.; Abe, R.; Higashi, M.; Morikawa, T.; Maeda, K.; Ueda, Y.; Ishitani, O. Photoelectrochemical CO2 Reduction Using a Ru(II)-Re(I) Multinuclear Metal Complex on a p-Type Semiconducting NiO Electrode. *Chem. Commun.* **2015**, *51*, 10722–10725.

(16) Sahara, G.; Kumagai, H.; Maeda, K.; Kaeffer, N.; Artero, V.; Higashi, M.;

Abe, R.; Ishitani, O. Photoelectrochemical Reduction of CO2 Coupled to Water Oxidation Using a Photocathode with a Ru(II)-Re(I) Complex Photocatalyst and a CoOx/TaON Photoanode. *J. Am. Chem. Soc.* **2016**, *138*, 14152–14158.

(17) Kumagai, H.; Sahara, G.; Maeda, K.; Higashi, M.; Abe, R.; Ishitani, O. Hybrid Photocathode Consisting of a CuGaO2 P-Type Semiconductor and a Ru(II)-Re(I) Supramolecular Photocatalyst: Non-Biased Visible-Light-Driven CO2 Reduction with Water Oxidation. *Chem. Sci.* **2017**, *8*, 4242–4249.

(18) Li, T. T.; Shan, B.; Meyer, T. J. Stable Molecular Photocathode for Solar-Driven CO2 Reduction in Aqueous Solutions. *ACS Energy Lett.* **2019**, *4*, 629–636.

(19) Kamata, R.; Kumagai, H.; Yamazaki, Y.; Sahara, G.; Ishitani, O. Photoelectrochemical CO2 Reduction Using a Ru(II)-Re(I) Supramolecular Photocatalyst Connected to a Vinyl Polymer on a NiO Electrode. *ACS Appl. Mater. Interfaces* **2019**, *11*, 5632–5641.

(20) Kamata, R.; Kumagai, H.; Yamazaki, Y.; Higashi, M.; Abe, R.; Ishitani, O. Durable Photoelectrochemical CO2 Reduction with Water Oxidation Using a Visible-Light Driven Molecular Photocathode. *J. Mater. Chem. A* **2021**, *9*, 1517–1529.

(21) Nandy, S.; Banerjee, A.; Fortunato, E.; Martins, R. A Review on Cu₂O and Cu^I-Based <I>p</I>-Type Semiconducting Transparent Oxide Materials: Promising Candidates for New Generation Oxide Based Electronics. *Rev. Adv. Sci. Eng.* **2013**, *2*, 273–304.

(22) Ueda, K.; Hase, T.; Yanagi, H.; Kawazoe, H.; Hosono, H.; Ohta, H.; Orita, M.; Hirano, M. Epitaxial Growth of Transparent P-Type Conducting

CuGaO2 Thin Films on Sapphire (001) Substrates by Pulsed Laser Deposition. *J. Appl. Phys.* **2001**, *89*, 1790.

(23) Yanagi, H.; Kawazoe, H.; Kudo, A.; Yasukawa, M.; Hosono, H. Chemical Design and Thin Film Preparation of P-Type Conductive Transparent Oxides. *J. Electroceramics* **2000**, *4*, 407–414.

(24) Yu, M.; Natu, G.; Ji, Z.; Wu, Y. P-Type Dye-Sensitized Solar Cells Based on Delafossite CuGaO 2 Nanoplates with Saturation Photovoltages Exceeding 460 MV. *J. Phys. Chem. Lett.* **2012**, *3*, 1074–1078.

(25) Renaud, A.; Chavillon, B.; Le Pleux, L.; Pellegrin, Y.; Blart, E.; Boujtita, M.; Pauporté, T.; Cario, L.; Jobic, S.; Odobel, F. CuGaO2: A Promising Alternative for NiO in p-Type Dye Solar Cells. *J. Mater. Chem.* **2012**, *22*, 14353–14356.

(26) Toe, C. Y.; Zheng, Z.; Wu, H.; Scott, J.; Amal, R.; Ng, Y. H. Photocorrosion Processes Photocorrosion of Cuprous Oxide in Hydrogen Production : Rationalising Self-Oxidation or Self-Reduction. *Angew. Chem. Int. Ed.* **2018**, *57*, 13613–13617.

(27) Zhang, S. N.; Li, M.; Hua, B.; Duan, N.; Ding, S.; Bergens, S.; Shankar, K.; Luo, J. L. A Rational Design of Cu2O−SnO2 Core-Shell Catalyst for Highly Selective CO2-to-CO Conversion. *ChemCatChem* **2019**, *11*, 4147–4153.

(28) Guzmán, H.; Zammillo, F.; Roldán, D.; Galletti, C.; Russo, N.; Hernández, S. Investigation of Gas Diffusion Electrode Systems for the Electrochemical CO2 Conversion. *Catalysts* **2021**, *11*, 482.

(29) Lee, M.; Kim, D.; Yoon, Y. T.; Kim, Y. Il. Photoelectrochemical Water Splitting on a Delafossite CuGaO2. *Bull. Korean Chem. Soc* **2014**, *35*, 3261.

(30) Lekse, J. W.; Underwood, M. K.; Lewis, J. P.; Matranga, C. Synthesis,

Characterization, Electronic Structure, and Photocatalytic Behavior of CuGaO2 and CuGa1-XFexO2 (x = 0.05, 0.10, 0.15, 0.20) Delafossites. *J. Phys. Chem. C* **2012**, *116*, 1865–1872.

(31) Choi, J.; Benedetti, T. M.; Jalili, R.; Walker, A.; Wallace, G. G.; Officer, D. L. High Performance Fe Porphyrin/Ionic Liquid Co-Catalyst for Electrochemical CO2 Reduction. *Chem. Eur. J.* **2016**, *22*, 14158–14161.

(32) Khadhraoui, A.; Gotico, P.; Boitrel, B.; Leibl, W.; Halime, Z.; Aukauloo, A. Local Ionic Liquid Environment at a Modified Iron Porphyrin Catalyst Enhances the Electrocatalytic Performance of CO2 to CO Reduction in Water. *Chem. Commun.* **2018**, *54*, 11630–11633.

(33) Li, X.; Yu, J.; Jaroniec, M.; Chen, X. Cocatalysts for Selective Photoreduction of CO2 into Solar Fuels. *Chem. Rev.* **2019**, *119*, 3962–4179.

(34) Guzm, H.; Salomone, F.; Bensaid, S.; Castellino, M.; Russo, N.; Hern, S. CO2 Conversion to Alcohols over Cu/ZnO Catalysts : Prospective Synergies between Electrocatalytic and Thermocatalytic Routes. *ACS Appl. Mater. Interfaces* **2022**, *14*, 517–530.

(35) Font, J.; De March, P.; Busqué, F.; Casas, E.; Benitez, M.; Teruel, L.; García, H. Periodic Mesoporous Silica Having Covalently Attached Tris(Bipyridine) Ruthenium Complex: Synthesis, Photovoltaic and Electrochemiluminescent Properties. *J. Mater. Chem.* **2007**, *17*, 2336–2343.

(36) Meister, S.; Reithmeier, R. O.; Ogrodnik, A.; Rieger, B. Bridging Efficiency within Multinuclear Homogeneous Catalysts in the Photocatalytic Reduction of Carbon Dioxide. *ChemCatChem* **2015**, *7*, 3562–3569.

(37) Ito, A.; Matsui, Y. Electrochemical and Spectroscopic Behaviors of a Novel Ruthenium(II) Complex with a Six-Membered Chelate Structure. *Inorg. Chem.* **2019**, *58*, 10436–10443.

(38) Gillaizeau-Gauthier, I.; Odobel, F.; Alebbi, M.; Argazzi, R.; Costa, E.; Bignozzi, C. A.; Qu, P.; Meyer, G. J. Phosphonate-Based Bipyridine Dyes for Stable Photovoltaic Devices. *Inorg. Chem.* **2001**, *40*, 6073–6079.

(39) Braumüller, M.; Schulz, M.; Staniszewska, M.; Sorsche, D.; Wunderlin, M.; Popp, J.; Guthmuller, J.; Dietzek, B.; Rau, S. Synthesis and Characterization of Ruthenium and Rhenium Dyes with Phosphonate Anchoring Groups. *Dalt. Trans.* **2016**, *45*, 9216–9228.

(40) Vogler, A.; Kisslinger, J. Bipyrimidine-Bridged Rhenium(I)/Rhenium(I) and Ruthenium(II)/Rhenium(I) Complexes. Synthesis, Electronic Absorption and Emission Spectra. *Inorganica Chim. Acta* **1986**, *115*, 193–196.

Chapter 5

Molecular hybrid photoanode catalysts for efficient water oxidation reaction

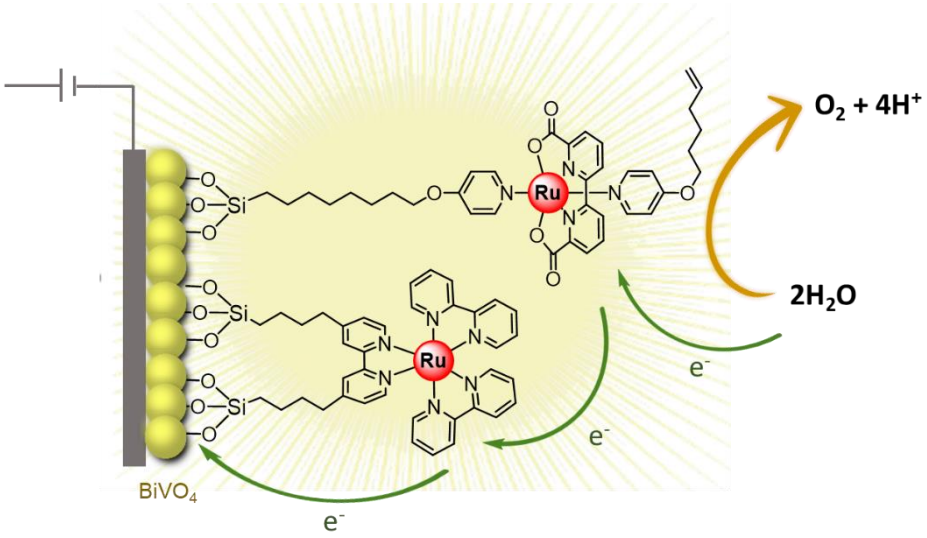

Chapter 5

Abstract

Two different immobilization strategies to anchor water oxidation molecular catalysts onto the $BiVO_4$ were studied. Both procedures were based on the functionalization of the $BiVO_4$. The first approach consisted in the functionalization of both the $BiVO_4$ and the Ru-complex with vinyl groups, and their coupling by electropolymerization procedure. In the second approach, the $BiVO_4$ was functionalized with thiol groups, and the anchoring of the Ru-complex functionalized with vinyl groups was performed via the formation of S-C bonds by photochemical thiol-ene click chemistry. The molecular hybrid photoanode materials obtained by these immobilization procedures were evaluated as catalysts in the photoelectrochemical water oxidation reaction. To date, a slight improvement of the photocurrent was obtained by the anchoring of the Ru complexes.

This work has been done in the framework of the European Union's Horizon 2020 SunCOChem project, Grant Agreement No 862192.[1]

5.1. Introduction

As mentioned in **Chapter 1**, in artificial photosynthesis, the liberation of electrons occurs by oxidation of water to form oxygen and protons, and these electrons are consumed for the reduction of target molecules, such as, CO_2 to produce added-value carbon-based molecules (*i.e.*, CO/HCOOH, CH_3OH or CH_3CH_2OH) or the reduction of protons ($[H^+]$) to generate dihydrogen. The efficiency of the water oxidation process is governed by the choice of a suitable and efficient water oxidation catalyst (WOC).[2] Water oxidation reaction takes place via transfer of four electrons, the breakage of four O-H bonds and the formation of the O=O double bond.

To the best of our knowledge, the state-of-the-art WOCs are based on Ru complexes bearing multidentate N-ligands coordinated in equatorial positions such as Ru-tda (tda = [2,2':6',2''-terpyridine]-6,6''-dicarboxylate) and Ru-bda (bda = [2,2'- bipyridine]-6,6'-dicarboxylate). These organometallic complexes were applied under homogeneous conditions, which limit their stability and recyclability.[3–5] Therefore, the immobilization of such molecular catalysts onto different semiconductor surfaces is required to obtain an efficient photoanode, and to maximize the advantages of both semiconductor and molecular water oxidation catalyst.[6,7]

Immobilized WOC systems are of interest for application in photoelectrochemical commercial cell devices. Over the last years, several examples of molecular-catalyst-modified photoanodes using Ru water oxidation catalysts and Ru visible light absorbers were reported for the preparation of efficient and stable dye sensitized photoelectrochemical (DSPEC) cell.[8–12]

To date, various immobilization strategies to anchor the molecular complexes onto semiconductor surfaces were developed to improve the stability of the

molecular catalysts. Among others, the approaches more extensively applied are: (i) covalent bonding of the molecular WOC to the semiconductor surface using anchoring groups, such as, carboxylic acids, phosphonic acid, hydroxamic acid and silatranes (Figure 1a),[13–15] (ii) electrografting of diazonium groups (Figure 1b),[16] (iii) electropolymerization of molecular complexes with previously modified surfaces (Figure 1c).[17–19] Different strategies have also been developed to stabilize the immobilized complexes: (i) via the use of a hydrophobic polymer overlayer (up to pH 12) (Figure 1d)[20] and (ii) via atomic layer deposition, where the immobilized metal complexes are covered by a metal oxide layer (wide pH range) (Figure 1e).[21–24]

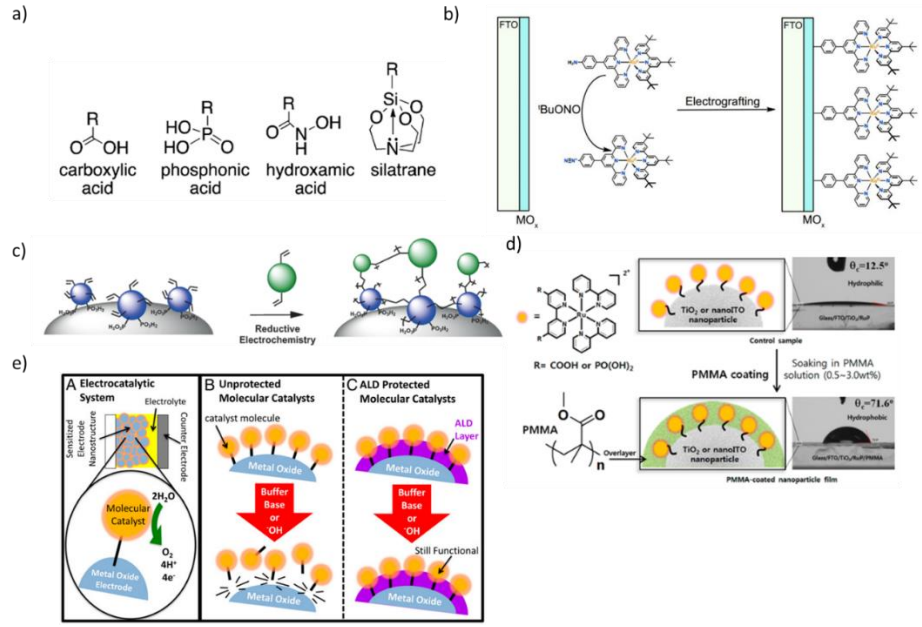

***Figure 1**: Representation of the different immobilization procedures and stabilizing methods, a) Structure of different anchor groups (reprinted from ref [15]), b) Electrografting of a diazonium (reprinted from ref [16]), c) Reductive electropolymerization of the molecular complexes (reprinted from ref [19]), d) Stabilization of the molecular complexes by coating with an hydrophobic polymer overlayer (reprinted from ref [20]) and e) Atomic layer deposition strategy to protect a catalyst surface (reprinted from ref [22]).*

Based on these immobilization procedures, dye sensitized photoelectrochemical cells (DSPEC) modified with molecular catalysts were developed. The first DSPEC cell was reported by Meyer and co-workers in 1999.[25] They prepared a photoanode based on TiO_2 modified with a Ru-Ru molecular photosensitizer-catalyst with a dark cathode (Figure 2). This system displayed very low photocurrent and no oxygen was produced. They demonstrated the possibility of construct a DSPEC cell modified with molecular complexes providing the basis for further studies.

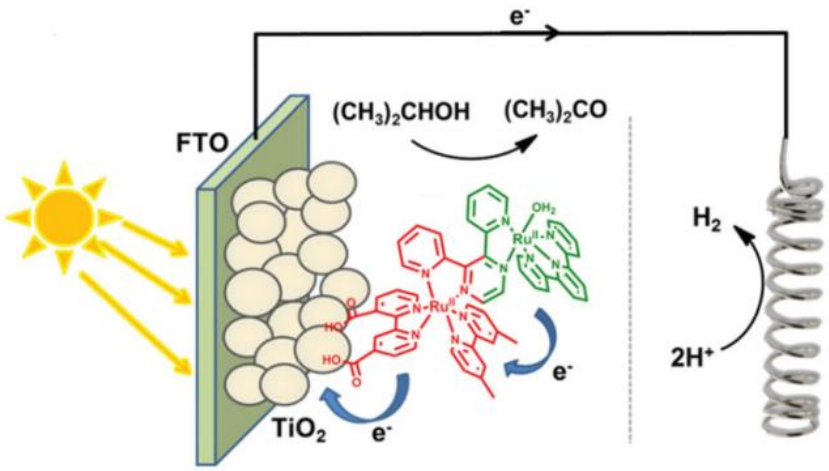

***Figure 2**: Schematic representation of the water splitting dye sensitized solar cell with the Ru–Ru chromophore-catalyst molecular assembly reported by Meyer and co-workers. Reprinted from ref* [12].

In 2009, Mallouk and co-workers reported the first visible light driven assisted by a small applied voltage water oxidation DSPEC cell.[26] This DSPEC cell consisted in a photoanode based on TiO_2, a molecular Ru chromophore and a IrO_2 water oxidation catalyst (Figure 3). Using this photoanode, they obtained a photocurrent of 30 µA for water oxidation. The same group later reported the incorporation of an electron transfer mediator, BIP tyrosine-histidine, which accelerated the electron transfer between IrO_2 and the chromophore.

The addition of this mediator improved the efficiency of the water oxidation reaction with a three-fold factor.[27]

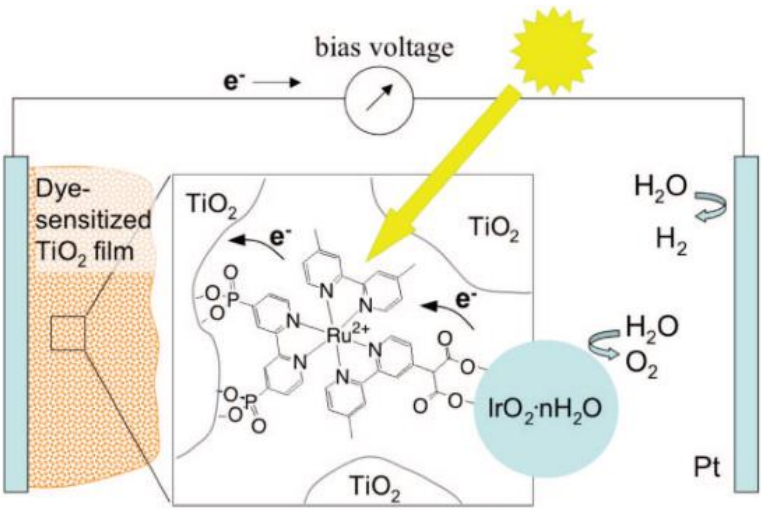

***Figure 3**: Schematic representation of the water splitting dye sensitized solar cell reported by Mallouk and co-workers. Reprinted from ref [26].*

Sun and co-workers[28] and Spiccia and co-workers[29] reported a similar DSPEC cell. In both cases, these systems were based on the immobilization of the WOC within a Nafion polymer layer, obtaining a simple method to construct a DSPEC cell (Figure 4). The photoanodes were prepared with Ru-bda WOC[28] and manganese molecular catalyst[29] immobilized onto a TiO_2 film containing a Ru photosensitizer. Using these DSPEC cells, photocurrents of a few µA were achieved due to inefficient electron transfer between the catalysts immobilized into the polymer films and the excited Ru dye absorbed onto the TiO_2.

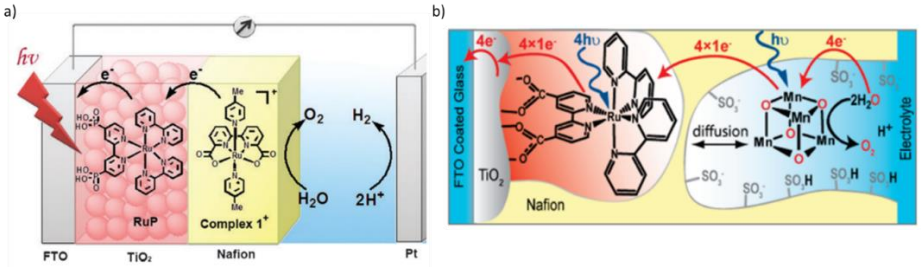

***Figure 4**: Schematic representation of the water splitting dye sensitized solar cell a) DSPEC cell reported by Sun and co-workers. Reprinted from ref [28] and b) DSPEC cell reported by Spiccia and co-workers. Reprinted from ref [29].*

In 2013, Sun and co-workers performed a great improvement in the performance of this kind of molecular catalyst modified DSPEC cells family using the Ru-dba WOC (Figure 5).[30] The Ru-dba WOC and a Ru photosensitizer were co-immobilized onto a TiO_2 surface constructing a photoactive anode. Upon application of an external bias of 0.2 V vs NHE, this system displayed an initial photocurrent higher than 1.7 $mA \cdot cm^{-2}$ with high Faradaic efficiency (FE_{O2} up to 83%). This improvement was attributed to the excellent efficiency of the Ru-dba WOC, and to the co-absorption method which did not involve Nafion polymer layer.

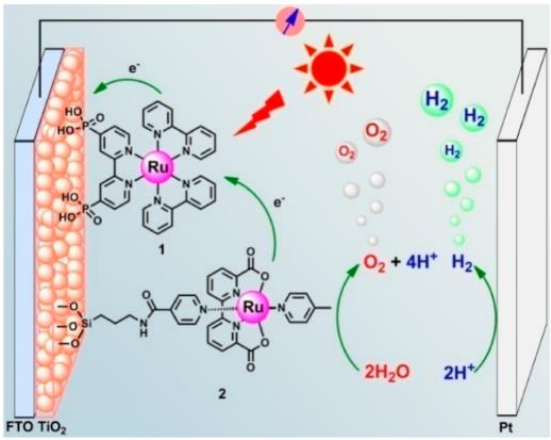

***Figure 5**: Schematic representation of the water splitting dye sensitized solar cell reported by Sun and co-workers. Reprinted from ref [30].*

Inspired by these results, Sun and co-workers performed further studies on DSPEC cell using Ru photosensitizer and Ru-dba WOC.[31] They studied the effect of the chain length spacer between the Ru-dba and the TiO_2, and they observed that the assembly containing the longer carbon chain length provided better efficiencies for light driven water oxidation, with almost the double of photocurrent density. Two possible reasons were proposed to explain this effect: (i) a long distance between Ru-dba complexes and TiO_2 was better to reduce the electron recombination, and (ii) the catalytic centers can easily swing with a flexible linkage, they can get closer to each other, and they can form the O-O bond via intermolecular reaction. Later, Sun and co-workers further studied the O-O bond formation via intramolecular radical coupling using a binuclear catalyst (Figure 6).[32] Using this binuclear catalyst, a higher photocurrent was obtained. The photocurrent was almost twice that using the mononuclear catalyst. Moreover, higher faradaic efficiencies were obtained. These results obtained by Sun and co-workers fitted well the reported mechanism, where the O-O bond formation was favored through an intramolecular radical coupling.[33,34]

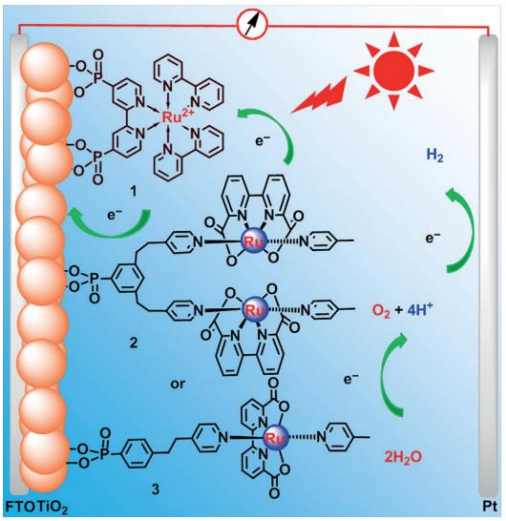

***Figure 6**: Schematic representation of the water splitting dye sensitized with the binuclear Ru WOC. Reprinted from ref [32].*

The co-adsorption of the photosensitizer and the WOC provided a simple and efficient route to prepare molecular-catalyst-modified photoanodes. However, this method has also some drawbacks, such as, it resulted in a decrease of light absorption, an increase of the electron recombination and a poor control over the ratios between the photosensitizer and the WOC. In this context, the use of supramolecular complexes to build hybrid photoanodes can be an interesting alternative to overcome these issues. Indeed, using supramolecular complexes, the electron recombination can only take place following two paths, as described in the Figure 7.[8]

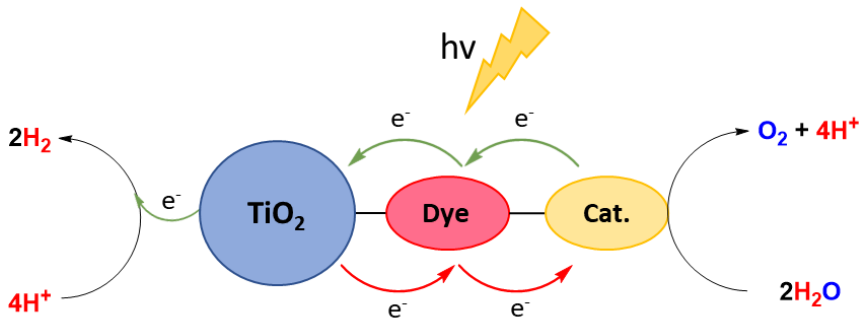

***Figure 7**: Schematic representation of a molecular modified photoanode with a supramolecular complex with the good electron transfer (green) and the electron recombination (red) processes at the photoanode for the water splitting reaction.*

Meyer and co-workers developed a molecular-catalyst modified photoanode using a Ru-Ru supramolecular complex immobilized onto TiO_2 (Figure 8).[35,36] The photosensitizer and the water oxidation catalysts are linked using a flexible saturated bridge to enable long-lived charge-separated states. Using this system they studied the electron injection, electron transfer and the recombination using transient absorption studies. With the transient absorption measurements, they demonstrated an electron injection efficiency of approximately 95% into TiO_2 followed by the transfer oxidative equivalent from the photosensitizer to the catalyst with a transfer time of 145 ps.[36] From

the spectroscopic point of view, the supramolecular complexes were proven to be effective to build an effective molecular-catalyst based photoanode.

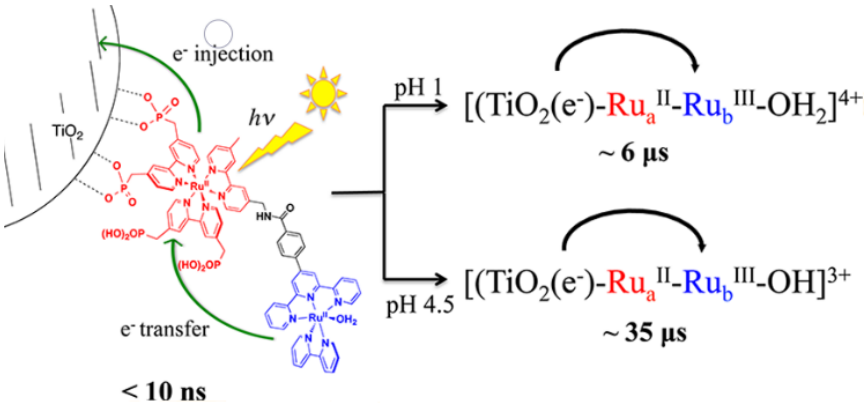

***Figure 8**: Schematic representation of the water oxidation dye sensitized photoanode with the Ru-Ru supramolecular complex. Reprinted from ref* [35].

In view of these potential benefits, various strategies were developed to construct supramolecular catalysts based on a photosensitizer linked with a water oxidation catalyst assemblies for DSPEC cells, including: (i) covalently linked photosensitizer and WOC (Figure 9a),[37–39] (ii) use of a layer-by-layer deposition assemblies with phosphonate-Zr(IV) as a bridging point between the photosensitizer and the WOC (Figure 9b),[40–42] and (iii) use of an assembly prepared by electropolymerization of the photosensitizer with the WOC (Figure 9c).[17–19]

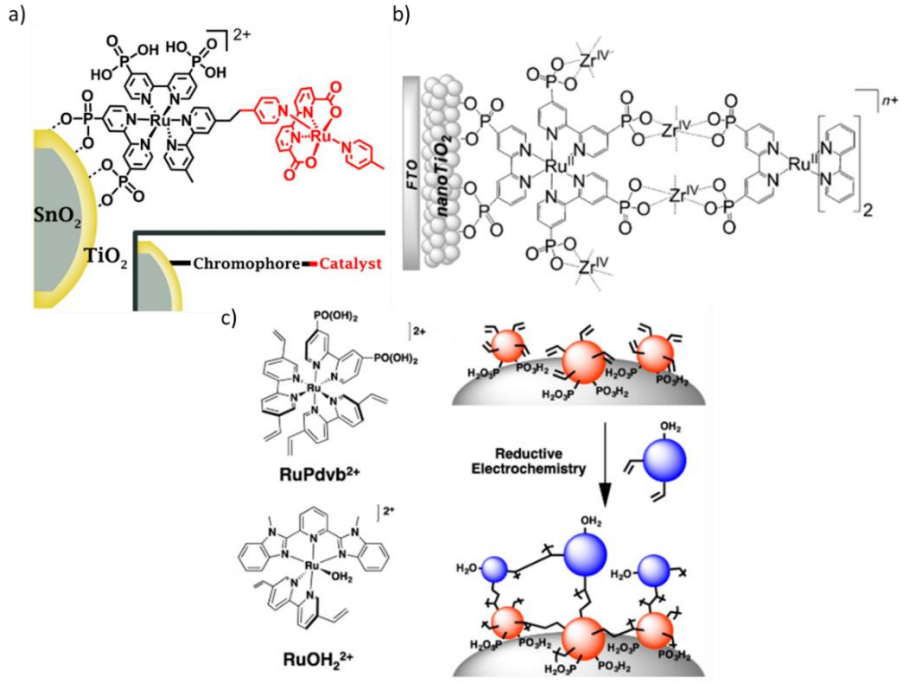

***Figure 9**: Schematic representation of the different strategies to construct a supramolecular catalyst: a) covalently linked (reprinted from [39]), b) layer-by-layer assembly using phosphonate-Zr as linker (reprinted from [40]) and c) by electropolymerization (reprinted from [18]).*

Visible light absorbing semiconductors (VLA-SC) with narrow band gap and with the appropriate energy band to drive reactions can be directly used to prepare PEC cells without the use of dyes. In the last years, n-type VLA-SC, such, as Fe_2O_3, $BiVO_4$ and WO_3, were used as photoanode to perform the water oxidation reaction.[43,44]

The efficiency of the VLA-SC was evaluated by the suitable combination of three properties: (i) good light absorption ability, (ii) efficient charge separation and migration and (iii) good energy band to drive photochemical reactions. However, evaluation of bare VLA-SCs resulted in low photocurrents due to the recombination of the photogenerated electrons and holes on the surface. The application of systems combining the use of molecular catalysts

and semiconductors reduced the side recombination processes and improved the efficiency of the process.[12]

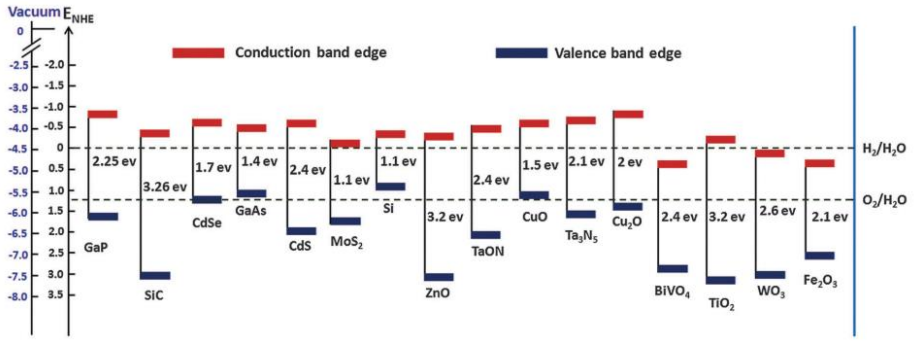

***Figure 10**: Band edge positions of different semiconductors in contact with the aqueous electrolyte at pH = 0 relative to NHE and the vacuum level. Reprinted from ref [43].*

Among the visible light absorbing semiconductor materials, $BiVO_4$ is of particular interest due to its narrow band gap, nontoxicity, low cost and the excellent photocurrent densities for water oxidation. However, the $BiVO_4$ photoanode performance is far from the theoretical capacity due to the poor electron transport, slow water oxidation kinetics and the poor charge separation. Various efforts were performed to improve the performance of the $BiVO_4$ materials based on four main strategies: (i) by metal doping of the $BiVO_4$,[45] (ii) by changing the morphology of the material,[45–47] (iii) by performing heterojunctions with conductive or semiconductive materials,[48–50] and (iv) by modifying the $BiVO_4$ surface with water oxidation catalyst (metal oxides or oxyhydroxides).[51–54]

The three first strategies (i to iii) were designed to improve the charge carrier mobility, the charge separation and/or to avoid the electron-hole recombination, whereas the last strategy (iv) was to reduce the water oxidation kinetic barrier of the reaction. However, several reports described a poor activity of this metal oxide as water oxidation catalysts, due to the slow hole transfer kinetics from the $BiVO_4$ to the metal oxide. Therefore, the metal

oxide cannot effectively compete with the direct water oxidation from $BiVO_4$. Furthermore, this effect also caused an increase of the recombination.[52,55]

On the other hand, improvements of the catalytic rates of the water oxidation reaction by three to four orders of magnitude with respect to the bare metal oxides were achieved by the anchoring of molecular water oxidation catalysts (Figure 11, and Table 1).[7,12,56]

Chapter 5

Selected examples of $BiVO_4$ hybrid photoanodes

i) Previous work using Ru water oxidation catalysts

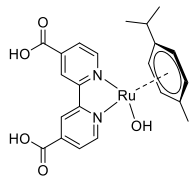

a) $BiVO_4$/RuCat

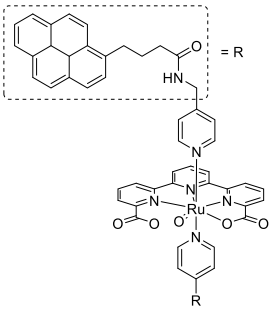

b) WO_3/$BiVO_4$/CNTf/Ru-WOC

ii) Previous work using earth-abundant water oxidation catalysts

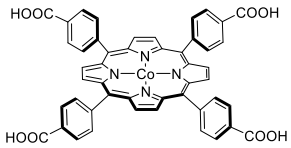

c) $BiVO_4$/Al_2O_3/CoTCPP

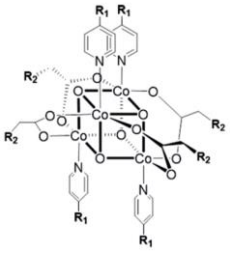

d) $BiVO_4$/Co_4O_4 cubane

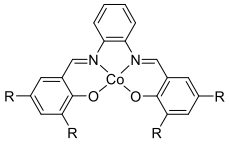

e) $BiVO_4$/Co

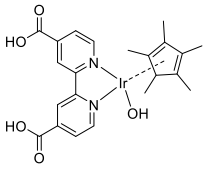

f) $BiVO_4$/TiO_2/Ir-COOH/TiO_2

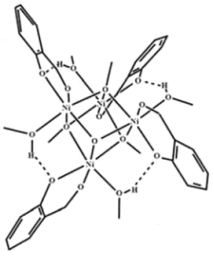

g) $BiVO_4$/Ni_4O_4 cubane

***Figure 11**: Structures of the selected examples of molecular water oxidation catalysts anchored onto $BiVO_4$ semiconductor. a) $BiVO_4$/RuCat,[57] b)WO_3/$BiVO_4$/CNT/Ru-WOC,[56] c) $BiVO_4$/Al_2O_3/CoTCPP,[58] d) $BiVO_4$/Co_4O_4 cubane,[59] e) $BiVO_4$/Co,[60] f) $BiVO_4$/TiO_2/It-COOH/TiO_2,[61] g) $BiVO_4$/Ni_4O_4 cubane.*[62]

***Table 1**: Representative summary of hybrid systems for PEC water oxidation reaction using $BiVO_4$ as semiconductor. Photocurrent value is in $mA \cdot cm^{-2}$ and it is defined as the value with potential at 0.8 V versus RHE.*

Catalyst	Photocurrent	Measured conditions	Ref.
$BiVO_4$/RuCAT	0.7	100 $mW \cdot cm^{-2}$, AM1.5G; 0.1 M phosphate buffer, pH 7	57
WO_3/$BiVO_4$/CNT/Ru_{WOC}	1.0	100 $mW \cdot cm^{-2}$, AM1.5G; 0.1 M phosphate buffer, pH 7	56
$BiVO_4$/Al_2O_3/CoTCPP	0.9	100 $mW \cdot cm^{-2}$, 0.1 M Na_2SO_4	58
$BiVO_4$/Co_4O_4	3.5	100 $mW \cdot cm^{-2}$, AM1.5G, borate buffer, pH 9.3	59
$BiVO_4$/Co	2.5	100 $mW \cdot cm^{-2}$, AM1.5G; 0.1 M phosphate buffer, pH 7	60
$BiVO_4$/TiO_2/Ir/TiO_2	1.8	100 $mW \cdot cm^{-2}$, AM1.5G; 0.2 M phosphate buffer, pH 7	61
$BiVO_4$/Ni_4O_4	2.5	100 $mW \cdot cm^{-2}$, AM1.5G; 0.2 M phosphate buffer, pH 7	62

Here, inspired by the results using the $BiVO_4$ semiconductor in the water oxidation reaction, we report the preparation of various hybrid assemblies based on $BiVO_4$ with a Ru visible light absorber and a Ru water oxidation catalyst. Electropolymerization and thiol-ene click reaction were evaluated for the immobilization of the Ru complexes. The prepared hybrid photoanodes were tested in the water oxidation reaction. A small improvement of the photocurrent respect to the bare material was observed by the anchoring of the Ru complexes.

5.2. Results and discussions

5.2.1. Synthesis of Ru molecular complexes

Three Ru molecular complexes containing a vinyl group in their structure were successfully synthetized in high yields. Their structures were assigned by combination of NMR and MS spectroscopy experiments. These complexes were: a Ru visible light absorber (**Ru_{VLA}**) and two Ru water oxidation catalysts (**Ru_{WOC} 1** and **Ru_{WOC} 2**) differing by the chain length between the ligand backbone and the vinyl group (**Ru_{WOC} 1**) and (**Ru_{WOC} 2**) (Scheme 1).

The **Ru_{VLA}** complex was prepared following a similar strategy than that explained for the Ru visible light absorber synthetized in the Chapter 4. First, the precursor [Ru(COD)Cl_2] was prepared starting from $RuCl_3 \cdot 3H_2O$. Then, the COD ligand was substituted by two 2,2'-bipyridine (bpy) ligands in 1,2-dichlorobenzene at 155 ^oC and the [Ru(bpy)Cl_2] complex was obtained. Later, the remaining chloride ligands were substituted by one 4,4'-Divinyl-2,2'-bipyridine (**bpy-V**) ligand in an acetone/water solution, and the final desired complex was obtained in 64 % isolated yield.

Concerning the two **Ru_{WOC}**, the [Ru(dmso)$_4Cl_2$] precursor was first prepared starting from the $RuCl_3 \cdot 3H_2O$. Then, two dimethyl sulfoxide (dmso) and two chloride ligands were substituted for one 2,2'-bipyridine-6,6'-dicarboxylate (**bda**) tetradentate ligand in methanol with triethylamine (Et_3N) under reflux to obtain [Ru(bda)(dmso)$_2$]. In a second step, the remaining dmso ligands were substituted by two pyridine ligands bearing a vinyl group in a methanol solution. To synthetize **Ru_{WOC} 1**, the reaction was carried at mild temperatures (ca. 40 ^oC) for 4 days. The low temperature was necessary to disfavor the metathesis reaction. The **Ru_{WOC} 1** complex was obtained in 58 % yield. In contrast, the synthesis of **Ru_{WOC} 2** was performed at 80 ^oC overnight (16h), and the complex was isolated in 57 % yield.

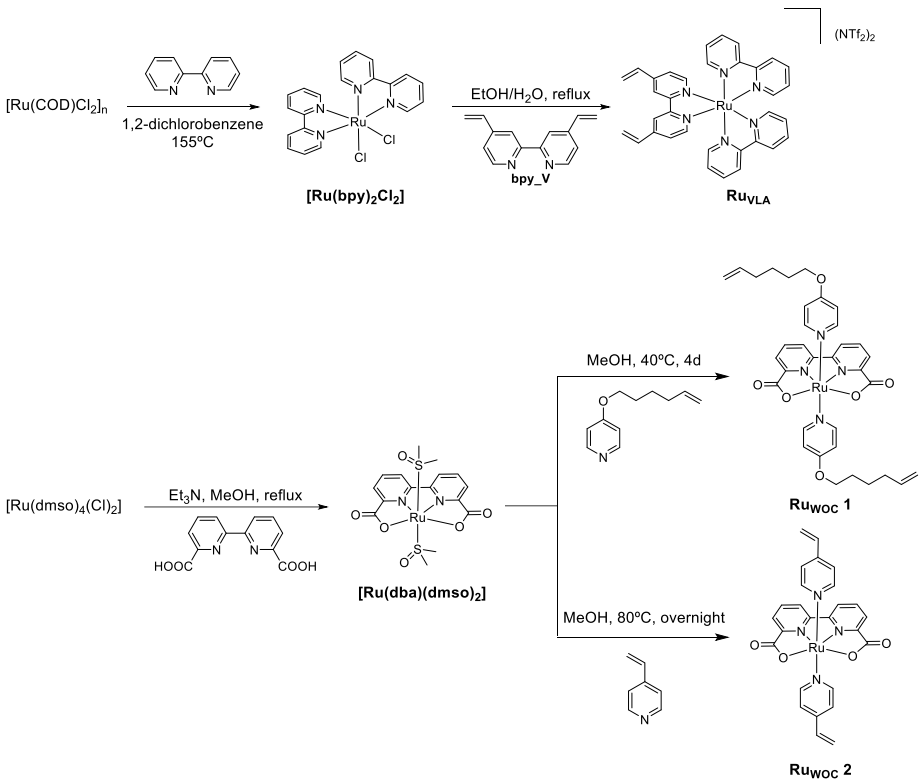

***Scheme 1**: Synthetic routes for the preparation of the Ru molecular complexes **Ru_{VLA}**, **Ru_{WOC}1-2**.*

5.2.2. $BiVO_4$ synthesis and VTES functionalization

The $BiVO_4$ semiconductor preparation and functionalization with vinyltriethoxysilane (VTES) was performed in collaboration with Dr. Alberto Lopera and Dra. Maria José López in Laurentia technologies in the framework of the Horizon 2020 project SunCOChem.[1]

Monoclinic $BiVO_4$ nanoparticles were prepared by hydrothermal routes for the direct formation of $BiVO_4$ from a low–temperature wet process. This process consisted in the reaction of an aqueous solution of $Bi(NO_3)_3$ and NH_4VO_3 at 100 ^oC. Polyethylene glycol (PEG–200) was applied in a nanometer-sized crystalline formation method from polyethylene glycol solution (NAC-PEG) (Scheme 2).[63] In a first stage, the precursor salts were dissolved in a water solution containing PEG–200, and later, this solution was stirred for 2 hours. In a

second stage, 1.5 M NaOH was added and the resulting solution was heated at 100 ºC for 2 hours obtaining a precipitate. This precipitate was filtrated and calcined giving the monoclinic phase $BiVO_4$ particles as a yellow powder.

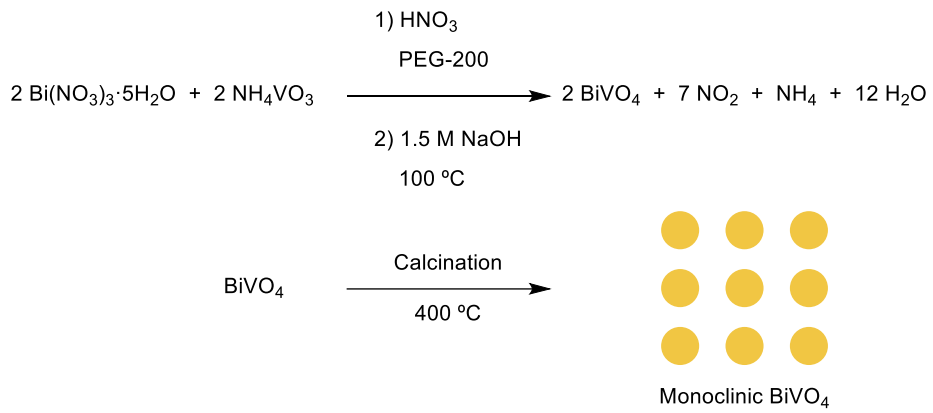

***Scheme 2**: Synthetic route for the preparation of monoclinic $BiVO_4$ particles.*

Calcination temperature was a critical parameter that controlled both the crystallinity and the BET surface (S_{BET}). A compromise between crystallinity and S_{BET} must be achieved in order to get appropriate mobility of the photogenerated charge carriers. In Table 2, the correlation data for calcination temperature, crystallinity and S_{BET} were collected. Then, calcination temperature at 400 ºC was selected in accordance with those data, as it provided high crystallinity and acceptable S_{BET}.

Scanning electron microscopy (SEM) analysis confirmed the spherical morphologies of the $BiVO_4$ particles and the average particle size was estimated in the range 5–10 µm (Figure 12).

***Table 2**: Correlation between calcination temperature (T_c), crystallinity and S_{BET}. The particle diameter was measured using X-ray diffraction analysis (XRD), and the surface area of the $BiVO_4$ particles using N_2-physisorption using the Brunauer-Emmett-Teller (BET) area model.*

Entry	T_c / °C	d_{XRD} / nm	S_{BET} / m^2g^{-1}
1	As-grown	20.5	8.8
2	400	21.6	3.6
3	500	37.6	1.3
4	600	27.7	1.2
5	700	33.8	0.6

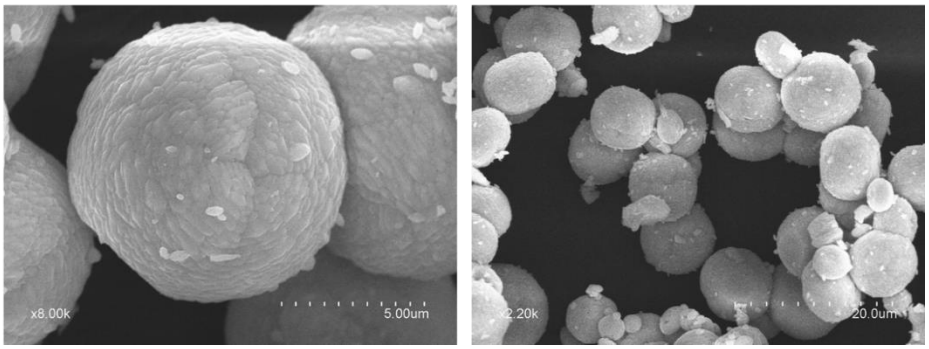

***Figure 12**: Scanning electron microscopy images of the $BiVO_4$ particles.*

The crystalline phase of the $BiVO_4$ particles was determined by X-ray diffraction (XRD). $BiVO_4$ particles exhibited the monoclinic phase after calcination at 400 °C as the patterns obtained fully agrees with the monoclinic clinobisvanite mineral (Figure 13).

Chapter 5

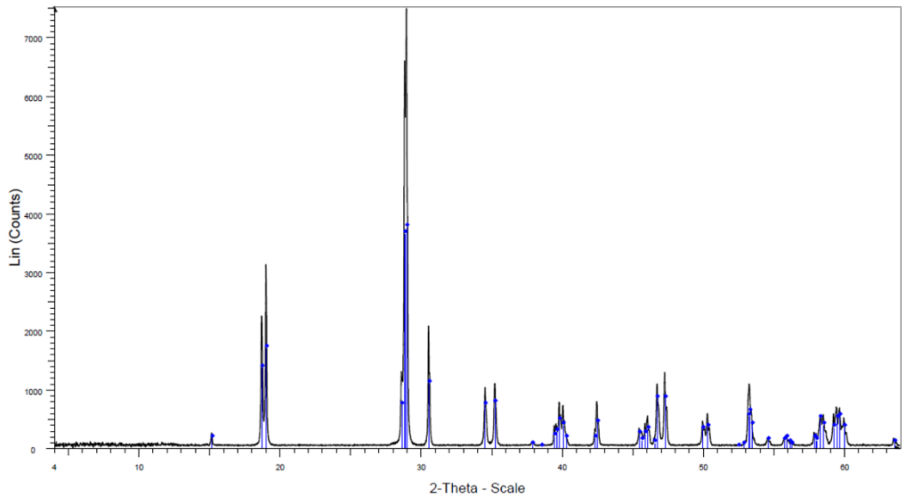

***Figure 13**: X-ray diffraction spectrum for the $BiVO_4$ particles after calcination at 400 ºC.*

Treatment with vinyltriethoxysilane (VTES) was employed to functionalize the $BiVO_4$ nanoparticles with an alkyl–siloxane anchoring group for subsequent immobilization of the molecular complexes. First, a pretreatment of the $BiVO_4$ particles with a solution of 1 mM of KOH was performed to hydroxylate the surface of the $BiVO_4$. This experiment was performed by stirring the $BiVO_4$ particles at room temperature in a 1 mM KOH solution for 2h. Then, the particles were filtrated, washed, dispersed in a solution of isopropanol/H_2O 95/5 containing 0.1 M of VTES and stirred under reflux for 2 hours (Scheme 3).

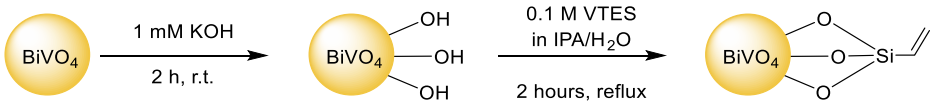

***Scheme 3**: $BiVO_4$ functionalization with VTES.*

No changes in size and shape were observed by SEM after functionalization of $BiVO_4$ with 0.1 M VTES solutions (Image 1a). Mapping experiments demonstrated the presence of silicon in $BiVO_4$–VTES samples, thus confirming the $BiVO_4$ functionalization with VTES (Image 1b). The mapping experiments also showed a homogeneous distribution of the $BiVO_4$–VTES samples.

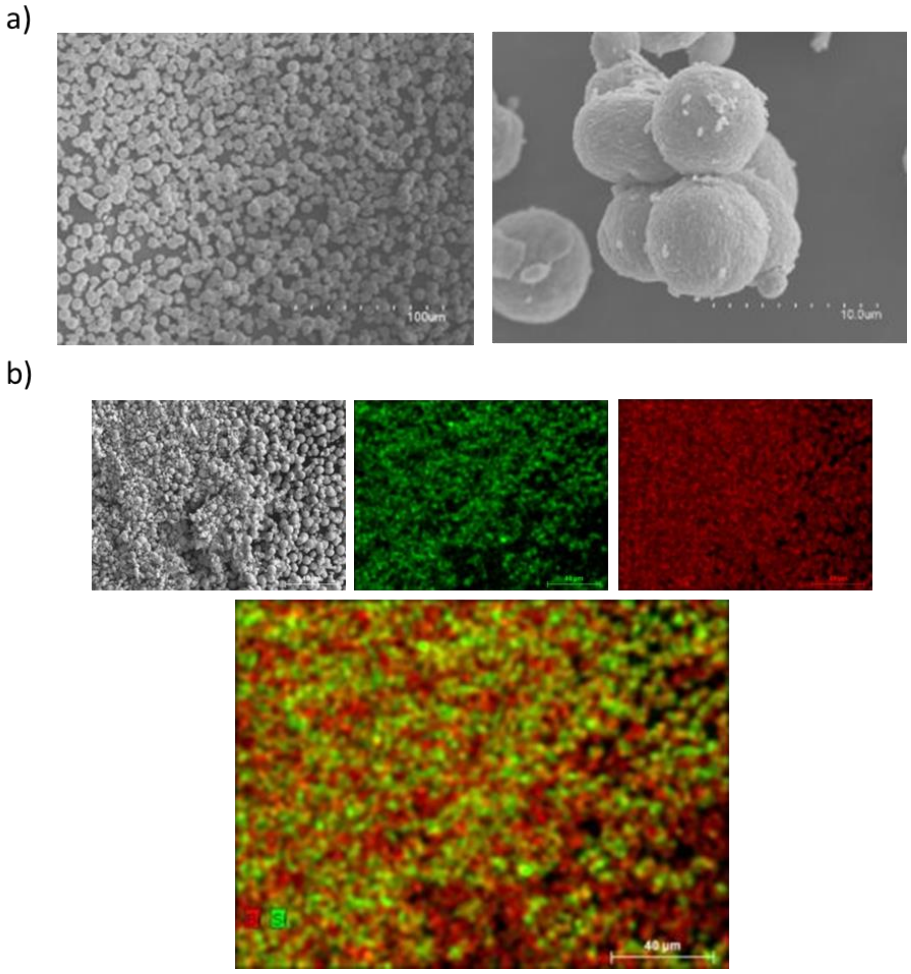

***Image 1**: a) Scanning electron microscopy images captured for the $BiVO_4$ nanoparticles functionalized with 0.1 M VTES solution. b) Mapping experiments for $BiVO_4$ nanoparticles functionalized with 0.1 M VTES. Red color indicates bismuth presence. Green color indicates silicon presence.*

5.2.3. Preparation of Ru@$BiVO_4$-VTES photoanodes

A 3 steps procedure was followed to immobilize the different Ru complexes onto the VTES functionalized $BiVO_4$ ($BiVO_4$-VTES) (Scheme 4a):

1) Dispersion of the $BiVO_4$-VTES particles in a mixture of ethylcellulose, ethanol and terpineol provided a fluid paste/ink with the help of

a planetary ball mill. The solvent was removed to obtain the desired ink. The ink was prepared by Dra. Stephanie Narbey and co-workers in Solaronix.[1]

2) The prepared ink was screen-printed onto an FTO-coated glass substrate using a commercial Coatmaster setup and heat-treated at 500 ^{o}C to form the $BiVO_4$-VTES photoanode. The heat-treatment at 500 ^{o}C was carried out to remove all the binders present in the ink and to improve the carrier transport and crystallinity of the $BiVO_4$.[64] The photoanode preparation was performed by Dr. Abdi Fatwa and co-workers in Helmholtz-Zentrum Berlin (HZB).[1]

3) With the prepared $BiVO_4$-VTES photoanodes, the electropolymerization of the synthetized Ru complexes was carried out by performing cyclic voltammetries using the prepared photoanodes as working electrode immersed in a solution of the synthetized Ru complexes.

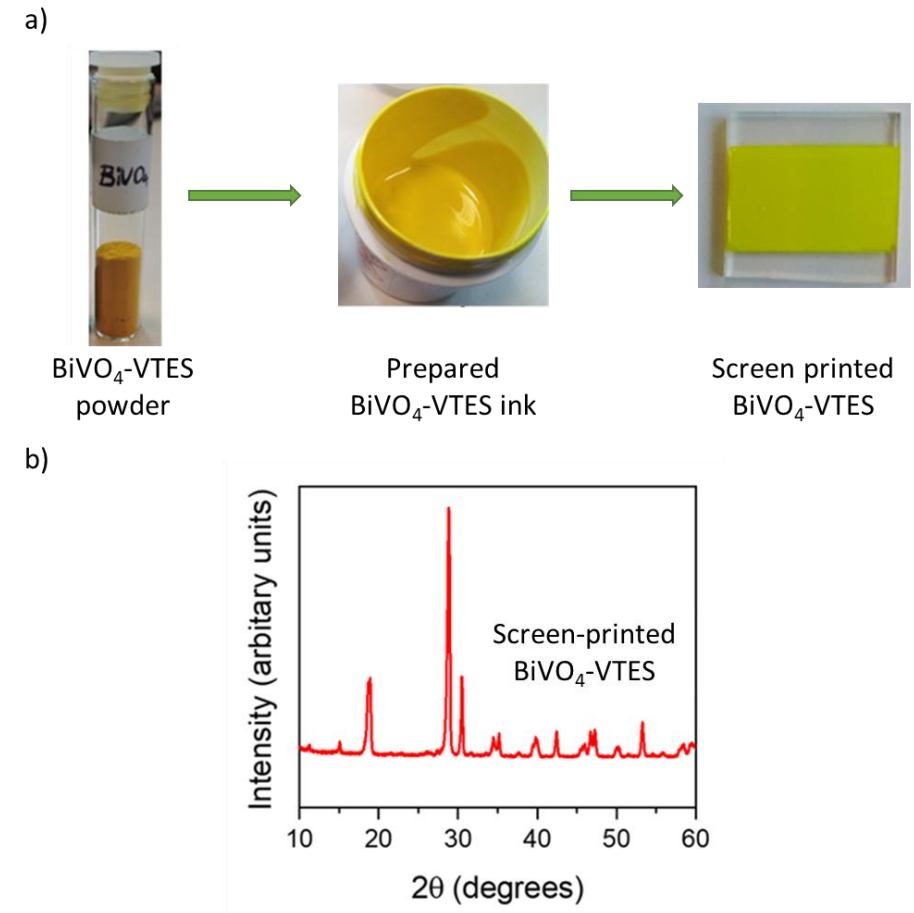

***Scheme 4**: Established deposition procedure for $BiVO_4$ films. (b) X-ray diffractograms of doctor-bladed $BiVO_4$ heat-treated at 500 °C.*

Before the electropolymerization experiment, the structure of the prepared $BiVO_4$-VTES photoanode obtained after the annealing at 500 °C was studied by X-ray diffraction spectroscopy (XRD). The XRD diffractogram displayed only the diffraction peaks corresponding to monoclinic $BiVO_4$, which is consistent with the crystal structure of the initial powder. This result confirmed the stability of the crystal structure of the $BiVO_4$ photoanode (Scheme 4b).

Later, the prepared $BiVO_4$-VTES electrodes provided by HZB were used to perform the electropolymerization experiments. These experiments were

performed by immersing the electrodes into a solution of the Ru complex and performing 60 scans from -1.9 to 0 V vs $Ag/AgNO_3$ (Scheme 5).[65]

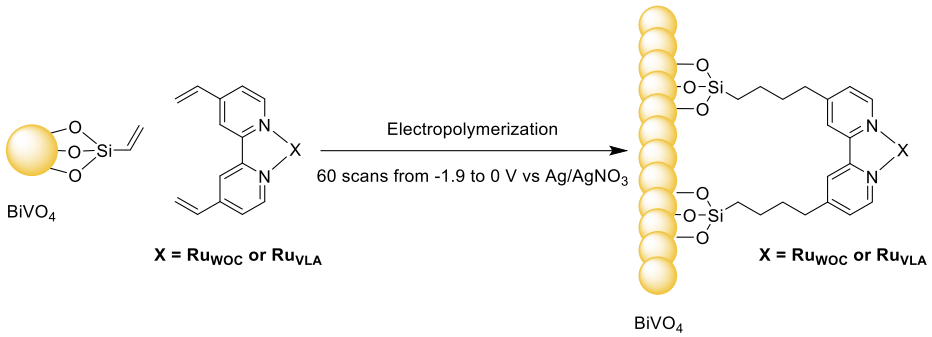

***Scheme 5**: Electropolymerization scheme using $BiVO_4$-VTES electrodes.*

The efficiency of the electropolymerization procedure was corroborated by the continuous enhancement of the current densities after each scan (Figure 14). This observation suggested the in-situ formation of polymeric layers onto the surface of the electrode. Furthermore, with the presence of multiple vinyl groups in the different Ru complexes, a combination of interconnected complexes can be obtained, forming a final layer-by-layer assembly of polymer achieving high molecular loadings onto the surface of the electrodes.[65,66]

Three different photoelectrodes were prepared by immobilization of a series of homogeneous complexes onto the $BiVO_4$-VTES: (i) immobilization of the Ru visible light absorber (**Ru_{VLA}**) complex (**Ru_{VLA}@$BiVO_4$-VTES**); (ii) Immobilization of the Ru water oxidation catalyst 1 (**Ru_{WOC} 1**) complex (**Ru_{WOC}@$BiVO_4$-VTES**); and (iii) co-immobilization of Ru visible light absorber (**Ru_{VLA}**) complex and Ru water oxidation catalyst 1 (**Ru_{WOC} 1**) performing 60 scans for each (**Ru_{VLA}+Ru_{WOC}@$BiVO_4$-VTES**).

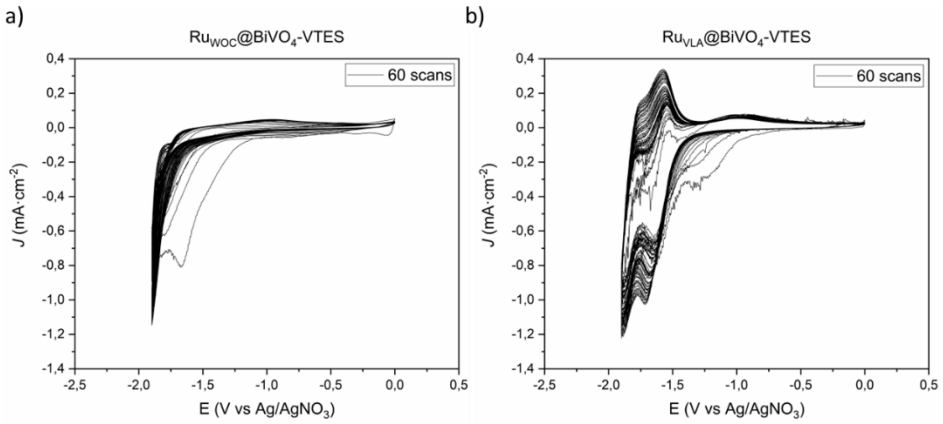

***Figure 14**: Cyclic voltammogram graphics of a) Electropolymerization of the **Ru_{WOC}** 1 complex; b) Electropolymerization of the **Ru_{VLA}** complex. All the CV are performed from 0 to -1.9 V vs Ag/$AgNO_3$ in an acetonitrile solution containing 0.1 M TBA·PF_6 and 0.5 mM of the corresponding complex.*

The electrodes prepared by electropolymerization experiments were analyzed by FESEM-EDX but no Ru was observed as the peak of the Ru is overlapped by the bismuth peak and made impossible the quantification of the Ru by EDX analysis. To determine the Ru loading, a XPS analysis of each electrode was performed (Table 3) and high ratios Ru:Bi were detected at the surface of the **Ru_{VLA}@$BiVO_4$-VTES** electrode (1.38:1 Ru:Bi).

In contrast, in the **Ru_{WOC}@$BiVO_4$-VTES** electrode, a very low Ru loading was detected (0.055:1 Ru:Bi), and it was therefore concluded that the immobilization of **Ru_{WOC} 1** complex by electropolymerization was unsuccessful. During the attempt of electropolymerization, a color change of the solution was observed, which could indicate that the **Ru_{WOC} 1** complex is not stable under electropolymerization conditions.

For the **Ru_{VLA}+Ru_{WOC}@$BiVO_4$-VTES** electrode, high amounts of Ru were measured (1.66:1 Ru:Bi). In view of the unsuccessful anchoring of **Ru_{WOC} 1,** the high Ru loading was mainly attributed to the immobilization of **Ru_{VLA}**.

***Table 3**: Ru:Bi ratios of the different prepared photoanodes. The ratios Ru:Bi were quantified by X-ray photoelectron spectroscopy (XPS) analysis.*

Entry	Electrode	Ru:Bi
1	Ru_{WOC}@$BiVO_4$-VTES	0.055 ± 0.001
2	Ru_{VLA}@$BiVO_4$-VTES	1.38 ± 0.03
3	Ru_{VLA}+Ru_{WOC}@$BiVO_4$-VTES	1.66 ± 0.04

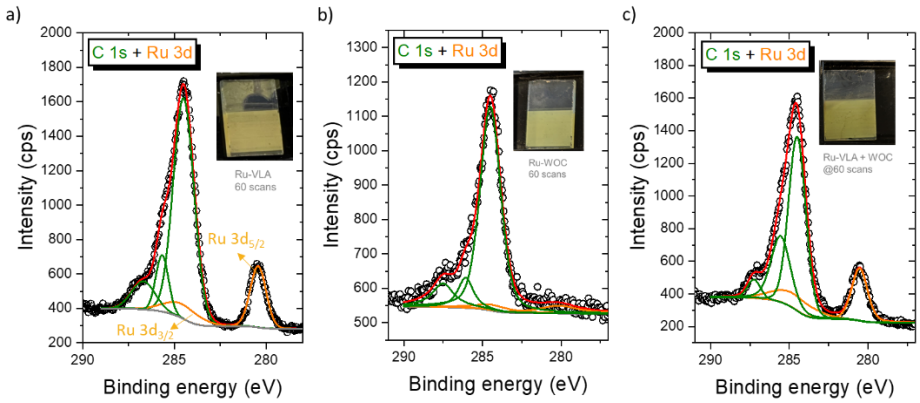

***Figure 15**: XPS analysis of a) Ru_{VLA}@$BiVO_4$-VTES; b) Ru_{WOC}@$BiVO_4$-VTES; c) Ru_{VLA}+Ru_{WOC}@$BiVO_4$-VTES electrodes.*

5.2.4. Photoelectrochemical tests using Ru@$BiVO_4$-VTES

The prepared photoanodes were tested in Helmholtz-Zentrum Berlin using a one-chamber custom Teflon cell with a transparent quartz window for sample illumination in a three-electrode configuration with the prepared photoanodes as working electrode, Pt wire as counter electrode and Ag/AgCl electrode as reference electrode (See experimental part for a detailed description). Measurements were performed under light (AM1.5 illumination, 100 mW/cm^2) using a calibrated Xenon solar simulator. The electrolyte used was 0.1 M potassium borate buffer (KB_i, pH ~ 9).

All the prepared samples were tested under simulated solar light (Figure 16). However, low photocurrents were observed in all cases. Using **Ru_{VLA}@$BiVO_4$-VTES**, a small increase in photocurrent was observed but as a general trend, the photocurrent was unaffected by the addition of the Ru complexes, which was attributed to the very low **Ru_{WOC}** loading onto the electrode.

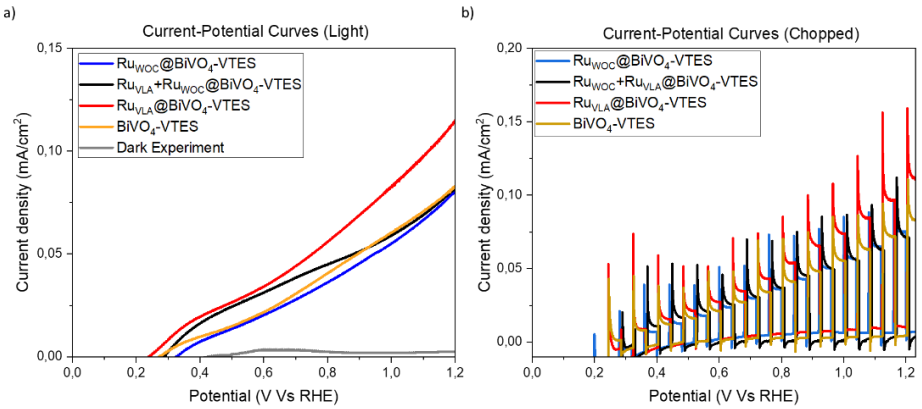

***Figure 16**: AM1.5 photocurrent-voltage curves of all the prepared photoanodes using 0.1 M potassium borate buffer as electrolyte. a) Experiment under continuous light irradiation, b) Chopped dark-light experiment.*

As the photocurrents were unaffected by the addition of the Ru complexes, as a probable result of the unsuccessful immobilization of the **Ru_{WOC}**, alternative immobilization methods were explored with the aim to increase the Ru loading onto the electrode surface.

5.2.5. Photoanode preparation and photoelectrochemical tests using Ru_{WOC} 2 complex

The immobilization of **Ru_{WOC} 2** was attempted by electropolymerization procedure. **Ru_{WOC} 2** is a water oxidation catalyst that was previously reported and immobilized by electropolymerization onto different material.[67–69]

First, the photoanode was prepared using the $BiVO_4$-VTES electrodes provided by HZB. The $BiVO_4$-VTES electrode was immersed in a 0.5 mM solution of the

Ru_{woc} 2 complex and cyclic voltammetries from -2.0 to 0.2 V vs $Ag/AgNO_3$ were performed over a total of 60 cycles to form the **Ru_{woc}2@$BiVO_4$-VTES** photoanode.

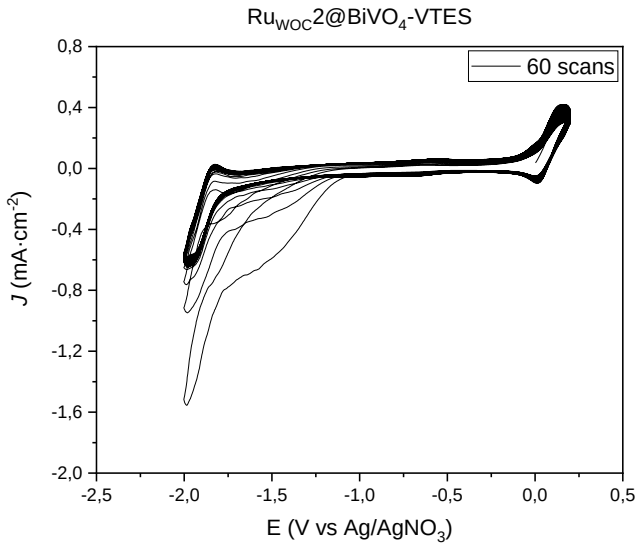

***Figure 17**: Cyclic voltammogram graphic of electropolymerization of the **Ru_{woc} 2** complex. The CV are performed from 0.2 to -2.0 V vs $Ag/AgNO_3$ in an acetonitrile solution containing 0.1 M $Et_4N{\cdot}PF_6$ and 0.5 mM of the **Ru_{woc} 2** complex.*

The electropolymerization efficiency was corroborated by the continuous enhancement of the current densities after each scan, suggesting the in-situ formation of polymeric layers onto electrode surface (Figure 17). The resulting electrode was then sent to HZB for Ru loading analysis by XPS. However, to date, the XPS results for this electrode were not received.

Nevertheless, the prepared photoanode was tested in HZB using a custom Teflon cell in a three-electrode configuration with the prepared photoanode as the working electrode, Pt wire as the counter electrode and Ag/AgCl electrode as the reference electrode. Measurements were carried out under chopped light irradiation (AM1.5 illumination, 100 mW/cm^2) using a calibrated

Xenon solar simulator. The electrolyte used was 0.1 M potassium borate buffer (KB_i, pH ~ 9).

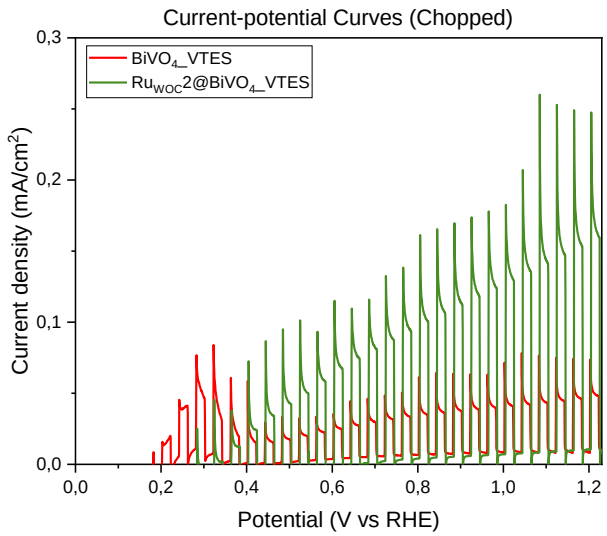

***Figure 18**: AM1.5 photocurrent-voltage curves under chopped dark-light irradiation of the prepared photoanodes using 0.1 M potassium borate buffer.*

A clear improvement of the photocurrent was observed using the electrode bearing the **Ru_{woc} 2** molecular complex (Figure 18) compared with the performance of the bare $BiVO_4$. Approximately the double of the photocurrent was achieved. This result demonstrated a positive effect of the anchoring of the Ru complex onto the $BiVO_4$ although the photocurrent obtained remained lower than those reported in the literature (Table 1).

In view of the low photocurrents obtained, a new immobilization procedure was explored for the **Ru_{woc}** molecular catalysts.

5.2.6. Preparation of Ru@$BiVO_4$-MPTMS photoanodes

To improve the immobilization of the Ru molecular complexes, a distinct functionalization of the $BiVO_4$ was tested and (3-

Mercaptopropyl)trimethoxysilane (MPTMS) was used instead of the vinyltriethoxysilane (VTES).

Using the MPTMS coupling agent, a thiol-ene click reaction was performed between the thiol group of the MPTMS and the double bond present in the Ru complexes.[70,71]

First, the thiol-ene click reaction was probed under homogeneous conditions, using the MPTMS, 1-octene and 2,2-Dimethoxy-2-phenylacetophenone (DMAP) as photoinitiator.

The mixture was irradiated for 5h with a 100 W xenon lamp and the reaction was monitored by ^{1}H NMR. After 5 h of irradiation, the thiol-ene process resulted in the quantitative transformation of the alkene into the thiol-ether compound (Figure 19).

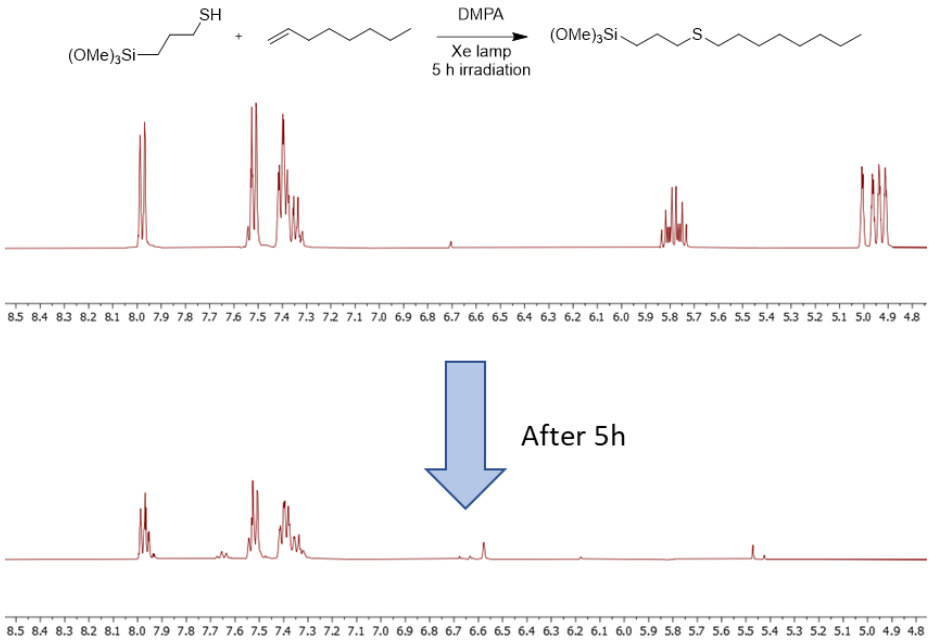

***Figure 19**: Thiol-ene click reaction using MPTMS, 1-octene and DMPA in EtOH. ^{1}H NMR of the thiol-ene click reaction mixture before irradiating light and (top) and ^{1}H NMR of the thiol-ene click reaction after 5 h of light irradiation (bottom).*

In view of this result, the functionalization of $BiVO_4$ with MPTMS was tested. The immobilization of the MPTMS was performed using a similar procedure than that applied in the VTES immobilization. First, a pretreatment of the $BiVO_4$ particles with 1 mM of KOH was performed to hydroxylate the surface of the $BiVO_4$. Then, the hydroxylated $BiVO_4$ particles were dispersed in a solution of isopropanol/H_2O 95/5 containing 0.1 M or 1.0 M of MPTMS and the mixture was stirred overnight at reflux (Scheme 6).

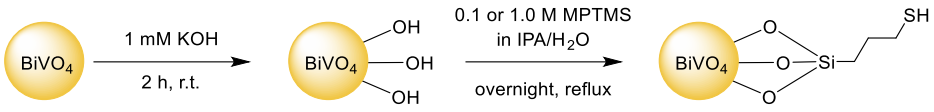

***Scheme 6**: $BiVO_4$ functionalization with MPTMS.*

After the reactions, the $BiVO_4$-MPTMS particles were characterized by FESEM and in both cases, using 0.1 M and 1.0 M of MPTMS, no changes in size or shape were observed (Image 2a).

However, the EDX analysis revealed very low amounts of MPTMS on the $BiVO_4$ with less than 1% of Si and S detected by EDX (Image 2b). This behavior was attributed to the low surface area of the $BiVO_4$ (3.6 $m^2 \cdot g^{-1}$) resulting in very low loadings of MPTMS.

Chapter 5

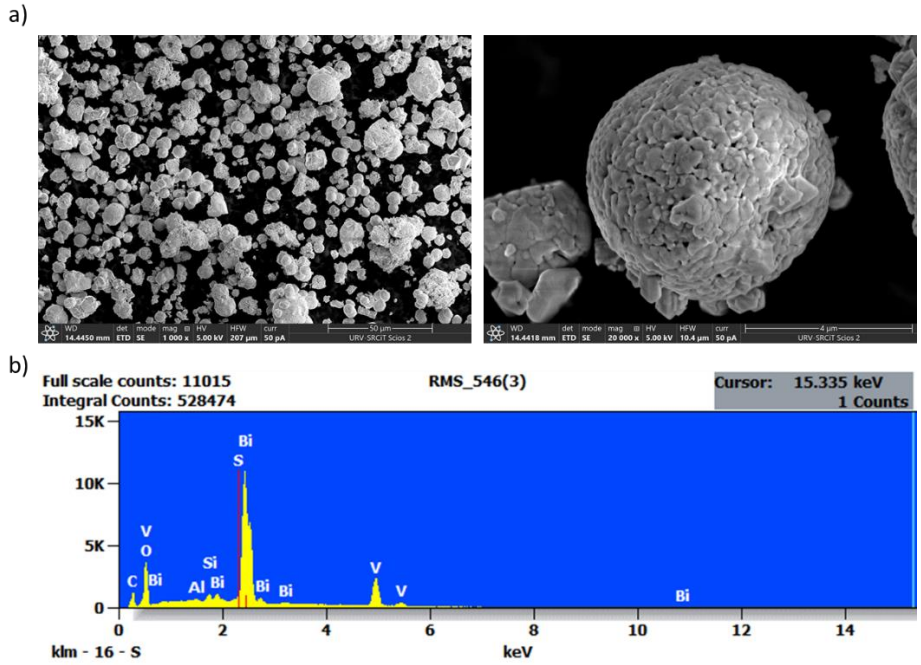

***Image 2**: a) FESEM images captured for the $BiVO_4$ nanoparticles functionalized with MPTMS solution. b) EDX analysis for $BiVO_4$ nanoparticles functionalized with MPTMS.*

Two alternative electrode preparation procedures were performed to enhance the immobilization of the Ru complexes using the thiol-ene approach:

- **Pathway 1**: Preparation of an ink containing a mixture of $BiVO_4$ and MPTMS. Then, the airbrushing of these ink onto a FTO. Finally, the anchoring of the Ru complex on the prepared electrodes.
- **Pathway 2**: Deposition of a thin layer of Al_2O_3 onto the provided $BiVO_4$ electrodes prepared by screen printing by Dr. Abdi Fatwa and co-workers in Helmholtz-Zentrum Berlin (HZB). These electrodes should display enhanced OH functionalization, and the surface area of these electrodes should be able to reach higher amounts of MPTMS functional group.

5.2.6.1. Pathway 1: $BiVO_4$ + MPTMS ink airbrushing

An ink containing $BiVO_4$ powder, 10% w/w of MPTMS, NAFION® solution and EtOH was prepared and airbrushed onto an FTO. The prepared electrodes were analyzed by ESEM-EDX to confirm the presence of MPTMS. A molar ratio of S:Bi of 1:8.5 was estimated in the prepared electrode (Image 3). This confirmed the presence of MPTMS in the prepared electrodes.

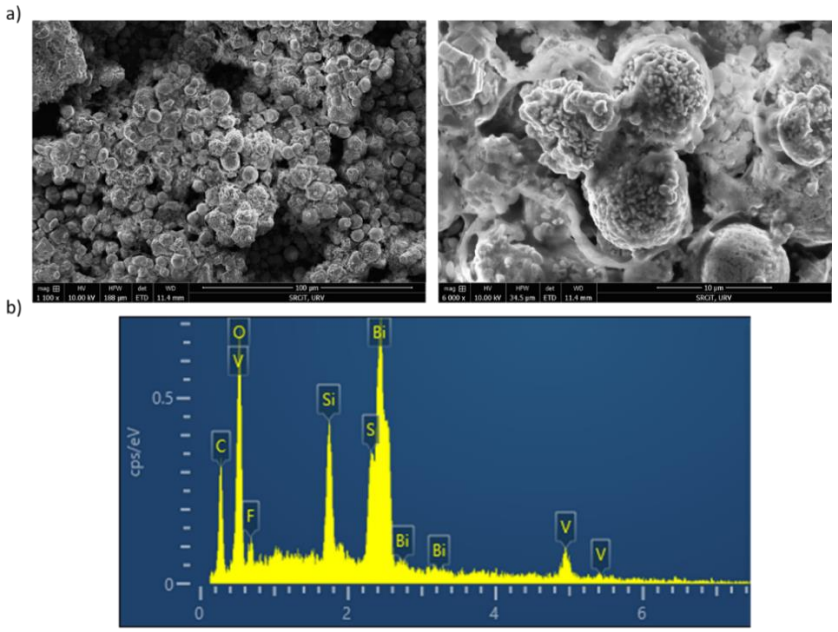

***Image 3**: a) ESEM images of the prepared electrodes by airbrushing of a $BiVO_4$ + MPTMS ink; b) EDX analysis of the prepared electrodes by airbrushing of a $BiVO_4$ + MPTMS ink.*

The prepared electrodes were first immersed in an EtOH solution (15 mL) of the corresponding Ru-complex (0.02 mmol) and DMPA (0.01 mmol). At this point, the mixture was irradiated overnight using the Xe lamp (100 W). During the reaction, a color change of the electrode from yellow to brown-red was observed (Figure 20) confirming the immobilization of the Ru complexes. This result confirmed the efficiency of the immobilization of Ru complexes. Furthermore, this confirmed that the immobilization procedure can be applied

onto the surface of the electrode and not only under homogeneous conditions.

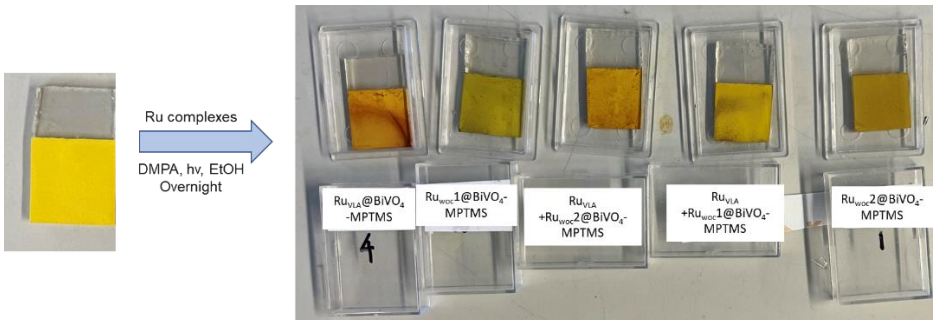

***Figure 20**: Images of the $BiVO_4$-MPTMS electrodes before and after the immobilization of the different Ru complexes by thiol-ene click chemistry.*

Various hybrid materials were prepared using this methodology: (i) Ru visible light absorber immobilized onto $BiVO_4$ (**Ru_{VLA}@$BiVO_4$-MPTMS**), (ii) Ru water oxidation catalyst 1 immobilized onto $BiVO_4$ (**Ru_{WOC}1@$BiVO_4$-MPTMS**), (iii) Ru water oxidation catalyst 2 immobilized onto $BiVO_4$ (**Ru_{WOC}2@$BiVO_4$-MPTMS**), (iv) co-immobilization of Ru visible light absorber with Ru water oxidation catalyst 1 (**Ru_{VLA}+Ru_{WOC}1@$BiVO_4$-MPTMS**) and (v) co-immobilization of Ru visible light absorber with Ru water oxidation catalyst 2 (**Ru_{VLA}+Ru_{WOC}2@$BiVO_4$-MPTMS**). The electrodes were sent to Helmholtz-Zentrum Berlin (HZB) to quantify the metal loading absorbed onto the semiconductor by XPS analysis. These experiments are currently in progress.

5.2.6.2. Pathway 2: Deposition of Al_2O_3 thin layer onto $BiVO_4$

The alternative approach for increasing the surface area of the screen-printed $BiVO_4$ electrodes was the deposition a thin layer of Al_2O_3 onto the electrode surface, followed by the functionalization of the coated electrodes with MPTMS, and finally, the immobilization of the Ru complexes by the thiol-ene click reaction under light irradiation conditions (Scheme 7).

Alumina (Al_2O_3) layers do not absorb in the visible light region (the band gap of Al_2O_3 was determined to be 7.0 ± 0.1 and 7.6 ± 0.1 eV for measured α- and γ-Al_2O_3, respectively[72]) and it will increase the surface area of the screen-printed $BiVO_4$ electrodes, as well as its, OH functionalization.

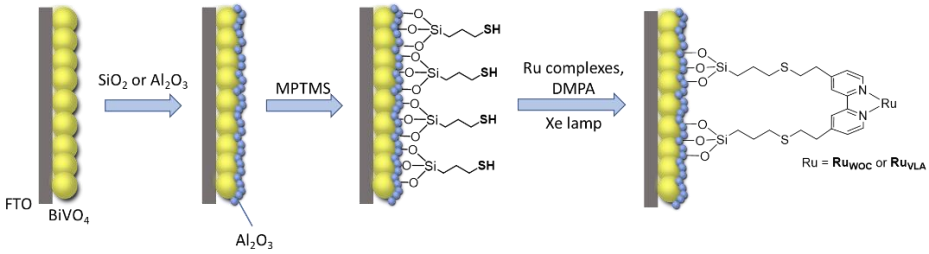

***Scheme 7**: Pathway 2 procedure: 1) deposition of a Al_2O_3 thin layer; 2) functionalization with MPTMS; 3) immobilization of the Ru complexes by thiol-ene click reaction.*

The deposition of a layer of Al_2O_3 was performed by impregnation of a solution containing aluminum tri-sec-butoxide followed by calcination at 200ºC.[73] Analysis by ESEM-EDX (Image 4a and Image 4b) confirmed the presence of Al_2O_3, showing a homogeneous deposition of Al_2O_3 on the electrode surface. An approximate ratio Al:Bi 1:6 was measured by EDX analysis.

Chapter 5

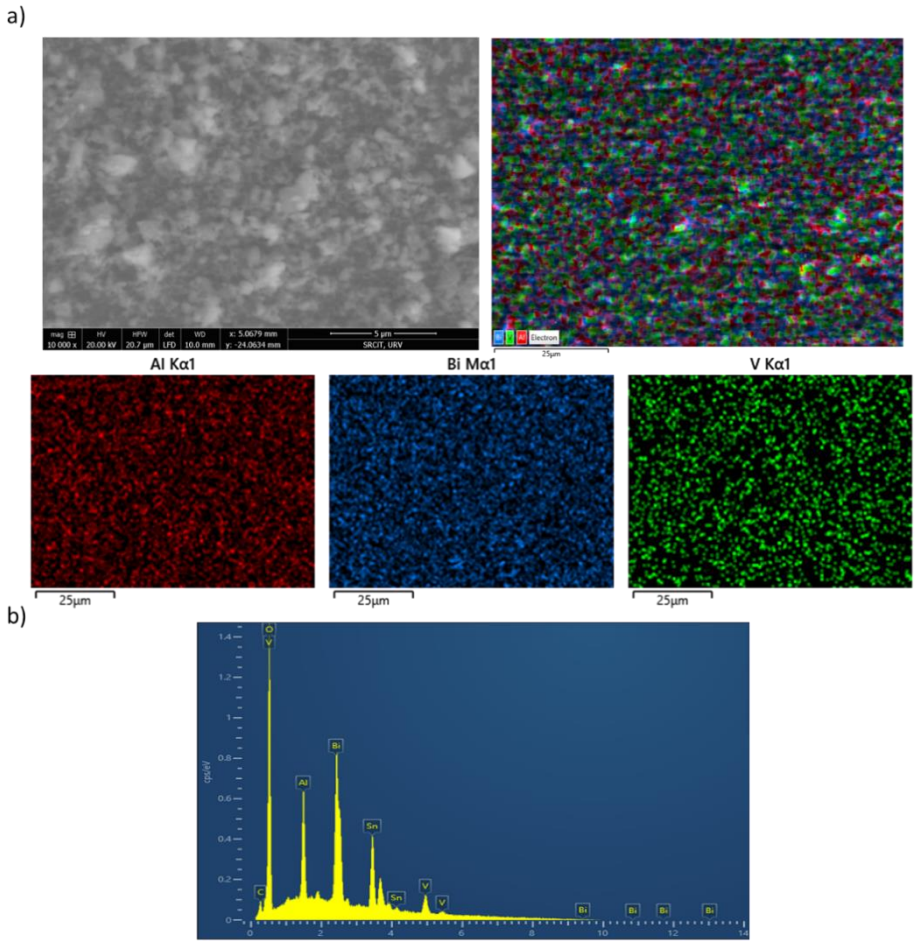

***Image 4**: a) ESEM image and mapping experiments of the screen-printed prepared $BiVO_4$ electrode after deposition of Al_2O_3, Aluminum (red), bismuth (blue), vanadate (green); b) EDX analysis of screen-printed prepared $BiVO_4$ electrode after deposition of Al_2O_3 performed at 10 KeV.*

The coated electrodes were then functionalized with MPTMS by immersion of the electrodes onto a 0.1 M MPTMS solution of 95:5 EtOH/H_2O. The solution was stirred overnight at 60 ^oC, and the electrode cleaned with EtOH. ESEM-EDX analysis indicated the presence of S and Si (**Image 5**). It should be highlighted that some of the detected Si could come from the FTO glass, although S can only arise from the MPTMS molecule. The ratio S:Bi measured was approximately 1:14. However, since the MPTMS is only located at the

surface (few nanometers) of the electrode, the electron beam of the EDX can go through the MPTMS and as such, the MPTMS is only partially detected. Due to the lack of time, the immobilization of the other Ru complexes could not be performed using this approach.

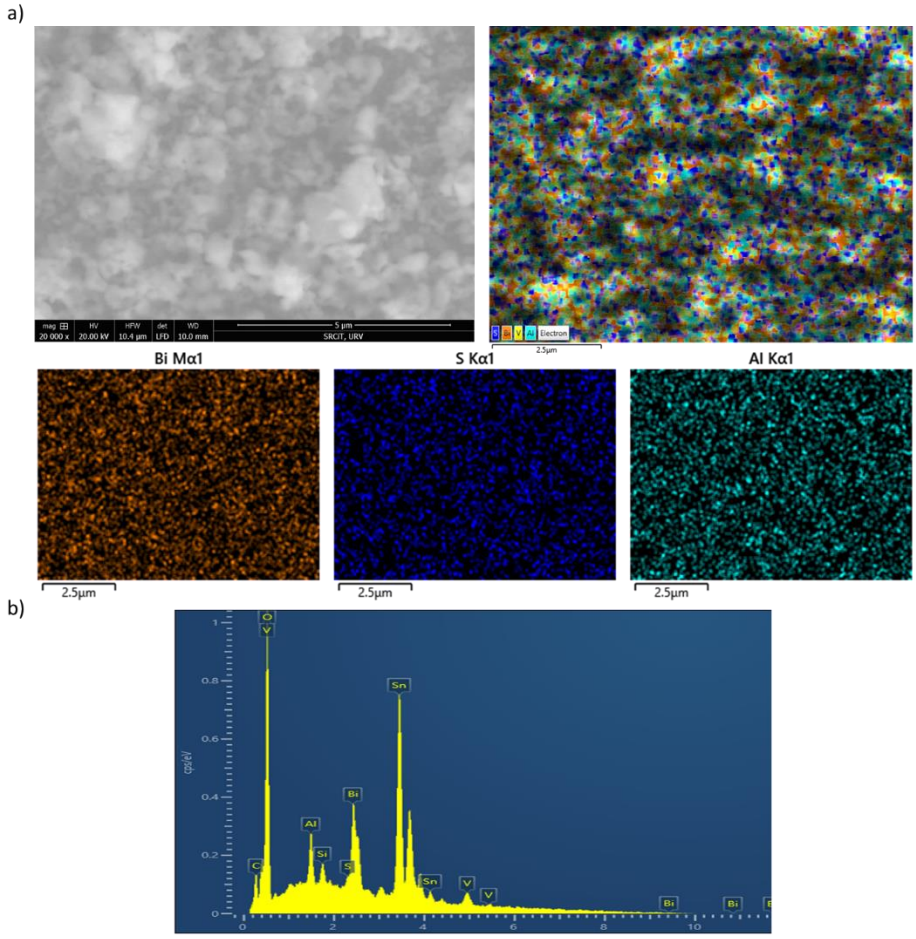

***Image 5**: a) ESEM image and mapping experiments of the prepared $BiVO_4@Al_2O_3$ electrode after the immobilization of MPTMS molecule, Aluminum (light blue), bismuth (orange), sulfur (blue); b) EDX analysis of the prepared $BiVO_4@Al_2O_3$ electrode after the immobilization of MPTMS molecule performed at 10 KeV.*

5.2.7. Photoelectrochemical tests using Ru@$BiVO_4$-MPTMS

The photoanodes prepared by airbrushing of an ink containing the $BiVO_4$ and MPTMS followed by immobilization of the Ru complexes by thiol-ene click reactions were tested in HZB using a custom Teflon cell in a three-electrode configuration. The prepared photoanodes were used as working electrode, Pt wire as counter electrode and Ag/AgCl electrode as reference electrode. The photoelectrochemical measurements were carried out under irradiation (AM1.5 illumination, 100 mW/cm^2) using a calibrated Xenon solar simulator. The electrolyte used was 0.1 M potassium borate buffer (KB_i, pH ~ 9).

Three different electrodes were tested: the bare **$BiVO_4$-MPTMS**, the **Ru_{VLA}@$BiVO_4$-MPTMS** and the **Ru_{WOC}2@$BiVO_4$-MPTMS**. However, no photocurrent was observed (Figure 21) and consequently, the other prepared photoanodes were not tested.

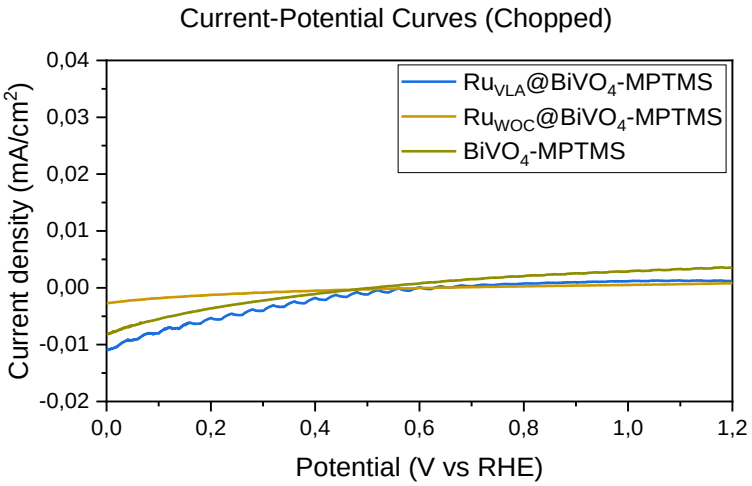

***Figure 21**: AM1.5 chopped photocurrent-voltage curves of the prepared photoanodes using 0.1 M potassium borate buffer.*

This lack of photoactivity was associated to the presence of defects and the low crystallinity of the $BiVO_4$ due to the absence of the annealing treatment.[64]

The screen-printed $BiVO_4$ electrode was thus heat treated at temperatures from 100 to 500 ºC and tested with the three electrodes configuration in 0.1 M KB_i buffer + 0.5 M Na_2SO_3 under chopped AM1.5 illumination (Figure 22) showing that the 500 ºC heat treated sample provided the highest photocurrent. Decreasing the heat treatment temperature led to a decrease in photocurrent and no photocurrent was observed when the treatment was performed at temperatures lower than 300 ºC.

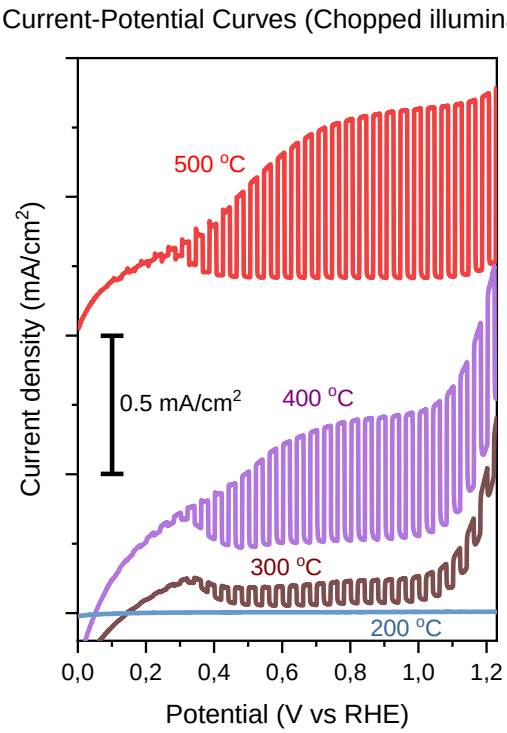

***Figure 22**: AM1.5 chopped photocurrent-voltage curves of the prepared photoanodes at different heat treatments temperature using 0.1 M potassium borate buffer and 0.5 M Na_2SO_3 as electrolyte.*

5.3. Conclusions

As a general conclusion, one new Ru water oxidation catalyst and two Ru complexes, a visible light absorber, and a water oxidation catalyst containing double bounds as coupling agent, were successfully synthesized, and characterized by NMR and MS spectroscopy.

The molecular Ru complexes were immobilized onto VTES or MPTMS modified $BiVO_4$. Using the VTES functional group, the Ru complexes were successfully immobilized with high Ru:Bi ratios except **Ru_{woc} 1** that resulted in a very low Ru:Bi ratio. Using MPTMS as functional group, the thiol-ene click reaction was successfully performed under both homogeneous and heterogeneous conditions using various Ru complexes.

Using the hybrid photoanodes prepared by electropolymerization, only an improvement of the photocurrent was obtained using **Ru_{woc}2@$BiVO_4$-VTES** photoanode, although the photocurrent remained lower than those reported using similar systems.

Using the hybrid photoanodes prepared by airbrushing of an ink containing the MPTMS group, no photocurrent was observed. This was attributed to the low carrier transport and low crystallinity of the $BiVO_4$ electrodes due to the absence of annealing treatment. This was confirmed when the photocurrent of the $BiVO_4$ electrodes was enhanced by the heat treatment temperature up to 500 ^oC.

Finally, a thin layer of Al_2O_3 was successfully deposited onto the prepared $BiVO_4$ electrodes by screen printing and functionalization using MPTMS was performed. Due to the lack of time, the immobilization of the Ru complexes and the testing of the corresponding samples could not be performed.

5.4. Experimental part

5.4.1. General considerations

Reagents: Commercially available reagents and solvents were purchased at the highest commercial quality from Sigma-Aldrich, Fisher scientific, Alfa Aesar and were used as received, without further purification, unless otherwise stated.

Analytical methods: ^{1}H, and $^{13}C\{^{1}H\}$ NMR spectra were recorded using a Varian Mercury VX 400 (400 and 100.6 MHz respectively). Chemical shift values (δ) were reported in ppm relative to residual solvent peak (^{1}H and $^{13}C\{^{1}H\}$), and coupling constants are reported in Hertz. The following abbreviations were used to indicate the multiplicity: s, singlet; d, doublet; t, triplet; q, quartet; m, multiplet; and bs, broad signal.

High-resolution mass spectra (HRMS) of the synthetized molecular complexes were recorded on an Agilent Time-of-Flight 6210 using ESI-TOF (electrospray ionization-time of flight). Samples were introduced to the mass spectrometer ion source by direct injection using a syringe pump and were externally calibrated using sodium formate. The instrument was operating in the positive ion mode.

Reactions were monitored by TLC carried out on 0.25 mm E. Merck silica gel 60 F254 glass. Developed TLC plates were visualized under a short-wave UV lamp (254 nm) and by heating plates that were dipped in potassium permanganate. Flash column chromatography was carried out using forced flow of the indicated solvent on Merck silica gel 60 (230-400 mesh).

The physicochemical properties of the synthesized $BiVO_4$ powders and of the $BiVO_4$ prepared electrodes were analyzed by X-Ray Diffraction (XRD, Bruker D8 ADVANCE X-ray diffractometer operating at 40 KV with Copper K-α

radiation (λ = 1.5406 Å)), scanning electron microscope (SEM) with energy Dispersive X-ray Spectroscopy (Hitachi S-4800), with Field Emission Scanning Electron Microscopy (FESEM) with Energy Dispersive X-ray Spectroscopy (Scios 2 Hi Vac de Thermofisher Scientific with EDX detector from Thermofisher), Environmental Scanning Electron Microscopy (ESEM) with Energy Dispersive X-ray Spectroscopy (FEI Quanta 600 with EDX detector from Oxford Systems) and X-ray photoelectron spectroscopy (SPECS FOCUS 500 monochromator, Al Kα radiation and *hv* = 1486.74 eV, and SPECS PHOIBOS 100 electron analyzer. All spectra were referenced with respect to the carbon C 1s peak at 284.8 eV and fitted using XPS PEAK software along with a Shirley background subtraction. The fitted spectra were further optimized by chi-square minimization).

The thermal treatment at 200 ^{o}C of the $BiVO_4$ electrode containing the Al_2O_3 layer was carried out in a muffle (Nabertherm muffle L15/13/B410 L-152T3RN3T).

5.4.2. Ru molecular complexes synthesis

One Ru visible light absorber (**Ru_{VLA}**) and two Ru water oxidation catalyst (**Ru_{WOC}**) were synthetized based on the state-of-the-art. The molecular catalysts were properly functionalized with double bounds as coupling agent in order to covalently immobilize them onto different semiconductors.

5.4.2.1. Non-commercial organic ligands synthesis

First, were synthetized the non-commercial organic ligands following different adapted reported procedures.

4,4'-Divinyl-2,2'-bipyridine (bpy_V)

The synthesis of the bipyridine ligand modified with vinyl groups was described in the **Chapter 4**.

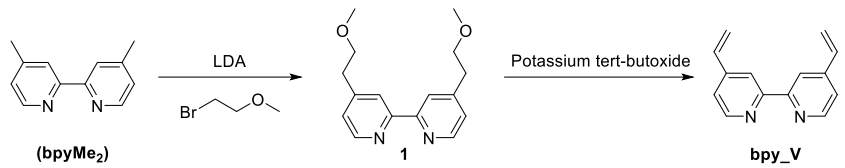

***Scheme 8**: Ligand **bpy_V** synthetic route.*

4-Hex-5-enyloxypyridine

The synthesis of the **4-Hex-5-enyloxypyridine** ligand was a one-step synthesis and it was described in the scheme below (Scheme 9):

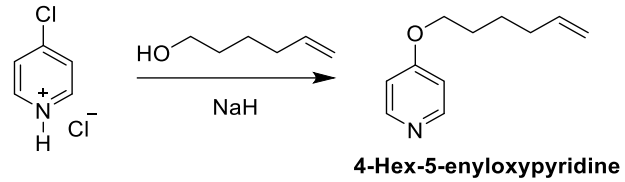

***Scheme 9**: Synthesis scheme of ligand **4-Hex-5-enyloxypyridine**.*

To synthetize the **4-Hex-5-enyloxypyridine** ligand, first, the 5-hexene-1-ol was deprotonated using NaH, and then, a nucleophilic aromatic substitution took place to obtain the final ligand.

4-Hex-5-enyloxypyridine: The synthesis was performed according to an adapted reported procedure.[74] To a solution of 5-hexen-1-ol (0.5 mL, 4.16 mmol) in dry DMSO (5.2 mL) was added NaH (60% dispersion in oil, 166.4 mg, 4.16 mmol). The mixture was stirred during 5 minutes, and then, 4-chloropyridine hydrochloric salt (312 mg, 2.08 mmol) was added. The reaction mixture was stirred overnight (18 h) at room temperature under argon. Then, water was added (20 mL), and the aqueous layer was extracted with CH_2Cl_2 (20 mL x 3). The organic layers were combined, dried over $MgSO_4$, and filtrated. The solvent was removed under vacuum. Purification by column chromatography on silica gel (Hexane/Ethyl acetate 7:3) gave pure **4-hex-5-enyloxypyridine** as yellowish oil obtained in 66 % yield (245 mg). **^{1}H NMR** (400

MHz, CD_2Cl_2) δ (ppm): 1.56 (quintet, J_{H-H} = 7.3 Hz, 2 H), 1.80 (m, 2H), 2.13 (q, J_{H-H} = 6.8 Hz, 2H), 4.01 (t, J_{H-H} = 6.5 Hz, 2H), 4.95-5.07 (m, 2H), 5.79-5.89 (m, 1H), 6.79 (dd, J_{H-H} = 1.6 Hz, J= 4.8 Hz, 2H), 8.37 (dd, J_{H-H} = 1.6 Hz, J= 4.8 Hz, 2H). These signals were in agreement with those reported in the literature.

2,2'-bipyridine-6,6'-dicarboxylic acid

The synthesis of the **2,2'-bipyridine-6,6'-dicarboxylic acid** ligand is one step synthesis described in the follow scheme (Scheme 10):

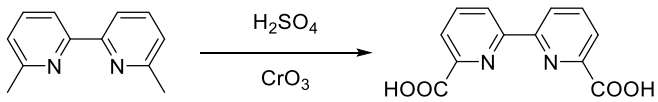

2,2'-bipyridine-6,6'-dicarboxylic acid

***Scheme 10**: Synthesis scheme of the **2,2'-bipyridine-6,6'-dicarboxylic acid** ligand.*

A strong oxidation of the 6,6'-dimethyl-2,2'-bipyridyl using H_2SO_4 and CrO_3 was performed to synthetize the **2,2'-bipyridine-6,6'-dicarboxylic acid** ligand.

2,2'-bipyridine-6,6'-dicarboxylic acid: The synthesis was performed according to an adapted reported procedure.[75] 6,6'-dimethyl-2,2'-bipyridyl (1.00 g, 5.43 mmol) was added slowly to concentrated sulphuric acid solution (20 mL). The resulting solution was cooled in an ice bath and chromium (VI) oxide (3.26 g, 32.6 mmol) was added in portion wise keeping the temperature below 40 °C. After the addition, the mixture was stirred overnight at room temperature, and then, quenched onto crushed ice. The white precipitate formed was filtered of, washed with cold water and dried under vacuum. The **2,2'-bipyridine-6,6'-dicarboxylic acid** was obtained in 85% yield (1.12 g). **^{1}H NMR** (400 MHz, dmso-d_6) δ (ppm): 8.17 (m, 4 H), 8.75 (dd, J_{H-H} = 1.3, 7.7 Hz, 2 H). These signals were in agreement with those reported in the literature.

5.4.2.2. Ru Visible light absorber (Ru_{VLA}) synthesis

The synthesis of the Ru visible light absorber (**Ru_{VLA}**) was performed with a bipyridine containing a vinyl group as a coupling agent (**bpy_V**). The schematic synthetic route for **Ru_{VLA}** is displayed in the Scheme 11.

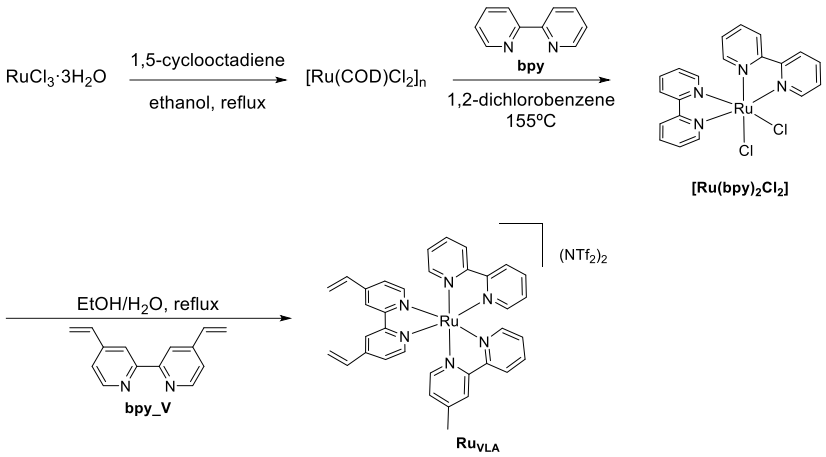

***Scheme 11**: Ruthenium visible light absorber (**Ru_{VLA}**) synthetic route.*

The synthesis for the **Ru_{VLA}** started with the commercial $RuCl_3 \cdot 3H_2O$ precursor. The first step was the preparation of the polymeric $[Ru(COD)Cl_2]_n$ by the reduction of $Ru^{III}Cl_3$ to Ru(II). The next step was the substitution of the COD ligand by two **bpy**, and the formation of $[Ru(bpyMe_2)_2Cl_2]$. Then, it is performed the substitution of the two chloride ligands by the modified bipyridine **bpy_V**. Finally, **Ru_{VLA}** was obtained in 64 % yield.

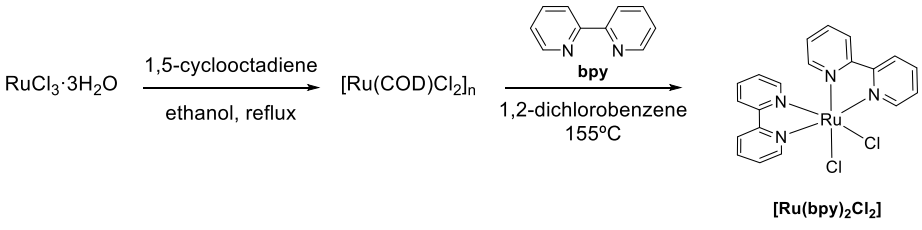

***Scheme 12**: Synthesis of **$[Ru(bpy)_2Cl_2]$**, two-step procedure.*

[Ru(bpy)$_2$Cl$_2$]: The synthesis was performed according to an adapted reported procedure.[76] $RuCl_3 \cdot 3H_2O$ (0.55 g, 2.7 mmol) was added to a mixture of 1,5-cyclooctadiene (3.25 mL, 27 mmol) and ethanol (12 mL). The mixture was refluxed under argon atmosphere for 64 h. After cooling to room temperature, resulting precipitates were collected by filtration and afforded dichlorido(1,5-cyclooctadiene)ruthenium(II) polymer ($[Ru(COD)Cl_2]_n$) **2** as brown solid obtained in 88 % yield (0.52 g). A suspension of $[Ru(COD)Cl_2]_n$ **2** (0.251 g, 0.89 mmol) and bpy **3** (0.281 g, 1.8 mmol) in o-dichlorobenzene (3.8 mL) was stirred at 155 ^oC under argon-gas atmosphere for 3.5 h. After cooling to room temperature, resulting precipitates were collected by filtration and dried in vacuo. [Ru(bpy)$_2$Cl$_2$] was obtained in 85 % yield (0.392 g) as black powders. This compound was used in the following step without any purification and identification.

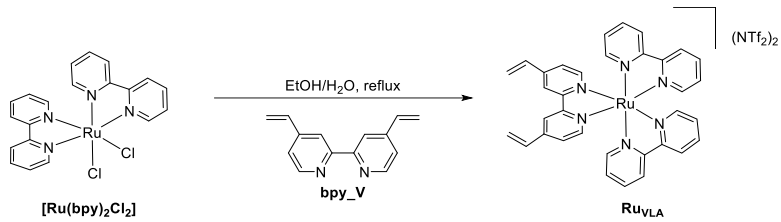

***Scheme 13**: Second step of synthesis of **Ru$_{VLA}$**.*

Ru$_{VLA}$: The synthesis was performed according to an adapted reported procedure.[77] A solution of the **bpy_V** ligand (104.13 mg, 0.5 mmol) and (290.6 mg, 0.6 mmol) of **[Ru(bpy)$_2$Cl$_2$]** in a 50 mL mixture of EtOH/H_2O (9:1 v:v) was heated at reflux in the dark under an argon atmosphere for 3 h. The solvents were removed, and the product was purified by silica gel column chromatography. Elution with an acetone/water mixture (8:2 v:v) removed the unreacted Ru(Me$_2$bpy)$_2$Cl$_2$. More rinsing with acetone/water/KNO_3 saturated aqueous solution (10 drops of KNO_3 added to a mixture of 80 mL of acetone and 20 mL of water) afforded the desired ester complex with NO_3^- as

counteranion. Pure fractions of the product were collected and evaporated under reduced pressure. The product was redissolved with dichloromethane. 0.2 g of $AgNTf_2$ was added and stirred during 10 min. $MgSO_4$ was added and the organic phase was filtered and dried to give the product **Ru_{VLA}** as a red powder obtained in 42 % yield (0.306 g). **^{1}H NMR** (400 MHz, CD_2Cl_2) δ (ppm): 5.76 (d, J_{H-H} = 10.9 Hz, 2 H), 6.24 (d, J_{H-H} = 17.5 Hz, 2 H), 6.86 (dd, J_{H-H} = 11.0, 17.5 Hz, 2 H), 7.46 (m, 6 H), 7.61 (d, J_{H-H} = 6.0 Hz, 2 H), 7.71 (d, J_{H-H} = 5.6 Hz, 2 H), 7.75 (d, J_{H-H} = 5.6 Hz, 2 H), 8.07 (td, J_{H-H} = 1.4, 7.9 Hz, 4 H), 8.37 (d, J_{H-H} = 1.7, 2H), 8.46 (d, J_{H-H} = 8.0, 4H). These signals were in agreement with those reported in the literature.

5.4.2.3. Ru water oxidation catalyst synthesis (Ru_{WOC})

Two different Ru water oxidation catalysts were synthetized. The ruthenium complex contained a 2,2'-bipyridine-6,6'-dicarboxylate (**bda**) ligand and two modified pyridines with a chain containing a double bound group, the **Ru_{WOC} 1** contained a ligand with a larger chain length, instead, the **Ru_{WOC} 2** contained a ligand with a smaller chain length.

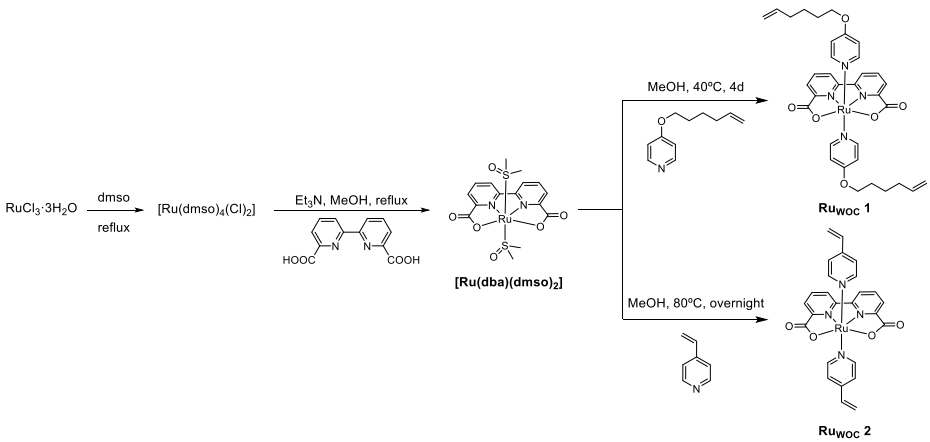

***Scheme 14**: Synthetic route scheme to synthetize both **Ru_{WOC}** complexes.*

The synthesis of both **Ru_{WOC}** was equal, except, for the last step in which a different pyridine ligand was used. The synthesis of the **Ru_{WOC}** started with the

commercial $RuCl_3 \cdot 3H_2O$ precursor. The first step was the preparation of the $[Ru(dmso)_4Cl_2]$ precursor. The next step was the substitution of two dmso, and two chlorine ligands for one bda ligand for the preparation of $[Ru(bda)(dmso)_2]$. Finally, the two remaining dmso ligands were substituted by two modified pyridines for the preparation of **Ru$_{woc}$ 1** and **Ru$_{woc}$ 2**. The **Ru$_{woc}$ 1** and **Ru$_{woc}$ 2** were obtained in 58 and 57 % yield, respectively.

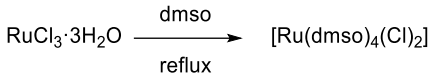

***Scheme 15**: Preparation of the **[Ru(dmso)$_4$(Cl)$_2$]**.*

cis-[Ru(dmso)$_4$Cl$_2$]: The synthesis was performed according to an adapted reported procedure.[78] $RuCl_3 \cdot 3H_2O$ (2.00 g, 7.65 mmol) was dissolved in ethanol (50 mL), and the mixture was heated to reflux for 3 h. Then, the mixture was filtrated on paper, and the ethanol was removed under vacuum. The remaining oil residue was dissolved in dmso (8 mL), and the mixture was heated at 150 ^{o}C for 2 hours. After cooling to room temperature, 60 mL of acetone were added and the precipitates formed were filtered, washed with acetone, and dried in vacuum yielding. The product was obtained in 32 % yield (1.16 g) a yellow solid. **^{1}H NMR** (400 MHz, D_2O) δ (ppm): 2.73 (s, 6 H, -CH_3), 3.41 (s, 6 H, -CH_3), 3.49 (s, 6 H, -CH_3), 3.51 (s, 6 H, -CH_3). These signals were in agreement with those reported in the literature.

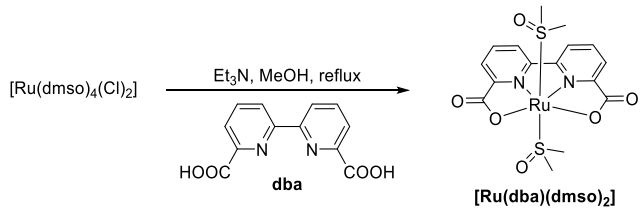

***Scheme 16**: Preparation of **[Ru(bda)(dmso)$_2$]**.*

[Ru(bda)(dmso)$_2$]: The synthesis was performed according to an adapted reported procedure.[79] A mixture of 2,2'-bipyridine-6,6'-dicarboxylic acid (122.1 mg, 0.5 mmol), [Ru(dmso)$_4$Cl$_2$] (242 mg, 0.5 mmol), and Et_3N (0.4 mL) in methanol (10 mL) under Ar atmosphere was refluxed during 4 h. After cooling the mixture to room temperature, precipitates were filtered and washed with methanol. The product **[Ru(bda)(dmso)$_2$]** was obtained in 47 % yield (117 mg) as dark brown solid. **^{1}H NMR** (400 MHz, dmso-d$_6$) d: 3.32 (s, 12 H), 8.04 (d, J_{H-H} = 7.7 Hz, 2 H), 8.16 (t, J_{H-H} = 7.8 Hz, 2 H), 8.65 (d, J_{H-H} = 8.0 Hz, 2 H). These signals were in agreement with those reported in the literature.

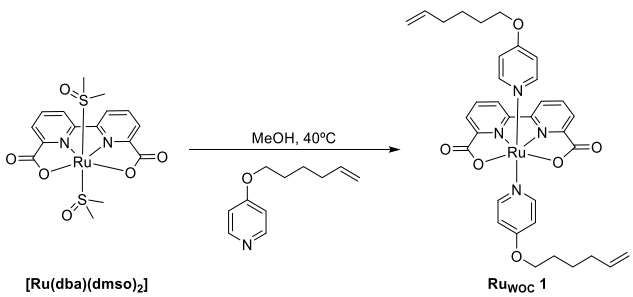

*Scheme 17. Synthesis scheme of the **Ru$_{woc}$ 1** complex.*

Ru$_{woc}$ 1: The synthesis was performed according to an adapted reported procedure.[80] Under Ar atmosphere, [Ru(bda)(dmso)$_2$] (100 mg, 0.2 mmol) was dissolved in methanol (20 mL) and the 4-Hex-5-enyloxypyridine ligand (83.7 mg, 0.47 mmol) was added to the reaction. The resulting mixture was heated at 40°C for 4 days. The reaction was cooled to room temperature and the solvent was evaporated under reduced pressure. The solid was dissolved with the minimum amount of methanol, and then, the product was precipitated by the addition of diethyl ether. Later, the precipitated was filtered and washed with diethyl ether. The product was obtained in 95 % yield (132.6 mg) as a black/purple powder. **^{1}H NMR** (400 MHz, CD_3OD) δ (ppm): 1.49 (m, 4 H), 1.74 (m, 4 H), 2.01 (m, 4 H), 3.99 (t, J_{H-H} = 6.4 Hz, 4 H), 4.97 (m, 4 H), 5.80 (m, 2 H), 6.78 (d, J_{H-H} = 7.2 Hz, 4 H), 7.57 (d, J_{H-H} = 7.2 Hz, 4 H), 7.88 (t, J_{H-H} = 7.9 Hz, 2 H),

8.06 (dd, J_{H-H} = 0.8, 7.7 Hz, 2 H), 8.58 (dd, J_{H-H} = 1.0, 8.1 Hz, 2 H). **$^{13}C\{^1H\}$ NMR** (100.6 MHz, CD_3OD) δ (ppm): 26.1, 29.1, 34.3, 69.8, 113.0, 115.3, 126.1, 127.1, 132.5, 139.5, 153.6, 157.7, 161.8, 167.3, 175.3. **ESI-HRMS:** Calculated for $C_{34}H_{36}N_4O_6Ru$. Exact: (M: 698.1678, M+H: 699.1757); Experimental: (M+H: 699.1754).

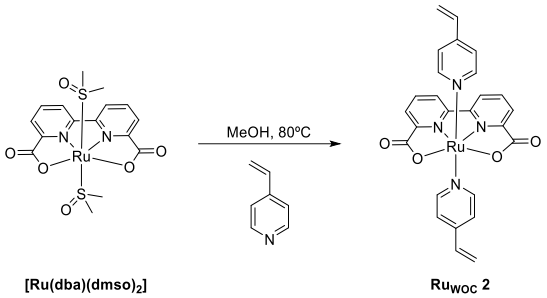

***Scheme 18**: Synthesis scheme of the **Ru_{WOC} 2** complex.*

Ru_{WOC} 2: The synthesis was performed according to an adapted reported procedure.[67] Under Ar atmosphere, [Ru(bda)(dmso)$_2$] (100 mg, 0.2 mmol) was dissolved in methanol (20 mL) and the 4-vinylpyridine ligand (49.4 mg, 51 µL, 0.47 mmol) was added to the reaction. The resulting mixture was heated at 80°C overnight. The reaction was cooled to room temperature, and the solvent was evaporated under reduced pressure. The solid was dissolved with the minimum amount of methanol, and then, the product was precipitated by the addition of diethyl ether, the precipitated was filtered and washed with diethyl ether. The product was obtained in 93 % yield (103.4 mg) as a dark red powder. **^1H NMR** (400 MHz, dmso-d_6) δ (ppm): 5.53 (d, J_{H-H} = 10.9 Hz, 2 H), 6.05 (d, J_{H-H} = 17.6 Hz, 2 H), 6.60 (q, J_{H-H} = 10.9, 17.6 Hz, 2 H), 7.32 (d, J_{H-H} = 6.8 Hz, 4 H), 7.64 (d, J_{H-H} = 6.8 Hz, 4 H), 7.89 (m, 4 H), 8.69 (d, J_{H-H} = 8.9 Hz, 2 H). These signals were in agreement with those reported in the literature.

5.4.3. Synthesis $BiVO_4$

The $BiVO_4$ particles were obtained according to an adapted reported procedure.[63] $Bi(NO_3)_3 \cdot 5H_2O$ (24.25 g, 50.0 mmol) and NH_4VO_3 (5.85 g, 50.0 mmol) were dissolved into 200 mL of a polyethylene glycol with a molecular weight of 200 (PEG-200) solution. The mixture was added to a 250 mL of a 2.0 M HNO_3 solution. Then, the mixture was stirred for 2 hours at room temperature. Later, 200 mL of a 1.5 M NaOH solution was dropwise added, and the mixture was subsequently heated at 100 ^oC for 2 h. The mixture was allowed to stand overnight. A precipitate was formed, it was collected and washed with distilled water in order to remove impurities. Finally, the precipitate was dried at 60 ^oC and then calcined at 400 ^oC giving the $BiVO_4$ particles in the monoclinic phase as a yellow powder.

5.4.4. $BiVO_4$ functionalization with VTES

The monoclinic $BiVO_4$ particles (15.00 g) were suspended for 1 h with 250 mL of 1 mM KOH solution, and then, it was washed with distilled water. Then, the hydroxylated $BiVO_4$ particles were suspended and refluxed at 100 ^oC for 2 h with 500 mL of a 0.1 M solution in isopropanol/H_2O (95:5). The precipitate formed was collected and washed with isopropanol in order to remove impurities. Finally, the precipitate was dried at 60 ^oC giving the product as a yellow powder.

5.4.5. General $BiVO_4$ Screen-Printing Ink Preparation

The ink preparation was performed in Solaronix by Dra. Stephanie Narbey and co-workers. $BiVO_4$ particles (3 g), Ethocel Std. 7 Ind. solution (9.6 g, 10%wt. in absolute ethanol), Ethocel Std. 45 Ind. solution (5.4 g, 10%wt. in absolute ethanol), terpineol (10.5 g) and absolute ethanol (50 mL) were placed in a 100 mL glass beaker equipped with a magnetic stir bar. The suspension was agitated for 1-2h prior to being sonicated (plunging probe) for 5 min. Then,

the mixture was transferred to two 250 mL zirconia grinding jars, each containing a set of zirconia beads (20 mm, 2 pcs; 10 mm, 32 pcs; and 5 mm, 160 pcs). A fraction of absolute ethanol was added to match the weight of the opposite grinding jar fitted on the planetary ball mill. The mixture was milled for 24 h using an alternating run of 9 min in each direction with 1 min pauses in between alternations. The content of the grinding jars was pipetted out to an evaporation beaker, and the grinding beads were rinsed with absolute ethanol, as well as the walls of the grinding jar. All rinsing waste was collected into the beaker so that all the materials are transferred out. Finally, ethanol was removed by evaporation under reduced pressure at 50°C, yielding to the desired ink.

5.4.6. General screen-printing procedure

The screen-printing procedure was performed in Helmholtz-Zentrum Berlin (HZB) by Abdi Fatwa and co-workers.[1] Fluorine doped tin oxide coated glass slide of thickness 2.2 mm, with a surface resistivity approximated of 7 Ω/sq from Sigma Aldrich has been used as substrate. To start with, a robust cleaning process was followed, as shown in the appended Figure 23.

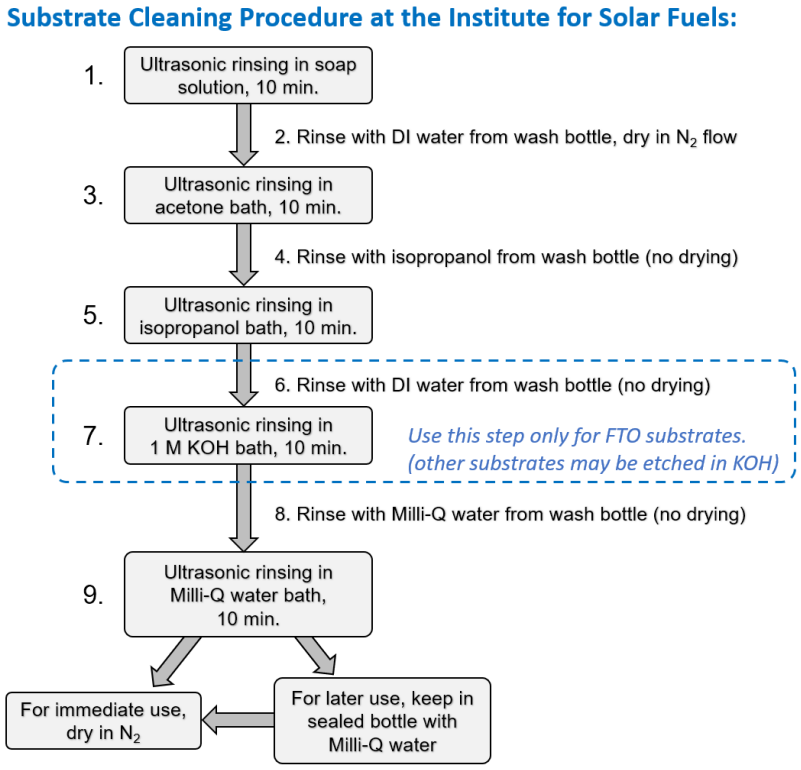

***Figure 23**: FTO substrate cleaning procedure.*

Once the substrate is cleaned and dried by N_2, the screen-printing process started by employing thin-film applicator equipment, COAT MASTER 509 MC from ERICHSEN GmbH & Co. KG (Figure 24). Different film applicator frames were available for making different thickness films and widths. The model model_360 96145 (60mm width, 10 microns thickness) film applicator frame was used to make thin films. The Microprocessor Controlled Film Applicator allowed for varying the processing speed of film application. The speed was optimized to achieve uniform thin films across the electrode surface. Once the parameters and film applicator frame were fixed on top of the FTO substrate, the $BiVO_4$ paste was filled across the tip of the frame. Using a microcontroller, one can control the distance and speed. Required thin film was achieved by choosing the corresponding film applicator frames.

The wet thin film needed a heat treatment process to get rid of the binders used to make it into a paste. Box furnace was used for the heat treatment process. The temperature was ramped up at a rate of 5 ^{o}C/min, and the wet films were heat-treated at 500 ^{o}C for two hours.

***Figure 24**: COAT MASTER 509 MC from ERICHSEN GmbH & Co. KG*

5.4.7. Electropolymerization of Ru complexes procedure

The prepared electrodes containing the $BiVO_4$-VTES were subjected to electropolymerization with the corresponding molecular complex.[65] The electropolymerization of the complexes was performed employing a three electrodes set-up with the $BiVO_4$-VTES, platinum wire and $Ag/AgNO_3$ as working, counter, and reference electrodes, respectively. The electrodes were submerged in an argon degassed acetonitrile solution containing the corresponding complex in a 0.5 mM concentration and tetraethylammonium hexafluorophosphate ($TBA{\cdot}PF_6$, 0.1 M) as electrolyte. Cyclic voltammetries were performed from 0 to -1.9 V *vs* $Ag/AgNO_3$, and the applied voltage was scanned multiple times with a scan rate of 100 $mV{\cdot}s^{-1}$. After 60 scans, the electrode was removed and washed with acetonitrile.

***Figure 25**: Image of the set-up used for the electropolymerization of the molecular complexes onto the electrode.*

5.4.8. Photoelectrochemical measurements

Photoelectrochemical measurements were performed using a custom-made one-chamber Teflon cell which is schematically represented in Figure 26. The cell had a transparent quartz window for sample illumination, the diameter of the illuminated area was d_{WE} = 6 mm, and this resulted in an illumination area of 0.28 cm^2. A three-electrode configuration set-up was used, with the $BiVO_4$ sample as the working electrode, an Ag/AgCl electrode (XR300, sat. KCl, Radiometer Analytical) as the reference electrode and a Pt wire as the counter electrode. Electrical contacting of the sample (i.e., the working electrode) was achieved by gluing a wire to the underlying transparent conducting oxide. EG&G Princeton Applied Research potentiostat (Model 273 A) coupled with a WACOM Class AAA solar simulator (AM1.5, 100 mW cm^{-2}) was used for the measurements. In the case where chopped AM1.5 illumination was used, an optical shutter (Uniblitz CS35 controlled with VCM-D1 driver) was placed in between the solar simulator and the photoelectrochemical cell. The electrolyte was 0.1 M potassium borate buffer (KB_i, pH 9.2) with or without the addition of 0.5 M Na_2SO_3 as hole scavengers. The applied potential was

converted to the reversible hydrogen electrode (RHE) using the Nernst equation (eq. 1) where $V_{Ag/AgCl}$ is the applied potential with respect to the Ag/AgCl reference electrode and $V^{\circ}_{Ag/AgCl}$ is the standard potential of reference electrode (0.199 V).

$$V_{RHE} = V_{Ag/AgCl} + (0.0591\ x\ pH) + V^{o}_{Ag/AgCl} \quad (eq.1)$$

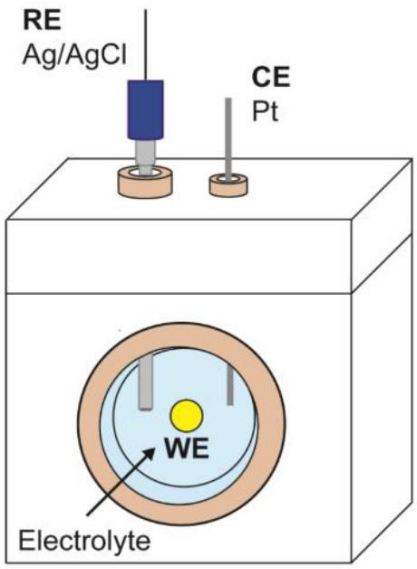

***Figure 26**: Schematic illustration of the three-electrode setup for the photoelectrochemical measurements, including the working electrode (WE), the reference electrode (RE) and the counter electrode (CE)*

5.4.9. General airbrushing procedure

The electrodes were manufactured by airbrushing a catalytic ink onto a FTO glass. The catalytic ink was constituted by various components: (i) $BiVO_4$ catalyst in the powder form; (ii) (3-mercaptopropyl)trimethoxysilane (10% w/w) (iii) NAFION® (dispersion, 5%wt in water and 1-propanol, from Sigma Aldrich) as a binder for the particles and ionomer, and (iv) ethanol as a carrier for the ink deposition, since the ink must be fluid to be uniformly spread on the area of interest. Each $BiVO_4$/MPTMS electrode was prepared with a

geometric area of 3 cm^2. The deposition process was performed by placing the FTO glass substrate on a heating plate at 100 ^oC to ensure the complete solvent evaporation. A pressure of 1.5 bar for the carrier gas (air) in the airbrush inlet was selected to have a continuous ink flow, avoiding undesired liquid drops. All the electrodes were then kept on the heating plate for 15 min before their use.

5.4.10. Deposition of Al_2O_3 thin layer

An adapted reported procedure was followed to deposit the thin layer of Al_2O_3.[73] The screen-printed $BiVO_4$ electrode was immersed into a solution of 48.5 mL isopropanol and 0.3 mL aluminum tri-sec-butoxide. The solution was stirred at 60 ^oC for 30 min. Then, the electrode was removed from the solution and heated in a muffle at 200 ^oC for 1 h in air obtaining the Al_2O_3 coated $BiVO_4$ electrode.

5.4.11. $BiVO_4/Al_2O_3$ functionalization with MPTMS

An adapted reported procedure was followed to immobilize the (3-mercaptopropyl)trimethoxysilane (MPTMS) onto the coated $BiVO_4$ electrodes.[73] The prepared coated ($BiVO_4@Al_2O_3$) electrode was immersed into 10 mL 95:5 EtOH/H_2O solution containing 0.1 M of MPTMS. Then, the solution was stirred overnight at 60 ^oC. Finally, the electrode was cleaned with EtOH and dried at 60 ^oC.

5.4.12. Immobilization of Ru complexes onto $BiVO_4$-MPTMS electrodes

An adapted reported procedure was followed to immobilize the Ru complexes onto the $BiVO_4$ prepared electrodes containing the MPTMS the prepared electrodes.[71] The prepared electrode was immersed in a solution of the corresponding Ru complex (0.02 mmol), DMPA (0.01 mmol, 2.6 mg) in EtOH

(15 mL). Then, the reaction mixture was stirred and irradiated with a 100 W Xe lamp overnight. Finally, the electrode was removed and cleaned with EtOH.

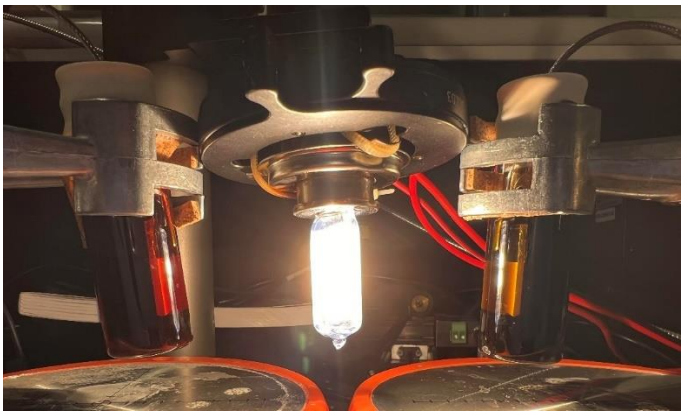

***Figure 27**: Image of the set-up used to perform the immobilization of the Ru complexes onto the electrode by thiol-ene click reaction.*

5.5. Supporting information

5.5.1. ^{1}H and $^{13}C\{^{1}H\}$ NMR spectra

^{1}H NMR (CD_2Cl_2, 400 MHz)

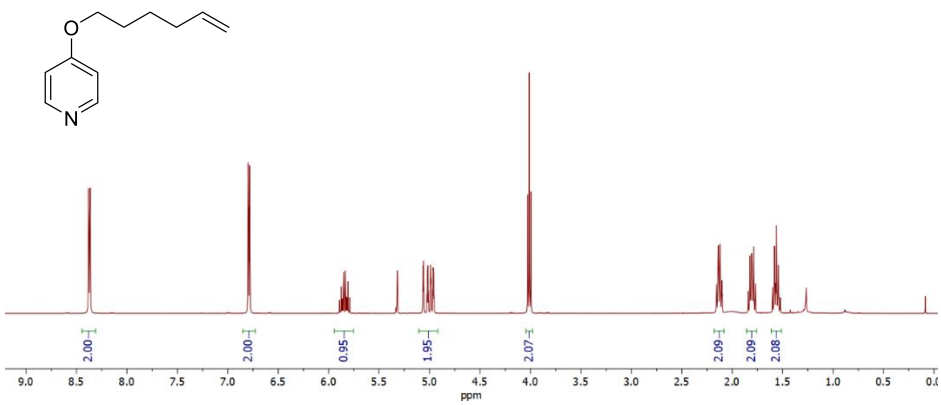

^{1}H NMR (dmso-d_6, 400 MHz)

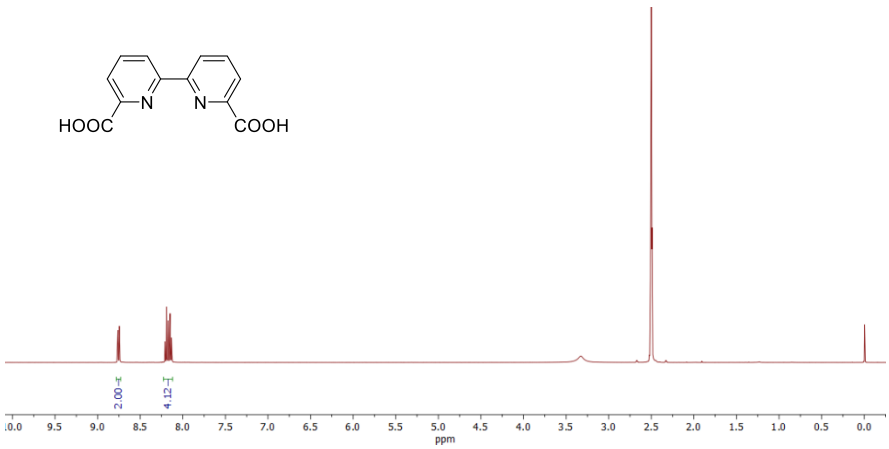

Chapter 5

^{1}H NMR (CD_2Cl_2, 400 MHz)

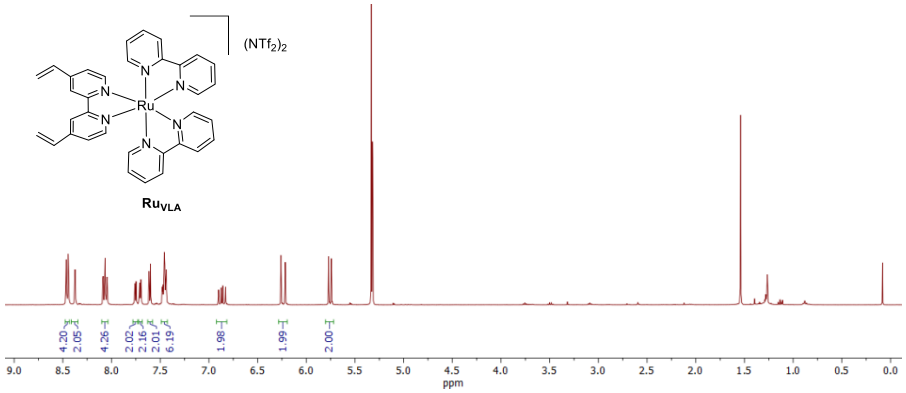

^{1}H NMR (D_2O, 400 MHz)

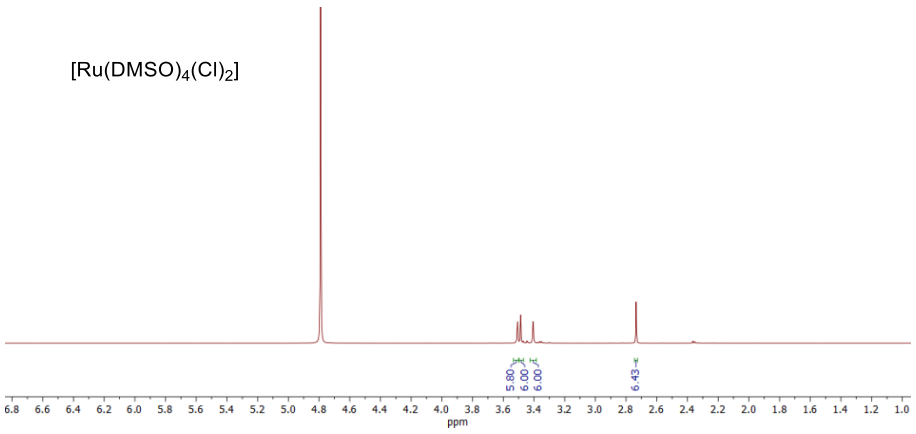

^{1}H NMR (dmso-d_6, 400 MHz)

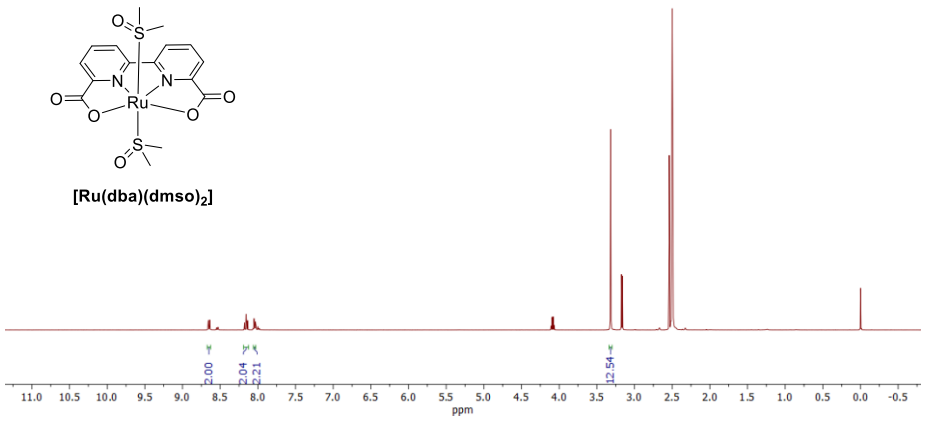

Molecular hybrid photoanode for efficient water oxidation

^{1}H NMR (CD_3OD, 400 MHz)

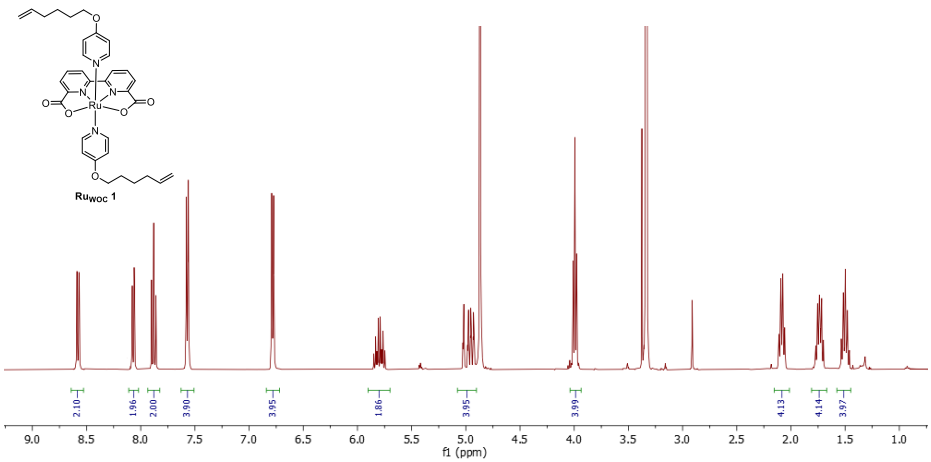

^{13}C NMR (CD_3OD, 400 MHz)

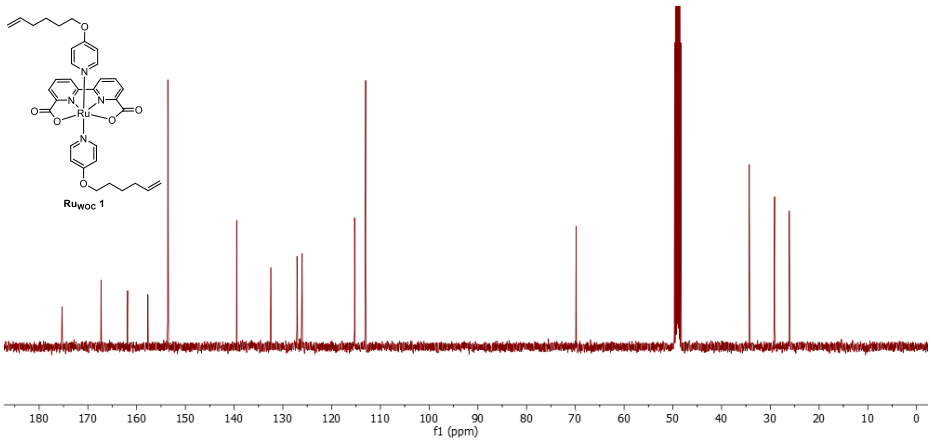

^{1}H NMR (CD_3OD, 400 MHz)

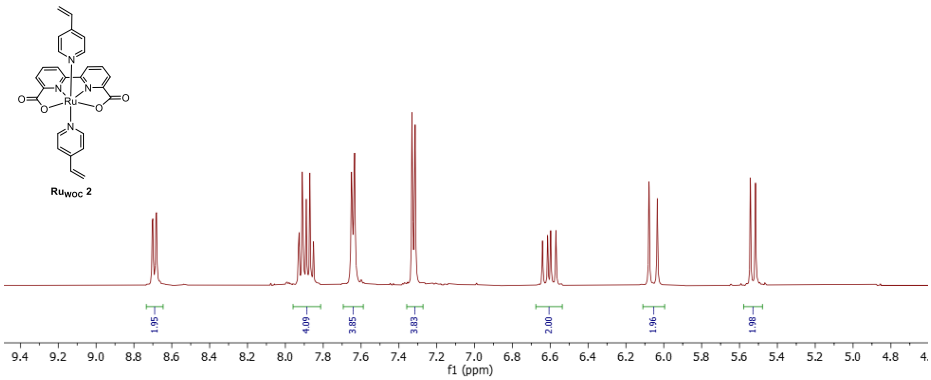

5.6. References

(1) Photoelectrocatalytic device for SUN-driven CO2 conversion into green CHEMicals https://cordis.europa.eu/project/id/862192/es (accessed 2022 -06 -12).

(2) Inoue, H.; Shimada, T.; Kou, Y.; Nabetani, Y.; Masui, D.; Takagi, S.; Tachibana, H. The Water Oxidation Bottleneck in Artificial Photosynthesis: How Can We Get through It? An Alternative Route Involving a Two-Electron Process. *ChemSusChem* **2011**, *4*, 173–179.

(3) Matheu, R.; Ertem, M. Z.; Gimbert-Suriñach, C.; Sala, X.; Llobet, A. Seven Coordinated Molecular Ruthenium-Water Oxidation Catalysts: A Coordination Chemistry Journey. *Chem. Rev.* **2019**, *119*, 3453–3471.

(4) Vereshchuk, N.; Matheu, R.; Benet-Buchholz, J.; Pipelier, M.; Lebreton, J.; Dubreuil, D.; Tessier, A.; Gimbert-Suriñach, C.; Ertem, M. Z.; Llobet, A. Second Coordination Sphere Effects in an Evolved Ru Complex Based on Highly Adaptable Ligand Results in Rapid Water Oxidation Catalysis. *J. Am. Chem. Soc.* **2020**, *142*, 5068–5077.

(5) Matheu, R.; Garrido-Barros, P.; Gil-Sepulcre, M.; Ertem, M. Z.; Sala, X.; Gimbert-Suriñach, C.; Llobet, A. The Development of Molecular Water Oxidation Catalysts. *Nat. Rev. Chem.* **2019**, *3*, 331–341.

(6) Duan, L.; Tong, L.; Xu, Y.; Sun, L. Visible Light-Driven Water Oxidation—from Molecular Catalysts to Photoelectrochemical Cells. *Energy Environ. Sci.* **2011**, *4*, 3296–3313.

(7) Niu, F.; Wang, D.; Li, F.; Liu, Y.; Shen, S.; Meyer, T. J. Hybrid Photoelectrochemical Water Splitting Systems: From Interface Design to System Assembly. *Adv. Energy Mater.* **2020**, *10*, 1900399.

(8) Ding, X.; Zhang, L.; Wang, Y.; Liu, A.; Gao, Y. Design of Photoanode-

Based Dye-Sensitized Photoelectrochemical Cells Assembling with Transition Metal Complexes for Visible Light-Induced Water Splitting. *Coord. Chem. Rev.* **2018**, *357*, 130–143.

(9) Ashford, D. L.; Gish, M. K.; Vannucci, A. K.; Brennaman, M. K.; Templeton, J. L.; Papanikolas, J. M.; Meyer, T. J. Molecular Chromophore-Catalyst Assemblies for Solar Fuel Applications. *Chem. Rev.* **2015**, *115*, 13006–13049.

(10) Li, F.; Yang, H.; Li, W.; Sun, L. Device Fabrication for Water Oxidation, Hydrogen Generation, and CO2 Reduction via Molecular Engineering. *Joule* **2018**, *2*, 36–60.

(11) Yu, Z.; Sun, L. Recent Advances in Dye-Sensitized Photoelectrochemical Cells for Solar Hydrogen Production Based on Molecular Components. *Energy Environ. Sci.* **2015**, *8*, 760–775.

(12) Zhang, B.; Sun, L. Artificial Photosynthesis: Opportunities and Challenges of Molecular Catalysts. *Chem. Soc. Rev.* **2019**, *48*, 2216–2264.

(13) Zhang, L.; Cole, J. M. Anchoring Groups for Dye-Sensitized Solar Cells. *ACS Appl. Mater. Interfaces* **2015**, *7*, 3427–3455.

(14) Brennan, B. J.; Llansola Portolés, M. J.; Liddell, P. A.; Moore, T. A.; Moore, A. L.; Gust, D. Comparison of Silatrane, Phosphonic Acid, and Carboxylic Acid Functional Groups for Attachment of Porphyrin Sensitizers to TiO2 in Photoelectrochemical Cells. *Phys. Chem. Chem. Phys.* **2013**, *15*, 16605–16614.

(15) Materna, K. L.; Crabtree, R. H.; Brudvig, G. W. Anchoring Groups for Photocatalytic Water Oxidation on Metal Oxide Surfaces. *Chem. Soc. Rev.* **2017**, *46*, 6099–6110.

(16) Bangle, R.; Sampaio, R. N.; Troian-Gautier, L.; Meyer, G. J. Surface Grafting of Ru(II) Diazonium-Based Sensitizers on Metal Oxides Enhances Alkaline Stability for Solar Energy Conversion. *ACS Appl. Mater. Interfaces* **2018**, *10*, 3121–3132.

(17) Lapides, A. M.; Ashford, D. L.; Hanson, K.; Torelli, D. A.; Templeton, J. L.; Meyer, T. J. Stabilization of a Ruthenium(II) Polypyridyl Dye on Nanocrystalline TiO2 by an Electropolymerized Overlayer. *J. Am. Chem. Soc.* **2013**, *135*, 15450–15458.

(18) Ashford, D. L.; Lapides, A. M.; Vannucci, A. K.; Hanson, K.; Torelli, D. A.; Harrison, D. P.; Templeton, J. L.; Meyer, T. J. Water Oxidation by an Electropolymerized Catalyst on Derivatized Mesoporous Metal Oxide Electrodes. *J. Am. Chem. Soc* **2014**, *136*, 6578–6581.

(19) Ashford, D. L.; Sherman, B. D.; Binstead, R. A.; Templeton, J. L.; Meyer, T. J. Electro-Assembly of a Chromophore–Catalyst Bilayer for Water Oxidation and Photocatalytic Water Splitting. *Angew. Chem. Int. Ed.* **2015**, *54*, 1–5.

(20) Wee, K.; Brennaman, M. K.; Alibabaei, L.; Farnum, B. H.; Sherman, B.; Lapides, A. M.; Meyer, T. J. Stabilization of Ruthenium(II) Polypyridyl Chromophores on Nanoparticle Metal-Oxide Electrodes in Water by Hydrophobic PMMA Overlayers. *J. Am. Chem. Soc* **2014**, *136*, 13514–13517.

(21) Hanson, K.; Losego, M. D.; Kalanyan, B.; Ashford, D. L.; Parsons, G. N.; Meyer, T. J. Stabilization of [Ru(Bpy)2(4,4'-(PO3H2)Bpy)]2+ on Mesoporous TiO2 with Atomic Layer Deposition of Al2O3. *Chem. Mater.* **2013**, *25*, 3–5.

(22) Vannucci, A. K.; Alibabaei, L.; Losego, M. D.; Concepcion, J. J.; Kalanyan, B.; Parsons, G. N.; Meyer, T. J. Crossing the Divide between

Homogeneous and Heterogeneous Catalysis in Water Oxidation. *Proc. Natl. Acad. Sci. U. S. A.* **2013**, *110*, 20918–20922.

(23) Hanson, K.; Losego, M. D.; Kalanyan, B.; Parsons, G. N.; Meyer, T. J. Stabilizing Small Molecules on Metal Oxide Surfaces Using Atomic Layer Deposition. *Nano Lett.* **2013**, *13*, 4802–4809.

(24) Lapides, A. M.; Sherman, B. D.; Brennaman, M. K.; Dares, C. J.; Skinner, K. R.; Templeton, J. L.; Meyer, T. J. Synthesis, Characterization, and Water Oxidation by a Molecular Chromophore-Catalyst Assembly Prepared by Atomic Layer Deposition. The "Mummy" Strategy. *Chem. Sci.* **2015**, *6*, 6398–6406.

(25) Treadway, J. A.; Moss, J. A.; Meyer, T. J. Visible Region Photooxidation on TiO2 with a Chromophore-Catalyst Molecular Assembly. *Inorg. Chem.* **1999**, *38*, 4386–4387.

(26) Youngblood, J. W.; Lee, S. H. A.; Kobayashi, Y.; Hernandez-Pagan, E. A.; Hoertz, P. G.; Moore, T. A.; Moore, A. L.; Gust, D.; Mallouk, T. E. Photoassisted Overall Water Splitting in a Visible Light-Absorbing Dye-Sensitized Photoelectrochemical Cell. *J. Am. Chem. Soc.* **2009**, *131*, 926–927.

(27) Zhao, Y.; Swierk, J. R.; Megiatto, J. D.; Sherman, B.; Youngblood, W. J.; Qin, D.; Lentz, D. M.; Moore, A. L.; Moore, T. A.; Gust, D.; Mallouk, T. E. Improving the Efficiency of Water Splitting in Dye-Sensitized Solar Cells by Using a Biomimetic Electron Transfer Mediator. *Proc. Natl. Acad. Sci. U. S. A.* **2012**, *109*, 15612–15616.

(28) Li, L.; Duan, L.; Xu, Y.; Gorlov, M.; Hagfeldt, A.; Sun, L. A Photoelectrochemical Device for Visible Light Driven Water Splitting by a Molecular Ruthenium Catalyst Assembled on Dye-Sensitized Nanostructured TiO2. *Chem. Commun.* **2010**, *46*, 7307–7309.

(29) Brlmblecombe, R.; Koo, A.; Dismukes, G. C.; Swlegers, G. F.; Spiccia, L. Solar Driven Water Oxidation by a Bioinspired Manganese Molecular Catalyst. *J. Am. Chem. Soc.* **2010**, *132*, 2892–2894.

(30) Gao, Y.; Ding, X.; Liu, J.; Wang, L.; Lu, Z.; Li, L.; Sun, L. Visible Light Driven Water Splitting in a Molecular Device with Unprecedentedly High Photocurrent Density. *J. Am. Chem. Soc.* **2013**, *135*, 4219–4222.

(31) Gao, Y.; Zhang, L.; Ding, X.; Sun, L. Artificial Photosynthesis-Functional Devices for Light Driven Water Splitting with Photoactive Anodes Based on Molecular Catalysts. *Phys. Chem. Chem. Phys.* **2014**, *16*, 12008–12013.

(32) Zhang, L.; Gao, Y.; Ding, X.; Yu, Z.; Sun, L. High-Performance Photoelectrochemical Cells Based on a Binuclear Ruthenium Catalyst for Visible-Light-Driven Water Oxidation. *ChemSusChem* **2014**, *7*, 2801–2804.

(33) Duan, L.; Fischer, A.; Xu, Y.; Sun, L. Isolated Seven-Coordinate Ru(IV) Dimer Complex with [HOHOH]- Bridging Ligand as an Intermediate for Catalytic Water Oxidation. *J. Am. Chem. Soc.* **2009**, *131*, 10397–10399.

(34) Jiang, Y.; Li, F.; Zhang, B.; Li, X.; Wang, X.; Huang, F.; Sun, L. Promoting the Activity of Catalysts for the Oxidation of Water with Bridged Dinuclear Ruthenium Complexes. *Angew. Chem. Int. Ed.* **2013**, *125*, 3482–3485.

(35) Ashford, D. L.; Song, W.; Concepcion, J. J.; Glasson, C. R. K.; Brennaman, M. K.; Norris, M. R.; Fang, Z.; Templeton, J. L.; Meyer, T. J. Photoinduced Electron Transfer in a Chromophore − Catalyst Assembly Anchored to TiO2. *J. Am. Chem. Soc* **2012**, *134*, 19189–19198.

(36) Wang, L.; Ashford, D. L.; Thompson, D. W.; Meyer, T. J.; Papanikolas, J.

M. Watching Photoactivation in a Ru(II) Chromophore − Catalyst Assembly on TiO2 by Ultrafast Spectroscopy. *J. Phys. Chem. C* **2013**, *117*, 24250–24258.

(37) Norris, M. R.; Concepcion, J. J.; Fang, Z.; Templeton, J. L.; Meyer, T. J. Low-Overpotential Water Oxidation by a Surface-Bound Ruthenium-Chromophore – Ruthenium-Catalyst Assembly. *Angew. Chem. Int. Ed.* **2013**, *52*, 13580–13583.

(38) Song, W.; Glasson, C. R. K.; Luo, H.; Hanson, K.; Brennaman, M. K.; Concepcion, J. J.; Meyer, T. J. Photoinduced Stepwise Oxidative Activation of a Chromophore-Catalyst Assembly on TiO2. *J. Phys. Chem. Lett.* **2011**, *2*, 1808–1813.

(39) Sherman, B. D.; Xie, Y.; Sheridan, M. V.; Wang, D.; Shaffer, D. W.; Meyer, T. J.; Concepcion, J. J. Light-Driven Water Splitting by a Covalently Linked Ruthenium-Based Chromophore–Catalyst Assembly. *ACS Energy Lett.* **2016**, *2*, 124–128.

(40) Hanson, K.; Torelli, D. A.; Vannucci, A. K.; Brennaman, M. K.; Luo, H.; Alibabaei, L.; Song, W.; Ashford, D. L.; Norris, M. R.; Glasson, C. R. K.; Concepcion, J. J.; Meyer, T. J. Self-Assembled Bilayer Films of Ruthenium(II)/Polypyridyl Complexes through Layer-by-Layer Deposition on Nanostructured Metal Oxides. *Angew. Chem. Int. Ed.* **2012**, *51*, 12782–12785.

(41) Ding, X.; Gao, Y.; Zhang, L.; Yu, Z.; Liu, J.; Sun, L. Visible Light-Driven Water Splitting in Photoelectrochemical Cells with Supramolecular Catalysts on Photoanodes. *ACS Catal.* **2014**, *4*, 2347–2350.

(42) Sheridan, M. V; Sherman, B. D.; Coppo, R. L.; Wang, D.; Marquard, S. L.; Wee, K.; Iha, N. Y. M.; Meyer, T. J.; Usp, P.; Prof, A.; Prestes, L. Evaluation of Chromophore and Assembly Design in Light-Driven

Water Splitting with a Molecular Water Oxidation Catalyst. *ACS Energy Lett.* **2016**, *1*, 321–236.

(43) Tamirat, A. G.; Rick, J.; Dubale, A. A.; Su, W. N.; Hwang, B. J. Using Hematite for Photoelectrochemical Water Splitting: A Review of Current Progress and Challenges. *Nanoscale Horizons* **2016**, *1*, 243–267.

(44) Yao, T.; An, X.; Han, H.; Chen, J. Q.; Li, C. Photoelectrocatalytic Materials for Solar Water Splitting. *Adv. Energy Mater.* **2018**, *8*, 1800210.

(45) Huang, Z.; Pan, L.; Zou, J.; Wang, L. Nanostructured Bismuth Vanadate-Based Materials for Solar-Energy-Driven Water Oxidation: A Review on Recent Progress. *Nanoscale* **2014**, *6*, 14044–14063.

(46) Kuang, Y.; Jia, Q.; Nishiyama, H.; Yamada, T.; Kudo, A. A Front-Illuminated Nanostructured Transparent BiVO4 Photoanode for >2% Efficient Water Splitting. *Adv. Energy Mater.* **2016**, *6*, 1501645.

(47) Kim, T. W.; Choi, K.-S. Nanoporous BiVO4 Photoanodes with Dual-Layer Oxygen Evolution Catalysts for Solar Water Splitting. *Science (80-.).* **2014**, *343*, 990–994.

(48) Hong, S. J.; Lee, S.; Jang, J. S.; Lee, J. S. Heterojunction BiVO4/WO3 Electrodes for Enhanced Photoactivity of Water Oxidation. *Energy Environ. Sci.* **2011**, *4*, 1781–1787.

(49) Shi, X.; Herraiz-cardona, I.; Bertoluzzi, L.; Lopez-varo, P.; Bisquert, J.; Park, J. H.; Gimenez, S. Understanding the Synergistic Effect of WO3-BiVO4 Heterostructures by Impedance Spectroscopy. *Phys. Chem. Chem. Phys.* **2016**, 9255–9261.

(50) Pagliaro, M.; Xu, Y. Artificial Photosynthesis over Graphene–Semiconductor Composites. Are We Getting Better? *Chem. Soc. Rev*

2014, *43*, 8240–8254.

(51) Zhang, B.; Wang, L.; Zhang, Y.; Ding, Y.; Bi, Y. Ultrathin FeOOH Nanolayers with Abundant Oxygen Vacancies on BiVO4 Photoanodes for Efficient Water Oxidation. *Angew. Chem. Int. Ed.* **2018**, *57*, 2248–2252.

(52) Ma, Y.; Kafi, A.; Pendlebury, S. R.; Formal, F. Le; Durrant, J. R. Photoinduced Absorption Spectroscopy of CoPi on BiVO4: The Function of CoPi during Water Oxidation. *Adv. Funct. Mater.* **2016**, *26*, 4951–4960.

(53) Wang, S.; He, T.; Yun, J.; Hu, Y.; Xiao, M.; Du, A.; Wang, L. New Iron-Cobalt Oxide Catalysts Promoting BiVO4 Films for Photoelectrochemical Water Splitting. *Adv. Funct. Mater.* **2018**, *28*, 1802685.

(54) Seabold, J. A.; Choi, K. S. Efficient and Stable Photo-Oxidation of Water by a Bismuth Vanadate Photoanode Coupled with an Iron Oxyhydroxide Oxygen Evolution Catalyst. *J. Am. Chem. Soc.* **2012**, *134*, 2186–2192.

(55) Zachäus, C.; Abdi, F. F.; Peter, L. M.; Van De Krol, R. Photocurrent of BiVO4 Is Limited by Surface Recombination, Not Surface Catalysis. *Chem. Sci.* **2017**, *8*, 3712–3719.

(56) Grau, S.; Berardi, S.; Moya, A.; MAtheu, R.; Cristino, V.; Vilatela, J. J.; Bignozzi, C. A.; Caramori, S.; Gimbert-Suriñach, C.; Llobet, A. A Hybrid Molecular Photoanode for Efficient Light- Induced Water Oxidation. *Sustain. Energy Fuels* **2018**, *2*, 1979–1985.

(57) De Respinis, M.; Joya, K. S.; De Groot, H. J. M.; D'Souza, F.; Smith, W. A.; Van De Krol, R.; Dam, B. Solar Water Splitting Combining a BiVO4

Light Absorber with a Ru Based Molecular Cocatalyst. *J. Phys. Chem. C* **2015**, *119*, 7275–7281.

(58) Liu, B.; Li, J.; Wu, H. L.; Liu, W. Q.; Jiang, X.; Li, Z. J.; Chen, B.; Tung, C. H.; Wu, L. Z. Improved Photoelectrocatalytic Performance for Water Oxidation by Earth-Abundant Cobalt Molecular Porphyrin Complex-Integrated BiVO4 Photoanode. *ACS Appl. Mater. Interfaces* **2016**, *8*, 18577–18583.

(59) Wang, Y.; Li, F.; Zhou, X.; Yu, F.; Du, J.; Bai, L.; Sun, L. Highly Efficient Photoelectrochemical Water Splitting with an Immobilized Molecular Co4O4 Cubane Catalyst. *Angew. Chem. Int. Ed.* **2017**, *129*, 7015–7019.

(60) Liu, Y.; Jiang, Y.; Li, F.; Yu, F.; Jiang, W.; Xia, L. Molecular Cobalt Salophen Catalyst-Integrated BiVO4 as Stable and Robust Photoanodes for Photoelectrochemical Water Splitting. *J. Mater. Chem. A* **2018**, *6*, 10761–10768.

(61) Kan, M.; Xue, D.; Jia, A.; Qian, X.; Yue, D.; Jia, J.; Zhao, Y. A Highly Efficient Nanoporous BiVO4 Photoelectrode with Enhanced Interface Charge Transfer Co-Catalyzed by Molecular Catalyst. *Appl. Catal. B Environ.* **2018**, *225*, 504–511.

(62) Gao, B.; Wang, T.; Fan, X.; Gong, H.; Li, P.; Feng, Y.; Huang, X.; He, J.; Ye, J. Enhanced Water Oxidation Reaction Kinetics on a BiVO4 Photoanode by Surface Modification with Ni4O4 Cubane. *J. Mater. Chem. A* **2019**, *7*, 278–288.

(63) Eda, S. I.; Fujishima, M.; Tada, H. Low Temperature-Synthesis of BiVO4 Nanorods Using Polyethylene Glycol as a Soft Template and the Visible-Light-Activity for Copper Acetylacetonate Decomposition. *Appl. Catal. B Environ.* **2012**, *125*, 288–293.

(64) Lamers, M.; Fiechter, S.; Friedrich, D.; Abdi, F. F.; Van De Krol, R. Formation and Suppression of Defects during Heat Treatment of BiVO4 Photoanodes for Solar Water Splitting. *J. Mater. Chem. A* **2018**, *6*, 18694–18700.

(65) Li, T. T.; Shan, B.; Meyer, T. J. Stable Molecular Photocathode for Solar-Driven CO2 Reduction in Aqueous Solutions. *ACS Energy Lett.* **2019**, *4*, 629–636.

(66) Kamata, R.; Kumagai, H.; Yamazaki, Y.; Sahara, G.; Ishitani, O. Photoelectrochemical CO2 Reduction Using a Ru(II)-Re(I) Supramolecular Photocatalyst Connected to a Vinyl Polymer on a NiO Electrode. *ACS Appl. Mater. Interfaces* **2019**, *11*, 5632–5641.

(67) Li, F.; Fan, K.; Wang, L.; Daniel, Q.; Duan, L.; Sun, L. Immobilizing Ru(Bda) Catalyst on a Photoanode via Electrochemical Polymerization for Light-Driven Water Splitting. *ACS Catal.* **2015**, *5*, 3786–3790.

(68) Ashford, D. L.; Sherman, B. D.; Binstead, R. A.; Templeton, J. L.; Meyer, T. J. Electro-Assembly of a Chromophore–Catalyst Bilayer for Water Oxidation and Photocatalytic Water Splitting. *Angew. Chem. Int. Ed.* **2015**, *54*, 4778–4781.

(69) Sherman, B. D.; Ashford, D. L.; Lapides, A. M.; Sheridan, M. V.; Wee, K. R.; Meyer, T. J. Light-Driven Water Splitting with a Molecular Electroassembly-Based Core/Shell Photoanode. *J. Phys. Chem. Lett.* **2015**, *6*, 3213–3217.

(70) Hoyle, C. E.; Bowman, C. N. Thiol – Ene Click Chemistry. *Angew. Chem. Int. Ed.* **2010**, *49*, 1540–1573.

(71) Krinsky, J. L.; Martínez, A.; Godard, C.; Castillón, S.; Claver, C. Modular Synthesis of Functionalisable Alkoxy-Tethered N-Heterocyclic Carbene

Ligands and an Active Catalyst for Buchwald-Hartwig Aminations. *Adv. Synth. Catal.* **2014**, *356*, 460–474.

(72) Filatova, E. O.; Konashuk, A. S. Interpretation of the Changing the Band Gap of Al2O3 Depending on Its Crystalline Form: Connection with Different Local Symmetries. *J. Phys. Chem. C* **2015**, *119*, 20755–20761.

(73) Jiang, W.; Yang, X.; Li, F.; Zhang, Q.; Li, S.; Tong, H.; Jiang, Y.; Xia, L. Immobilization of a Molecular Cobalt Cubane Catalyst on Porous BiVO4 via Electrochemical Polymerization for Efficient and Stable Photoelectrochemical Water Oxidation. *Chem. Commun.* **2019**, *55*, 1414–1417.

(74) Dreas-Wlodarczak, A.; Müllneritsch, M.; Juffmann, T.; Cioffi, C.; Arndt, M.; Mayor, M. Immobilization of Zinc Porphyrin Complexes on Pyridine-Functionalized Glass Surfaces. *Langmuir* **2010**, *26*, 10822–10826.

(75) Bozoklu, G.; Marchal, C.; Gateau, C.; Pécaut, J.; Imbert, D.; Mazzanti, M. Diastereoselective Self-Assembly of a Homochiral Europium Triangle from a Bipyoxazoline-Carboxylate Ligand. *Chem. Eur. J.* **2010**, *16*, 6159–6163.

(76) Ito, A.; Matsui, Y. Electrochemical and Spectroscopic Behaviors of a Novel Ruthenium(II) Complex with a Six-Membered Chelate Structure. *Inorg. Chem.* **2019**, *58*, 10436–10443.

(77) Gillaizeau-Gauthier, I.; Odobel, F.; Alebbi, M.; Argazzi, R.; Costa, E.; Bignozzi, C. A.; Qu, P.; Meyer, G. J. Phosphonate-Based Bipyridine Dyes for Stable Photovoltaic Devices. *Inorg. Chem.* **2001**, *40*, 6073–6079.

(78) Bratsos, I.; Alessio, E. Ruthenium Complexes. In *Inorganic Syntheses*; Wiley Blackwell, 2010; Vol. 35, pp 148–163.

(79) Wang, L.; Mirmohades, M.; Brown, A.; Duan, L.; Li, F.; Daniel, Q.; Lomoth, R.; Sun, L.; Hammarström, L. Sensitizer-Catalyst Assemblies for Water Oxidation. *Inorg. Chem.* **2015**, *54*, 2742–2751.

(80) Wang, D.; Marquard, S. L.; Troian-Gautier, L.; Sheridan, M. V.; Sherman, B. D.; Wang, Y.; Eberhart, M. S.; Farnum, B. H.; Dares, C. J.; Meyer, T. J. Interfacial Deposition of Ru(II) Bipyridine-Dicarboxylate Complexes by Ligand Substitution for Applications in Water Oxidation Catalysis. *J. Am. Chem. Soc.* **2018**, *140*, 719–726.

Chapter 6

General conclusions

Chapter 6

Considering the general objectives described in **Chapter 2** and according to the results described in **Chapters 3-5**, the following conclusions can be drawn:

- General conclusions Chapter 3:

The effect of various combinations of anions and cations in the ionic liquid electrolytes on the Fe-porphyrin catalyzed CO_2-electrochemical reduction was addressed. The obtained results indicated that:

(i) The anion structure does not have a relevant effect in the performance of Fe-porphyrin catalyzed CO_2 electroreduction.

(ii) The cation structure is crucial in the Fe-porphyrin catalyzed CO_2 electroreduction. An important decrease of overpotential was observed in the CO_2 reduction reaction using ionic liquids containing a proton in the C2 position of the imidazolium ring. The use of the dicationic ionic liquid electrolyte resulted in improved Fe-porphyrin catalyzed CO_2 electroreduction performance. The combination of dicationic IL and Fe-catalyst resulted in higher productivity at much lower CO_2 reduction overpotential than the system containing monocationic IL and Fe-catalyst. This behavior was attributed to the synergism created by the IL dication and anionic iron-porphyrin intermediates.

An optimization of the reaction conditions was performed showing that CO can be obtained selectively or within a syngas mixture (CO/H_2). Under optimized conditions, a CO production of 0.1 $mmol_{CO}\cdot h^{-1}$ was achieved at low potentials and tandem reactions involving CO_2 electroreduction coupled with different Pd catalyzed carbonylations were successfully performed. Furthermore, for the first time, a tandem approach involving the Rh catalyzed hydroformylation reaction was successfully performed with aldehyde yields up to a 78 %.

Our reaction system allowed the carbonylation reaction using low overpotentials and thus resulted in a high energetic efficiency (KWh/mol_{CO}). Our system required 0.08 W·h to produce 1 mmol of CO, much less energy than in previous reports.

- General conclusions Chapter 4:

A series of four new molecular complexes containing vinyl groups were successfully synthesized and characterized.

These molecular complexes were successfully immobilized onto VTES modified Cu_2O/SnO_2 or $CuGaO_2$ semiconductors. Higher molecular loadings were obtained using an electropolymerization pathway.

Evaluation of the hybrid photocathodes in photoelectrochemical tests revealed an enhancement of both carrier transport and catalytic activity with respect to the bare semiconductor. Concerning the Cu_2O/SnO_2 semiconductor, higher performance was achieved using the co-immobilized complexes than with the immobilization of only $\mathbf{Re_{CAT}}$ or $\mathbf{Ru_{VLA}}$. Concerning $CuGaO_2$ semiconductor, higher photovoltage generation and electron transfer were obtained with the supramolecular **RuRe1** and the binuclear **RuRe2** complexes than with the materials resulting from the co-immobilization procedure of the separate $\mathbf{Ru_{VLA}}$ and $\mathbf{Re_{CAT}}$ complexes. These hybrid photocathodes displayed an improvement of up to 30 % of faradaic efficiencies with respect to the bare semiconductor and enhanced the production of CO_2 reduction products (CO, HCOOH and C_{2+} alcohols).

The use of ionic liquid as electrolyte resulted in an enhancement of the CO_2 reduction selectivity (and suppression of H_2 evolution reaction) and thus in a higher total faradaic efficiencies to CO_2 reduction products, and additionally, the stability of these systems was improved.

Chapter 6

- General conclusions Chapter 5:

Ru water oxidation catalysts and one Ru visible light absorber containing vinyl groups were successfully synthesized and characterized.

The Ru complexes were immobilized via two immobilization approaches. In the first approach, VTES was used as linker, and the Ru complexes were successfully immobilized by electropolymerization. High Ru:Bi molar ratios were obtained, except for **Ru_{woc} 1**, which resulted in low Ru:Bi molar ratio. In the second approach, MPTMS was used as linker. The Ru complexes were successfully immobilized using the thiol-ene click reaction. The results demonstrated that this reaction was successfully performed under both homogeneous and heterogeneous conditions.

A reaction set-up for photoelectrochemical water oxidation was developed during the last period of this thesis, and the preliminary water oxidation tests using the hybrid photoanodes prepared by electropolymerization revealed a small improvement of the photocurrent. Optimization of the system is still required as the photocurrent obtained is lower those previously reported.

No photocurrent was observed using the hybrid photoanodes prepared by airbrushing of the ink containing the MPTMS group. This result was attributed to the need of annealing treatment to increase the carrier transport and crystallinity of the $BiVO_4$.

As an alternative approach, a thin layer of Al_2O_3 was successfully deposited onto the prepared $BiVO_4$ electrodes and the functionalization with MPTMS was performed. Due to the lack of time, the application of this material in the immobilization of the Ru complexes and their application in the H_2O oxidation photoelectrochemical tests could not be performed.

Appendix

Appendix

Publications

- **"Solar-driven CO_2 reduction catalysed by Hybrid Supramolecular Photocathodes and enhanced by Ionic Liquids"** Roger Miró, Hilmar Guzmán, Cyril Godard, Aitor Gual, Federica Zammillo, Thomas J. S. Schubert, Boyan Iliev, Angelica Chiodoni, Simelys Hernandez, and Miriam Diaz de los Bernardos. *Manuscript Submitted.*
- **"Synergism between iron porphyrins and dicationic imidazolium ionic liquids: CO_2 electrochemical reduction to CO and tandem carbonylation"** Roger Miró, Emma Fernández-Llamazares, Cyril Godard, Miriam Díaz de los Bernardos, and Aitor Gual. *Manuscript Submitted.*

Conferences

6-10th June 2022 *Turin, Italy*	*11th European Conference on Solar Chemistry and Photocatalysis: Environmental Applications (SPEA)*. **Oral communication** entitled "Facile Electropolymerization Procedure to Immobilize Molecular Catalysts onto $CuGaO_2$ and its Utilization in CO_2 Reduction". Roger Miró, Hilmar Guzmán, Cyril Godard, Aitor Gual, Federica Zammillo, Angelica Chiodoni, Simelys Hernandez, and Miriam Diaz de los Bernardos. **Awarded** with the "*Oral prize*"
22-25th September 2019 *Tarragona, Spain*	*4th EuCheMS Conference on Green and Sustainable Chemistry.* **Poster communication** entitled "Rh-Catalysed Asymmetric Carbonylation of 1,1-Disubstituted Olefins" Roger Miró, Anton Cunillera, Cyril Godard, Montserrat Diéguez, and Oscar Pàmies

UNIVERSITAT
ROVIRA i VIRGILI

eurecat
Technology Centre of Catalonia